Preparation of Enhanced Visible and Near Infrared Lights Responsive Photocatalysts for Environmental Cleanup

PREPARATION OF ENHANCED VISIBLE AND NEAR INFRARED LIGHTS RESPONSIVE PHOTOCATALYSTS FOR ENVIRONMENTAL CLEANUP

（可視光および近赤外光応答高活性光触媒の創製と環境浄化への応用）

A Thesis

Submitted for the Degree of

DOCTOR OF PHILOSOPHY (Ph.D.)

By

Xiaoyong Wu

Supervisor: Prof. Tsugio Sato

Graduate School of Environmental Studies

TOHOKU UNIVERSITY

Aoba-ku, Sendai, 980-8577, JAPAN

JANUARY 2015

Contents

ACKNOWLEDGMENTS

First and foremost, I would like to express my sincerest gratitude towards my supervisor, **Prof. Tsugio Sato**, whose profound knowledge and vast experience have inspired and enriched me at every stage of my study and life. Moreover, during my doctor application to Tohoku University in 2011, I often disturbed him by some tiny things, but he always helped me as possible as he can without any complaint. Without his kind acceptance and nice help, I could not have this precious opportunity to study in Japan, fulfilling one of my dreams. Without his generous support in these past years, I could not have the chance to fulfill this thesis. So thanks a lot.

Second, I wish to greatly appreciate **Associate Prof. Shu Yin** for his invaluable discussions in my research, considerate care and help in all aspects. In particular, when I first came to Japan, I was unknown to so many things, especially for my research. At this hard moment, his tireless explanation and constant encouragement motivated and guided me to the road of photocatalyst.

I am very thankful to **Prof. Masato Kakihana** and **Prof. Toshiaki Yoshioka** for their valuable discussion, constructive suggestions and timely help.

I hope to acknowledge the secretary of our lab, **Ms. Saori Sato**, for her

warm and thoughtful help.

My honest thanks to all of my colleagues in Sato lab for keeping friendly, helpful atmosphere inside and outside of the lab such as **Dr. Chongshen Guo, Dr. Huihui Li, Dr. Bin Liu, Dr. Takeshi Kimura, Dr. Qiang Dong, Dr. Miyuki Tanaka, Mr. Ryusuke Akita, Mr. Shunsuke Tonouchi, Ms. Kimie Imakawa, Mr. Hisaya Hama** to name a few.

I owe my due respect and honest regards to **my beloved family** for their selfless dedication and unconditional trust and care.

I also would like to convey my appreciation to "**China Scholarship Council**" for providing the scholarship to support my study and life in Japan.

Last but not least, many thanks to **anyone that I have not mentioned here but helped me in the past decades**. In my past life, so many names and faces have passed through and left trace or not in my memory. Nevertheless, all of you have encouraged me not only to be a doctor but also to be a person.

Xiaoyong Wu

12:15, 21/11/2014, Sendai

Chapter 1 GENERAL INTRODUCTION

With industrialization and urbanization increasing, the abusive use and dispose of pharmaceutical and pesticides, personal care products, surfactants, industrial chemicals, and combustion byproducts, etc. have become more and more serious. Subsequently, a great amount of contaminants have been undesirably released and accumulated in groundwater, surface water, sewage water, drinking water and air, which have greatly exceeded the self-cure function of nature.[1,2] In order to alleviate or solve these increasing pollutants' problem, two main techniques, physical treatment approaches (ultrafiltration, adsorption, coagulation, etc.) and chemical degradation methods (supercritical water oxidation, the Fenton method, ozone/UV radiation/H_2O_2 oxidation, sonochemical destruction, electrochemical treatment, semiconductor photocatalysis, enzymatic treatment ways, etc.), have been employed in our daily life.[3,4] Among them, semiconductor photocatalysis has fascinated considerable attention for environmental cleanup in recent years, since it is a green chemical method for degrading majority of contaminants in water and air with the activation of natural solar light in the ambient conditions. In this case, the development of high efficiency of solar light induced photocatalysts reasonably becomes a hot topic for researchers. To date, two dominant strategies were proposed to meet this demand. The first method is to modify the most promising photocatalysts (TiO_2, $NaTaO_3$, etc.) by doping, sensitizing, loading and coupling with other semiconductors or substances. The other way is developing other new efficiency compounds (BiOX, $BiWO_6$, etc.) for photocatalysis utilization.[5,6]

In this chapter, a general introduction of photocatalysis and relevant environmental cleanup applications was presented. In addition, the structure and properties of popular photocatalysts with corresponding drawbacks were also depicted. Furthermore, the brief review of the strategies to improve the visible and NIR lights responsive photocatalysts was given. Finally, the research objectives of this thesis were induced as well.

1.1 Definition of photocatalysis

With the development of humans' science and technology, semiconductors play a more and more essential role in our daily life and extensively used as modern electronics, including solar cells, light-emitting diodes, transistors, sensor, quantum dots and digital and analog integrated circuits, etc..[7-10] Semiconductor is a unique substance, the electrical conductivity of which is between conductor (such as metals) and insulator (such as glass). The conductivity of semiconductor usually increases with increasing temperature, which is opposite to that of metal, and insulator presents no conductivity. The peculiar electronic structure of semiconductor is represented by its valence band (VB) and conduction band (CB). The band gap of semiconductor is formed by the utmost of conduction band and the lowest of the valence band. As for the semiconductor photocatalyst, the relative band positions of VB and CB are of great importance since they can determine the light-harvesting capability and the redox performance of a photocatalyst. [11-15]

The concrete definition of photocatalysis can be obviously observed in Fig. 1-1. From the viewpoint of semiconductor photochemistry, the role of photocatalyst is used to initiate or boost some reduction and oxidation reactions with the existence of irradiated semiconductor. When the semiconductor photocatalyst is irradiated by a light whose energy is equal to or greater than the band gap (E_g) of semiconductor, the electron (e^-) in the VB can be excited to the CB by leaving a positive hole (h^+) in the VB (Eq. 1-1). After that, three possible processes maybe happened. The first one is that the photogenerated electron-hole pairs will be captured by the defects in bulk and/or on the surface of semiconductor. The second process is the recombination of photoinduced electron-hole pairs to release the heat or the light again. The last way is the migration of photoexcited electron-hole pairs to the surface of semiconductor. The first two processes are commonly recognized as deactivation ways since the photogenerated electron-hole pairs can't be utilized for the photocatalytic redox reaction. Only the third migration process is beneficial for the photocatalytic

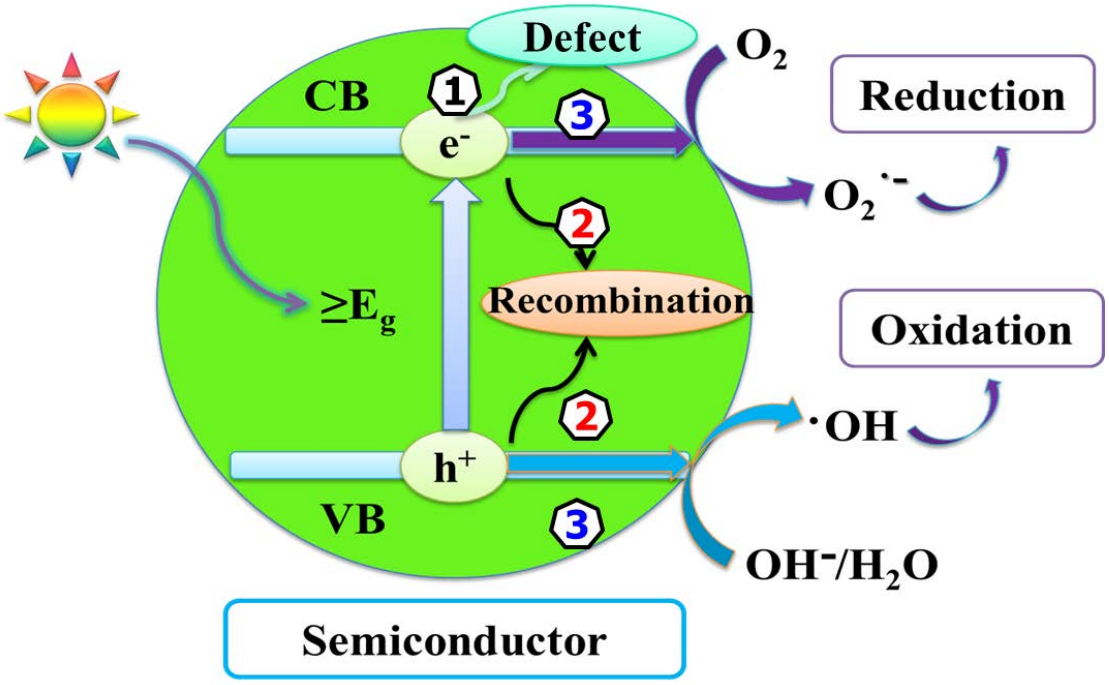

Figure 1-1. Possible mechanism for the semiconductor photocatalysis.

performance. In this process, the photogenerated hole in the valence band (h_{VB}^+) can react with OH^- or water on the surface of semiconductor to produce ·OH radicals (Eq. 1-2 and 1-3), which is one of the most active oxidants. The as-induced ·OH radicals are able to further oxidize the organic contaminants with mineralization producing CO_2 and H_2O (Eq. 1-4). Meanwhile, the photoproduced electron in the conduction band (e_{CB}^-) can be trapped by the absorbed O_2 on the surface of semiconductor to form superoxide radical anion ($O_2^{\cdot-}$) (Eq. 1-5). In addition, the $O_2^{\cdot-}$ enables to further react with H^+ to produce hydroperoxyl radical (·OOH) (Eq. 1-6), finally leading to the production of H_2O_2 (Eq. 1-7). The above mentioned oxygen related species may also dedicate to the oxidation of pollutants as well as the reduction of contaminants. (Eq. 1-8 and 1-9). Therefore, under the irradiation of suitable light sources, the semiconductor photocatalysts can be greenly used to degrade organic pollutants and toxic gases in the water and air. [16-23]

$$\text{Photocatalyst} + h\nu \rightarrow h_{VB}^+ + e_{CB}^- \quad (1\text{-}1)$$

$$h_{VB}^+ + OH^- \rightarrow \cdot OH \quad (1\text{-}2)$$

$$h_{VB}^+ + H_2O \rightarrow \cdot OH + H^+ \quad (1\text{-}3)$$

$$\cdot OH + \text{pollutant} \rightarrow \text{Intermediate} \rightarrow CO_2 + H_2O \quad (1\text{-}4)$$

$e_{CB}^- + O_2 \rightarrow \cdot O_2^-$ (1-5)

$\cdot O_2^- + H^+ \rightarrow \cdot OOH$ (1-6)

$\cdot OOH + \cdot OOH \rightarrow H_2O_2 + O_2$ (1-7)

$\cdot O_2^-$ + pollutant $\rightarrow$ Oxidation/reduction products (1-8)

$\cdot OOH/ H_2O_2$ + pollutant $\rightarrow$ Oxidation/reduction products (1-9)

1.2 Environmental applications of photocatalysts

Nowadays, the environmental pollution and energy consumption problems become more and more serious. Subsequently, the semiconductor photocatalysis, as a green chemical method to solve these issues, has fascinated increasing attention and has also been extensively used in many areas such as print, medicine, cosmetics, food, hospital, water and air purification, energy conversion and so on. Herein, the applications of photocatalyst for water decontamination, air purification, water splitting and self-cleaning have been briefly introduced as follows.

1.2.1 Water decontamination

In modern times, the abusive discharging of emerging organic contaminants such as phenolic compound, hormones, pharmaceutical substances, pesticides and personal care products, etc. in the water environment becomes extremely serious especially for the volatile organic compounds (VOC), owing to the fast development of science and technology with the sacrifice of our living environment.[1] In this case, lots of methods including physical processes (filtration, sedimentation, distillation, etc.), biological processes (slow sand filters, biologically active carbon, etc.) and chemical strategies (flocculation, photocatalysis, etc.) have been employed to purify this contaminated water to meet the requirements of medical, pharmacological, chemical and industrial applications.[24] Among them, the photocatalysis has attracted peculiar interest over other methods, due to its low cost, environmental benign, high efficiency and so on.[25-27] Enormous research on water decontamination by semiconductor photocatalysis has been carried out.[28-32] Senthilnatan and Philip investigated the

decomposition of lindane, an organochlorine pesticide, by different TiO_2 photocatalysts with the irradiation of light.[33] Pelaez et al. also reviewed many researches about water purification by using visible light induced photocatalysts.[34] As for practical photocatalytic water treatment application, Fig. 1-2 demonstrates a truly used contaminated ground water system in Japan to remove volatile organic compounds (VOC).[35]

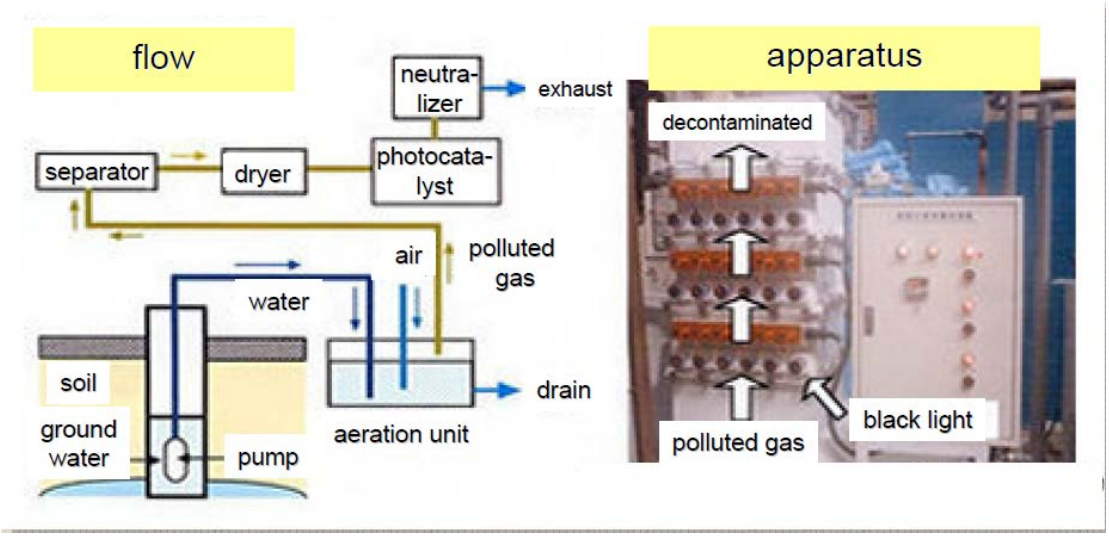

Figure 1-2. Schematic of contaminated ground water treatment system.[35]

Besides the application of organic pollutant treatment, photocatalysis can also be utilized in remediation of metal contamination,[36,37] disinfection[38-41] and oxidation of arsenite,[42] etc. The solar light responsive photocatalytic disinfection is even expected as a promising strategy to generate drinking water for developing countries.[43]

1.2.2 Air purification

Up to date, the air pollution has become one of the most serious environmental problems in our daily life and much increasing attention has been paid to control or alleviate this issue. The air pollution mainly contains outdoor and indoor air pollution. The outdoor air pollution can also divide into natural and man-made ones. The natural outdoor air pollution is dominantly originated from the volcanoes, oceans, biological decay, lightning strikes and forest fires to release oxides of sulphur and nitrogen. However, most of these released air pollution is under the control of natural self-cure

ability. What's of more concerns should be the man-made pollution. The man-made outdoor air pollution is generally produced by the burning of fossil fuels (oil, coal and gas) from industries, power stations, homes and road vehicles. The air pollutant substances mainly consist of nitrogen oxides, carbon monoxide, sulphur dioxide, lead, particulate matter and volatile organic compounds (VOCs).[44-46]

Although lots of methods have been proposed to treat this outdoor air pollution, photocatalysis as a green chemical strategy is still a promising technology for air pollution treatment, due to its high efficiency, low cost, simple treatment, environmental benign. The photocatalysis can deal with various kinds of toxic gases such as car exhausts NO_x, SO_x, VOCs, etc.[47-51] In the presence of light, semiconductor photocatalysts can generate hydroxyl radicals and holes, which enable to effectively react with the harmful gases to produce other harmless materials. In addition, the photocatalyst reacts as a catalyst in the chemical reaction so that it can perform for a long time without the consumption of mass.[52,53] Fig. 1-3 presents a practical application of photocatalyst to deal with the vehicle released harmful NO_x gas using natural solar light as the light source.[54,55]

Figure 1-3. The usage of photocatalyst painting on the road to eliminate NO_x toxic gas from the vehicles in Japan.

On the other hand, the indoor air pollution is another great concerned issue. Because the indoor air pollution can cause serious diseases (asthma and atopy) for people or even lead to death. Furthermore, most of the people in the world should spend large part of time in indoor house and have little control over the exposure time and atmosphere in the workplace. In this case, a healthy indoor atmosphere is

extremely essential for us. The indoor air pollution mainly arises from the emissions of building insulation, furniture, carpets, wall paintings, decorations and also factories, producing from pumps, dryers, tanks and other process equipment. The indoor air contaminants contain carbon monoxide, toluene, formaldehyde, mold spores and bacteria, all of which are harmful for our health.[56-58] In order to control this contamination, three general strategies have been proposed, including using air purifiers, increasing the air exchange rate and controlling pollution sources.[59] Nowadays, the utilization of air purifiers becomes popular to remove the indoor air pollutants.[60,61] However, this method simply transfers these contaminants to other phases or just absorbs them instead of eliminating them permanently. Under this circumstance, the environmental friendly and effectively photocatalysis technique has become a potential choice to alleviate the pollution from indoor air.[62-64] Driven by this requirement, some air purification systems using a UV or visible-light-responsive photocatalysts and various LED light sources in a package have been introduced and also practically applied as shown in Fig. 1-4.[65-67]

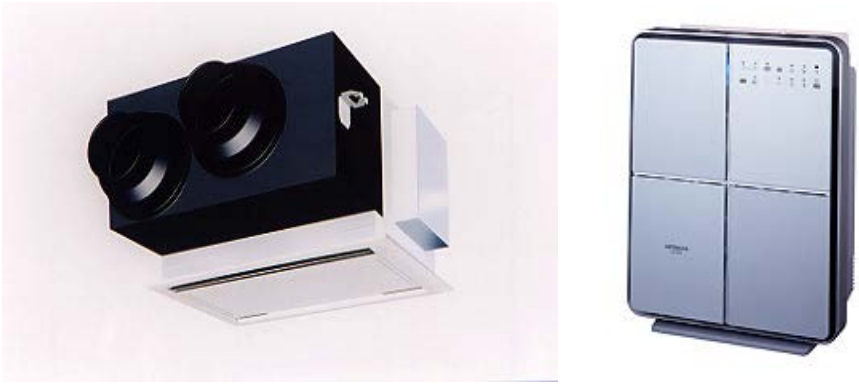

(a) Air conditioner (b) Air purifier

Figure 1-4. The practical application of photocatalyst in the air conditioner and air purifier for indoor air pollution treatment.

1.2.3 Water splitting

With the rapid increase of world's population and fast growth of many developing economies, the energy consumption is dramatically increased. Meanwhile, the

released concentration of CO_2 in atmosphere, as a result of the combustion of the carbon-based fuels, has also significantly enhanced. In this case, the energy depletion and environmental contamination have been two essential issues in modern times and a renewable and infinite energy source is strongly required.[68,69] Since Fujishima and Honda[70] firstly generated hydrogen by water photoelectrolysis, the hydrogen fuel by solar-chemical energy conversion has been gradually considered as a promising alternative for environmental benign and renewable energy source, which can be produced from the abundant of water without the release of CO_2 and other contaminating gas. Subsequently, the photocatalysis production of hydrogen has also become a hot topic, and many efforts have been made to improve the high efficiency of hydrogen production by the photocatalysis. Fig. 1-5 illustrates a simple photoelectronchemical water splitting system to produce hydrogen in the presence of TiO_2 photocatalyst under the light irradiation.[71-73]

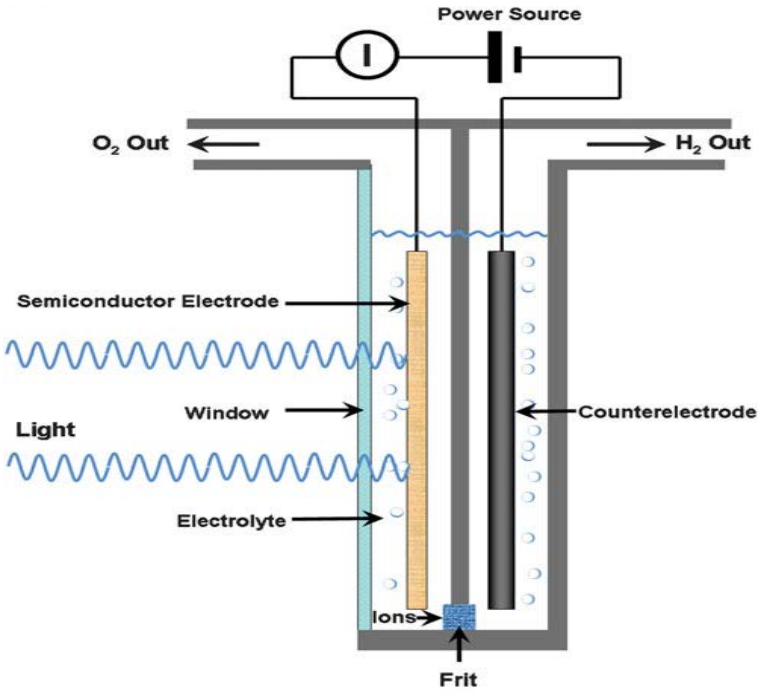

Figure 1-5. Schematic of water splitting by TiO_2 photocatalys.[71, 7]

1.2.4 Self-cleaning

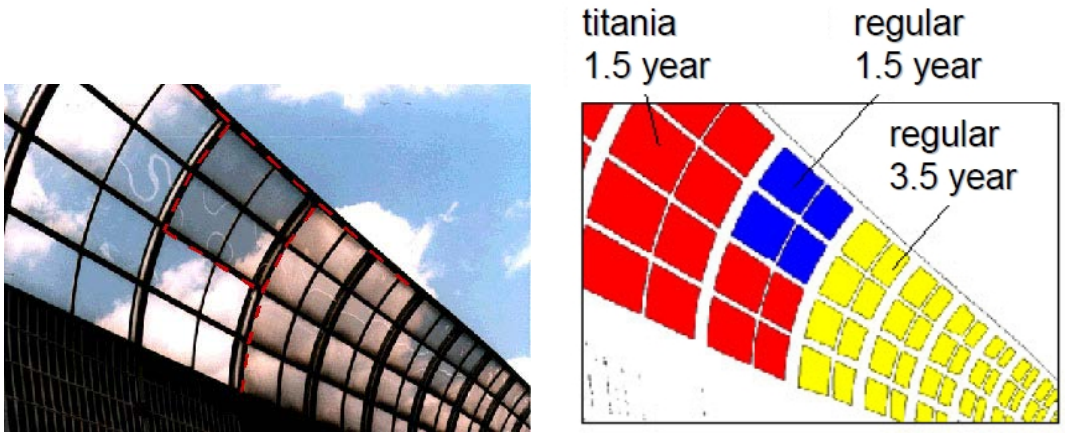

Figure 1-6. The polycarbonate plates covered with titania photocatalyst.

Figure 1-7. The anti-fogging application by hydrophilicity property.

Up to date, many novel technologies in our daily life have been inspired by the nature. Self-cleaning technique is one of them, which is aroused from the wings of butterflies and the leaves of lotus. Nowadays, the self-cleaning coating has been extensively applied in many areas such as cement, glass coatings, paints, textiles, building, etc. due to its labour-saving. In particular, the photocatalyst combined coating attracts the increasing interest owing to multi-function.[74-76] In 2001, Pilkington Glass company developed the first self-cleaning windows, which was coated with a thin transparent layer of TiO_2. This window has two functions: photocatalysis and hydrophilicity. When this special window is exposed in the

sunlight, on one hand, the TiO_2 can chemically break down the adsorbed organic dirt by photocalysis; on the other hand, the dirt and grime in the windows can be easily cleaned by the rain or other water since the water has very low contact angles to the glass as a result of hydrophilicity in the presence of TiO_2.[77] Fig. 1-6 and 1-7 present some practical applications of photocatalyst, such as self-cleaning coating and anti-fogging, respectively.[54,78]

1.3 Structure and properties of popular photocatalysts and corresponding common problems

Photocatalysis, as a green chemical method to alleviate the energy and environmental issues, has fascinated considerable attention in recent years. In order to meet the urgent requirement for the rapid development of photocatalysis, various photocatalysts have been introduced. However, among them, three peculiar substances based photocatalysts, including TiO_2, $NaTaO_3$ and BiOX (X=Cl, Br and I), have been greatly highlighted for the high efficiency of photocatalysis.[79-81] Therefore, the followings will give a brief introduction for the structure and properties of these three photocatalysts. In addition, the current problems existed in these materials are also discussed.

1.3.1 TiO_2

TiO_2, one of the most promising photocatalyst, is of great concern due to its high stability, low cost, environmental benign, abundant and nice photo-activity.[82-84] TiO_2 is also a typical n-type semiconductor, as a result of the existence of oxygen vacancies.[85] The lower part of the conduction band of TiO_2 is consisted by the 3d orbitals of Ti^{4+} and the valence band is mainly formed by the overlap of the O 2p orbitals.[86] Besides, TiO_2 has three polymorphs: anatase, rutile and brookite, where rutile presents the most thermodynamical stability, and anatase displays excellent kinetic stability. The anatase and brookite can be easily synthesized at low

temperature and transformed to rutile at a high calcination temperature exceeding 600^{o}C. In addition, the structure of three phases has significant difference, leading to the final variety of properties. The crystal structures of three phases are shown in Fig. 1-8. It is explicit that all of three types of TiO_2 are composed of TiO_6 octahedra, but vary from the distortion of the octahedron units, shared manner of edges and corners. For anatase, each octahedron shares four corners with neighbors and also shares four edges with other neighbors to form a zigzag chain with a screw axis {221}. Whereas the octahedron in rutile shares eight corners with neighbors, and it only shares two edges with other neighbors, connecting to form a linear chain parallel to {001}. As for brookite, only three edges are shared, additionally, both edges and corners are connected. Due to the difference in preparation process and crystal structure, anatase and rutile have been frequently studied, whereas brookite has been rarely investigated. Furthermore, compared with the photocatalytic performance of rutile, the anatase generally shows higher activity. On one hand, the intrinsic band gap of anatase is ca. 3.2 eV corresponding to 384 nm absorption edge, whereas rutile is a little bit smaller about 3.02 eV relating to 410 nm absorption edge. In this case, although rutile presents slightly larger light absorption range over that of anatase, anatase obtains the relatively higher redox ability than rutile, which is probably much more essential for photocatalytic performance. On the other hand, rutile is usually produced in relatively higher temperature with larger particle size compared with that of anatase. Under this circumstance, although rutile has higher crystallinity for better charge carrier mobility over anatase, anatase presents much more active sites on the surface with relatively larger specific surface area. Meanwhile, anatase reveals the much more efficient charge separation ability owing to the existence of more oxygen vacancies in anatase. As a result of the above-mentioned reasons, the photocatalytic performance of anatase is usually superior to that of rutile.[87-91]

Nevertheless, regardless of phase type, all of the TiO_2 presents two main drawbacks. The first one is the limitation of light-harvesting ability. It is well known that the natural solar light consists of 5% of UV, 45% of visible light and 50% of infrared light.

Because of the large intrinsic band gap of TiO_2 above 3 eV equaling to 413 nm, it can only absorb UV light and majority of visible and infrared lights cannot be utilized, which is detrimental for the practical applications of TiO_2 under the solar light irradiation. The other shortcoming is the rapid recombination rate of photogenerated electron-hole pairs, suppressing the quantum efficiency.[92,93]

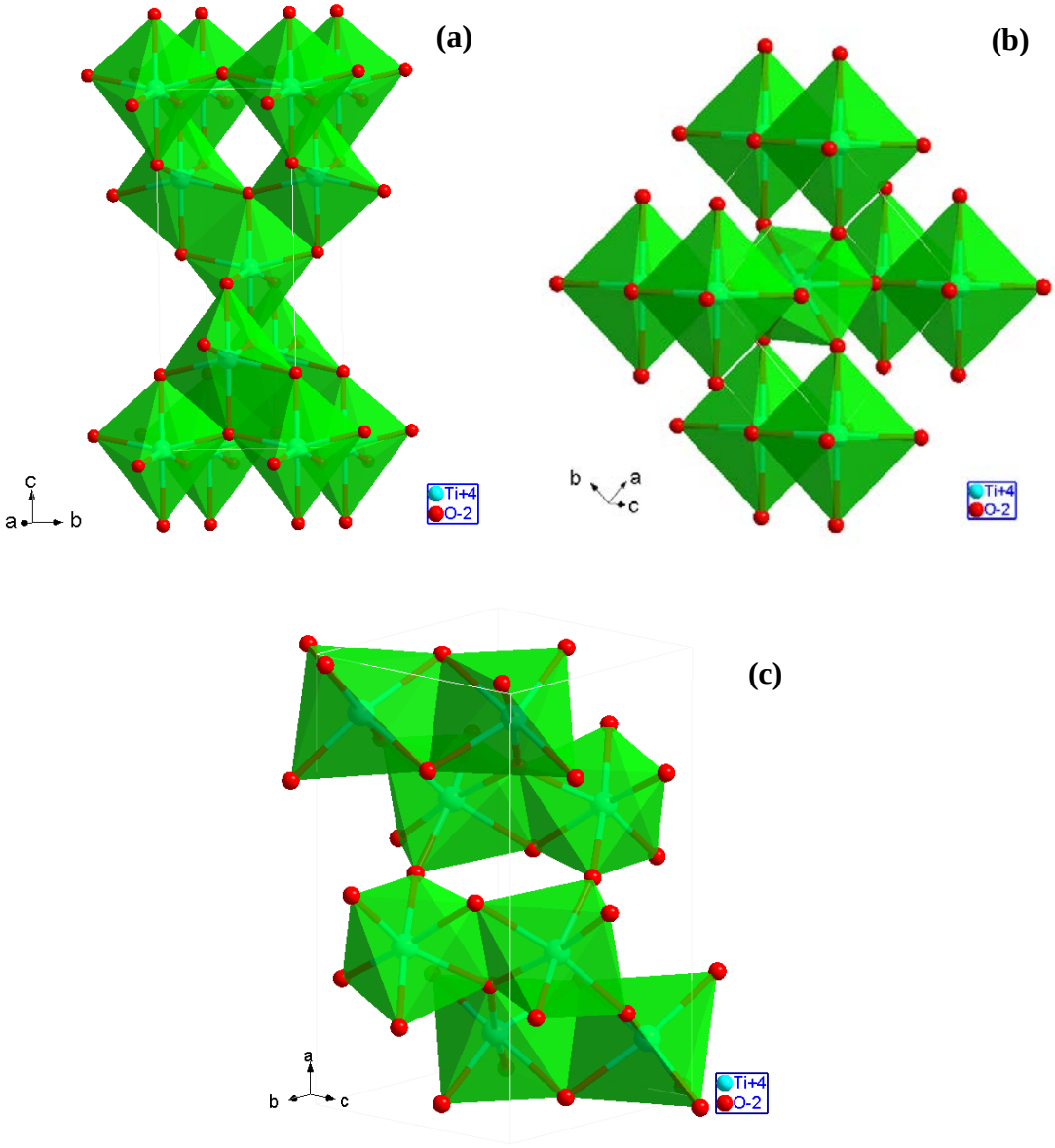

Figure 1-8. The crystal structures of anatase (a), rutile (b) and brookite (c).

1.3.2 $NaTaO_3$

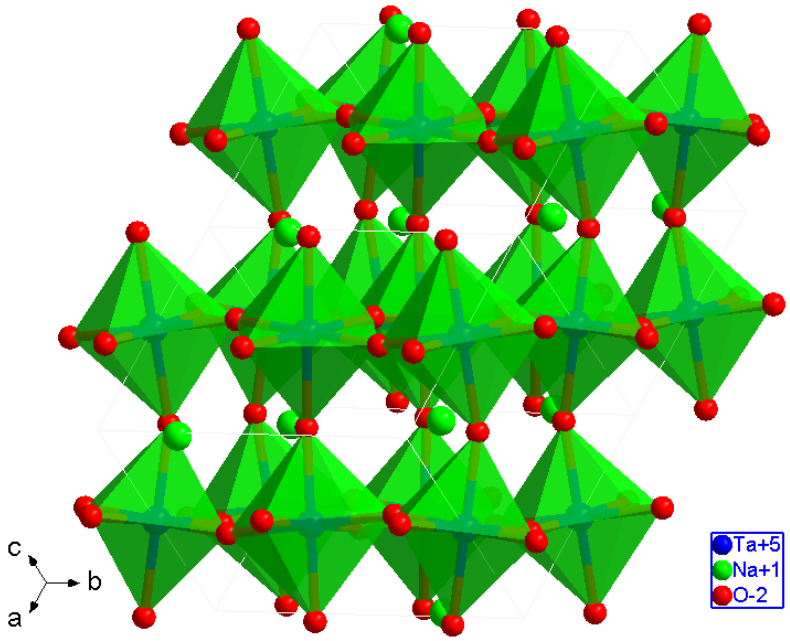

Figure 1-9. The crystal structure of orthorhombic $NaTaO_3$.

In recent years, the perovskite structure of tantalates, especially alkali metal tantalates ($ATaO_3$, (A=Li, Na and K)), have attracted considerable attention due to their widespread photocatalytic applications in various industrial fields.[94-96] Furthermore, the conduction band position of tantalates consisting of Ta_{5d} orbital is more negative than that of popular TiO_2, indicating much higher reduction activity for tantalates.[97] Besides, among three types of tantalates, $NaTaO_3$ has fascinated peculiar interest in researchers and is considered as the most active one owing to its nice crystal structure, suitable band positions and high efficiency.[98] It is well acknowledged that $NaTaO_3$ has two common phases, including cubic and orthorhombic ones. However, the orthorhombic phase of $NaTaO_3$ has been made much more efforts compared with that of cubic one since the cubic one usually needs high temperature preparation conditions and shows relatively lower photocatalytic performance.[99,100]

Fig. 1-9 illustrates the crystal structure of orthorhombic type of $NaTaO_3$ with the

space group Pcmn. It can be clearly seen that one Ta atom is coordinated by six O to form a TaO_6 octahedra. The TaO_6 octahedra units are corner-connected by each other. In addition, the TaO_6 octahedra forms layer structure in (011) facet and the Na atoms are located in this interlayer. In this case, the electric structure of $NaTaO_3$ can be easily adjusted by the substitution of Na and Ta atoms by other atoms, finally leading to the change of properties for $NaTaO_3$.

Although orthorhombic $NaTaO_3$ has a promising prospect, it still has some shortcomings. Firstly, as a result of the large intrinsic band gap of $NaTaO_3$ (ca. 4.0 eV), it can only be excited by the UV light which just accounts for 5% of solar light and 45% of visible light and 50% of infrared light cannot be utilized for photocatalysis. Moreover, the charge carriers' separation ability of $NaTaO_3$ is still limited since it is a direct band gap semiconductor and also a solely pure compound. Finally, the as-reported $NaTaO_3$ powders almost present large particle sizes with relatively small specific surface area, detrimental for the high efficiency of photocatalysis.[100-102]

1.3.3 BiOX

Nowadays, Bismuth oxyhalides (BiOX, X=Cl, Br and I), as typical V-VI-VII ternary oxide semiconductors, have attributed great deal of attention because of their peculiar hierarchical structures, optical properties and high chemical stability.[103-105] Fig. 1-10 exhibits the crystal structures of BiOCl, BiOBr and BiOI. It is apparent that three types of BiOX all have a tetragonal matlockite structure with P4/nmm space group, a peculiar layer structure formed by $[Bi_2O_2]$ slabs interleaved by double slabs of halogen atoms. Due to the relatively strong intra-layer bonding in $[Bi_2O_2]$ slabs and relatively weak interlayer van der Waal's interaction in the BiOX, they reveal lots of excellent physical and chemical properties, especially in the area of photocatalysis.[106,107] However, owing to the difference of Cl^-, Br^- and I^- ion radius (0.181 nm for Cl^-, 0.196 nm for Br^- and 0.220 nm for I^-), the corresponding crystal structures for BiOCl, BiOBr and BiOI are slightly different. BiOI obtains the largest c

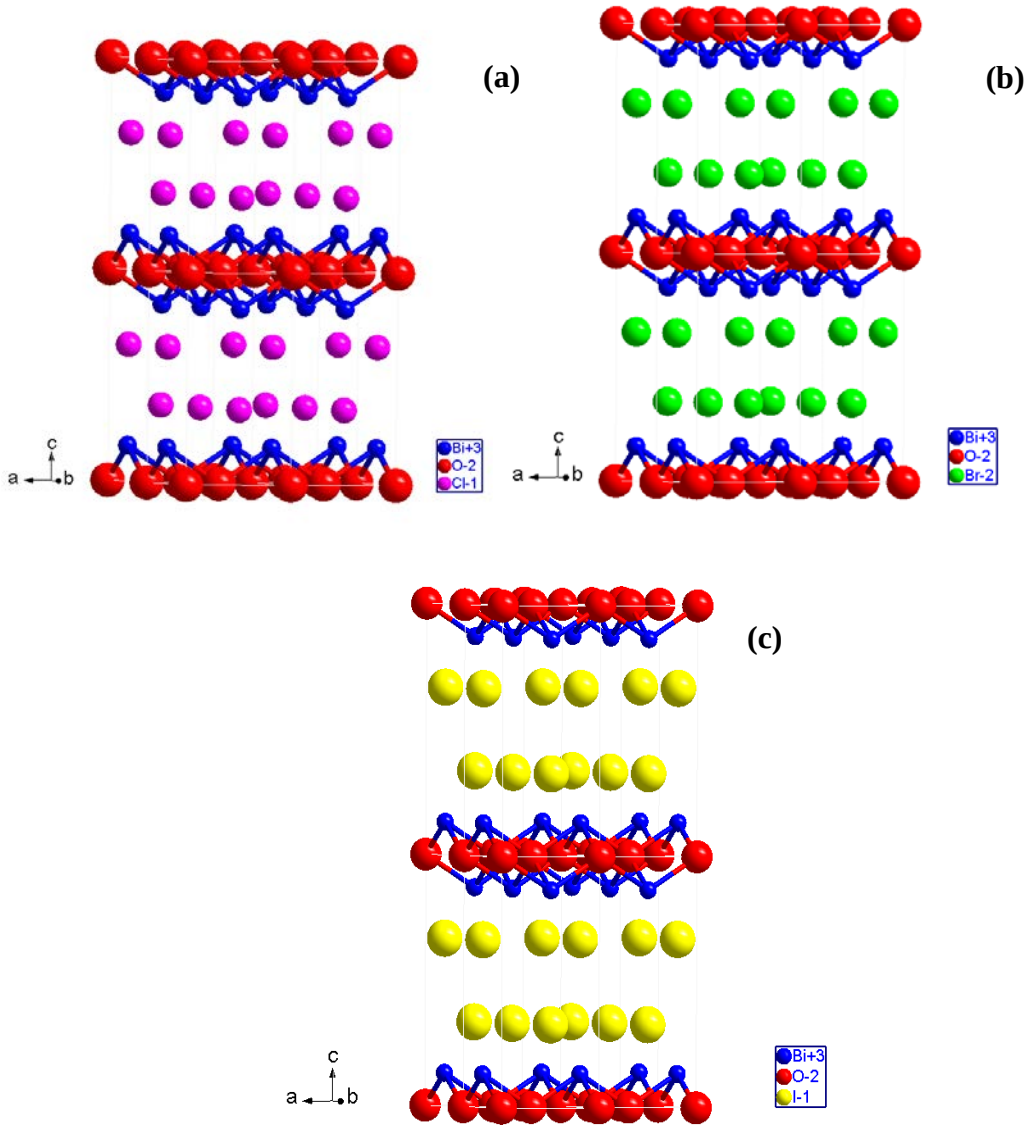

Figure 1-10. Crystal structures of BiOCl (a), BiOBr (b) and BiOI (c).

constant (ca. 0.9128 nm) followed by those of BiOBr and BiOCl about 0.8105 and 0.7354 nm, respectively, in the decrease order of X^- ion radius. Under the influence of electric structure of BiOX, BiOCl, BiOBr and BiOI show huge difference in intrinsic band gaps of ca. 3.2 eV, 2.6 eV and 1.8 eV, respectively. It is well known that the BiOX series usually present nice photocatalytic activity, even over TiO_2 in the degradation of organic pollutants. This excellent performance should be mainly ascribed to the open crystalline structures and indirect optical as a p-type semiconductor. On one hand, the open layered structure offers a great amount of space to polarize the relevant atoms and orbitals, and then generates the internal static

electric fields perpendicular to the [Bi_2O_2] slabs and halogen anionic slabs in the crystal of BiOX, which is great beneficial for the separation of charge carriers along the [001] direct as shown in Fig. 1-10. On the other hand, in the indirect semiconductors, the photogenerated electrons have to move a certain k-space distance, firstly, and then return back to the valence band, the process of which can significantly diminish the recombination probability of the photogenerated electron-hole pairs, which is also an advantage to the quantum efficiency of photocatalysis.[108,109]

Nevertheless, there is still a drawback for all the BiOX. It has been commonly confirmed that the BiOBr exhibits the best UV-visible lights induced photocatalytic activity followed by BiOCl, which only be active in UV light assigning to the large intrinsic band gap. On account of the much negative valence band position, BiOI usually represents the poorest photocatalytic performance in spite of excellent visible light absorption capability. In addition, although BiOBr demonstrates the most promising UV-visible lights responsive photo-activity, it possesses the visible light absorption ability only in a narrow range up to ca. 480 nm and no infrared light absorption ability. Therefore, the BiOX series possess the still disadvantages for the solar light irradiation in the consideration of high efficiency of photocatalysis.[110,111]

Based on the above description, it can be learned that there are two common problems for current photocatalysts to achieve the high efficiency of solar light induced photocatalysis. The first one is the limited light absorption capability in the area of visible light and no infrared light absorption ability. The other problem is the relatively high recombination rate of photogenerated electron-hole pairs.

1.4 Strategies for improving photocatalytic activity

Up to date, a lot of promising photocatalysts have been developed in the driven force of environmental and energy issues. However, for the practical application, the photocatalytic efficiency and light-harvesting ability are still far away from industrial

requirement. In this case, great amounts of strategies, including various doping, noble metal plasmon, cocatalyst loading, sensitizing and coupling with other semiconductors, etc. have been proposed to improve these performances as much as possible.[112-114] The followings will give a brief review for these improvement strategies popular in recent years.

1.4.1 Doping

In order to extend the light responsive ability in the whole solar light range and also to enhance the charge carriers' separation ability, doping ions in the target photocatalysts has become one of the most potential methods since doping in crystal usually can induce some intermediate energy levels in the forbidden band and also sometimes boost the electron-hole pairs' separation. Doping ways mainly contain nonmetal doping, metal doping, nonmetal metal or/and metal codoping and oxygen rich.[115]

1.4.1.1 Nonmetal doping

Recently, nonmetal doping, including the nonmetals of C,[116,117] N,[118,119] S,[120,121] F[122] and I,[123] etc., has attracted a great deal of attention to improve the photocatalytic activity. In particular, the C and N doping have been paid much more efforts owing to their nice effect in the narrowing band gap. J. Yu et al.[124] has prepared C doped BiOCl by a facile wet chemical process. As shown in Fig. 1-11, compared with pure BiOCl, doping C in BiOCl crystal can introduce some C related impurity levels above the valence band of BiOCl. In this case, the band gap is narrowed to extend light absorption ability and finally promoting the photocatalytic performance. F. Dong et al.[125] reported a mesoporous C doped TiO_2 nanomaterials, which were prepared by a one-pot green chemical approach using sucrose as the C doping source. With the incorporation of C doping in TiO_2, the visible absorption ability of samples had been significantly improved in the whole range of visible light. Furthermore, after the

post-C doping calcination in 200°C, the samples presented much better light-harvesting capability and visible light induced photocatalytic property due to the increased C doping content and decreased surface defects by the help of post-C doping calcination.

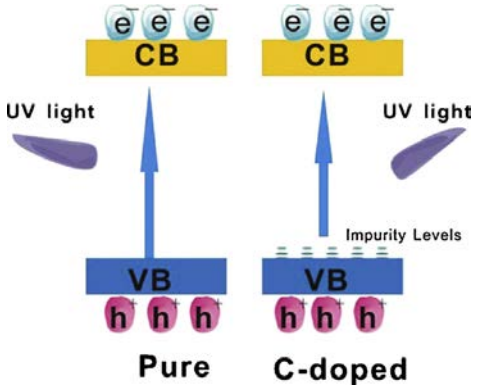

Figure 1-11. Schematic diagrams of photocatalytic mechanisms for pure BiOCl and C doped BiOCl products.[124]

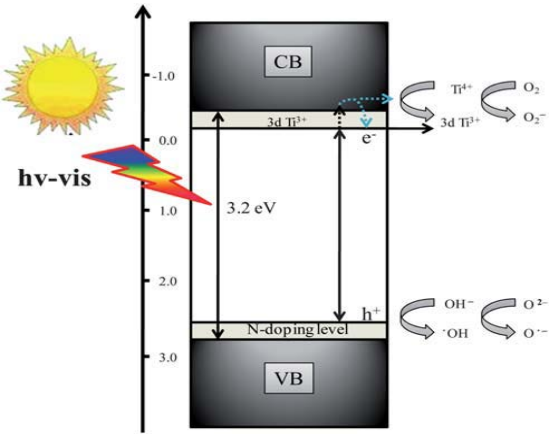

Figure 1-12. A possible photocatalytic mechanism for N doped TiO_2 under visible light irradiation.[126]

As for N doping in photocatalyst, G. D. Yang, et al.[126] synthesized a series of N doped anatase TiO_2 samples by a solvothermal method in an organic amine/ethanol-water reaction system. According to the electron paramagnetic resonance (EPR) measurement, some of the reduced Ti^{3+} ions have been induced owing to the N doping by replacing O site and charge balance. As described in this work, with the dopant of N in TiO_2, some Ti^{3+} related energy levels and N doping levels could be generated under the conduction band of TiO_2 and above the valence

band of it, respectively (as shown in Fig. 1-12). Under this circumstance, the band gap of TiO_2 has been dramatically narrowed, and visible light-harvesting ability was improved greatly. Besides, the produced impurity levels were also beneficial for the charge carriers' separation of samples. So, after N doping, the samples exhibited the excellent degradation ability for methylene blue and methylene orange solution under the irradiation of visible light.

1.4.1.2 Metal doping

In addition to nonmetal doping, metal doping is also a potential way for the improvement of visible-light induced photocatalysis since metal doping probably can extend the light absorption range, elevate the redox potential of the photoinduced radicals and hinder the recombination rate of photogenerated electron-hole pairs.[127] The common used metal doping elements contain In, W, Nd, Ta, Nb, Fe, Bi, V and Cr, etc.[128,129] Among them, Bi and Fe have attracted the special interest in enhancing visible light driven photocatalytic performance. P. D. Kanhere, et al.[130] prepared nice visible light induced Bi doped $NaTaO_3$ powders. The author found that the visible light absorption capability of $NaTaO_3$ could be nicely enhanced by tuning the starting molar ratio of Na and Ta which could affect the site occupancy of Bi doping in the lattice as shown in Fig. 1-13.

According to the first principles calculation, it confirmed that the largest band gap narrowing could be achieved as Bi was substituted at both Na and Ta sites. S. George, et al.[131] studied a Fe doped TiO_2 nanoparticles fabricated by a versatile flame spray pyrolysis synthetic method. The particles were used to check the photo-activity of cytotoxicity with the visible light irradiation. After Fe doping, the TiO_2 was capable for the visible light absorption by introducing some impurity levels above the valence band of TiO_2 (as seen in Fig. 1-14). In addition, the band gap energy of TiO_2 could be obviously adjusted by the Fe doping content.

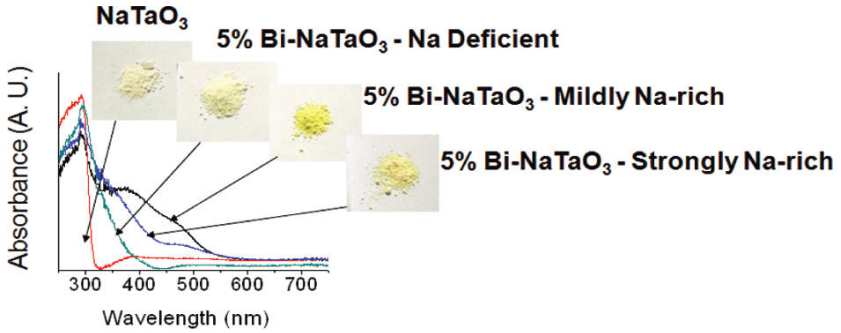

Figure 1-13. DRS of Bi doped $NaTaO_3$ as a function of various Na/Ta starting molar ratios.[130]

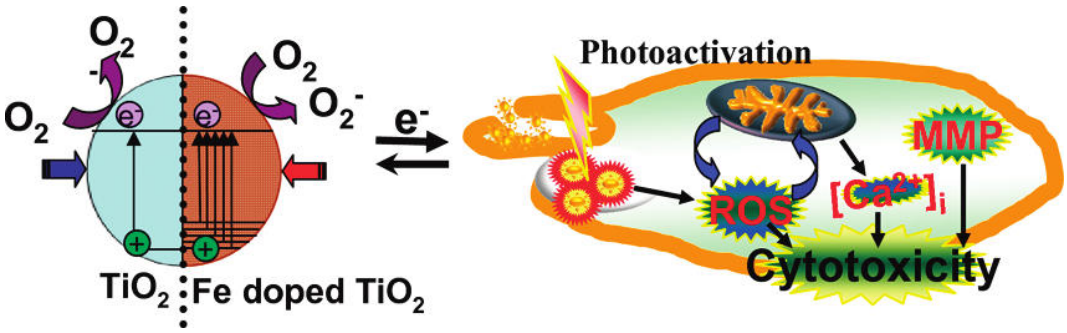

Figure 1-14. Possible photocatalytic mechanism of Fe doped TiO_2.[131]

1.4.1.3 Nonmetal/metal codoping

Compared with nonmetal or metal solely doping, codoping of nonmetals or/and metals has been of great concern since it has some advantages over that of solely doping. Firstly, the band gap of photocatalyst could be further narrowed in comparison of that of solely doping. In addition, the recombination rate of charge carriers could be more effectively suppressed by donor-acceptor codoping. Basically, codoping can be divided into three types, including nonmetal-nonmetal codoping, metal-metal codoping and nonmetal-metal codoping. For example, G. Liu, et al.[132] investigated the synergistic effects of B and N codoping on the visible light induced photocatalytic activity of mesoporous TiO_2. The results found that the visible light absorption property of TiO_2 has been considerably enhanced by B and N codoping over that of B or N solely doping. Besides, due to the B and N synergistic effect, the separation ability of charge carriers has also been greatly improved by the

construction of a new O-Ti-B-N structure on the surface of TiO_2 particles. S. Tonda, et al.[133] synthesized the Cr and La codoped $SrTiO_3$ nanoparticles by a facile polymeric citrate strategy. It revealed that the absorption edge of $SrTiO_3$ shifted towards the visible light region after Cr and La codoping. Furthermore, the photocatalytic activity of codoped samples was about 6 times higher than that of pure one and 3 times better than that of solely doped one, as a result of the synergetic effect between Cr and La in $SrTiO_3$ crystal. X. G. Ma, et al. [134] studied a compensated codoping in TiO_2 by C and Nb. According to the calculated results, they demonstrated that the codoping of C and Nb in TiO_2 not only reduces the energy gap to enhance the optical absorption by narrowing the band gap and improves the separation ability of charge carriers but also does not lower the reduction potential of the conduction band edge of TiO_2 as displayed in Fig. 1-15.

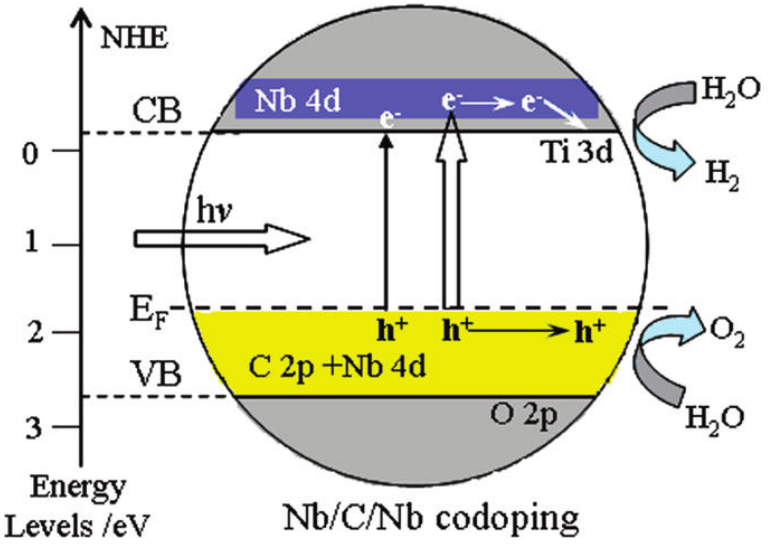

Figure 1-15. Photocatalytic mechanism of Nb and C codoped TiO_2. [134]

1.4.1.4 Oxygen rich

In addition to the above doping approach, the induction of oxygen rich in photocatalyst is also a promising way.[135] For example, V. Etacheri, et al.[136] prepared the oxygen rich TiO_2 by the addition of H_2O_2. They found that the valence band maximum of TiO_2 could be upward shifted owing to the existence of excessive oxygen. In this case, the band gap could be nicely narrowed by controlling the amount

of excessive oxygen in TiO_2 as shown in Fig. 1-16. In addition, X. Xiao, et al. also synthesized the oxygen-rich bismuth oxyhalides by a generalized one-pot method. In this work, the band gap of samples could be controllably tuned by adjusting the content of oxygen excess in the samples, finally leading to the much improved visible light absorption capability.[137]

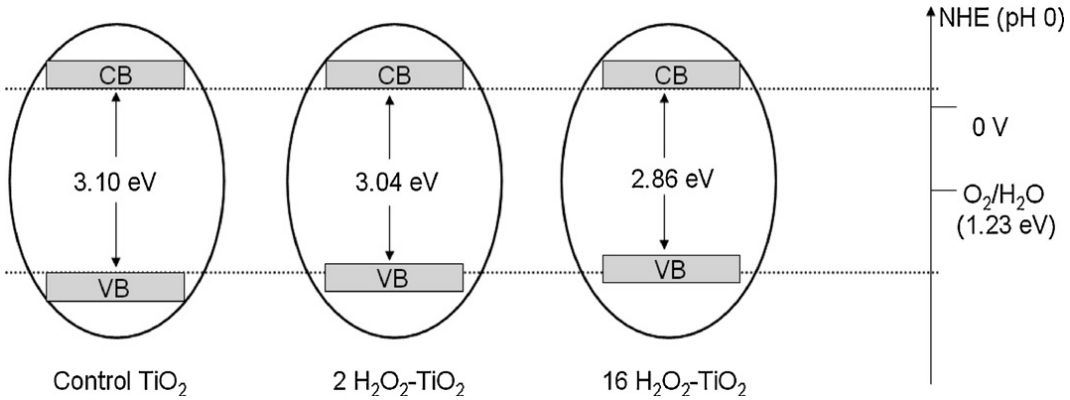

Figure 1-16. Possible mechanism of narrowed band gap of TiO_2 by oxygen rich. Numbers 2 and 16 in samples' names were used to identify two different samples.[136]

1.4.2 Noble metal plasmon

Recently, the surface plasmon resonance (SPR) effect has drawn a great deal of attention in the improvement of visible light absorption ability of photocatalysts by loading noble metal nanoparticles (e.g., Ag, Au). SPR is defined that when a spherical noble metal nanoparticle is irradiated by light with the wavelength much longer than the size of this particle, the charge density in the noble metal powder will be redistributed. Meanwhile, a coulombic restoring force is going to be established, and the charge density will coherently oscillate just like a harmonic oscillator in particle with the incident light. In a word, SPR is collective oscillations of electrons in the conduction band of noble metal induced by the electromagnetic field of the incident light.[138-140] As noble metal is loaded on the surface of photocatalyst and illuminated by a visible light, noble metal can be excited by visible light owing to the effect of SPR and then photogenerated electron can be further transferred to the photocatalyst to produce photocatalysis. For example, Z. K. Zheng, et al.[141] prepared the noble

metals (Au, Pt and Ag) loaded TiO_2 nanoparticles by a facile in situ method using the Ti^{3+} as the reduction reagent. The visible light induced oxidation of benzene to phenol has been investigated for the photocatalytic activities of samples. The results found that due to the SPR effect of noble metal loading, the noble metal was excited by the visible light, and then the photoinduced electron was transferred from noble metal to the TiO_2 particles, finally presenting a high yield (63%) and selectivity (91%) for the oxidation of benzene to phenol. The corresponding mechanism for high efficiency of visible light induced photocatalytic activity of samples is shown in Fig. 1-17.

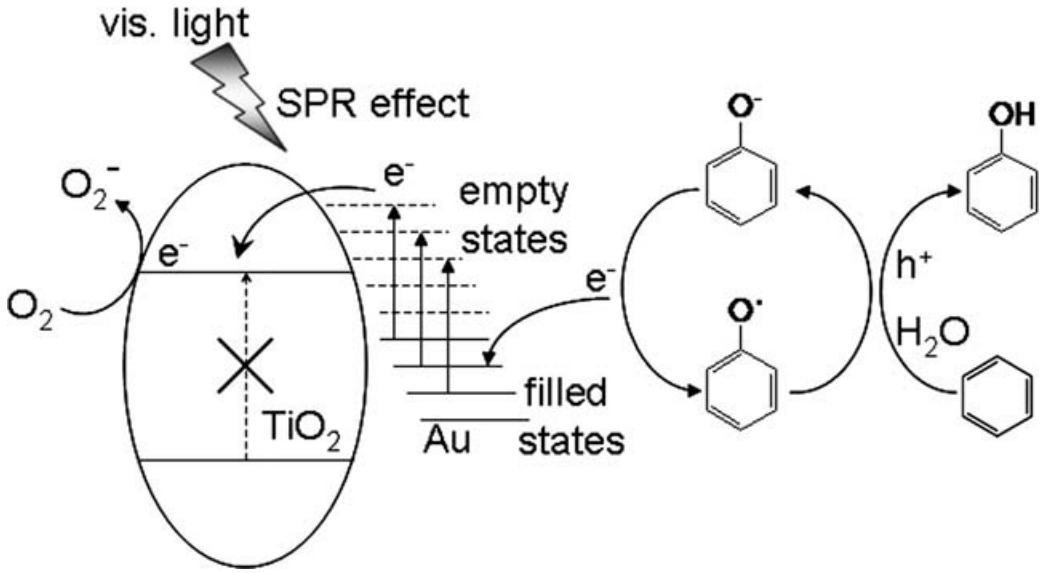

Figure 1-17. Proposed mechanism for the SPR induced photocatalytic activity of samples under the irradiation of visible light. [141]

Besides, Z. Y. Zhang, et al.[142] presented a direct evidence for the noble metal plasmon-enhanced H_2 generation by using TiO_2 electrospun nanofibers co-decorated with Au and Pt nanoparticles. After Au and Pt loading on TiO_2 particles, the visible light absorption performance of samples had been significantly improved owing to the SPR effect as shown in Fig. 1-18 A. In this case, the noble metal loaded TiO_2 could be excited by visible light to produce photocatalytic activity and the relevant mechanism is illustrated in Fig. 1-18 B.

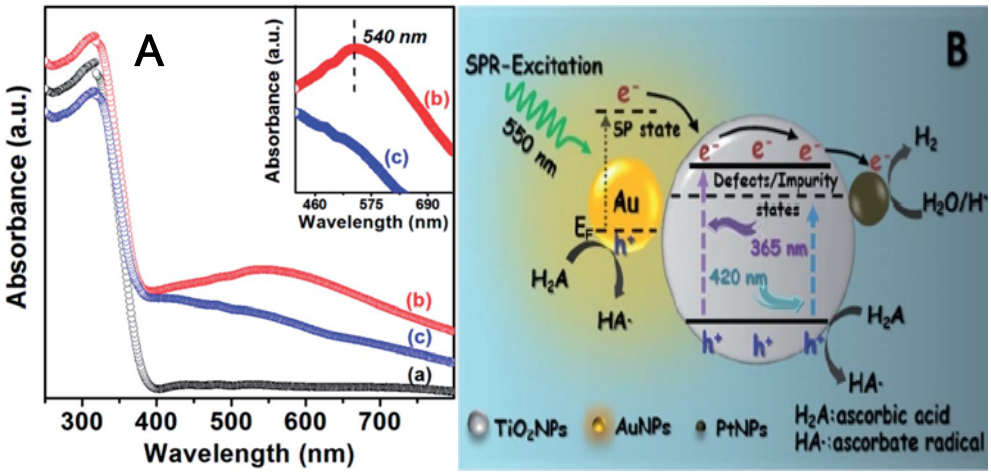

Figure 1-18. DRS of pure TiO_2 (a), $Au_{0.75}/Pt_{0.25}/TiO_2$ (b), Pt_1/TiO_2 nanofibers (A) and corresponding possible photocatalytic mechanism (B).[142]

1.4.3 Cocatalyst loading

In order to significantly improve the separation ability of charge carriers, the cocatalyst loading has become one of the most potential approaches. Fig. 1-19 shows the photocatalytic mechanism for water splitting over a semiconductor photocatalyst loaded with different cocatalysts.[143] It is apparent in this figure that with the loading of cocatalyst on the surface of photocatalyst, the photogenerated electron or hole can be transferred from photocatalyst to the cocatalyst for photocatalysis under the irradiation of light. Under this circumstance, the photoinduced electron-hole pairs are able to be effectively separated. Furthermore, the loading cocatalyst on the surface of semiconductor photocatalyst is beneficial for the photocatalytic stability of products. Generally, the cocatalysts can be divided into two main types, containing electron capturing and hole capturing. NiO, CuO, Cu_2O, Cr_2O_3, RuO_2, MoS_2, graphene, etc. are usually regarded as the electron capturing cocatalysts.

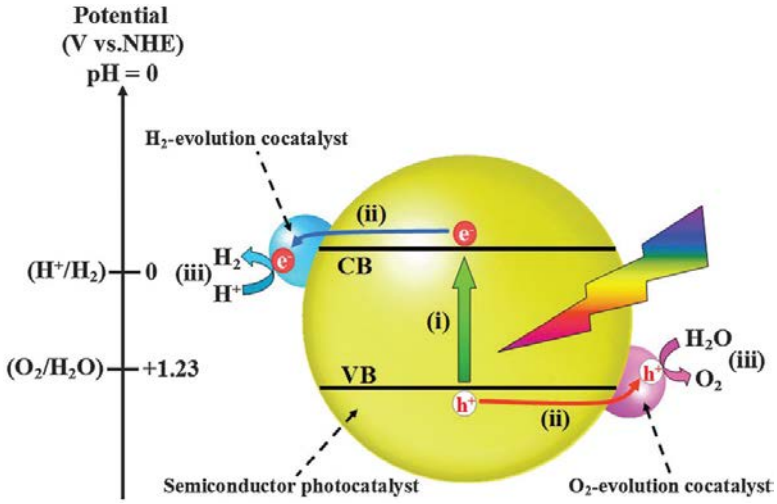

Figure 1-19. Proposed photocatalytic mechanism for water splitting by a photocatalyst with the loading of various cocatalysts. [143]

For instance, M. K. Tian, et al. prepared a series of single-phase metal oxide photocatalysts $K_4Ce_2M_{10}O_{30}$ (M=Ta, Nb). After incorporating NiO_x as cocatalysts, the produced amount of H_2 during 4 h by sample achieved 135 μmol, which is far higher than that of sample without loading NiO_x.[144] Q. J. Xiang, et al.[145] developed a new photocatalyst composite consisting of TiO_2/MoS_2/graphene by a two-step facile hydrothermal process using MoS_2 and graphene hybrid as cocatalyst. This composite displayed excellent H_2 evolution ability much superior to that of pure TiO_2 as shown in Fig. 1-20 (a). The corresponding mechanism for much improved H_2 evolution activity is illustrated in Fig. 1-20 (b). After the irradiation of light on the composite, the photoinduced electrons in the conduction band of TiO_2 can be transferred to MoS_2 nanosheets in the help of graphene sheets as a conductive electron transport channel and then to produce H_2 evolution. In this case, charge recombination could be largely suppressed, and interfacial charge transfer could be significantly enhanced as well as the increment of the number of active absorption sites, finally leading to high efficiency of H_2 evolution performance of composite.[143]

On the other hand, CoO_x, MnO_x, FeO_x, $B_2O_{3-x}N_x$, IrO_2, etc. are popularly utilized as the hole-capturing cocatalyst for photocatalysis.[146] Among them, the Co-based cocatalysts attract peculiar attention because of their excellent performance for O_2

evolution. For example, R. G. Li, et al.[147] reported a CoO_x and IrO_2 loaded $Sm_2Ti_2S_2O_5$ (STSO) photocatalyst for water oxidation under the irradiation of visible light. The results found that as the CoO_x loaded on STSO by in situ sulfurization-assisted deposition, the sample presented the highest O_2 evolution activity with the apparent quantum efficiency of 5.0% at 420 nm, which was much superior to pure STSO, IrO_2 loaded STSO, CoO_x loaded STSO by impreganation and also the highest O_2 evolution performance for oxysulfides reported so far (as seen in Fig. 1-21).

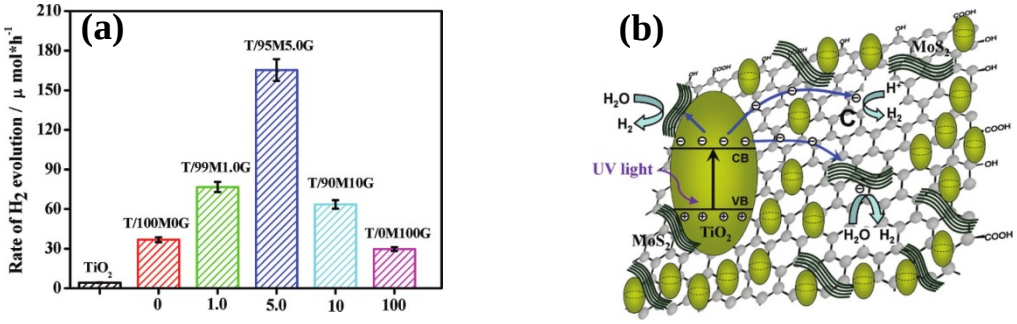

Figure 1-20. Photocatalytic H_2 evolution of TiO_2/MoS_2 (M)/graphene (G) composites. (the T/95M5.0G composite means consisting of 95% MoS and 5% graphene in the cocatalysts.) (a), proposed photocatalytic mechanism for the charge transfer in TiO_2/MG composites (b).[145]

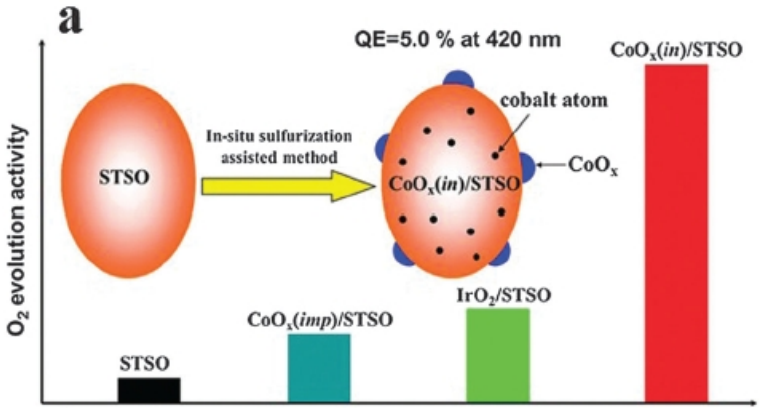

Figure 1-21. O_2 evolution performances of $Sm_2Ti_2S_2O_5$ (STSO) loaded with CoO_x by impregnation (CoO_x(imp)), IrO_2 by deposition and CoO_x by in situ sulfurization-assisted deposition (CoO_x(in)).[147]

1.4.4 Sensitizing

In order to significantly enhance the visible light absorption capability of photocatalyst, dye sensitization has become a promising strategy and fascinates great deal of interest from researchers in recent years. The simple sensitizing mechanism for photocatalysis can be divided into five steps in Fig. 1-22.[148] As a visible light is illuminated the dye sensitized photocatalyst, firstly, the absorbed dye on the surface of photocatalyst can be excited by the electron transformation from the highest occupied molecular orbital (HOMO) to the lowest unoccupied molecular orbital (LOMO); Secondly, owing to the nice alignment of LOMO position of dye and conduction band position of photocatalyst substrate, the photogenerated electron in dye can be further transferred to the conduction band of the photocatalyst host; After that, the photoinduced electron can be moved through two different ways. As a third step, the excited electron probably moves to the surface of photocatalyst host and reacts with surface O_2 to product active species for photocatalysis; Alternatively, as a fourth step, the photoproduced electron returns back to the dye for recombination, which is detrimental for the photocatalysis; finally, the oxidized dye can be regenerated by the suitable electron donors (e.g. water, organic acids, EDTA, etc.).[149] To be an efficient photocatalytic sensitizer, the dye should meet some requirements. To begin with, the dye should have high efficiency for light absorption and a wide range of visible light and even infrared light absorption capability; Secondly, the excited states of the dye should present a good lifetime and an excellent quantum yield. Last but not least, the excited state position of the dye should be nicely matched with the lower bound of the conduction band of photocatalyst substrate to minimize the energy loss in the process of photogenerated electron transfer.[84,150]

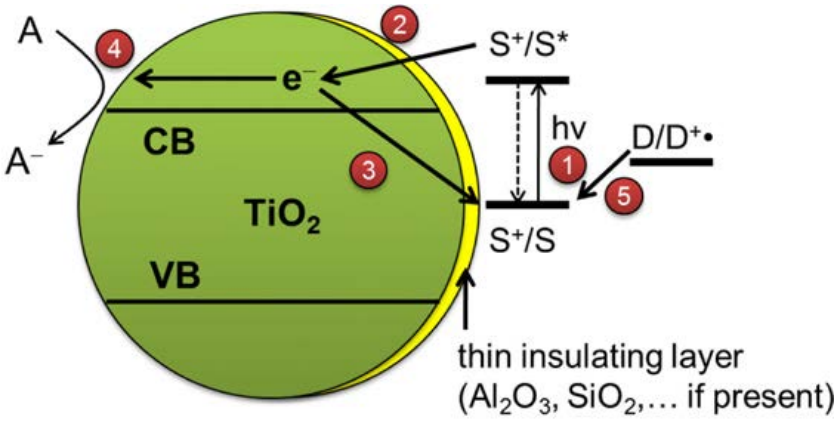

Figure 1-22. Photocatalytic mechanism for dye sensitization on the photocatalyst.[148]

The popular used dyes can be mainly separated into two series, including transition-metal complex dye and pure organic dye. For instance, K. Hirano, et al.[151] studied the effect of $Ru(bpy)_3^{2+}$, tris(bipirimidine)Ru(II)($Ru(bpym)_3$) and porphines dyes on the photocatalytic activity of TiO_2. The author found that among three types of dyes, $Ru(bpy)_3^{2+}$ presented the best sensitizing effect for H_2 production under the visible light irradiation in the presence of EDTA electron donor, which was much better than that of pure TiO_2. The results indicated that the high efficiency of H_2 evolution performance was strongly related to the high affinity of Ru complex on the surface of TiO_2 since it is probably beneficial for photogenerated electron transfer from the excited dye to the TiO_2 substrate. As for organic dye sensitizing, S. H. Lee, et al.[152] prepared a series of organic dyes (hydrophobic D-H, hydrophilic DEO1-DEO3 and slightly hydrophilic DMOM) sensitized TiO_2 photocatalysts as shown in Fig. 1-23. It found that after the dye sensitizing, the H_2 evolution performance had been significantly improved under the irradiation of visible light due to the much improved visible light absorption induced from coupled dyes. In addition, the moderately hydrophilic DEO_2 coupled TiO_2 sample presented the best visible light responsive photocatalytic activity among all samples.

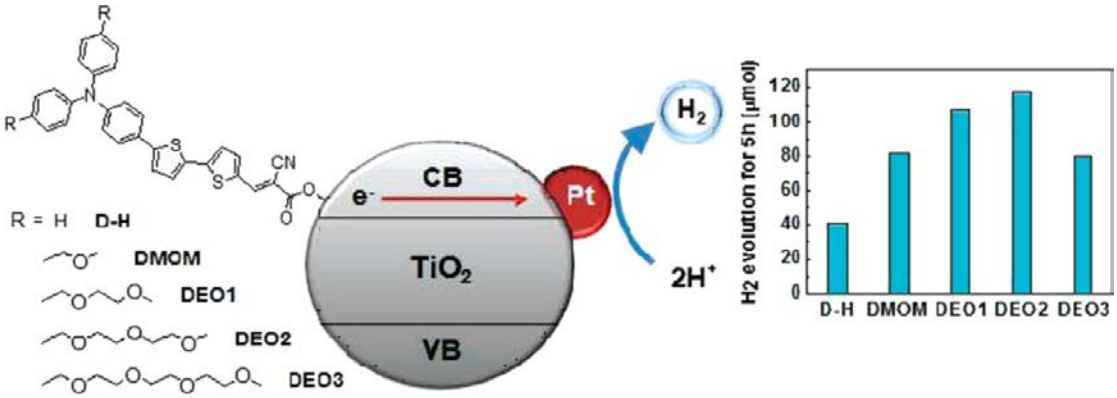

Figure 1-23. H_2 evolution ability of various organic dyes sensitized TiO_2 samples and corresponding photocatalyic mechanism. [152]

1.4.5 Coupling with other semiconductors

Coupling two semiconductor photocatalysts to form a heterostruture has become an extremely efficiency approach to significantly improve the separation ability of photogenerated electron-hole pairs and also sometimes to further enhance the visible light responsive range for high performance of photocatalytic activity. As presented in Fig. 1-24, the photocatalyst composites can commonly be divided into three categories of type I, type II and type III as a result of relatively various VB and CB positions of coupled photocatalysts.[153,154] Among these three types, the type II has attracted peculiar interest due to its efficiency performance in the charge carriers' separation. As a light is used to irradiate the type II kind of heterostructure, the photogenerated electron in the CB of semiconductor 1 can transfer to the CB of semiconductor 2 and the photoinduced hole in the VB of semiconductor 2 is able to transfer to the VB of semiconductor 1 owing to the difference of band potentials for two coupled semiconductor photocatalysts. In this case, the photogenerated electron-hole pairs can be effectively separated in space for this heterostructure. In addition, as a high photocatalytic performance of UV light induced material couples with a poor photocatalytic performance of visible light responsive substrate for type II heterostructure, the visible light induced photocatalytic activity of composites can be significantly improved, which is much superior to those of solely components in the

composite.

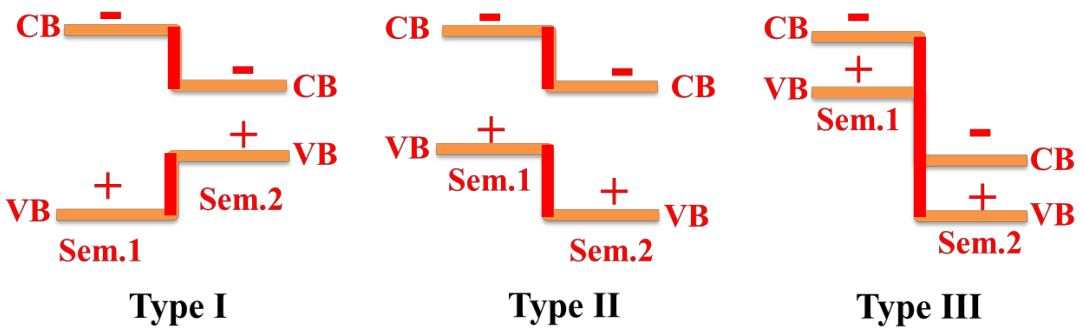

Figure 1-24. Schematic illustrations of band gap positions of three different types of photocatalyst heterostructures.

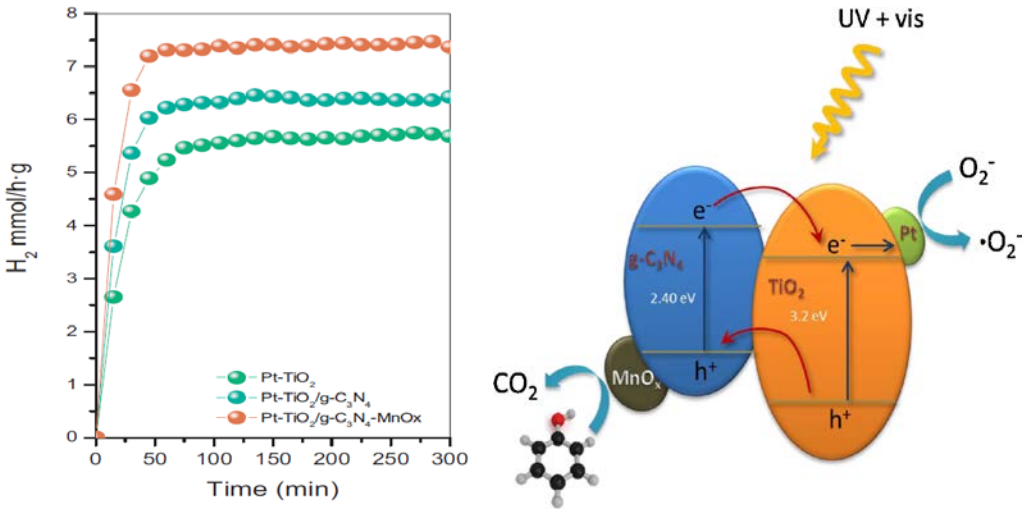

Figure 1-25. H_2 evolutions of Pt-TiO_2, Pt-TiO_2/g-C_3N_4 and Pt-TiO_2/g-C_3N_4-MnO_x under the irradiation of UV-visible lights and the corresponding photocatalytic mechanism for Pt-TiO_2/g-C_3N_4-MnO_x composite.[156]

For example, L. L. Ruan, et al.[155] developed a type II kind of BiOBr-TiO_2 heterojunction by anodization followed by a sequential chemical bath deposition approach. The BiOBr-TiO_2 heterostructure presented excellent visible light induced methylene orange degradation ability, which was much better than those of pure BiOBr and TiO_2. This outstanding photocatalytic performance was assigned to the nice separation ability of charge carriers originated from heterostructure, good visible

light absorption capability from BiOBr and enlarged specific surface area. S. Obregón, et al.[156] reported a TiO_2/g-C_3N_4 heterostructure. Owing to the nice band gap alignment of TiO_2 and g-C_3N_4, the photogenerated electron-hole pairs could be effectively separated, moreover, the visible light could be considerable absorbed by g-C_3N_4 and then be utilized by TiO_2 for photocatalysis as seen in Fig. 1-25. In order to further improve the photocatalytic activity of samples, Pt and MnO_x were also loaded. Under this circumstance, the H_2 evolution ability of Pt-TiO_2/g-C_3N_4 was much higher than that of solely Pt-TiO_2.

1.5 The aims of thesis

As introduced above, photocatalysis, as a green chemical approach, has fascinated great deal of attention for the environmental cleanup. Subsequently, great amounts of photocatalysts (e.g. TiO_2, $NaTaO_3$, BiOX, etc.) have been developed to meet the increasing requirement in our worsening atmosphere. However, for the practical application, great efforts are still needed as mentioned before. Although lots of strategies have been proposed to improve the photocatalytic performance of semiconductor photocatalysts for the sake of solar light responsive photocatalysis, the detailed effective ways for high efficiency of visible and infrared light induced photocatalysis are still few and strongly required.

Therefore, in this thesis, some promising methods have been proposed to enhance the visible and NIR lights induced photocatalysis significantly. On one hand, in order to improve visible light responsive photocatalytic activity, firstly, TiO_2 has been modified by anion doping, anion and cation codoping, and forming multiphase, being eager for dramatically enhance the visible light absorption capability by narrowing band gap and considerably improve separation activity of charge carriers. Then, as for $NaTaO_3$ series, a facile solvothermal method was utilized to synthesize the visible light responsive C doped $NaTaO_3$ (designated as C-$NaTaO_3$) particles via narrowing band gap. Furthermore, in order to further improve the separation ability of photogenerared electron-hole pairs, a new C-$NaTaO_3$/Cl-TiO_2 composite was

proposed. Besides, it is well known that large specific surface area is generally of great importance for high performance of photocatalysis. Under this consideration, an excellent visible light induced C modified $NaTaO_3$ mesocrystal nanoparticles have been prepared by a one-pot solvothermal method in the presence of glucose. Regarding BiOX series, a simple room temperature fabrication method has been developed, moreover, a glycerol/mixed solution was employed in this reaction to induce oxygen vacancies for long wavelength visible light active photocatalysis, which could introduce some impurity energy levels to narrow the band gap. On the other hand, a novel strategy, combining high efficiency of up-conversion phosphors with suitable photocatalysts to form composite, was developed, expecting to fulfill UV, visible and NIR lights induced photocatalytic activity simultaneously. Therefore, for TiO_2 and BiOBr series, various up-conversion phosphors coupled C doped TiO_2 or BiOBr composites have been prepared to investigate the UV, visible and NIR lights responsive photocaalytic properties.

1.6 References

1. R. Daghrir, P. Drogui, D. Robert, Ind. Eng. Chem. Res. **2013**, 52, 3581-3599.
2. J. Zhang, Y. Wu, M. Xing, S. A. Khan Leghari, S. Sajjad, Energy Environ. Sci. **2010**, 3, 715-726.
3. M. M. Khin, A. S. Nair, V. J. Babu, R. Murugan, S. Ramakrishna, Energy Environ. Sci. **2013**, 5, 8075-8109.
4. R. Andreozzi, V. Caprio, I. Ermellino, A. I. Tufano, Ind. Eng. Chem. Res. **1996**, 35, 1467-1471.
5. M. R. Hoffmann, S. T. Martin, W. Choi, D. W. Bahnemannt, Chem. Rev. **1995**, 95, 69-96.
6. S. Linic, P. Christopher, D. B. Ingram, Nat. Mater. **2011**, 10, 911-921.
7. M. R. Hoffmann , S. T. Martin , W. Choi , D. W. Bahnemann, Chem. Rev. **1995**, 95, 69-96.
8. R. Asahi, T. Morikawa, T. Ohwaki, Science, **2002**, 295, 626-627.
9. J. M. Rothberg, W. Hinz, T. M. Rearick, J. Schultz, W. Mileski, M. Davey, J. H. Leamon, K. Johnson, et al., Nature, **2011,** 475, 348-352.

10. N. P. Dasgupta, J. W. Sun, C. Liu, S. Brittman, S. C. Andrews, J. Lim, H. W. Gao, R. X. Yan, P. D. Yang, Adv. Mater. **2014**, 26, 2137-2184.
11. Y. Ma, X. L. Wang, Y. S. Jia, X. B. Chen, H. X. Han, C. Li, Chem. Rev. **2014**, DOI: 10.1021/cr500008u.
12. B. G. Yacobi, Semiconductor Materials: an Introduction to Basic Principles; Kluwer Academic/Plenum Publishers: New York, **2003**.
13. M. Matsuoka, M. Kitano, M. Takeuchi, K. Tsujimaru, M. Anpo, J. M. Thomas, Catal. Today **2007**, 122, 51-56.
14. X. B. Chen, S. H. Shen, L. J. Guo, S. S. Mao, Chem. Rev. **2010**, 110, 6503-6570.
15. S. K. Lee, A. Mills, J. Ind. Eng. Chem. **2004**, 10, 173-187.
16. I. K. Konstantinou, T. A. Albanis, Appl. Catal. B **2004**, 49, 1-14.
17. K. Pirkanniemi, M. Sillanpaa, Chemosphere **2002**, 48, 1047-1060.
18. P. R. Gogate, A. B. Pandit, Adv. Environ. Res. **2004**, 8, 501-551.
19. A. W. Maijenburg, J. Veerbeek, R. de Putter, S. A. Veldhuis, M. G. C. Zoontjes, G. Mul, J. M. Montero-Moreno, K. Nielsch, H. Schafer, M. Steinhart, J. E. ten Elshof, J. Mater. Chem. A **2014**, 2, 2648-2656.
20. F. T. Chen, P. F. Fang, Z. Liu, Y. P. Gao, Y. Liu, Y. Q. Dai, H. Luo, J. W. Feng, J. Mater. Sci. **2013**, 48, 5171-5179.
21. C. Chen, W. Cai, M. Long, B. Zhou, Y. Wu, D. Wu, Y. Feng, ACS Nano, **2010**, 4, 6425-6432.
22. Q. J. Xiang, J. G. Yu, M. Jaroniec, Phys. Chem. Chem. Phys. **2011**, 13, 4853-4861.
23. Y. Ma, Q. Xu, R. F. Chong, C. Li, J. Mater. Res. **2013**, 28, 394-399.
24. http://en.wikipedia.org/wiki/Water_purification.
25. D. S. Bhatkhande, V. G. Pangarkar, A. Beenackers, J. Chem. Technol. Biotechnol. **2002**, 77, 102-116.
26. P. R. Gogate, A. B. Pandit, Adv. Environ. Res. **2004**, 8, 501-551.
27. U. I. Gaya, A. H. Abdullah, J. Photochem. Photobiol., C **2008**, 9, 1-12.
28. W. Zhang, L. D. Zou, L. Z. Wang, Appl. Catal. A **2009**, 371, 1-9.
29. J. H. Pan, H. Q. Dou, Z. G. Xiong, C. Xu, J. Z. Ma, X. S. Zhao, J. Mater. Chem. **2010**, 20, 4512-4528.

30. S. Mozia, Sep. Purif. Technol. **2010**, 73, 71-91.

31. C. Wang, H. Liu, Y. Z. Qu, J. Nanomater. **2013**, 2013, 319637.

32. M. N. Chong, B. Jin, C. W. K. Chow, C. Saint, Water Res. **2010**, 44, 2997-3027.

33. J. Senthilnatan, L. Philip, Chem. Eng. J. **2010**, 161, 83-92.

34. M. Pelaez, N. T. Nolan, S. C. Pillai, M. K. Seery, P. Falaras, A. G. Kontos, P. S. M. Dunlop, J. W. J. Hamilton, J. A. Byrne, K. O'Shea, M. H. Entezari, D. D. Dionysiou, Appl. Catal. B **2012**, 125, 331-349.

35. http://www.sumitomometals.co.jp/news/monthly/2001/140.html.

36. M. I. Litter, Appl. Catal. B: Environ. **1999**, 23, 89-114.

37. M. R. Prairie, L. R. Evens, B. M. Stange, S. L. Martinez, Environ. Sci. Technol. **1993**, 27, 1776-1782.

38. C. McCullagh, J. M. C. Robertson, D. W. Bahnemann, P. K. J. Robertson, Res. Chem. Intermed. **2007**, 33, 359-375.

39. T. Matsunaga, R. Tomoda, T. Nakajima, H. Wake, FEMS Microbiol. Lett. **1985**, 29, 211-214.

40. T. Saito, T. Iwase, J. Horie, T. Morioka, J. Photochem. Photobiol. B: Biol. **1992**, 14, 369-379.

41. Z. Huang, P. C. Maness, D. M. Blake, E. J. Wolfrum, S. L. Smolinski, W. A. Jacoby, J. Photochem. Photobiol. A **2000**, 130, 163-172.

42. M. A. Ferguson, M. R. Hoffmann, J. G. Hering, Environ. Sci. Technol. **2005**, 39, 1880-1886.

43. A. G. Rincón, C. Pulgarin, Solar Energy **2004**, 77, 635-648.

44. http://www.enviropedia.org.uk/Air_Quality/Outdoor_Air_Pollution.php.

45. M. Delucchi, J. Murphy, D. McCubbin, J. Environ. Manage. **2002**, 64, 139-152.

46. D. Mage, G. Ozolins, P. Peterson, A. Webster, R. Orthofer, Atmos Environ. **1996**, 30, 681-686.

47. S. Suárez, R. Portela, M. D. Hernández-Alonso, B. Sánchez, Environ. Sci. Pollut. Res. **2014**, 21, 11208-11217.

48. M. M. Ballari, M. Hunger, G. Husken, H. J. H. Brouwers, Catal. Today **2010**, 151, 71-76.

49. M. M. Ballari, H. J. H. Brouwers, J. Hazard. Mater. **2013**, 254-255, 406-414.

50. R. Cámara, L. Crespo, R. Portela, S. Suárez, L. Bautista, F. Gutiérrez-Martin, B. Sánchez, Catal. Today **2013**, doi:10.1016/j.cattod.2013.10.049.

51. M. Chen, J. W. Chu, J. Clean. Prod. **2011**, 19, 1266-1272.

52. J. S. Dalton, P. A. Janes, N. G. Jones, J. A. Nicholson, K. R. Hallam, G. C. Allen, Environ. Pollut. **2002**, 120, 415-422.

53. G. Hüsken, M. Hunger, H. J. H. Brouwers Build. Environ. **2009**, 44, 2463-2474.

54. http://www.hucc.hokudai.ac.jp/~k15391/index_e.html.

55. http://www.fujita.co.jp.

56. R. Albalak, N. G. Bruce, J. P. McCracken, K. R. Smith, Environ. Sci. Technol. **2001**, 35, 2650-2655.

57. M. Ando, M. Tadano, S. Asanuma, K. Tamura, S. Matsushima, T. Watanabe, Environ. Health. Perspect. **1998**, 106, 239-2344.

58. B. Barnes, A. Mathee, L. Shafritz, L. Krieger, L. Sherburne, M. Favin, Health. Educ. Res. **2004**, 19, 543-550.

59. M. R. Pandey, J. S. Boleij, K. R. Smith, Lancet **1989**, 1, 427-429.

60. N. Britigan, A. Alshawa, S. A. Nizkorodov, J. Air. Waste Manage. Assoc. **2006**, 56, 601-610.

61. W. J. Fisk, D. Faulkner, J. Palonen, O. Seppanen, Indoor Air, **2002**, 12, 223-234.

62. Y. Y. Yao, T. Ochiai, H. Ishiguro, R. Nakano, Y. Kubota, Appl. Catal. B **2011**, 106, 592-599.

63. Y. X. Li, Y. A. Jiang, S. Q. Peng, F. Y. Jiang, J. Hazard. Mater. **2010**, 182, 90-96.

64. X. P. Wang, T. T. Lim, Appl. Catal. B **2010**, 100, 355-364.

65. C. C. Pan, J. C. S. Wu, Mater. Chem. Phys. **2006**, 100, 102-106.

66. http://www.daikinaircon.com/.

67. http://www.hitachi-hl.com/.

68. O, Khaselev, J. A.Turner, Science **1998**, 280, 425-427.

69. D. A. Tryk, A. Fujishima, K. Honda, Electrochem. Acta. **2000**, 45, 2363-2376.

70. A. Fujishima, K. Honda, Nature, **1972**, 238, 37-38.

71. N. Meng, K.H. L. Michael, Y. C. L. Dennis K. Sumathy, Renew. Sust. Energ. Rev. **2007**, 11, 401-425.

72. F. E. Osterloh, B. A. Parkinson, MRS Bull. **2011**, 36, 17-22.

73. Y. Tachibana, L. Vayssieres, J. R. Durrant, Nat. Photonics, **2012**, 6, 511-518.

74. V. A. Ganesh, H. K. Raut, A. S. Nair, S. Ramakrishna, J. Mater. Chem. **2011**, 21, 16304-16322.

75. W. Barthlott, C. Neinhaus, Planta, **1997**, 202, 1-8.

76. P. Ragesh, V. A. Ganesh, S. V. Naira, A. S. Nair, J. Mater. Chem. A, **2014**, 2, 14773-14797.

77. http://en.wikipedia.org/wiki/Self-cleaning_glass.

78. http://www.sekisuijushi.co.jp/.

79. A. P. Alivisatos, Science **1996**, 271, 933-937.

80. B. C. Wang, P. D. Kanhere, Z. Chen, J. Nisar, B. Pathak, R. Ahuja, J. Phys. Chem. C, **2013**, 117, 22518-22524.

81. L. Q. Ye, Y. R. S, X. L. Jin, H. Q. Xie, C. Zhang, Environ. Sci.: Nano **2014**, 1, 90-112.

82. J. B. Asbury, E. Hao, Y. Wang, H. N. Ghosh, T. Lian, J. Phys. Chem. B **2001**, 105, 4545-4557.

83. Y. Yin, A. P. Alivisatos, Nature **2005**, 437, 664-670.

84. X. B. Chen, S. S. Mao, Chem. Rev. **2007**, 107, 2891-2959.

85. M. D. Hernàndez-Alonso, F. Fresno, S. Suàrez, J. M. Coronado, Energy Environ. Sci. **2009**, 2, 1231-1257.

86. U. Diebold, Appl. Phys. A: Mater. Sci. Process. **2003**, 76, 681-687.

87. Y. Ma, X. L. Wang, Y. S. Jia, X. B. Chen, H. X. Han, C. Li, Chem. Rev. **2014**, 114, 9987-10043.

88. S. Banerjee, S. C. Pillai, P. Falaras, K. E. O'Shea, J. A. Byrne, D. D. Dionysiou, J. Phys. Chem. Lett. **2014**, 5, 2543-2554.

89. R. Asahi, T. Morikawa, H. Irie, T. Ohwaki, Chem. Rev. **2014**, 114, 9824-9852.

90. X. Ye, J. Sha, Z. Jiao, Z. Peng, L. Zhang, J. Mater. Sci. Technol. **1997**, 13, 359-360.

91. R. Thiruvenkatachari, S. Vigneswaran, I. S. Moon, Korean J. Chem. Eng. **2008**, 25, 64-72.

92. M. V. Dozzi, A. Saccomanni, E. Selli, J. Hazard. Mater. **2012**, 211-212, 188-195.

93. C. Z. Jiang, Y. L. Dou, Adv. Mater. Res. **2011**, 239-242, 2671-2674.

94. H. Kato, A. Kudo, Chem. Phys. Lett. **1998**, 295, 487-492.

95. H. Kato, K. Asakura, A. Kudo, J. Am. Chem. Soc. **2003**, 125, 3082-3089.

96. S. H. Lee, K. Teshima, Y. Mizuno, K. Yubuta, T. Shishido, M. Endo, S. Oishi, Cryst. Eng. Comm. **2010**, 12, 2871-2877.

97. X. Li, J. L. Zang, J. Phys. Chem. C **2009**, 113, 19411-19418.

98. Z. H. Li, G. Chen, J. W. Liu, Solid State Commun. **2007**, 143, 295-299.

99. C. C. Hu, C. C. Tsai, H. Teng, J. Am. Ceram. Soc. **2009**, 92, 460-466.

100. A. Kudo, H. Kato, Chem. Phys. Lett. **2000**, 331, 373-377.

101. W. H. Lin, C. Cheng, C. C. Hu, H. S. Teng, Appl. Phys. Lett. **2006**, 89, 211904-211906.

102. D. G. Porob, P. A. Maggard, J. Solid State Chem. **2006**, 179, 1727-1732.

103. L. J. Zhao, X. C. Zhang, C. M. Fan, Z. H. Liang, P. D. Han, Physica B **2012**, 407, 3364-3370.

104. S. J. Wu, C. Wang, Y. F. Cui, T. M. Wang, B. B. Huang, X. Y. Zhang, X. Y. Qin, P. Brault, Mater.Lett. **2010**, 64, 115-118.

105. M. A. Gondal, X. F. Chang, M. A. Ali, Z. H. Yamani, Q. Zhou, G. B. Ji, Appl. Catal. A **2011**, 397, 192-200.

106. Z. T. Deng, D. Chen, B. Peng, F. Q. Tang, Cryst. Growth Des. **2008**, 8, 2995-3003.

107. H. L. Peng, C. K. Chan, S. Meister, X. F. Zhang, Y. Cui, Chem. Mater. **2009**, 21, 247-252.

108. L. Q. Ye, Y. R. Su, X. L. Jin, H. Q. Xie, C. Zhang, Environ. Sci.: Nano **2014**, 1, 90-112.

109. H. Zhang, L. Liu, Z. Zhou, RSC Adv. **2012**, 2, 9224-9229.

110. F. D. Gao, D. W. Zeng, Q. W. Huang, S. Q. Tian, C. S. Xie, Phys. Chem. Chem. Phys. **2012**, 14, 10572-10578.

111. J. Y. Xiong, G. Cheng, G. F. Li, F. Qin, R. Chen, RSC Adv. **2011**, 1, 1542-1553.

112. B. L. Cushing, V. L. Kolesnichenko, C. O'Connor, J. Chem. Rev. **2004**, 104, 3893-3897.

113. R. Katoh, A. Furube, K. Yamanaka, T. Morikawa, J. Phys. Chem. Lett. **2010**, 1, 3261-3265.

114. C. Di Valentin, G. Pacchioni, Catal. Today **2013**, 206, 12-18.

115. Y. C. Nah, I. Paramasivam, P. Schmuki, Chem. Phys. Chem. **2010**, 11, 2698-2713.

116. H. Wang, J. P. Lewis, J. Phys.: Condens. Matter. **2005**, 17, L209-L213.

117. S. U. M. Khan, M. Al-Shahry, W. B., Jr. Ingler, Science **2002**, 297, 2243-2245.

118. C. D. Valentin, E. Finazzi, G. Pacchioni, A. Selloni, S. Livraghi, M. C. Paganini, E. Giamello, Chem. Phys. **2007**, 339, 44-56.

119. S. Sakthivel, H. Kisch, Chem. Phys. Chem. **2003**, 4, 487-490.

120. T. Umebayashi, T. Yamaki, S. Tanaka, K. Asai, Chem. Lett. **2003**, 32, 330-331.

121. T. Umebayashi, T. Yamaki, H. Itoh, K. Asai, J. Phys. Chem. Solids **2002**, 63, 1909-1920.

122. W. Yang, G. Q. Tan, H. J. Ren, A. Xia, Y. Y . Luo, L. X. Yin, J. Mater. Sci.: Mater. Electron. **2014**, 25, 3807-3815.

123. H. Li, D. Wang, P. Wang, H. Fan, T. Xie, Chem. Eur. J. **2009**, 15,12521-12527.

124. J. H. Yu, B. Wei, L .Zhu, H. Gao, W. J. Sun, L. L. Xu, Appl. Surf. Sci. **2013**, 284, 497-502.

125. F. Dong, S. Guo, H. Q. Wang, X. F. Li, Z. B. Wu, J. Phys. Chem. C **2011**, 115, 13285-13292.

126. G. D. Yang, Z. Jiang, H. H. Shi, T. C. Xiao, Z. F. Yan, J. Mater. Chem. **2010**, 20, 5301-5309.

127. O. Carp, C. L. Huisman, A. Reller, Prog. Solid State Chem. **2004**, 32, 33-177.

128. J. Choi, H. Park, M. R. Hoffmann, J. Phys. Chem. C **2010**, 114, 783-792.

129. S. J. Pearton, D. P. Norton, M. P. Ivill, A. F. Hebard, J. M. Zavada, W. M. Chen, I. A. Buyanova, IEEE Trans. Electr. Dev. **2007**, 54, 1040-1048.

130. P. D. Kanhere, J. W. Zheng, Z. Chen, J. Phys. Chem. C **2011**, 115, 11846-11853.

131. S. George, S. Pokhrel, Z. X. Ji, B. L. Henderson, T. Xia, L .J. Li, J. I. Zink, A. E. Nel, L. Mädler, J. Am. Chem. Soc. **2011**, 133, 11270-11278.

132. G. Liu, Y. N. Zhao, C. H. Sun, F. Li, G. Q. Lu, H. M. Cheng, Angew. Chem. Int. Ed. **2008**, 47, 4516 -4520.

133. S. Tonda, S. Kumar, O. Anjaneyulu, V. Shanker, Phys. Chem. Chem. Phys., **2014**, 16, 23819-23828.

134. X. G. Ma, Y. Wu, Y. H. Lu, J. Xu, Y. J. Wang, Y. F. Zhu, J. Phys. Chem. C **2011**, 115, 16963-16969.

135. L. L. Tan, W. J. Ong. S. P. Chai, A. R. Mohamed, Chem. Commun. **2014**, 50, 6923-6926.

136. V. Etacheri. M. K. Seery, S. J. Hinder, S. C. Pillai, Adv. Funct. Mater. **2011**, 21, 3744-3752.

137. X. Xiao, C. Liu, R. P. Hu, X. X. Zuo, J. M. Nan, L. S. Li, L. S. Wang, J. Mater. Chem. **2012**, 22, 22840-22843.

138. X. M. Zhou, G. Liu, J. G. Yu, W. H. Fan, J. Mater. Chem. **2012**, 22, 21337-21354.

139. S. Ling, M. A. El-Sayed, J. Phys. Chem. B **1999**, 103, 8410-8426.

140. S. K. Ghosh, T. Pal, Chem. Rev. **2007**, 107, 4797-4862.

141. Z. K. Zheng, B. B. Huang, X.Y. Qin, X. Y. Zhang, Y. Dai, M. H. Whangbo, J. Mater. Chem.

2011, 21, 9079-9087.

142. Z. Y. Zhang, A. R. Li, S. W. Cao, M. Bosman, S. Z. Li, C. Xue, Nanoscale, **2014**, 6, 5217-5222.

143. J. R. Ran, J. Zhang, J. G. Yu, M. Jaroniec, S. Z. Qiao, Chem. Soc. Rev. **2014**, 43, 7787-7812.

144. M. K. Tian, W. F. Shangguan, J. Yuan, L. Jiang, M. X. Chen, J. W. Shi, Z. Y. Ouyang, S. J. Wang, Appl. Catal. A- Gen. **2006**, 309, 76-84.

145. Q. J. Xiang, J. G. Yu, M. Jaroniec, J. Am. Chem. Soc. **2012**, 134, 6575-6578.

146. F. Zhang, A. Yamakata, K. Maeda, Y. Moriya, T. Takata, J. Kubota, K. Teshima, S. Oishi and K. Domen, J. Am. Chem. Soc. **2012**, 134, 8348-8351.

147. R. G. Li, Z. Chen, W. Zhao, F. X. Zhang, K. Maeda, B. K. Huang, S. Shen, K. Domen, C. Li, J. Phys. Chem. C. **2013**, 117, 376-382.

148. H. Park, Y. Park, W. Kim, W. Choi, J. Photoch. Photobio. C, **2013**, 15, 1-20.

149. S. Rehman, R. Ullah, A. M. Butt, N. D. Gohar, J. Hazard. Mater. **2009**, 170, 560-569.

150. G. J. Meyer, Inorg. Chem. **2005**, 44, 6852-6864.

151. K. Hirano, E. Suzuki, A. Ishikawa, T. Moroi, H. Shiroishi, M. Kaneko, J. Photochem. Photobiol. A **2000**, 136, 157-161.

152. S. H. Lee, Y. Park, K. R. Wee, H. J. Son, D. W. Cho, C. Pac, W. Y. Choi, S. O. Kang, Org. Lett. **2010**, 12, 460-463.

153. Y. J. Wang, Q. S. Wang, X. Y. Zhan, F. M. Wang, M. Safdar, J. He, Nanoscale, **2013**, 5, 8326-8339.

154. R. Ghosh Chaudhuri, S. Paria, Chem. Rev. **2011**, 112, 2373-2433.

155. L. L. Ruan, J. Q. Liu, Q. Zhou, J. J. Hu, G. Q. Xu, X. Shu, Y. C. Wu, New J. Chem. 2014, 38, 3022-3028.

156. S. Obregón, G. Colón, Appl. Catal. B: Environ. **2014**, 144, 775-782.

Chapter 2 PREPARATION AND ENHANCEMENT OF VISIBLE LIGHT INDUCED PHOTOCATALYSTS

Photocatalysis as a green chemistry technology has drawn considerable attention due to its extensively potential applications in the air purification, degradation of organic pollutant and solar energy conversion.[1-5] Although a lot of novel compounds with various photocatalytic activities have been proposed until now, [6-9] three promising photocatalys, TiO_2, $NaTaO_3$ and BiOX, have attracted peculiar attention in recent years because of their excellent photocatalytic properties.[10-14] As we all know, the natural solar light is composed of 5% UV light, 45% visible light and 50% infrared light. However, these three potential photocatalysts are mostly active for UV light solely and still present limited visible light absorption capability and corresponding visible light induced photocatalytic activity, which is not beneficial for the practical application. In addition, they also show relatively low separation ability for photogenerated hole-electron pairs, leading to confined photocatalytic peformance. It is well acknowledged that light-harveting capability, separation ability of charge carriers and specific surface area are three dominant points for the high efficiency of visible light induced photocatalytic activity. Therefore, in order to much improve the visible light responsive photocatalytic properties of TiO_2, $NaTaO_3$ and BiOX, some strategies based on the above mentioned three factors were employed in this chapter.

Firstly, series of C doped TiO_2 (C-TiO_2), C and Nd codoped TiO_2 (C-Nd-TiO_2), W solely doped TiO_2 (W-TiO_2), C and W codoped TiO_2 (C-W-TiO_2) as well as multi-phase of C-TiO_2 have been prepared, expecting to narrow band gap and promote separation ability of charge carriers. Secondly, three series of C doped $NaTaO_3$ C-$NaTaO_3$ particles, C doped $NaTaO_3$/Cl doped TiO_2 (C-$NaTaO_3$/Cl-TiO_2) composite and C modified $NaTaO_3$ mesocrystals have been successfully synthesized, expecting to much improve visible light induced photocatalytic activity via narrowing

band gap, elevating separation ability of photoinduced hole-electron pairs and enlarging specific surface area of products. Finally, visible light active BiOX nanostructures were also fabricated by a facile method at room temperature, intending promoting visible light responsive photo-activity by inducing oxygen vacancy in crystal.

2.1 Preparation of visible light active TiO_2 based materials

2.1.1 Hydrothermal-calcination synthesis of visible light induced C doped TiO_2

2.1.1.1 Introduction

Recently, doping, as an effective approach to improve the visible light driven photocatalytic activity of photocatalysts, has been made considerable efforts since it sometimes can introduce some impurity levels to narrow the band gap of semiconductors. Among lots of doping elements (e.g. C, N, Cl, Bi, Ag, Ta, etc.), the C-TiO_2[15-18] has received special attention after S. Sakthivel, et al.[19] reported that carbon doped particles presented five times higher active than that of nitrogen-doped TiO_2 in the degradation of 4-chlorophenol under visible light irradiation. According to the density functional theory calculations within the generalized gradient approximation reported by C.D. Valentin, et al.,[20] carbons can be doped into TiO_2 lattice and then strongly enhance the visible light absorption of TiO_2 via substituting oxygen sites or getting into the interstitial positions of TiO_2, which is due to the introduction of series of localized occupied states into the band gap of TiO_2 lattice. Y. Park, et al.[21] presented that high visible light induced photocatalytic performance of C-TiO_2 has been successfully realized by a conventional sol-gel synthesis. F. Dong, et al.[22] demonstrated that mesoporous C-TiO_2 nanomaterials with an anatase phase can be prepared by a one-pot green synthetic approach using sucrose as a carbon doping source. H. Irie, et al.[23] reported that carbon doped anatase TiO_2 powders were

obtained by oxidizing commercial TiC powders under O_2 flow at 600^{o}C. However, to the best of our knowledge, most of the C-TiO_2 products are prepared in the presence of extra carbon raw materials (tetrabutylammonium hydroxide, sucrose, urea, glucose), high heating temperature or without consideration of effect of ethanol from the reaction solution.

On the other hand, air pollution by NO_x, SO_2, CO, etc. has become more and more serious due to the use of liquefied petroleum gas cooking stoves, infiltration from nearby vehicular emissions and the combustion of nitrogen gas with oxygen in the air with the rapid development of society.[16] Generally, these pollutants were mainly disposed by remediation techniques, including adsorption and filtration methods, which have very low efficiency to remove gases and also have disposal and regeneration problems. Therefore, photocatalysis as a green process would be a promising method for the disposition of poison gas. [24, 25]

In this section, C-TiO_2 with high visible light photocatalytic activities has been prepared by a facile calcination assisted solvothermal method using titanium tetra-n-butoxide or titanium (III) chloride and ethanol as raw materials without the addition of any other carbon precursors. Meanwhile, the effect of ethanol used as a reaction solution on the carbon doping in the TiO_2 was also studied. Furthermore, the decomposition of NO gas and degradation of methyl orange have been employed to investigate the photocatalytic activity of C-TiO_2. [26]

2.1.1.2 Experimental

2.1.1.2.1 Sample preparation

C-TiO_2 nanoparticles have been successfully prepared by a facile calcination assisted solvothermal method. In a typical solvothermal synthesis process, 13 ml titanium tetra-n-butoxide were added dropwise to 35 ml ethanol/water (30:5) mixed solution with continuous stirring for 30 min. Subsequently, the solution was

transferred into a 100 mL Teflon-lined stainless steel autoclave and heated at 190^{o}C for 2h. After that, the products were centrifuged, washed with distilled water and ethanol four times, respectively, followed by drying in a vacuum oven at 60^{o}C overnight. The as-prepared white precursor powder was designated as CT-BE. Then, CT-BE sample was calcined at 165, 265 and 400^{o}C for 1h in a muffle furnace, and the products were designated as CT-BE-165, CT-BE-265 and CT-BE-400, respectively. For comparison, two samples were also fabricated by the similar process using titanium (III) chloride as Ti resource and different solvents, such as mixed ethanol/water (30:5) solution and pure distilled water at 190^{o}C for 2h, followed by calcination at 265^{o}C for 1h, and the products were designated as CT-CE-265 and T-CW-265, respectively. The sample names and concrete synthesis conditions are listed in Table 2-1.

Table 2-1. Detailed synthesis conditions of the samples.

Sample name	Ti source		Solvent		Calcined temperature (^{o}C)
	Titanium tetra-n-butoxide (ml)	Titanium(III) chloride (ml)	Ethanol (ml)	Distilled Water (ml)	
CT-BE	13	0	30	5	None
CT-BE-165	13	0	30	5	165
CT-BE-265	13	0	30	5	265
CT-BE-400	13	0	30	5	400
CT-CE-265	0	10	30	5	265
T-CW-265	0	10	0	35	265

Note: The first C indicates carbon doping; T indicates Ti; B indicates titanium tetra-n-butoxide; E indicated ethanol; the second C indicates titanium chloride; W indicates distilled water.

2.1.1.2.2 Characterization

The crystalline phases of the products were identified by X-ray diffraction analysis (XRD, Bruker AXS D2 Phaser) using graphite-monochromized CuKα radiation. The

UV–Vis diffuse reflectance spectra (DRS) were measured out using a UV–vis spectrophotometer (Shimadazu, UV-2450). The specific surface areas were determined by the BET method (Quantachrome Instruments, NOVA4200e). The size and shape of the nanoparticles were observed by transmission electron microscopy (TEM, JEOLJEM-2010). FT-IR measurements were conducted by using the FTS7000 series (DIGILIB). The surface compositions and binding energies of the samples were determined by X-ray photoelectron spectroscopy (XPS, Perkin Elmer PHI 5600). The shift of the binding energy owing to relative surface charging was corrected using the C 1s level at 284.6 eV as an internal standard and Ar^+ sputtering was employed to clean the surface of samples.

2.1.1.2.3 Photocatalytic activity tests

The photocatalytic activity of C-TiO_2 was investigated by evaluating the decomposition of NO (deNO_x) using a flow type reactor under irradiation of a 450 W high pressure mercury lamp at room temperature. The photocatalyst was spread in the hollow (20 mm×16 mm×0.5 mm) of a glass plate and then was placed at the bottom center of the reactor (373 cm^3 of internal volume) in which a 1:1 mixed gas of air and nitrogen containing 1 ppm of NO was flowed at the rate of 200 cm^3 min^{-1}. The sample powder was kept in the dark for 30 min to reach the adsorption and desorption equilibrium of NO gas. After that, the mercury light was turned on to irradiate the sample, where the light wavelengths were controlled by several filters: Pyrex glass for > 290 nm, Kenko L41 Super Pro (W) filter > 400 nm and Fuji triacetyl cellulose filter >510 nm. The measuring time for each sample under each wavelength was 10 min.[18] The concentration of NO was checked by a NO_x analyzer (Yanaco, ECL-88A).

In addition, the degradation of methyl orange (MO) was also used to characterize the photocatalytic activity of samples under the irradiation of 300W simulated solar light (ASAHI SPECTRA HAL-302) with a 400 nm cut-off long-pass filter. The experiment was carried out at the ambient temperature. The same amount (0.05 g) of sample powder was introduced into a 50 mL of 15 mg/L MO solution. Before

irradiation, the MO aqueous solution was stirred for 1h in the dark to reach the adsorption–desorption equilibrium for MO. At the desired illumination time intervals, 5 mL suspensions were withdrawn and then centrifuged to remove the sample particles. The concentration of MO was monitored by recording the maximum absorbance of MO at 464 nm with a UV-Vis spectrohotometer.

2.1.1.3 Results and discussion

2.1.1.3.1 The effect of post solvothermal heating temperature on the carbon doping in TiO_2

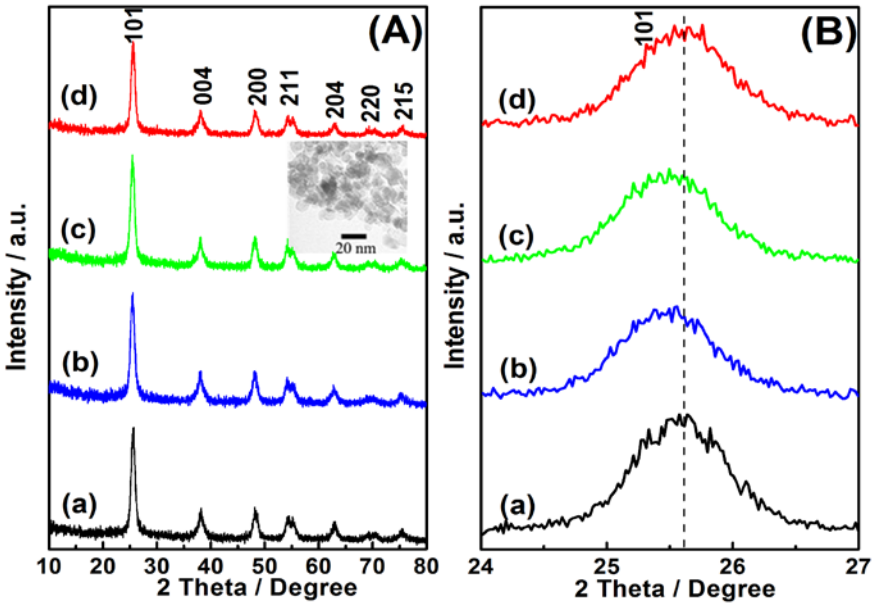

Figure 2-1. (A) XRD patterns of C-TiO_2 samples (the inset is the TEM image of CT-BE-265), (B) the amplified diffraction profiles in the range from 24 to 27 °. (a) CT-BE (without calcination), (b) CT-BE -165, (c) CT-BE -265, (d) CT-BE -400.

Figure 2-1 shows the XRD patterns of C-TiO_2 samples prepared by the solvothermal reaction followed by calcinations at different temperatures and corresponding TEM image for sample CT-BE-265. From Fig. 2-1 (A), it can be clearly seen that all the diffraction peaks could be indexed to the anatase phase of

TiO_2 (JCPDS file No. 21-1272) and no other impurity peaks were appeared. The average crystallite sizes of CT-BE, CT-BE-165, CT-BE-265 and CT-BE-400 were calculated from the full widths at half-maximum of the (101) peak according to the Scherrer equation ($D=0.9\lambda/(\beta\cos\theta)$) as 11.5, 11.6, 11.7 and 12.2 nm, respectively, indicating the average particle of samples increased a little with the increase of post solvothermal reaction heating temperature. In addition, it could be found that the particle size of CT-BE-265 agreed well with that observed from inserted TEM image. Fig. 2-1 (B) demonstrates the enlarged diffraction region of corresponding samples between 24 and 27 ^{o}. It is apparent that when the samples were calcined at 165 and 265^{o}C, the (101) peak shifted a little to the lower degree compared with that of sample without calcination, and the corresponding lattice parameter changed from a=3.7917 Å, c=9.5040 Å (sample CT-BE) to a=3.8108 Å, c=9.5432 Å (sample CT-BE-165) and a=3.8197 Å, c=9.5486 Å (sample CT-BE-265). This shift may be mainly due to the carbon doping in the TiO_2 lattice, since the bond length of Ti-C (2.008 and 2.217 Å) is longer than that of Ti-O (1.942 and 2.002 Å), and the radius of C^{4-} is also larger than that of O^{2-} in the TiO_2 lattice.[20] However, when the sample was calcined at 400 ^{o}C, the position of (101) peak shifted back to the original position of the sample CT-BE. It should be assigned to the release of doped carbon from TiO_2 lattice at a high temperature.[21]

The diffuse reflectance spectra and corresponding Kubelka–Munk plots of CT-BE, CT-BE-165, CT-BE-265 and CT-BE-400 are displayed in Fig. 2-2. As shown in Fig. 2-2 (A), it is clear that the visible light absorption from 400 to 800 nm increased with an increase in heating temperature up to 265^{o}C, but decreased dramatically at 400^{o}C to that of CT-BE. The band gap energy of CT-BE, CT-BE-165, CT-BE-265 and CT-BE-400 were determined as 3.11, 2.39, 2.78 and 3.01eV, respectively, by the intercept of the plots of $(\alpha h\upsilon)^{1/2}$ versus photon energy ($h\upsilon$) (in Fig. 2-2 (B)).[6] Meanwhile, the corresponding color of four samples changed as white, brown, deep brown and white, respectively. The enhancement of visible light absorption for CT-BE-165 and CT-BE-265 should be ascribed to the carbon doping in the TiO_2

lattice, which would introduce a series of localized occupied states into the band gap of TiO_2 lattice, leading to the strong visible light absorption.[20] As for CT-BE-400, its reflectance spectra became similar to that of CT-BE, since the doped carbon was eliminated from the TiO_2 lattice by the high temperature calcination. These light absorption profiles were nicely consistent with the XRD results.

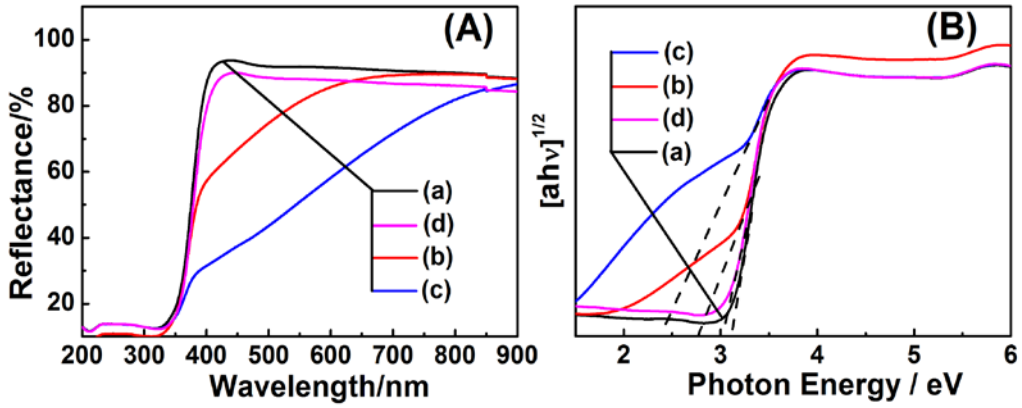

Figure 2-2. (A) Diffuse reflectance spectra of (a) CT-BE (without calcination), (b) CT-BE-165, (c) CT-BE-265, (d) CT-BE-400, and (B) the Kubelka–Munk plots for the corresponding reflectance spectra of samples.

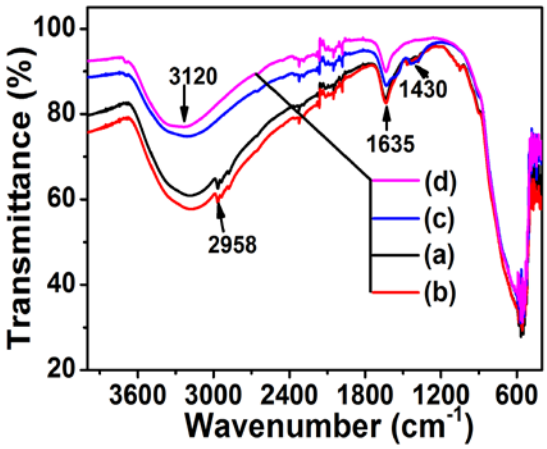

Figure 2-3. The FTIR spectra of (a) CT-BE (without calcination), (b) CT-BE-165, (c) CT-BE-265 and (d) CT-BE-400.

Figure 2-3 represents the FTIR spectra of CT-BE, CT-BE-165, CT-BE-265 and CT-BE-400. The peak at about 3120 cm^{-1} is attributed to the stretching vibration mode

of hydroxyls and adsorbed water, and the peak located at 1635 cm^{-1} is ascribed to bending vibration mode of O-H bond from hydroxyls and adsorbed water.[27] It can be obviously seen that when the sample was calcined at above 265 ^{o}C, the peak at 2958 cm^{-1} belonged to C-H bond disappeared, due to the decomposition of organics at the high temperatures. More importantly, FTIR spectra of CT-BE, CT-BE-165 and CT-BE-265 had a common peak at about 1430 cm^{-1}, which can be assigned to a carbon-related substrate. However, this peak didn't appear in the FTIR profile of CT-BE-400, indicating the complete decomposition of carbonaceous materials at 400 ^{o}C.

2.1.3.2 Effect of Ti source and solvent on the characteristics of TiO_2

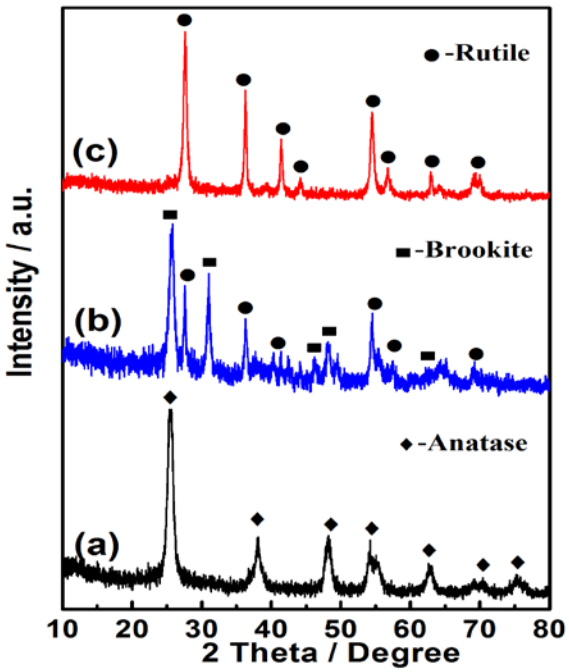

Figure 2-4. XRD patterns of (a) C-TiO_2 prepared by the solvothermal reaction using titanium tetra-n-butoxide and ethanol/water mixed solution followed by calcination at 265 ^{o}C (CT-BE -265), (b) C-TiO_2 prepared by the solvothermal reaction using $TiCl_3$ and ethanol/water mixed solution followed by calcination at 265 ^{o}C (CT-CE-265), (c) undoped TiO_2 prepared by the solvothermal reaction using $TiCl_3$ and pure water followed by calcination at 265 ^{o}C (T-CW-265).

Figure 2-4 shows the XRD patterns of CT-BE-265, CT-CE-265 and T-CW-265 synthesized by different Ti sources and solvents followed by the calciantion at 265 ^{o}C. Although CT-BE-265 prepared using titanium tetra-n-butoxide and ethanol/water mixed solution consisted of the single phase of anatase, CT-CE-265 prepared using titanium (III) chloride and ethanol/water mixed solution consisted of a rutile/brookite mixed phase. Besides, undoped titania, T-CW-265 produced using raw materials including no carbon element, such as titanium (III) chloride and pure distilled water consisted of a pure rutile phase.

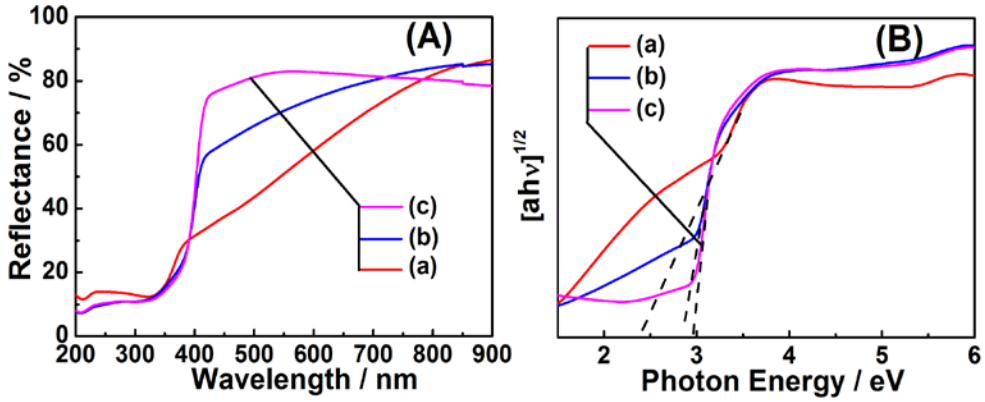

Figure 2-5. (A) Diffuse reflectance spectra of (a) C-TiO_2 prepared by the solvothermal reaction using titanium tetra-n-butoxide and ethanol/water mixed solution followed by calcination at 265 ^{o}C (CT-BE-265), (b) C-TiO_2 prepared by the solvothermal reaction using $TiCl_3$ and ethanol/water mixed solution followed by calcination at 265 ^{o}C (CT-CE-265), (c) undoped TiO_2 prepared by the solvothermal reaction using $TiCl_3$ and pure water followed by calcination at 265 ^{o}C (T-CW-265), and (B) the Kubelka–Munk plots for the corresponding reflectance spectra.

The diffuse reflectance spectra and Kubelka–Munk plots of CT-BE-265, CT-CE-265 and T-CW-265 are illustrated in Fig. 2-5. It could be seen that in addition to CT-BE-265 (2.39 eV), CT-CE-265 also presented nice visible light absorption with a small band gap of 2.84 eV, which was owing to carbon doping in the TiO_2 lattice. These results suggested that the doped carbon in TiO_2 can come from not only titanium tetra-butoxide used as a Ti source but also ethanol used as a solvent. As

expected, the undoped titania, T-CW--265 prepared using the Ti source and solvent including no carbon element demonstrated only UV light absorption.

2.1.3.3 XPS analysis

The XPS measurements were employed to investigate the chemical state and binding energy of the elements for three representative samples. Fig. 2-6 shows the XPS surveys, C 1s, O 1s and Ti 2p XPS spectra of CT-BE (a), CT-BE-265 (b) and CT-CE-265 (c). The peaks of C, O and Ti could be obviously seen in the survey spectrum of three samples (Fig. 2-6 (A)). All peaks in three samples were similar except for the relative intensity. Especially, the relative intensity of C 1s increased as CT-BE < CT-CE-265 < CT-BE-265 (inset), indicating that sample CT-BE-265 contains the highest carbon content. Fig. 2-6 (B) displays the C 1s XPS spectra of the CT-BE (a), CT-BE-265 (b) and CT-CE-265 (c). CT-BE showed three peaks at 285.6, 284.6 and 281.6 eV. The peak around 285.6 eV is attributed to the elemental carbon, which had the same binding energy as that of carbon in the graphite intercalation compound.[6, 28] The peak at 284.6, which was also appeared in CT-BE-265 and CT-CE-265, could be ascribed to adventitious carbon species from the XPS measurement. While the peak at 281.6 eV with low intensity is close to the C 1s peak reported for TiC (218.8 eV),[18,23,29] indicating the C-Ti bond formation in the sample CT-BE. However, according to XRD, DRS results and the color of samples, it can be learned that the carbon was not doped into the inner TiO_2 lattice in CT-BE. In addition, if carbon was doped into inner TiO_2 lattice, the binding energy of C-Ti should be shifted to higher energy (about 282 eV). It is well known that the electronegativity of carbon is smaller than that of oxygen. As carbon was doped into TiO_2 lattice by substituting the O site, the O-Ti-C bond would be formed, and the electron density around Ti atom should be decreased compared to that in C-Ti-C bond of TiC, which led to the shift of binding energy of C-Ti bond to higher energy.

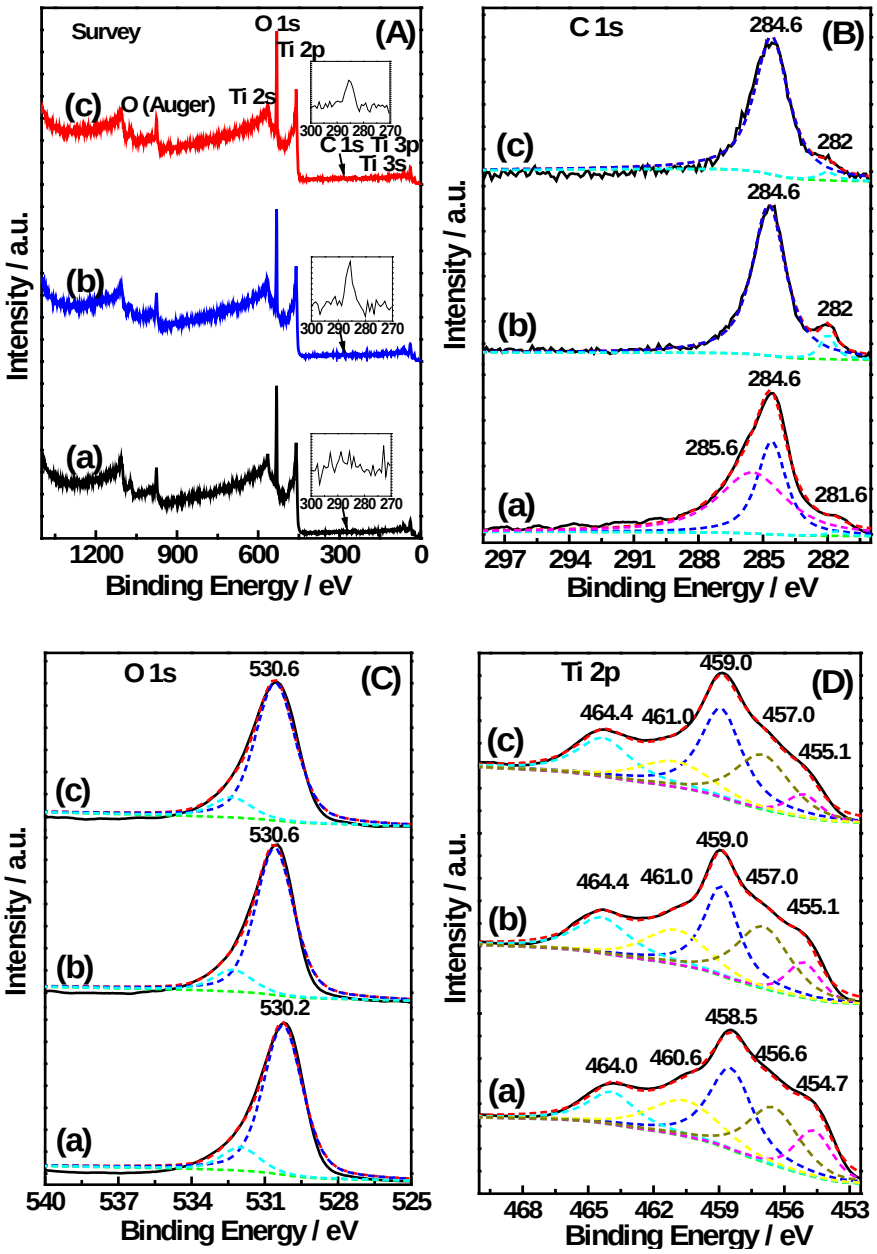

Figure 2-6. The XPS spectra of (A) survey, (B) C 1s , (C) O 1s and (D) Ti 2p of (a) C-TiO_2 prepared by the solvothermal reaction using titanium tetra-n-butoxide and ethanol/water mixed solution without calcination (CT-BE), (b) C-TiO_2 prepared by the solvothermal reaction using titanium tetra-n-butoxide and ethanol/water mixed solution followed by calcination at 265 ^{o}C (CT-BE-265), (c) C-TiO_2 prepared by the solvothermal reaction using $TiCl_3$ and ethanol/water mixed solution followed by calcination at 265 ^{o}C (CT-CE-265), and the inset plots in (A) are the corresponding enlarged region of (A) from 270 to 300 eV.

However, the binding energy of C-Ti did not shift to higher energy in the sample CT-BE.[27, 30, 31] Based on the above mentioned reasons, we deduced that the C-Ti bond should be formed only on the surface of CT-BE, which probably produced by the reaction happened between elemental carbon (285.6 eV) and surface TiO_2 during Ar^+ sputtering. The carbon concentration in the C-Ti bond of CT-BE was determined as 0.6 at. %. As for CT-BE-265 and CT-CE-265, the peak at 284.6 eV belonged to environmental carbon were also appeared but the elemental carbon peaked at 285.6 eV was disappeared in both samples, indicating that the elemental carbon in the sample had been eliminated or formed new bond with other atoms during the post solvothermal reaction calcination. Furthermore, the peak at 282 eV appeared in CT-BE-265 and CT-CE-265, which was also attributed to the binding energy of C-Ti bond.[27, 30] According to the above explanation, from the peak at 282 eV, it could be confirmed that carbon had been successfully doped into TiO_2 lattice by forming an O-Ti-C bond, i.e., carbon replaced the oxygen site in the TiO_2 lattice. The doped carbon concentrations in CT-BE-265 and CT-CE-265 were determined to be 0.42 and 0.20 at. %, respectively.

The O 1s XPS spectra of CT-BE, CT-BE-265 and CT-CE-265 is demonstrated in Fig. 2-6 (C). The peak around 532.0 eV, which was assigned to OH groups,[32, 33] appeared in all samples. The binding energy at 530.2 eV in CT-BE was ascribed to Ti-O band. This peak of CT-BE-265 and CT-CE-265 shifted to higher energy of 530.6 eV, which was due to the formation of oxygen vacancies in the TiO_2 lattice.[34-36] When C^{4-} was doped into TiO_2 lattice by substituting O^{2-} site, some oxygen vacancies would be produced simultaneously to compensate the charge balance. Consequently, the electron density around O atoms and Ti atoms in TiO_2 decreased and then led to the enhancement of binding energy for O 1s and Ti 2p. Therefore, the same shift happened in the Ti 2p XPS spectra. Five peaks appeared at 454.7, 456.6, 458.5, 460.6 and 464.0 eV in CT-BE, which are corresponded to the binding energy of Ti^{2+}, Ti^{3+}, Ti^{4+}, Ti^{2+} and Ti^{4+}, respectively. The peak positions of CT-BE-265 and CT-CE-265 shifted to 455.1, 457.0, 459.0, 461.0 and 464.4 eV (Fig. 2-6 (D)).[37] The appearance of

Ti^{2+} and Ti^{3+} in TiO_2 lattice is owing to the Ar^+ sputtering during the XPS measurement.[38,39]

The particle sizes, BET specific surface areas, phase compositions, band gap energies and C doping concentrations of the samples are listed in Table 2-2.

Table 2-2. Particle sizes, BET specific surface areas, phase compositions, band gap energies and C doping concentrations of the as-prepared samples.

Sample No.	Particle size (nm)	B.E.T. (m^2g^{-1})	Phase	Band gap (eV)	Doped C concentration (at%)
CT-BE	11.5	135.3	Anatase	3.11	0.06
CT-BE-165	11.6	131.5	Anatase	2.78	---
CT-BE-265	11.7	128.1	Anatase	2.39	0.42
CT-BE-400	12.2	116.6	Anatase	3.01	---
CT-CE-265	17.2	65.2	Brookite+Rutile	2.84	0.20
T-CW-265	21.6	55.3	Rutile	2.96	None

2.1.1.3.4 Visible light induced photocatalytic activities

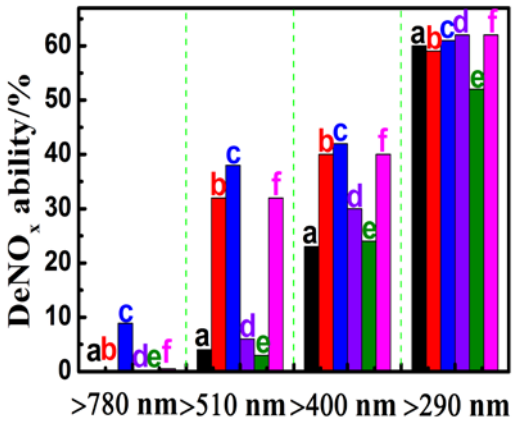

Figure 2-7. $DeNO_x$ ability of CT-BE (without calcination) (a), CT-BE-165 (b), CT-BE-265 (c), CT-BE-400 (d), P25 (e) and N-TiO_2 (f).

The photocatalytic activities of C-TiO_2 samples prepared by post solvothermal heating at different temperatures were investigated by the oxidative destruction of NO and the degradation of methyl orange. Fig. 2-7 shows the deNO_x ability of CT-BE (a), CT-BE-165 (b), CT-BE-265 (c), CT-BE-400 (d), P25 (e) and N-TiO_2 (f) prepared by the conventional solvothermal method using $TiCl_3$, HMT and ethanol as raw materials, where the different wavelength lights (>510 nm, >400 nm and >290 nm) were irradiated to the samples. From Fig. 2-7, it can be clearly seen that the deNO_x ability of CT-BE were about 4%, 23% and 60% under the irradiation of light wavelength >510 nm, >400 nm and >290 nm, respectively. By heating CT-BE, the visible light induced deNO_x ability greatly increased, i.e., the deNO_x ability of CT-BE-165 and CT-BE-265 under the irradiation of visible light (>510 nm) were 32 and 38%, respectively. This is mainly attributed to the enhancement of visible light absorption (in Fig. 2-2) and also probably due to the effect of oxygen vacancies induced by carbon doping. Because the oxygen vacancies could introduce some defect levels between the conduction band and valence band of TiO_2, resulting in the visible absorption of TiO_2.[40-43] However, the calcination at a too high temperature resulted in the decrease in the activity, i.e., the ability of CT-BE-400 was only 7% due to the elimination of doped carbon. Consequently, the sample CT-BE-265 presents the best performance for the visible light induced deNO_x destruction, which is even superior to N-TiO_2.

The oxidative destruction of NO by CT-CE-265 and T-CW-265 with the comparison of CT-BE-265 and P25 is displayed in Fig. 2-8. It is apparent that when $TiCl_3$ was used as the Ti source instead of titanium tetra-n-butoxide, the deNO_x ability under visible light (>510 nm) decreased to 19%, which is assigned to the relatively lower carbon doping concentration of CT-CE-265 compared to that of CT-BE-265. While T-CW-265 showed the lowest deNO_x activity because of the absence of carbon doping, i.e., poor visible light absorption ability. Therefore, it might be confirmed that the high visible light induced deNO_x ability of the samples might be due to the carbon doping in the TiO_2 lattice, leading to the narrowing of band gap and introduction of

oxygen vacancies in TiO_2. The stability of photocatalytic activity of CT-BE-265 was evaluated as shown in Fig. 2-9, and it was confirmed that no noticeable degradation of the photocatalytic performance was observed after three cycles.

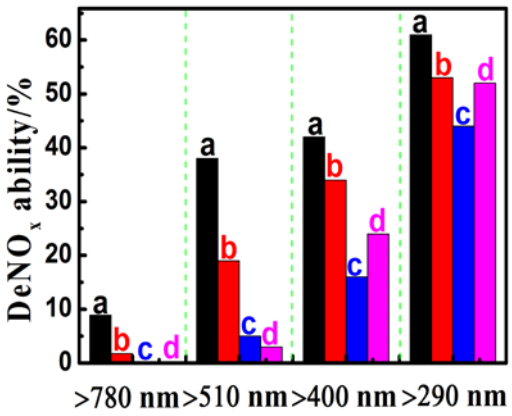

Figure 2-8. $DeNO_x$ ability of C-TiO_2 prepared by the solvothermal reaction using titanium tetra-n-butoxide and ethanol/water mixed solution followed by calcination at 265 ^oC (CT-BE-265) (a), C-TiO_2 prepared by the solvothermal reaction using $TiCl_3$ and ethanol/water mixed solution followed by calcination at 265 ^oC (CT-CE-265) (b), undoped TiO_2 prepared by by the solvothermal reaction using $TiCl_3$ and pure water followed by calcination at 265 ^oC (T-CW-265) (c), and P25 (d).

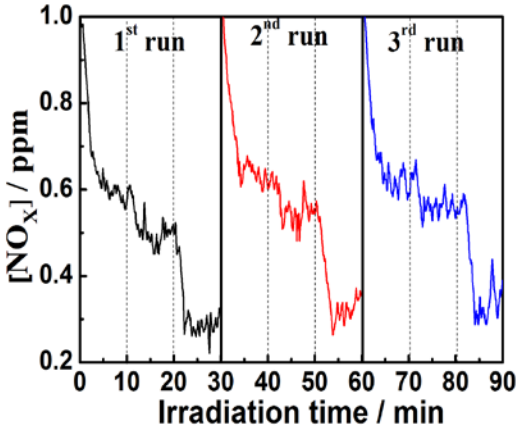

Figure 2-9. The multi-cycles of $deNO_x$ ability of C-TiO_2 prepared by the solvothermal reaction using titanium tetra-n-butoxide and ethanol/water mixed solution followed by calcination at 265 ^oC (CT-BE-265).

The mechanism of $deNO_x$ reaction of C-TiO_2 samples might be explained as

follows.[10, 44, 45] First of all, the C-TiO_2 photocatalyst irradiated by suitable light with the energy of hυ, produces a pair of hole and electron in TiO_2 lattice. The photogenerated hole in the conduction band will be trapped by water in the air to generate hydroxyl radicals •OH.[46] Meanwhile, the photoinduced electron in the valence band will form $•O_2^-$ in the presence of oxygen. When NO gas flows through the surface of TiO_2 powders, the NO will be oxidized by •OH, $•O_2^-$ and finally transferred to HNO_2 or HNO_3 which might be easily eliminated by water (eqs 2-1---eqs 2-6), and the corresponding schematic diagram is shown in Fig. 2-10. It is noteworthy that the influence of oxygen vacancies on the photocatalytic activity of TiO_2 as described above was not depicted in Fig. 2-10. Because this effect was probably existed in this work. However, the position of oxygen vacancy related defect levels in the band gap of TiO_2 are still contradiction that some researchers thought this level should be located below the conduction band of TiO_2 [43,47] but others deduced this level should be situated above the valence band of TiO_2.[42, 48] In addition, it has been reported that about 20% of NO can also be directly decomposed into N_2 and O_2 under the irradiation of light. [49]

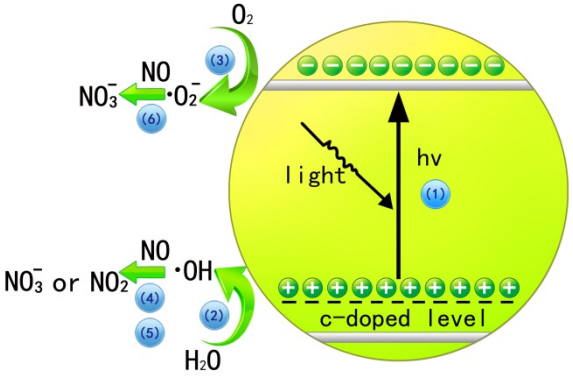

Figure 2-10. Schematic illustration of the photocatalytic process on C-TiO_2.

$TiO_2 + hυ \rightarrow TiO_2*(h^+_{VB} + e^-_{CB})$ (2-1)

$h^+_{VB} + H_2O \rightarrow •OH + H^+$ (2-2)

$e^-_{CB} + O_2 \rightarrow •O_2^-$ (2-3)

$NO + 2•OH \rightarrow NO_2 + H_2O$ (2-4)

$NO_2 + \bullet OH \rightarrow NO_3^- + H^+$ (2-5)

$NO_x + \bullet O_2^- \rightarrow NO_3^-$ (2-6)

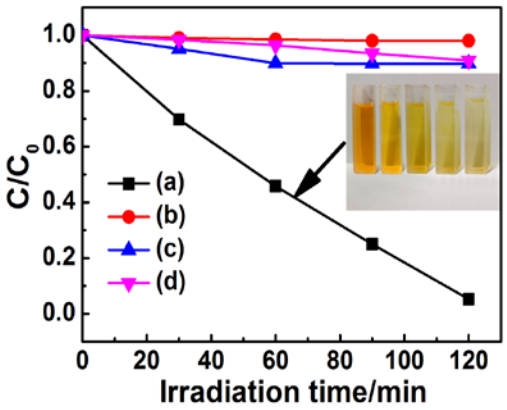

Figure 2-11. The photocatalytic activity for MO degradation of C-TiO_2 prepared by the solvothermal reaction using titanium tetra-n-butoxide and ethanol/water mixed solution followed by calcination at 265 ^oC (CT-BE-265) (a), Blank without sample (b), P25 (c) and N-TiO_2 (d) (light source λ>400 nm).

In addition to the deNO_x ability, the degradation of MO by CT-BE-265, P25 and N-TiO_2 as well as a blank test under visible light irradiation is also shown in Fig. 2-11. It is explicit that the degradation of MO was due to the addition of the photocatalyst, since no noticeable destruction of MO was observed by the blank test. Furthermore, The MO was degraded about 98% by CT-BE-265 within 120 min under the visible light (>400 nm), which is much higher than that of P25 and N-TiO_2. The color change of corresponding MO solution was also displayed in the inset. It implies that C-TiO_2 samples presented the very good destruction ability on not only NO gas but also MO solution, being much superior to P25 and N-TiO_2.[26]

2.1.2 Preparation of visible light induced C doped TiO_2 with multi-phases

2.1.2.1 Introduction

As introduced above, TiO_2 has three common polymorphs, including anatase, rutile and brookite. Owing to the various crystal structure and other physical properties, three phases of TiO_2 exhibit obvious difference for photocatalytic activity. Anatase presents the best performance followed by rutile and brookite. It is well acknowledged that the most popular photocatalyst in industry is commercial P25 TiO_2 rather than anatase TiO_2, which is owing to the unique constitution of P25 that consists of ca. 71% of anatase and ca. 29% of rutile. The anatase and rutile have different band gaps and subsequently various VB and CB positions. In this case, the composite formed by anatase and rutile can present a nice separation ability for charge carriers in comparison of solely anatase and rutile phases of TiO_2. Nevertheless, the P25 still exhibits poor visible light induced photocatalytic activity because of limited light-harvesting ability. In this section, an excellent visible light responsive TiO_2 with multi-phase has been prepared by a post-solvothermal reaction calcination method.

2.1.2.2 Experimental

2.1.2.2.1 Sample preparation

Series of C-TiO_2 with different morphologies have been prepared by solvothermal method with the help of post-solvothermal reaction calcination as follows: Firstly, 8 mL titanium tetra-n-butoxide were added into 0.5 mL concentrated HCl solution with severely stirring. After 10 min, 40 mL oleic acid was introduced into the above mixed solution with another 30 min strong stirring followed by dropwise adding 2 mL water and different volumes of acetic acid (0, 1, 2, 4, 8 mL). Subsequently, the solution was transferred into a 100 mL Teflon-lined stainless steel autoclave and heated at 180^{o}C

for 12h. Finally, the particles were centrifuged, washed with distilled water and ethanol four times, respectively, followed by drying in a vacuum at 60^{o}C overnight. In order to induce the carbon doping, the dried particles were calcined at 350^{o}C for 1h.

2.1.2.2.2 Photocatalytic activity tests

The photocatalytic activity of C-TiO_2 with multi-phase was evaluated by measuring the destruction ability of NO (deNO_x) using a continuous flow type reactor under irradiation of a 300 W simulated solar light (ASAHI SPECTRA HAL-302) at room temperature.

2.1.2.3 Results and discussion

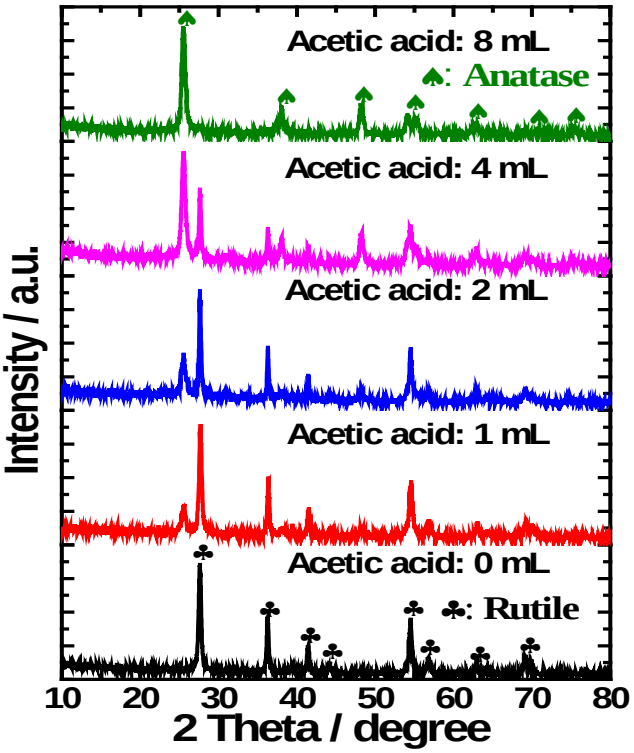

Figure 2-12. XRD patterns of C-TiO_2 particles with respect to the added acetic acid volume.

Fig. 2-12 shows the XRD patterns of C-TiO_2 samples as a function of the acetic acid contents. It can be clearly seen that the sample prepared without the addition of

acetic acid in the reaction solution exhibited the pure rutile phase, while after inroducing the acetic acid to the solvent, some diffraction peaks belonged to anatase phase appeared in addition to those attributed to rutile phase. Furthermore, with the increment of acetic acid content, the ratio of anatase phase increased. As 8 mL acetic acid was induced, a pure anatase phase could be obtained, indicating that the phases of TiO_2 crystal could be nicely tuned by adjusting the concentration of acetic acid in the solvothermal reaction solution.

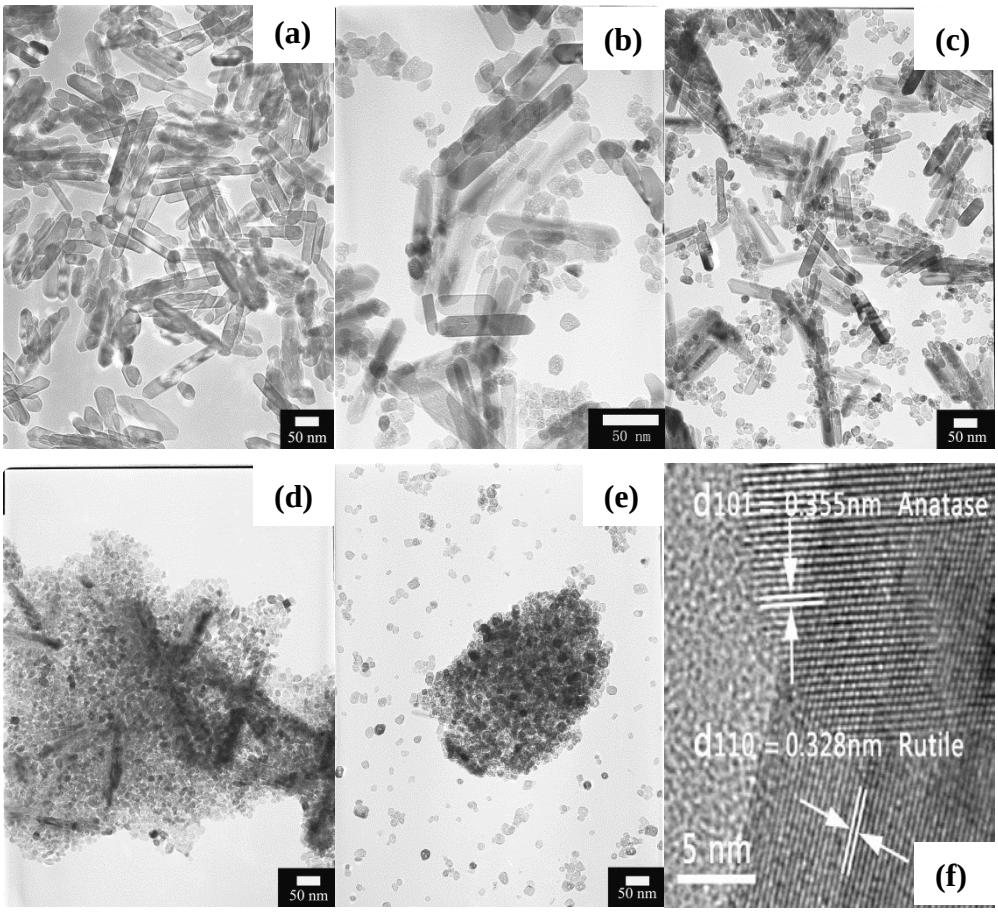

Figure 2-13. TEM images of C-TiO_2 products prepared by various acetic acid volumes of 0 mL (a), 1 mL (b), 2 mL (c), 4 mL (d), 8 mL (e), respectively, and the HRTEM image of sample prepared by 2 mL acetic acid.

The corresponding TEM images of samples synthesized by different contents of acetic acid are presented in Fig. 2-13. As seen in this figure, it is explicit that the sample prepared without the addition of acetic acid (Fig. 2-13 (a)) showed a nanorod shape with the specific surface area of 39.6 m^2g^{-1}; as the acetic acid was introduced

into the reaction solvent, some of nanoparticles appeared. Furthermore, the amount of nanoparticles increased with rising acetic acid contents and when 8 mL acetic acid was used (Fig. 2-13 (e)), only nanoparticles were produced. The tendency of the morphology change corresponds well with the change in the crystalline phase as shown in Fig. 2-12. Besides, the specific surface area of samples fabricated by using 0 (Fig. 2-13 (a)), 1 (Fig. 2-13 (b)), 2 (Fig. 2-13 (c)), 4 (Fig. 2-13 (d)), 8 mL (Fig. 2-13 (e)) of acetic acid also greatly increased from 39.6 to 50.3, 60.4, 100.5, 137.2 m^2g^{-1}, respectively. On the other hand, the HRTEM image of sample prepared by using 2 mL acetic acid was also illustrated in Fig. 2-13 (f). It can be seen that the nanorod was corresponding to the rutile phase of TiO_2, whereas the nanoparticle was assigned to the anatase phase of TiO_2. Therefore, based on the XRD, TEM and HRTEM results, we can confirm that the change of sample morphologies by tuning the acetic acid contents in the solvothermal reaction solvent was perfectly consistent with that of sample phases. As we all know, the rutile phase of TiO_2 is generally produced in the low pH value of acid solution, while the anatase is preferred to produce in the high pH value of base solution. Because the acidic condition is commonly beneficial for the corner share of [TiO_6] octahedron units, while the basic condition is an advantage for the edge share of [TiO_6] octahedron units; moreover, the formation of anatase TiO_2 is needed much more edge share of [TiO_6] octahedron units in crystal than that of rutile TiO_2.[50] Regarding the research in this work, the pure rutile phase of TiO_2 was normally obtained under the strong acid solution since the oleic acid and concentrated HCl were used as reaction solution. However, when the acetic acid was added to further increase the acidic condition, the anatase phase of TiO_2 appeared inversely, and as 8 mL of acetic acid was induced, a pure anatase phase of particle was obtained instead of rutile phase. This abnormal phenomenon should be owing to the reason as follows: in the hydrothermal or solvothermal reaction, the formation of crystal generally happens by the dissolution-precipitation process that the small particle is, firstly, dissolved by surface protonation or hydroxylation and then the most stable phase in this aqueous solution will reprecipitate to produce larger crystal. In this

pathway, the phase with relatively higher free energy prefers to dissolve, while the phase with relatively lower surface energy intends to precipitate. Regarding the solution chemistry, Ti^{4+} species in aqueous solution will be octahedrally coordinated by using vacant "d" orbitals of Ti^{4+} to obtain electrons from nucleophilic ligands such as H_2O or –OH groups, forming species as $[Ti(OH)_n(H_2O)_{6-n}]^{(4-n)+}$.[50] When the reaction temperate increases, the mononuclear structure is going to dehydrate and condense to form special amorphous $TiO_2 \cdot nH_2O$ species, which includes a metal-oxo-polymer (Ti-O-Ti) network. The key point for the formation of kinds of phase is mainly determined by the process of octahedral coordination in the beginning. Furthermore, the types of octahedral coordination can be significantly affected by the pH of the reaction solution and the addition of species utilizing as complexing agents.[51-53] In this work, there was no big difference in the pH value before and after the addition of acetic acid in the reaction solution since the original oleic acid and concentrated HCl mixed solution presented high acidity, and the introduction of weak acetic acid does not cause large change in pH value of this solution. Therefore, the change of phase from rutile to anatase in the presence of acetic acid should be dominantly attributed to the effect of acetic acid related complexing agents. As a result of the various co-ordination ability and spatial steric effects of anions such as F^-, Cl^-, NO_3^- and organic species, etc., it will present different bonding modes of the linkage of six-fold coordinated monomers under the various anions. These induced complexing agent of anion in the reaction solution can replace the H_2O and -OH species to form difference ΞTi–anion modes, finally leading to different phases.[53] In this experiment, the addition of acetic acid as a special complexing agent was beneficial for the formation of anatase phase. As for the change of morphology as the transformation of phases, it should be assigned to the nature of rutile and anatase phases that in most cases, the rutile prefers to form nanorod and anatase intends to form rounded shapes. Because the rutile has 4_2 screw axes along with the crystallographic c-axis. This unique structure derives the crystal growth in this direction to form nanorod with a {110} explored faces as shown in Fig. 2-13 (f).[54,55]

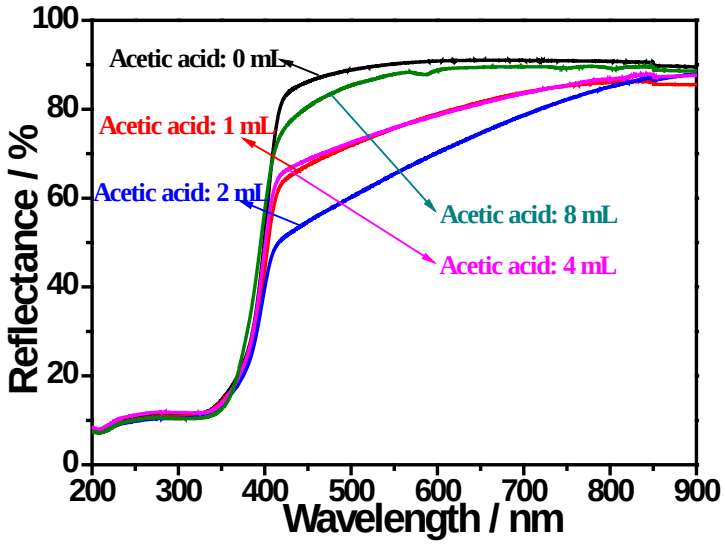

Figure 2-14. DRS of C-TiO_2 multi-phase particles varied with the content of acetic acid.

The DRS of C-TiO_2 with multi-phase synthesized by employing different volumes of acetic acid is exhibited in Fig. 2-14. It is explicit that the sample fabricated without the induction of acetic acid presented very poor visible light absorption capability because of the wide band gap of pristine rutile TiO_2. However, when the acetic acid was introduced into the reaction solution, the visible light-harvesting ability was significantly improved. Furthermore, as 2 mL acetic acid was added, the sample displays the optimal light-harvesting activity with rutile/anatase mixed phases, which should be owing to the C doping in TiO_2 induced by post-solvothermal reaction calcination as explained in the above section 2.1. Nevertheless, further increasing acetic acid content, the visible light absorption dramatically decreased. This interesting phenomenon is probably as a result of that the multi-phase was beneficial to connect much more carbonaceous species on the surface and finally led to much more doped C contents after calcination. According to the XPS calculation, about 0.20 at% of C was doped in the sample prepared with the addition of 2 mL acetic acid and only 0.08 at% for 4 mL acetic acid added one.

The corresponding photocatalytic activity of C-TiO_2 with multi-phase evaluated by the continuous NO destruction under the irradiation of simulated solar light is

presented in Fig. 2-15. It can be clearly seen that C-TiO_2 with pure rutile phase prepared by 0 mL acetic acid presented the relatively better deNO_x ability than that of commercial P25. As the acetic acid was introduced to form multi-phase of C-TiO_2 particles, the visible light induced photocatalytic activity of the samples was further improved, and when 2 mL acetic acid was added, the sample revealed the best photoctalytic destruction ability, followed by a little bit decrement with the elevation of acetic acid content. The high efficiency of photocatalytic activity for C-TiO_2 with multi-phase should be owing to the much improved visible light absorption capability and also the formation of heterostructure consisting of rutile and anatase phase to enhance the separation ability of charge carriers. Therefore, in this section, it can be learned that the much improved visible light induced photocatalytic activity of TiO_2 has been successfully realized by forming multi-phase and introducing C doping simultaneously.

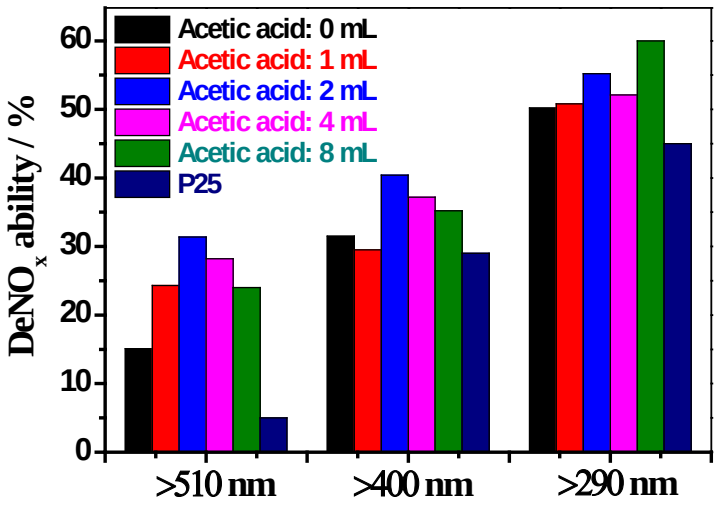

Figure 2-15. DeNO_x ability of C-TiO_2 samples prepared by using various acetic acid volumes.

2.1.3 Preparation of the whole visible light responsive C and Nd codoped TiO_2 nanoparticles*

2.1.3.1 Introduction

Codoping with different types of ions has also been proposed by many researchers to reach some synergetic effects between co-doped ions. For instance, Huang, et al. [56] reported that the photocatalytic activity of TiO_2 could be further enhanced by Fe and N co-doping compared with that of N or Fe solely-doped TiO_2 owing to the decrement of charge carriers recombination. Ding, et al.[57] demonstrated that the visible absorption of TiO_2 was able to be greatly increased by I and B co-doping, which eventually led to improved photocatalytic activity. However, there are still some shortages in doping, i.e., most of the dopants in photocatalysts cannot sufficiently extend the absorption of TiO_2 into the whole visible range (390-780 nm) for photocatalysis and effectively separate the charge carriers. Therefore, the effective doping ways are still few and greatly required.

In this section, Nd and C were, firstly, employed to co-dope in TiO_2 by a facile calcination assisted solvothermal method, expecting to extend the absorption of TiO_2 into the whole visible range of solar light by introducing some C electron states above the valence band and some Nd electron states below the conduction band of TiO_2 simultaneously, and effectively separate the photogenerated hole-electron pairs via Nd/C co-doping or some synergetic effects between Nd and C doping. [58]

*Reprinted (adapted) with permission from (X. Y. Wu, S. Yin, Q. Dong, C. S. Guo, T. Kimura, T. Sato, J. Phys. Chem. C 2013, 117, 8345-8352.). Copyright (2013) American Chemical Society.

2.1.3.2 Experimental

2.1.3.2.1 Sample preparation

A series of C and Nd co-doped TiO_2 (1 at.% Nd-C-TiO_2, 2 at.% Nd-C-TiO_2, 3 at.% Nd-C-TiO_2 and 4 at.% Nd-C-TiO_2) have been prepared by a simple calcination assisted solvothermal method. In a typical synthesis of Nd-C-TiO_2 particles, an appropriate amount of Nd_2O_3 was dissolved in a concentrated nitric acid to form $Nd(NO_3)_3$ solution in a beaker, and then dried to get rid of remnant nitric acid and water. After that, 2.5 mL titanium tetra-n-butoxide and 10 mL ethanol were introduced to the beaker with continuous stirring for 30 min. Subsequently, 11.5 mL ethanol/water (10:1.5) mixed solution was added dropwise to above solution with another 30 min magnetic stirring before transferring into a 100 mL Teflon-lined stainless steel autoclave. Finally, the solution was heated at 190^oC for 2h, and the products were separated by centrifugation, washed and calcined at 265^oC for 1h in ambient condition. For comparison, the pure TiO_2, Nd-TiO_2 and C-TiO_2 were also prepared by a similar process without the addition of Nd_2O_3 and calcination, with the addition of Nd_2O_3 and without calcination, and without the introduction of Nd_2O_3 and with calcination, respectively.

2.1.3.2.2 Photocatalytic activity tests

The photocatalytic activity of Nd-C-TiO_2 was investigated by evaluating the decomposition of NO_x ($deNO_x$) in a flow type reactor under irradiation of a 300 W simulated solar light (ASAHI SPECTRA HAL-302) at room temperature.

In addition, the degradation of MO was also used to characterize the photocatalytic activity of prepared samples under the irradiation of 300 W simulated solar light (ASAHI SPECTRA HAL-302) with a 400 nm cut-off long-pass filter. The experiment was carried out at the ambient temperature. The same amount (0.10 g) of sample powder was introduced into a 100 mL of 15 mg/L MO solution. Before irradiation,

the MO aqueous solution was stirred for 1h in the dark to reach the adsorption–desorption equilibrium for MO. At the desired illumination time intervals, 5 mL suspensions were withdrawn and then centrifuged to remove the sample particles. The concentration of MO was monitored by recording the maximum absorbance of MO at 464 nm with a UV-Vis spectrohotometer.

2.1.3.3 Results and Discussion

2.1.3.3.1 Characterization of prepared Nd, C co-doped TiO_2 photocatalysts

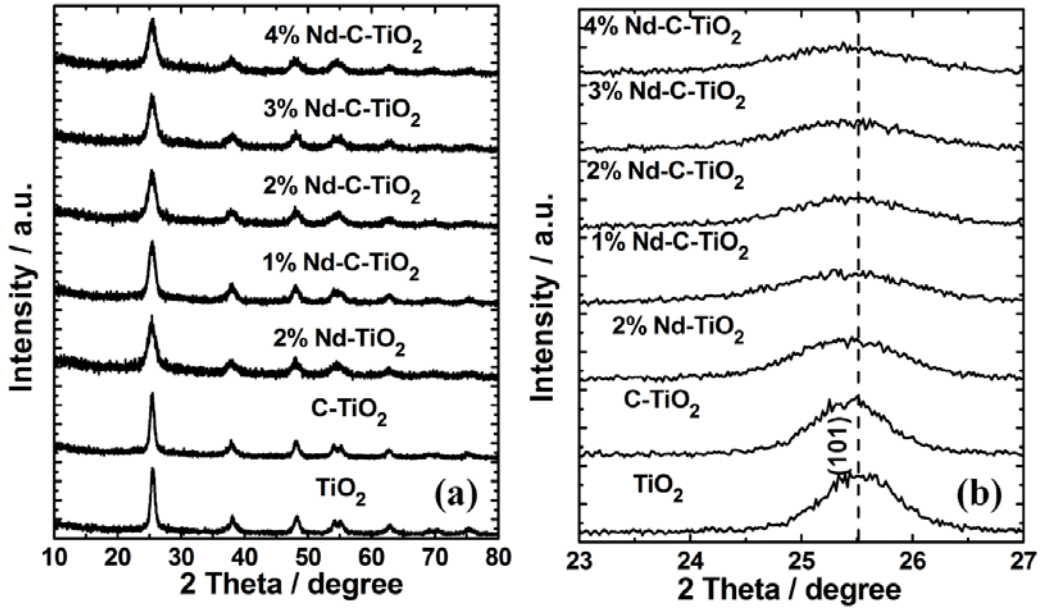

Figure 2-16. (a) XRD patterns of prepared TiO_2 based samples, (b) the amplified diffraction profiles in the range from 23 to 27 ^{o}.

Figure 2-16 shows the XRD patterns of synthesized TiO_2 based samples along with corresponding enlarged diffraction profiles ranging from 23 to 27 ^{o}. In Fig. 2-16 (a), it can be clearly seen that all the diffraction peaks of 7 samples were well indexed to the anatase phase of TiO_2 (JCPDS file No. 21-1272). No crystalline phase assigned to neodymium oxides could be found, probably due to the reason that the Nd content in

the samples was out of detection limits of the XRD instrument, or the neodymium ions had been doped into TiO_2 lattice. From corresponding enlarged profiles in Fig. 2-16 (b), it can also be observed that the main (101) peak of carbon doped sample shifted a little to the lower degree compared with that of pure TiO_2, which should be assigned to the carbon doping in the TiO_2 lattice. Although the ionic radius of Nd^{3+} (0.098 nm) is much larger than that of Ti^{4+} (0.068 nm), no obvious shift was observed when Nd was doped in C-TiO_2. However, the relative peak intensity greatly decreased and the corresponding full widths at half-maximum of the (101) peak significantly increased, indicating the decrease of particle size. The similar result has also been reported in others' works.[59,60] It is well known that without surface-bonding molecules the lattice parameters decrease in the nanoscale due to the quantitative decreasing of constituent bond length data[61] and the large surface compressive stress in nanoparticles.[62] Thus, no obvious XRD peak shift for Nd doped samples might be due to the co-effect of ionic radius difference (Nd^{3+} and Ti^{4+}) and the reduced particle size.

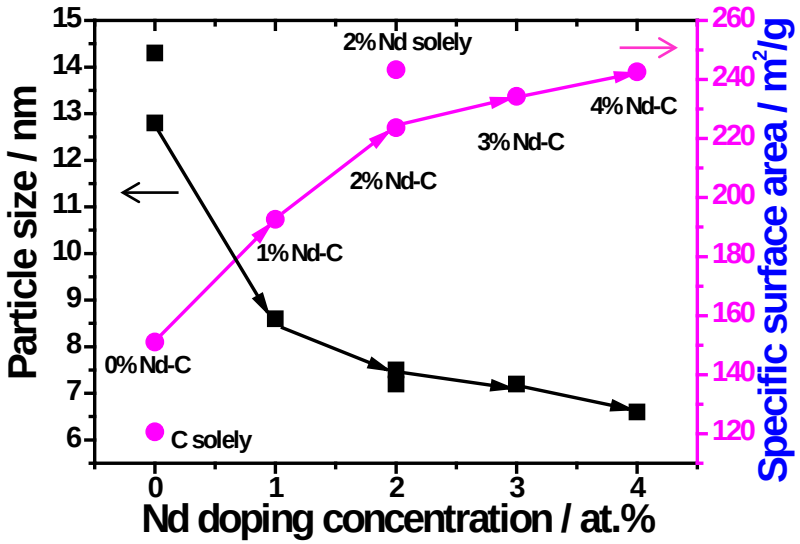

Figure 2-17. Nd doping concentration dependence of particle sizes and specific surface areas of samples.

The average crystallite size and specific surface area of as-prepared samples are shown in Fig. 2-17. The average crystallite sizes were calculated from the full widths

at half-maximum of the (101) peak according to the Scherrer equation ($D=0.9\lambda/(\beta\cos\theta)$). In this figure, it can be found that with the addition of Nd, the particle size of samples decreased, accompanying with the increment of the specific surface area. Following with the chemical bonding theory of single crystal growth,[63] the above results implied that the introduction of Nd would hamper the crystal growth of TiO_2 and then led to the decrement of particle size and increment of specific surface area.[62]

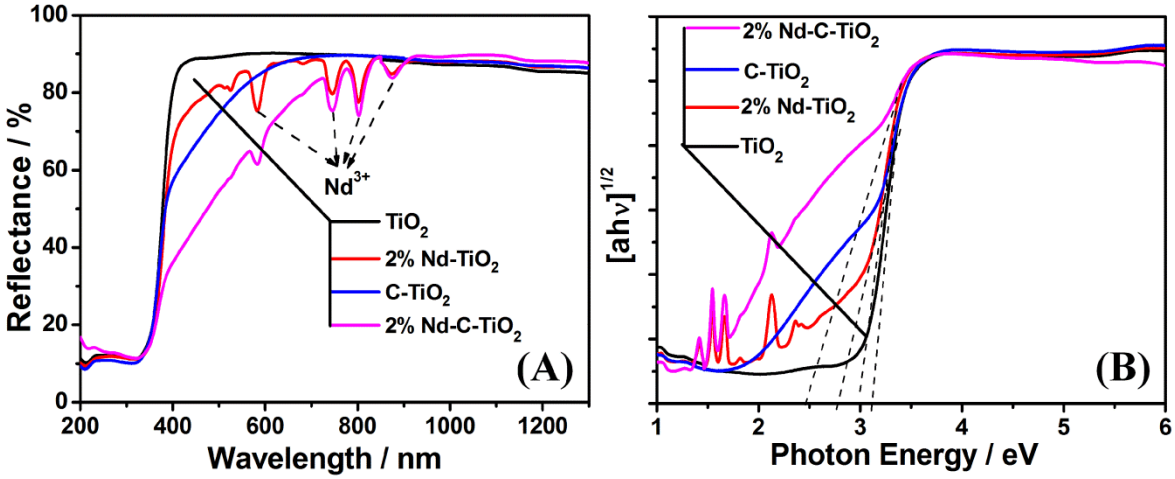

Figure 2-18. Diffuse reflectance spectra of prepared TiO_2, C-TiO_2, 2% Nd-TiO_2 and 2% Nd-C-TiO_2 (A), the Kubelka–Munk plots for the corresponding reflectance spectra (B).

Figure 2-18 shows the diffuse reflectance spectra and Kubelka-Munk plots of the prepared TiO_2, C-TiO_2, 2% Nd-TiO_2 and 2% Nd-C-TiO_2. It was explicit that C-TiO_2 displayed very good visible absorption with the relative band gap of 2.77 eV (Fig. 2-18 B), which was much smaller than that of undoped TiO_2 (3.13 eV). The enhancement of visible light absorption for C-TiO_2 should be attributed to the carbon doping in the TiO_2 lattice, in which a series of localized occupied states were introduced to the band of TiO_2, resulted in the strong visible light absorption.[40,41] When Nd alone was doped into TiO_2 lattice, we can observe an obvious red shift compared with that of undoped TiO_2 sample. This red shift should be due to the charge transfer from O 2p to Nd 4f instead of Ti 3d. Because when Nd was doped into

TiO_2 lattice, some of the new unoccupied molecular orbitals, which are located below the lowest edge of the conduction band of TiO_2,[64] would be formed. In addition, five extra absorption peaks located at 525, 582, 744, 803 and 874 nm corresponding to the f-f electron transitions of Nd^{3+} [65] were appeared in the DRS of Nd-TiO_2 samples. More importantly, when Nd and C were co-doped in the TiO_2, not only five absorption peaks belonged to Nd^{3+} transitions were appeared, but also the visible absorption had been dramatically enhanced in comparison with those of C-TiO_2 and Nd-TiO_2. The light absorption covered the UV and whole visible range of 200-900 nm. The significantly improved visible absorption of 2% Nd-C-TiO_2 was probably because of the increased C doping content in the TiO_2 accompanied with Nd co-doping.

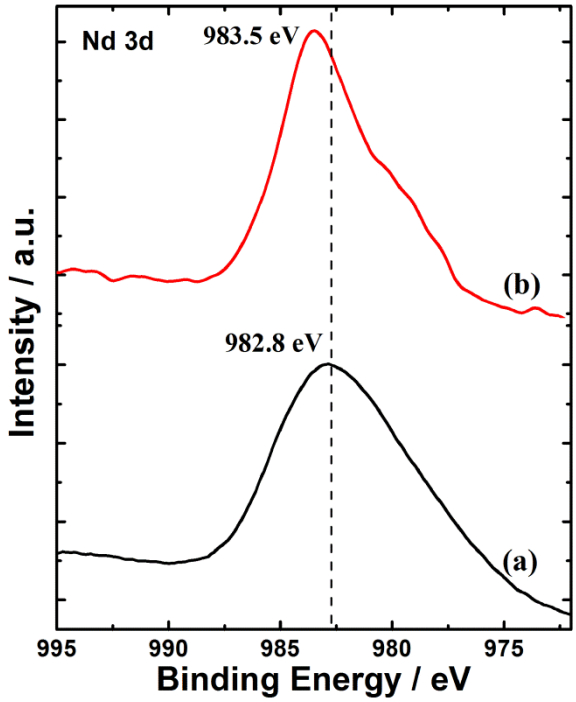

Figure 2-19. XPS spectra of Nd3d for Nd_2O_3 prepared by the same method as that of Nd-C-TiO_2 without the addition of Ti source (a) and 2% Nd-C-TiO_2 (b).

The status of Nd^{3+} in the 2% Nd-C-TiO_2 was studied by XPS analysis (see Fig. 2-19). As shown in Fig. 2-19, it is clear that the pure Nd_2O_3 presented a strong peak at about 982.8 eV, corresponding to the binding energy of Nd-O in Nd_2O_3.[66] When Nd^{3+} was co-doped into C-TiO_2, this peak was shifted a little to the higher energy (983.5

eV), which should be due to the introduction of Nd^{3+} into TiO_2 lattice. Because when Nd was doped into TiO_2 lattice by substituting the Ti site, some Nd-O-Ti bonds would be formed in TiO_2 instead of Nd-O-Nd bonds in Nd_2O_3. In this case, the binding energy of Nd-O would increase since the electronegativity of Nd is smaller than that of Ti.[67] According to the XPS result, 1.54 at.% of Nd was existed in the sample of 2% Nd-C-TiO_2.

Figure 2-20 shows the XPS spectra of C 1s for TiO_2, C-TiO_2 and 2% Nd-C-TiO_2. It can be clearly seen that all samples exhibited a strong peak at 284.6 eV, which is ascribed to the adventitious carbon species from the XPS measurement. Meanwhile, a peak around 285.6 eV, corresponding to the elemental carbon which has the same binding energy as that of carbon in the graphite intercalation compound,[6,28] is also presented in these three samples but with different peak intensities. The decrement of peak intensity for doped TiO_2 samples implied that the elemental carbon in the sample had been decreased or formed new bond with other atoms during the post solvothermal reaction calcination.

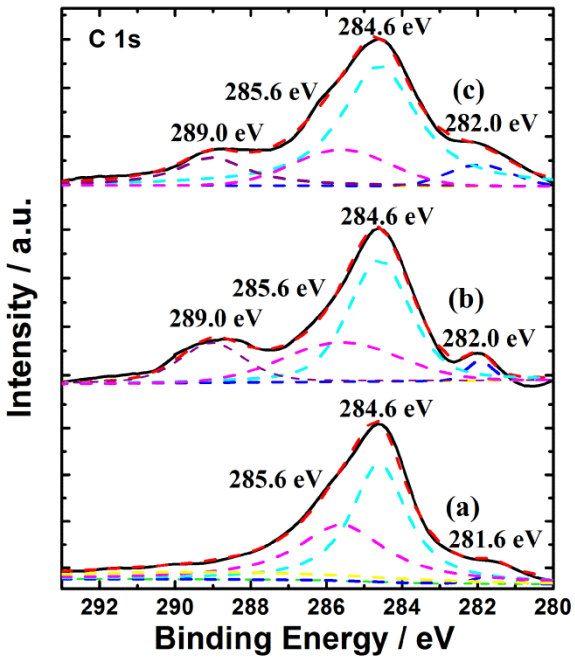

Figure 2-20. XPS spectra of C1s for (a) TiO_2, (b) C-TiO_2 and (c) 2% Nd-C-TiO_2.

In addition, a weak peak at 281.6 eV in the TiO_2 shifted to the higher energy of 282.0 eV with a much larger peak area in the C-TiO_2 and C-Nd-TiO_2 samples. As reported,[23] the binding energy of C-Ti bond in pure TiC lattice is 281.8 eV. If the carbon is doped into TiO_2 lattice forming C-Ti bond, the binding energy of C-Ti bond in TiO_2 should shift to the higher energy since the electronegativity of C is smaller than that of O. So the 282.0 eV of the peak in the C-TiO_2 and 2% Nd-C-TiO_2 should be due to the C doping in TiO_2 lattice by replacing O site.[6,28] While the weak peak at 281.6 eV in TiO_2 was probably attributed to the effect of the Ar^+ sputtering in the XPS test. Furthermore, compared to TiO_2, a new strong peak at 289.0 eV appeared in both C-TiO_2 and C-Nd-TiO_2, which was ascribed to the carbonate species.[22,31] However, the carbonate species were not chromophores in nature.[68] Thus, the strong visible absorption of C-TiO_2 and 2% Nd-C-TiO_2 should be due to the C doping in O site and forming C-Ti bond (282.0 eV) instead of carbonate species. It is well known that some impurity C energy levels will be introducd above the valence band of TiO_2 when C is doped in O site of TiO_2, and then the electrons can be excited from impurity C energy levels instead of the valence band of TiO_2 to the conduction band of TiO_2, which eventually leads to the strong visible light absorption of TiO_2.[40,42] The doped C concentration in C-TiO_2 and 2% Nd-C-TiO_2 were about 0.18 at.% and 0.28 at.%, respectively. It seemed that the doped C content increased after Nd co-doping, and the visible absorption of co-doped sample would be improved, which is good agreement with the DRS results in Fig. 2-18.

2.1.3.3.2 Photocatalytic activities

The photocatalytic activities of the prepared samples were investigated by NO_x destruction and MO degradation in comparison with commercial titania (P25). Fig. 2-21 illustrates the deNO_x ability of the specimens irradiated by different wavelengths of light (>510 nm, >400 nm and >290 nm). It can be obviously seen that pure TiO_2 (a) presented 5.2%, 28%, 40% of NO_x destruction under the irradiation of >510 nm light, >400 nm light and >290 nm light, respectively. The high deNO_x activity of pure

TiO_2 under the irradiation of >400 nm light probably be due to the contamination of C related substances in TiO_2 during solvothermal reaction since the reflectance spectrum of pure TiO_2 in Fig. 2-18 presented an absorption tail until to about 415 nm and the similar result has also been observed in section 2.1. After C doping in TiO_2 (C-TiO_2) (b), the $deNO_x$ ability was increased a little by the light of the wavelength >400 nm and significantly enhanced to 21% as the light of the wavelength longer than 510 nm was employed. When Nd was doped alone into TiO_2 (c) (C-TiO_2), the visible induced $deNO_x$ activity under > 510 nm light irradiation was also much higher (17.8%) than that of pure TiO_2. More importantly, the C and Nd co-doped samples (Nd-C-TiO_2) presented the excellent $deNO_x$ activity much superior to those of TiO_2, C-TiO_2, Nd-TiO_2 and P25 under the irradiation of not only UV light (>290 nm) but also visible light (>400 nm, >510 nm). When 2% of Nd was co-doped into C-TiO_2 (e), the best $deNO_x$ ability was represented. Further increasing Nd concentration led to the decrement of the $deNO_x$ activity, probably due to the formation of some recombination centers under the high Nd contents.

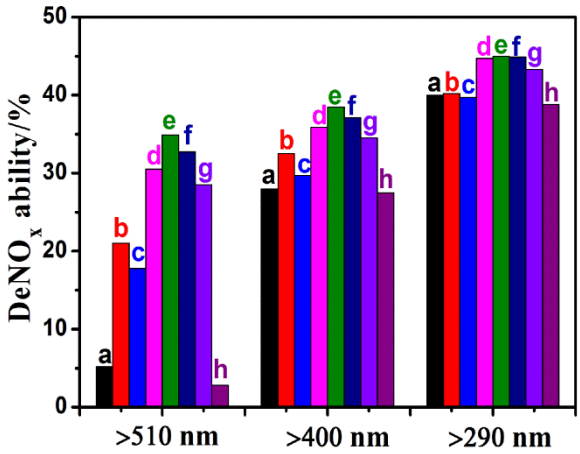

Figure 2-21. $DeNO_x$ ability of (a) TiO_2, (b) C-TiO_2, (c) 2% Nd-TiO_2, (d)1% Nd-C-TiO_2, (e) 2% Nd-C-TiO_2, (f) 3% Nd-C-TiO_2, (g) 4% Nd-C-TiO_2 and (h) P25 TiO_2.

In addition, the MO degradation of the samples monitored by visible light (>400 nm) irradiation is also shown in Fig. 2-22. It was apparent that the degradation of MO was due to the existence of TiO_2 based photocatalysts. The P25 presented poor MO

degradation activity, which could eliminate the effect of sensitization on MO degradation under the irradiation of visible light. Besides, the Nd doping was much more efficiency than that of C doping in TiO_2 for MO degradation. When C and Nd were co-doped in TiO_2, the activity was further improved, i.e., Nd-C-TiO_2 demonstrated the highest MO degradation ability under the visible light irradiation as that of NO_x destruction.

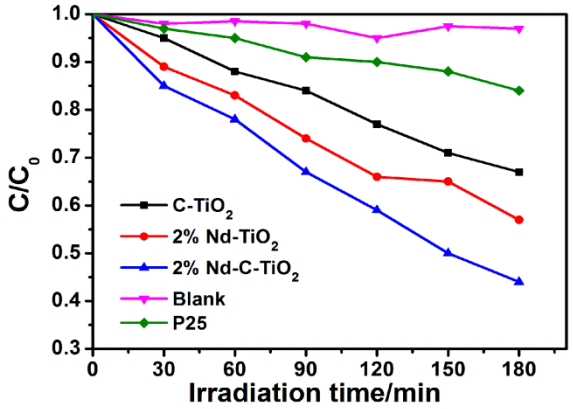

Figure 2-22. Photocatalytic MO degradation activity of the prepared samples under irradiation of visible light (λ>400 nm).

2.1.3.3.3 Mechanism for improved photocatalytic activity of C-TiO_2, Nd-TiO_2 and Nd-C-TiO_2

The photocatalytic properties of photocatalysts are known to depend on the crystallinity, specific surface area, light absorption, recombination rate of photo-generated hole-electron pairs and so on.[69] Fig. 2-23 exhibits the proposed mechanism for improved photocatalytic activity of doped TiO_2 samples. As shown in this figure, some energy levels were formed above the valence band of TiO_2 by C doping in TiO_2.[40] In this case, the visible absorption was accessible when the electron was excited from doped C energy level to the conduction band of TiO_2. Subsequently, the visible light induced photocatalytic activity of C-TiO_2 would be better than that of pure TiO_2 due to the enhancement of visible light adsorption. For Nd doped TiO_2, two

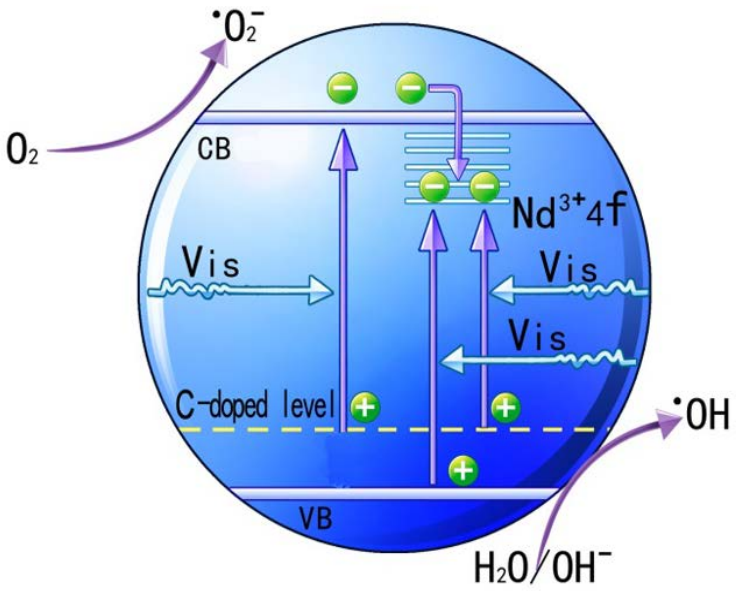

Figure 2-23. Schematic illustration of the mechanism for photocatalytic activity of doped TiO_2 samples.

reasons were probably related to the increment of the photocatalytic activity compared with that of pure TiO_2 under the irradiation of visible light. On one hand, the doping Nd would induce some unoccupied Nd^{3+} 4f energy level below the conduction band of TiO_2, and the electron could be transferred from the valence band of TiO_2 to this doped Nd energy level to achieve the visible absorption. [70] On the other hand, the decreased particle size with large specific surface area of TiO_2 after Nd doping was also a key point for high photocatalytic activity, because small nanoparticles with large specific surface area would be benefited for photocatalysis owing to the reduction of the distance for photo-induced electrons toward the surface of the photocatalyst and increase of reaction sites on the surface.[70] In case of Nd-C-TiO_2, the concrete mechanism for much improved photocatalytic activity might be probably as follows: Firstly, the visible absorption was further enhanced to cover the UV and whole visible light range in comparison with C-TiO_2 and Nd-TiO_2. With the irradiation of visible light, the electron can be transited not only from the valence band of TiO_2 to Nd^{3+} 4f energy levels or from C doped energy level to the conduction band of TiO_2, but also from C doped energy level to Nd^{3+} 4f energy levels (Fig. 2-23), resulting in much increased visible absorption. Moreover, the increment of C doping

content by Nd co-doping was another crucial key for the enhancement of visible absorption. These processes could be also deduced from DRS, XPS results (see Figs. 2-18 and 2-20) and corresponding discussion.

Secondly, the photo-generated hole-electron pairs could be effectively separated by Nd and C co-doping in TiO_2. The photoluminescence spectra of as-prepared samples are shown in Fig. 2-24. It is clearly observed that the emission intensity of Nd-C-TiO_2 by the excitation of 225 nm light was considerably weaker than those of pure TiO_2, C-TiO_2 and Nd-TiO_2. It means that much less photo-generated hole-electron pairs in Nd-C-TiO_2 were recombined to emit light, indicating that more photo-generated holes were trapped by water and adsorbed OH^- species to create hydroxyl radicals $^{\bullet}OH$ and/or more photoinduced electron reacted with absorbed O_2 on the surface to produce $^{\bullet}O_2^-$ radical anion.[47] Both of $^{\bullet}OH$ and $^{\bullet}O_2^-$ were eventually used to destruct NO_x and MO. The reduced recombination rate of photogenerated hole-electron pairs might be due to the transition of photogenerated electrons from the conduction band of TiO_2 to Nd^{3+} 4f energy levels and the increased amount of oxygen vacancies when C and Nd were co-doped into TiO_2 by replacing O site and Ti site, respectively.[41,42] Based on the above-mentioned mechanism, Nd-C-TiO_2 presented the excellent photocatalytic ability superior to pure TiO_2, C-TiO_2 and Nd-TiO_2. [58]

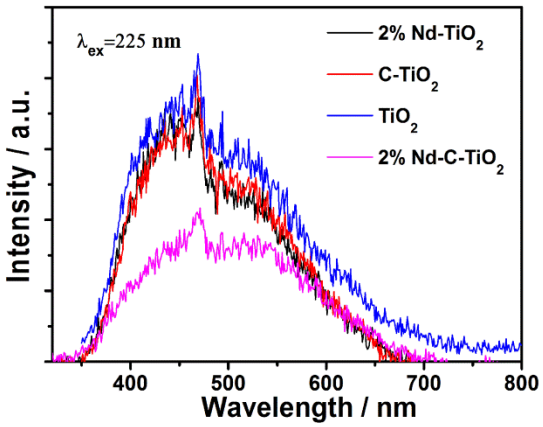

Figure 2-24. Photoluminescence spectra of as-prepared samples.

2.1.4 Preparation of visible light induced W solely doped and C and W codoped TiO_2 particles with photocatalysis and infrared light absorption

2.1.4.1 Introduction

As introduced in section 2.3, the codoping of different ions in TiO_2 results in not only getting benefits belonged to the solely doping but also synergy effect to further enhance optical properties of TiO_2. Besides, the codoping can also play an essential role in the suppression of charge carriers' recombination and improvement of physical absorption ability of products by some synergetic effects between the doped ions. [71]

In this section, high performance of W solely doped, C and W codoped TiO_2 nanoparticles have been prepared by a facile solvothermal method, expecting to considerably improve the visible light responsive photocatalytic performance. In addition, as a result of special reductive effect of ethanol during solvothermal process and unique optical performance of reduced WO_{3-x} in the near infrared light range,[72] the near infrared property of samples was also evaluated in addition to the photocatalytic activity. [73]

2.1.4.2 Experimental

2.1.4.2.1 Sample preparation

Two series of samples, W solely doped TiO_2 (W-TiO_2) and C, W codoped TiO_2 (W-C-TiO_2) with various W doping molar ratios (0.6% W-TiO_2, 1.2% W-TiO_2, 2.4% W-TiO_2, 4.8% W-TiO_2, 9.6% W-TiO_2, 0.6% W-C-TiO_2, 1.2% W-C-TiO_2, 2.4% W-C-TiO_2, 4.8% W-C-TiO_2 and 9.6% W-C-TiO_2), have been prepared by a facile solvothermal method.[26] In a typical synthesis process of W-TiO_2, 2.5 mL titanium tetra-n-butoxide and appropriate amount of WCl_6 were added into 10 mL ethanol with

fiercely stirring for 30 min. After that, 11.5 mL ethanol/water (10:1.5) mixed solution was dropped into the above solution with another 60 min continuous stirring before transferring into a 100 mL Teflon-lined stainless steel autoclave and then heat-treated at 190^{o}C for 2h. Finally, the W-TiO_2 particles were obtained by centrifuging, washing and vacuum drying at 60^{o}C overnight. As for the preparation of W-C-TiO_2 samples, the as-synthesized W-TiO_2 particles were further calcined at 265^{o}C for 1h in ambient condition to introduce the C codoping in W-TiO_2. In addition, the pure TiO_2, WO_{3-x} and C-TiO_2 were also prepared by a similar process as above described without the addition of WCl_6 and calcination, without the introduction of titanium tetra-n-butoxide and calcination, and without the incorporation of WCl_6, respectively.

On the other hand, the dependence of calcination temperature was also considered in the preparation of W-C-TiO_2 samples. Two other W-C-TiO_2 samples, which were named 2.4% W-C-TiO_2-90 and 2.4% W-C-TiO_2-150 were synthesized by calcining as-prepared 2.4% W-TiO_2 particles in 90 ^{o}C and 150 ^{o}C for 1 h, respectively.

2.1.4.2.2 Photocatalytic activity tests

The photocatalytic activities of W-TiO_2 and W-C-TiO_2 were measured by evaluating the destruction of continuous NO_x gas (deNO_x) in a flow type reactor with the irradiation of a 300 W simulated solar light (ASAHI SPECTRA HAL-302) at room temperature.

2.1.4.3 Results and discussion

Figure 2-25 shows the XRD patters of W-TiO_2, undoped TiO_2, WO_{3-x} and the enlarged plots in the degree range of 23-28^{o}. It is apparent that when W was introduced into TiO_2 with the doping concentration below 9.6%, all samples were well indexed to the anatase phase of TiO_2 (JCPDS: No. 21-1272) and no other impurity peaks were appeared in the patterns. However, as the W doping content increased to 9.6%, some characteristic peaks belonged to the WO_{3-x} were observed

probably due to the solubility limits of W doping ions in the TiO_2 lattice. In addition, it could be obviously seen in the Fig. 2-25 (b) that after incorporating W into TiO_2 particles, some minor peak shifts occurred. With the increase of W doping content up to 4.8%, the main peak shifted a little bit to the higher degree compared with that of undoped TiO_2, which may be assigned to the ionic radius difference between W^{6+}, W^{5+} (0.060 nm, 0.062 nm) and Ti^{4+} (0.068 nm) as the W was doped into TiO_2 lattice by substituting for the Ti site. However, the main peak was moved to the lower degree inversely as the W doping concentration increased to more than 4.8%. Such adverse result was probably ascribed to the partial interstitial doping of W in the TiO_2 lattice in addition to the substitution doping when the doped W content was further enhanced to some extent.

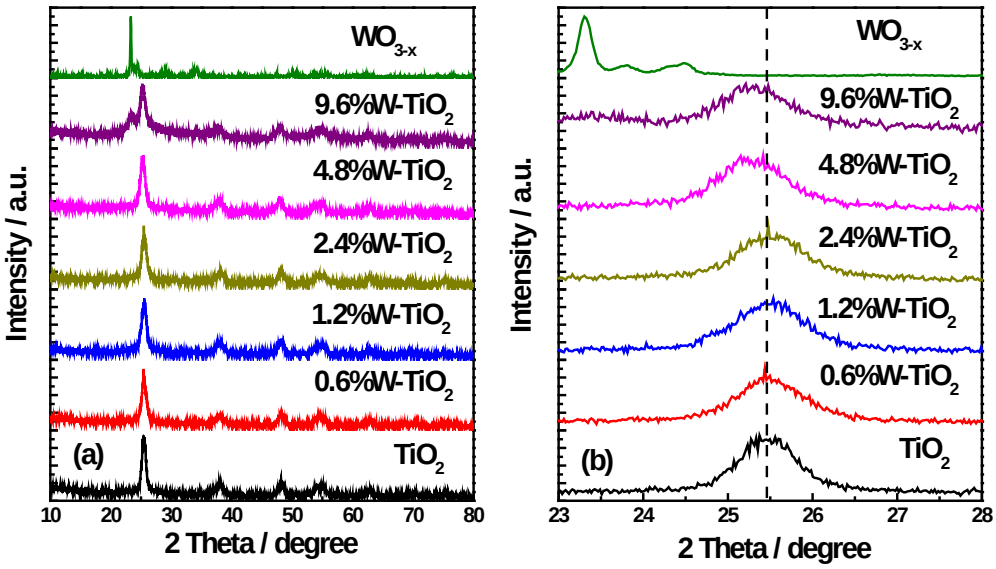

Figure 2-25. XRD patterns of series of W-TiO_2 varied with the W doping content, pure TiO_2, WO_{3-x} (a) and the corresponding magnified profiles from 23^o to 28^o (b).

The as-prepared tungsten oxide was denoted as WO_{3-x} instead of WO_3, because some amount of W^{6+} ion was reduced to W^{5+} by ethanol solvent under the solvothermal conditions according to our previous works.[72] Fig. 2-26 presents the corresponding XRD patterns for the commercial WO_3 and as-prepared WO_{3-x}. It was found that there was no big difference between the diffraction profiles of WO_3 and as-prepared WO_{3-x} except for the relative intensity. Nevertheless, in Fig. 2-26 (b), it is

clear that compared with that of commercial WO_3, the diffraction peak of WO_{3-x} shifted a little to the large degree. Since the ionic radius of W^{5+} and W^{6+} was very similar (0.060 nm, 0.062 nm), this minor shift was probably owing to the formation of oxygen vacancies in the WO_{3-x} lattice induced by the mixed valence state of tungsten.

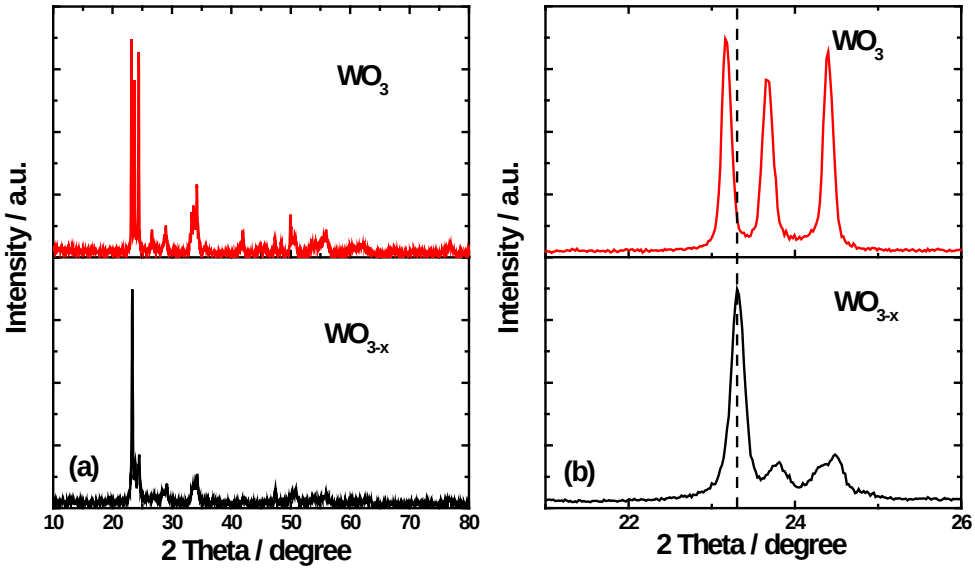

Figure 2-26. XRD patterns of commercial WO_3, WO_{3-x} prepared by the similar method as that of solely W doped TiO_2 without the addition of Ti source (a) and the corresponding magnified profiles from 21^o to 26^o (b).

Figure 2-27 shows the XRD patterns of W-C-TiO_2 series samples. The diffraction profiles of the codoped samples were similar to that of W-TiO_2, which were all well agreements with the anatase phase of TiO_2, and no impurity was introduced with the W codoped amount less than 9.6% W. However, the main peak shift shown in Fig. 2-27 (b) significantly differed from that of W-C-TiO_2. When the C was solely doped into the oxygen site of TiO_2 lattice by calcination, the main peak was changed to the lower degree due to the larger radius of C^{4-} over that of O^{2-}.[40,42] While the diffraction peak of W-C-TiO_2 obtained by calcining W-TiO_2 samples at 265 ^oC was turned back to the position as that of undoped TiO_2. It might be related to the balance of C and W codoping in the lattice of TiO_2, i.e., the diffraction peak shifted to the lower degree by of C doping, while to the higher degree by W doping. Interestingly, as the W doping

concentration increased to 4.8 % or 9.6% in the codoped samples, almost all main peaks of the samples were kept at the similar position. It might be contributed to the reason that more tungsten ions have doped into the Ti site originating from the interstitial doped tungsten ions after calcination, since sometimes the heat treatment is beneficial for the ion doping.[42] Based on the above XRD patterns analysis, it might be preliminary deduced that the C and W were codoped into the TiO_2 lattice by replacing O and Ti sites, respectively.

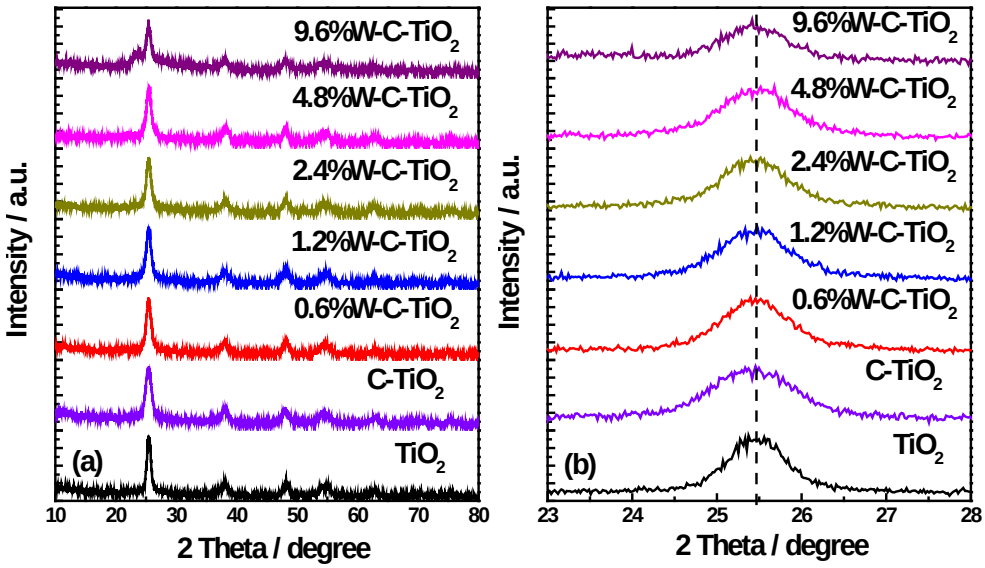

Figure 2-27. XRD patterns of W-C-TiO_2 with respect to the W doping content, pure TiO_2, C-TiO_2 (a) and the corresponding magnified profiles from 23^o to 28^o (b).

Figure 2-28 illustrates the DRS of W-TiO_2 depended on the W doping concentration along with those of undoped TiO_2, commercial bulk WO_3 and solvothermal prepared WO_{3-x}. It can be explicitly seen that the undoped TiO_2 mainly presented the UV light absorption due to the wide intrinsic band gap. When the W was incorporated into the TiO_2, the visible light absorption ability of the samples was enhanced significantly. Besides, with the increase of W doping contents, the visible light absorption of samples increased step by step, indicating that the improved visible light absorption capability was assigned to the W doping in the TiO_2. Based on the intercept of the Taucs plot of $(ahv)^n$ (n = 1/2 for an indirect band gap of TiO_2 semiconductor) versus photon energy (hv), the calculated band gap of the undoped

TiO_2 was about 3.12 eV and gradually decreased with an increase in w content as 2.9, 2.87, 2.7, 2.65 and 2.5 eV for 0.6% W-TiO_2, 1.2% W-TiO_2, 2.4% W-TiO_2, 4.8% W-TiO_2 and 9.6% W-TiO_2, respectively. The possible reason for this decreased band gap of W solely doped TiO_2 products might be related to the introduction of W impurity levels in the W-C-TiO_2, some W impurity levels would be introduced below the bottom of the conduction band of TiO_2, finally leading to the narrowed band gap and improved optical performance. More importantly, it is noteworthy that with the incorporation of W in TiO_2, the samples displayed an excellent near infrared light absorption ability compared with that of the undoped TiO_2. Particularly, 9.6% W doped TiO_2 possessed the similar near infrared light absorption property to that of WO_{3-x}, which was much superior over that of commercial bulk WO_3. It was well investigated that the excellent near infrared light absorption ability of WO_{3-x} was mainly attributed to the small polarons existed in the mixed valence state WO_{3-x} structure, and the oxygen deficiency induced by the induction of W^{5+} in the WO_{3-x}.[72] As W was incorporated into the TiO_2 lattice by substituting Ti site, the surrounding circumstance of W in the TiO_2 would be similar to that of WO_{3-x} so that the fabulous

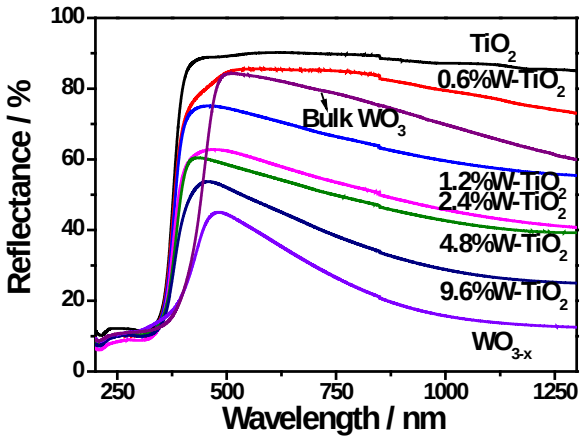

Figure 2-28. DRS of W-TiO_2 samples varied with W doping contents, pure TiO_2, WO_{3-x} and commercial WO_3 (bulk WO_3).

near infrared light absorption performance was induced. Based on the above discussion, it might be seen that the addition of W in TiO_2 was not only beneficial for the enhancement of visible light absorption ability but also contributed to the

excellent near infrared light absorption, which would have a promising application in the field of the near-infrared light shielding.

The optical properties of W-C-TiO_2 specimens are also revealed in Fig. 2-29. It is apparent that after calcination of the undoped TiO_2 particles at 265 ^oC for 1h, the visible light absorption of the sample has been greatly enhanced, which was corresponding to the C doping in the TiO_2 lattice by replacing the O site and then inducing some C related impurity levels above the valence band of TiO_2. When W-TiO_2 samples were heat treated at the same conditions, the visible light absorption was improved to even more than that of C doped TiO_2. What's more, the absorption increased along with the increment of W doping content. The possible reason for this interesting phenomenon was due to the positive effect of W on the C doping process during the calcination and the C related materials absorption ability on the surface of TiO_2 powders. However, the near infrared light absorption capability of W-C-TiO_2 samples was considerably decreased compared with that of W-TiO_2 samples before calcination, which should be owing to the oxidation of W^{5+} and the reduced amount of oxygen vacancies after heat treatment.[72] It implies that the W-TiO_2 samples would lose the near infrared light absorption performance with the increase of atmosphere temperature.

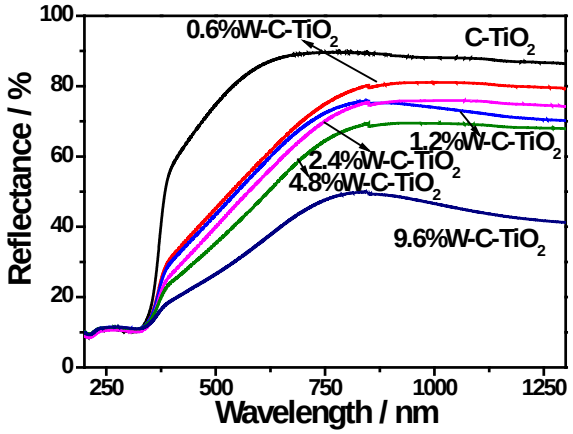

Figure 2-29. DRS of W-C-TiO_2 samples as a function of W doping content, C solely doped TiO_2.

The photocatalytic activity of samples was investigated by evaluating the destruction ability of NO gas using a flow type reactor under the irradiation of different wavelengths of lights. Fig. 2-30 shows the $deNO_x$ ability of W-TiO_2 samples. It is obviously that the photocatalytic activity gradually decreased by W doping, in spite of their much improved light absorption ability. What's more, when the doping concentration was above 4.8%, the $deNO_x$ activity reduced seriously. The decreased photocatalytic activity of W-TiO_2 might be as a result of the formation of hole and electron trapping centers, such as doped W^{5+} and $W^{6+}$and the lattice defects induced by the substitution of W with Ti site in TiO_2.[74] In addition, the appearance of impurity phase of WO_3, which is a direct band gap of semiconductor and presents relatively poor photocatalytic performance, also led to the reduced $deNO_x$ efficiency of the samples doped with W above 4.8%. On the other hand, even if 2.4% W was doped in TiO_2, it still presented similar photocatlytic activity as that of commercial P25 and also exhibited relatively good near infrared light absorption capability as shown in Fig. 2-28, implying the potential applications for the photocatalysis together with near infrared light shielding.

Fig. 2-31 shows the $deNO_x$ ability of W-C-TiO_2. W-TiO_2 revealed not only the excellent UV light induced photocatalytic activity but also excellent visible light responsive $deNO_x$ property even under the irradiation of the light with wavelength above 510 nm. Furthermore, when the W was co-incorporated into the C-TiO_2, the $deNO_x$ performance was further promoted. In addition, when the W codoping concentration was increased to about 2.4%, the sample presented the best $deNO_x$ ability of about 32%, 37% and 45% under the irradiation of lights with wavelength above 510nm, 400nm and 290 nm, respectively. The significant improvement of $deNO_x$ performance by C-W codoping was probably due to the following factors. Firstly, the visible light absorption capabilities of the samples were strongly enhanced up to 900 nm owing to the C-W codoping which could increase the valence band position and decrease the conduction band position of TiO_2 simultaneously.[75] Based on the XPS analysis, the C doping content for this optimal sample 2.4% W-C-TiO_2

was about 0.38 at. %, which was much higher than that of C-TiO_2 (0.18 at. %). It has been confirmed in our precious work that the doped C content in TiO_2 could be tuned by calcination temperature and co-doped ions, finally leading to various light-harvesting capabilities of samples. Secondly, the C and W codoping were greatly beneficial for the separation of photogenerated electron-hole pairs, which has been systematically investigated by the I. S. Cho groups.[76] Moreover, the enhanced photocatalytic property of the codoped samples was also ascribed to the change of surface acidity. It is well known that the surface of WO_3 particles displays much higher Lewis acidity than pure TiO_2. It has an advantage for absorbing not only chemical species containing unpaired electrons such as OH^- and H_2O and also pollutants with polarized functional groups.[75] When the W was doped into TiO_2 lattice, the surface acidity of samples would be greatly improved. In this case, more OH^- radicals could be produced and more photocatalytic targets adsorbed on the surface of the samples during the light irradiation, finally led to the high photocatalytic activity. Nevertheless, further increasing the W doping content to 4.8 or 9.6%, the $deNO_x$ property of the codoped samples was seriously weakened irrespective of the irradiation wavelengths, which was attributed to the appearance of impurity WO_3 phase and increase in lattice defects, which act as a recombination center of photo-nduced electrons and holes.[73]

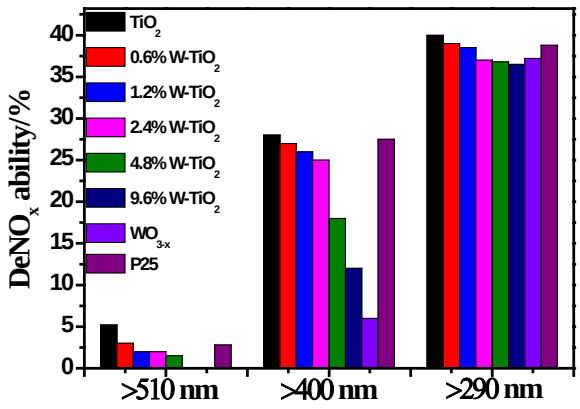

Figure 2-30. $deNO_x$ ability of W-TiO_2 powders varied with W doping content, undoped TiO_2 and as-prepared WO_{3-x} as well as commercial P25.

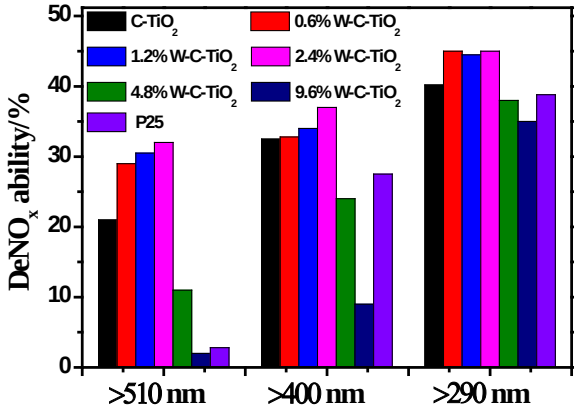

Figure 2-31. $DeNO_x$ ability of W-C-TiO_2 powders, C-TiO_2 and commercial P25.

2.2 Preparation of visible light active $NaTaO_3$ based materials

2.2.1 Preparation of visible light induced C doped $NaTaO_3$ material and C doped $NaTaO_3$/Cl doped TiO_2 composite

2.2.1.1 Introduction

It is well known that carbon as a non-metal element has become one of the most favourable dopants, since it can introduce series of localized occupied states into the band gap of substrates and sometimes also produce oxygen vacancies simultaneously, enabling to significantly improve visible light absorption and subsequent photocatalytic ability. H. W. Kang et al.[77] proposed spherical powders of visible light driven C/$NaTaO_3$ composite prepared by an one step process in a continuous spray pyrolysis reactor. In this composite, the carbon was existed as a solely material rather than the dopant in the lattice. Furthermore, extra carbon precursor and high temperature were required in the synthesis process. Nevertheless, the carbon doped $NaTaO_3$ particle with excellent visible light induced photocatalytic performance is still rare, let alone the C doped $NaTaO_3$ based composite.

Therefore, in this section, a nice visible light responsive C doped $NaTaO_3$

(C-$NaTaO_3$) particle was originally prepared by a facile solvothermal reaction using water/ethylene glycol (EG) mixed solution as the solvent without adding any other special carbon precursors. More importantly, a new C-doped $NaTaO_3$/Cl-doped TiO_2 (designated as C-$NaTaO_3$/Cl-TiO_2) composite was developed in expecting synergy effect to further optimize the visible light induced photocatalytic activity for both C-$NaTaO_3$ and Cl-TiO_2, i.e., effectively supressing the recombination rate of photogenerated hole-electron pairs. [78]

2.2.1.2 Experimental

2.2.1.2.1 Sample preparation

Preparation of C-$NaTaO_3$: A series of $NaTaO_3$ and C-$NaTaO_3$ were prepared by dispersing 6 g NaOH and 0.441 g Ta_2O_5 in 60 mL distilled water/EG (60:0, 30:30, 20:40, 10:50 and 0:60) mixed solution with magnetic stirring for 2 h. After that, the mixed solution was transferred into a 100 mL Teflon-lined stainless steel autoclave and heat-treated at 180 ^oC for 12 h. Finally, the products were separated by centrifugation, washed and dried in a vacuum at 60^oC overnight. For comparison, some samples were also synthesized by the similar solvothermal reaction but with different alcohols. The corresponding sample names and synthesis conditions of the samples are summarized in Table 2-3. In addition, one sample, which was denoted as $NaTaO_3$-EG40, was fabricated by dispersing 0.2 g of pure $NaTaO_3$ powder in 60 mL distilled water/EG (20:40) solution followed by the solvothermal reaction at 180 ^oC for 12 h.

Table 2-3. Synthesis conditions of the samples.

Sample name	Reagent		Solvent				
	Ta_2O_5 (g)	NaOH (g)	Water (mL)	EG (mL)	Ethanol (mL)	Methanol (mL)	Propanol (mL)
$NaTaO_3$-W	0.441	5.6	60	0	0	0	0
C-$NaTaO_3$-EG30	0.441	5.6	30	30	0	0	0
C-$NaTaO_3$-EG40	0.441	5.6	20	40	0	0	0
C-$NaTaO_3$-EG50	0.441	5.6	10	50	0	0	0
$NaTaO_3$-EG60	0.441	5.6	0	60	0	0	0
$NaTaO_3$-E	0.441	5.6	20	0	40	0	0
$NaTaO_3$-M	0.441	5.6	20	0	0	40	0
$NaTaO_3$-P	0.441	5.6	20	0	0	0	40

Preparation of C-$NaTaO_3$/Cl-TiO_2: A series of C-$NaTaO_3$/Cl-TiO_2 composites powders were prepared by dispersing 0.1 g of above prepared sample of C-$NaTaO_3$-EG40 in 30 mL distilled water followed by fiercely stirring for 1 h. After that, desired volumes of $TiCl_3$ (20 wt.%) solution, which were based on the calculated weight ratios of 0:1, 1:3, 1:2, 1:1 2:1 and 1:0 for C-$NaTaO_3$/Cl-TiO_2 composites, were added dropwise to the solution, and the mixed solutions were magnetically stirred for another 1h. The mixed solution was then transferred into a 100 mL Teflon-lined stainless steel autoclave and reacted at 180 ^oC for 12 h. Finally, the products were separated by centrifugation, washed and dried in a vacuum at 60^oC overnight. For comparison, the $NaTaO_3$/Cl-TiO_2 composite with the weight ratio of 1:1 was also prepared by the similar method, using the sample of $NaTaO_3$-W as a starting material rather than C-$NaTaO_3$-EG40 powder.

2.2.1.2.2 Photocatalytic activity tests

The photocatalytic activity of samples was investigated by evaluating the

decomposition of NO_x ($deNO_x$) using a flow type reactor under irradiation of a 300 W simulated solar light (ASAHI SPECTRA HAL-302) at room temperature.

2.2.1.3 Results and discussion

2.2.1.3.1 Preparation of C doped $NaTaO_3$ particles

Figure 2-32 shows the XRD patterns of samples prepared by solvothermal reactions with various EG volumes. It can be clearly seen that when the EG volumes was less than 50 mL in the reaction solvent, the diffraction peaks of $NaTaO_3$-W, C-$NaTaO_3$-EG30 and C-$NaTaO_3$-EG40 were all well indexed to the pure orthorhombic phase of $NaTaO_3$ (JCPDS file No. 25-0863), and no other impurity was observed. However, when the EG content increased to 50 mL, a few peaks belonged to Ta_2O_5 appeared in C-$NaTaO_3$-EG50, and only Ta_2O_5 phase was represented in $NaTaO_3$-EG60, which was prepared in 60 mL EG solution without distilled water. It is well acknowledged that the formation of $NaTaO_3$ can be achieved by two main steps. Firstly, the Ta_2O_5 powder, which is insoluble in the ambient condition, will be gradually dissolved and hydroxylated to form a $Ta(OH)_5$ related precursor in the NaOH solution with rising temperature and pressure. Subsequently, due to the relatively higher solubility of $Ta(OH)_5$ than that of $NaTaO_3$ in the aqueous solution, the $Ta(OH)_5$ can be dissolved slowly and then reacts with Na^+ to form $NaTaO_3$ when the concentration of Na^+ is increased enough.[79] Nevertheless, when the EG content is too high, it is difficult for Ta_2O_5 to dissolve and react with NaOH to form $NaTaO_3$. Therefore, the sample $NaTaO_3$-EG60 exhibited solely Ta_2O_5 phase rather than $NaTaO_3$ phase.

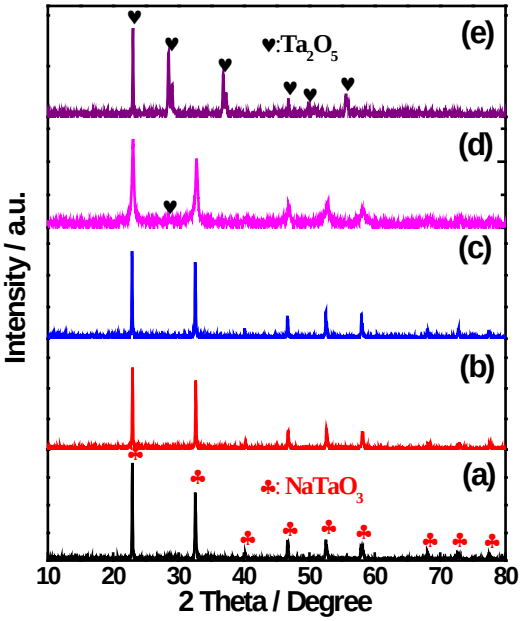

Figure 2-32. XRD patterns of $NaTaO_3$-W (a), C-$NaTaO_3$-EG30 (b), C-$NaTaO_3$-EG40 (c), C-$NaTaO_3$-EG50 (d) and $NaTaO_3$-EG60 (e) prepared with different volumes of EG solution.

The diffuse reflectance spectra of samples prepared by different volumes of EG solution are displayed in Fig. 2-33. It is apparent that $NaTaO_3$-W prepared in the absence of EG solution presented only UV absorption owing to the wide band gap of $NaTaO_3$ about 3.82 eV calculated by the intercept of the Taucs plot of $(\alpha h\upsilon)^n$ (n＝2 for indirect band gap of semiconductor) versus photon energy ($h\upsilon$). With the increase of EG volumes in the solvent, the visible absorption of $NaTaO_3$ was improved significantly due to the narrowed band gap, where the corresponding calculated band gap of C-$NaTaO_3$-EG40 has shifted from 3.82 eV to 2.03 eV. However, $NaTaO_3$-EG60 prepared in pure EG solution did not show the visible light-harvesting capability, and the band gap was moved back to the 3.85 eV, since the sample consisted of Ta_2O_5. These results indicated that the visible light absorptions of C-$NaTaO_3$-EG30, C-$NaTaO_3$-EG40 and C-$NaTaO_3$-EG50 were induced by the solvothermal reaction of Ta_2O_5 and NaOH to form the carbon-doped $NaTaO_3$ in distilled water/EG mixed solvents. It will be further explained later by the FTIR and XPS analysis results. Furthermore, $NaTaO_3$-M, $NaTaO_3$-E and $NaTaO_3$-P were also prepared by using 20/40 volume ratio of water/A (A: Methanol, Ethanol, Propanol)

mixed solutions as solvent, respectively, to investigate the effect of alcohols on the light absorption of the samples. These three samples showed no obvious visible absorption (not presented here), indicating that the primary alcohols used had no explicit influence on the visible absorption of $NaTaO_3$. Therefore, we deduced that the visible absorptions of C-$NaTaO_3$-EG30, C-$NaTaO_3$-EG40 and C-$NaTaO_3$-EG50 were due to the special structure and properties of EG. It is well known that EG might be utilized as a complex agent during solution chemical reactions. This might be one of the reasons why the formation of C-$NaTaO_3$ could be proceeded during the solvothermal treatment process.[40,41]

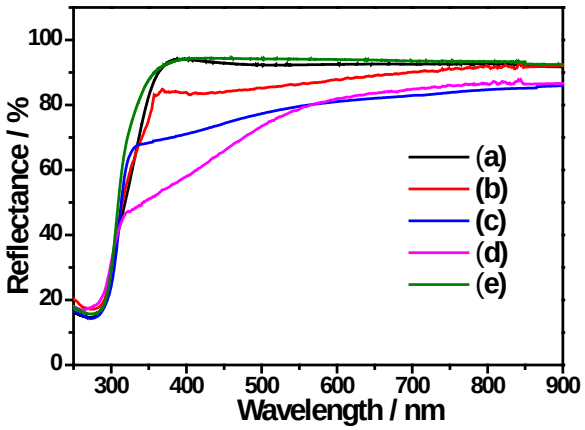

Figure 2-33. Diffuse reflectance spectra of $NaTaO_3$-W (a), C-$NaTaO_3$-EG30 (b), C-$NaTaO_3$-EG40 (c), C-$NaTaO_3$-EG50 (d) and $NaTaO_3$-EG60 (e).

Figure 2-34 illustrates the FTIR spectra of $NaTaO_3$-W and C-$NaTaO_3$-EG40. It is obvious that both samples presented a wide band peaked at ca. 3334 cm^{-1}, corresponding to the stretching vibration mode of hydroxyls and adsorbed water. In addition, compared with the spectrum of $NaTaO_3$-W, C-$NaTaO_3$-EG40 presented three new peaks located at 1467 cm^{-1}, 1354 cm^{-1} and 1081 cm^{-1}, which were assigned to the carbon related substances, indicating that some carbon related species were truly existed in C-$NaTaO_3$-EG40.

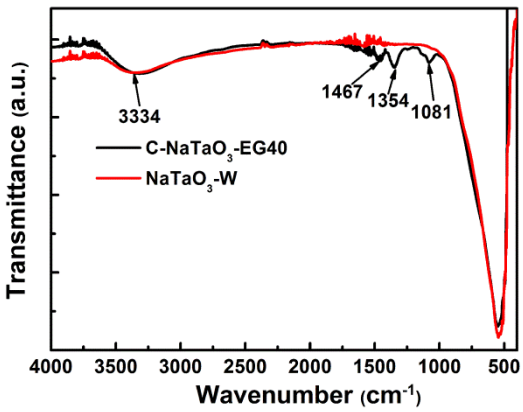

Figure 2-34. FTIR spectra of of $NaTaO_3$-W and C-$NaTaO_3$-EG40.

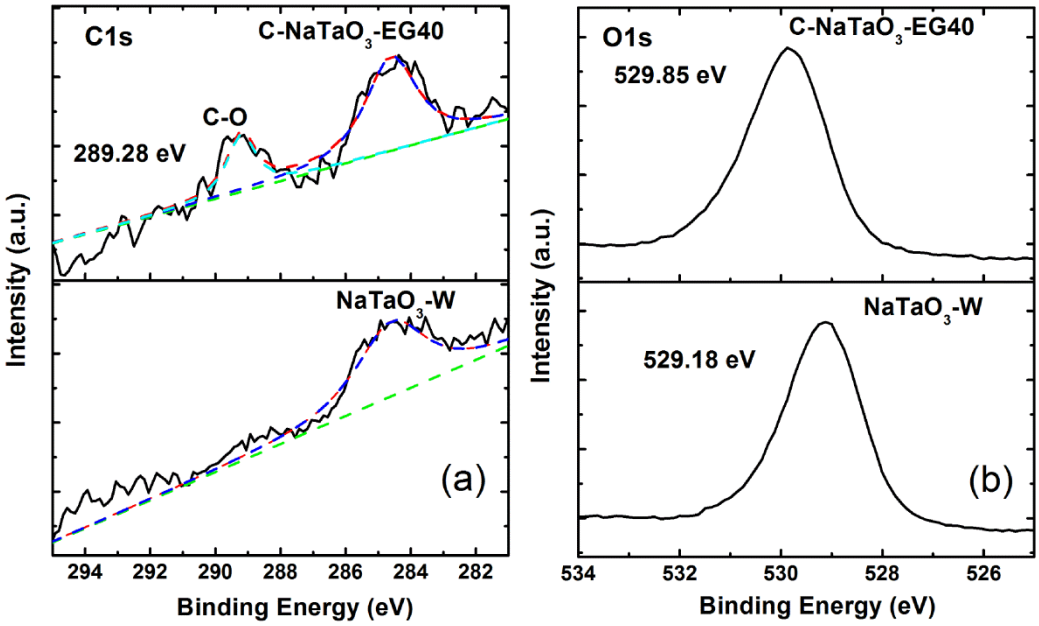

Figure 2-35. The XPS spectra of C1s (a) and O1s (b) for $NaTaO_3$-W and C-$NaTaO_3$-EG40.

For the sake of clarifying detailed status of carbon in $NaTaO_3$, the XPS test was employed with the assistance of Ar^+ sputtering (shown in Fig. 2-35). It is explicit that C-$NaTaO_3$-EG40 exhibited a new peak at 289.28 eV in addition to the adventitious carbon peak at 284.60 eV. The peak at 289.28 eV was ascribed to the C-O bond related species, indicating that carbon was incorporated in the $NaTaO_3$ crystal to form C-O-Ta bond or C-O-Na bond.[80] It can be further confirmed by XPS analysis of O1s in Fig. 2-35 (b), i.e., the main peak of C-$NaTaO_3$-EG40 was shifted to 529.85 eV from 529.18 eV of $NaTaO_3$, which is corresponding to the binding energy of bulk

oxygen (O^{2-}).[80] This shift could be explained by the formation of C-O-Ta bond or C-O-Na bond. Because when the C-O-Ta bond or C-O-Na bond was formed in $NaTaO_3$ instead of Ta-O-Ta bond or Na-O-Na bond, the electron density around oxygen would decrease since the electronegativity of C is higher than those of Ta and Na. Subsequently, the binding energy of O1s of C-$NaTaO_3$-EG40 could move to higher energy level after the carbon doping.[80] The calculated carbon doping content from XPS in C-$NaTaO_3$-EG40 was about 0.43 at.%. Therefore, based on the above analysis, it can be deduced that the carbon was existed in the $NaTaO_3$ crystal by an interstitial doping in C-$NaTaO_3$-EG30, C-$NaTaO_3$-EG40 and C-$NaTaO_3$-EG50. Furthermore, the enhanced visible absorption of these three samples in Fig. 2-33 should be due to the mentioned carbon doping in the $NaTaO_3$.

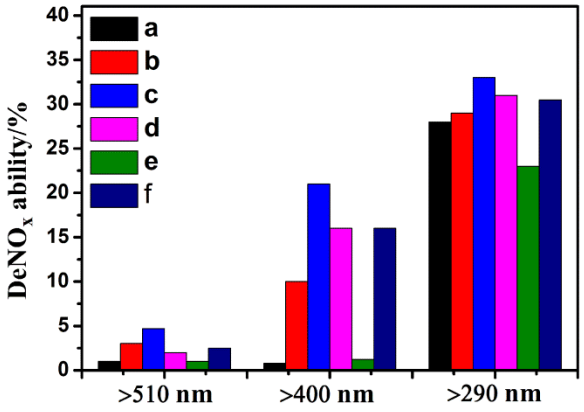

Figure 2-36. $DeNO_x$ ability of $NaTaO_3$-W (a), C-$NaTaO_3$-EG30 (b), C-$NaTaO_3$-EG40 (c), C-$NaTaO_3$-EG50 (d), $NaTaO_3$-EG60 (e) and P25 (f).

Figure 2-36 presents the continuous NO_x gas destruction ability of $NaTaO_3$-W, C-$NaTaO_3$-EG30, C-$NaTaO_3$-EG40, C-$NaTaO_3$-EG50 and $NaTaO_3$-EG60 prepared by solvothermal method with various volumes of EG solution, together with that of P25. It could be obviously observed that $NaTaO_3$-W only showed an UV light induced $DeNO_x$ ability due to its poor visible absorption ability (see Fig. 2-33). With the increase of EG solution in the solvothermal reaction, the visible light driven $deNO_x$ performance of samples increased, and C-$NaTaO_3$-EG40 displayed the best visible and UV light responsive photocatalytic activities superior to P25. These result

might be related to the strong visible light absorption induced by C-doping in $NaTaO_3$, since the specific surface areas of $NaTaO_3$-W (10.0 m^2g^{-1}) and C-$NaTaO_3$-EG40 (12.5 m^2g^{-1}) were similar. However, with further increasing the EG volume to 50 mL, although C-$NaTaO_3$-EG50 showed the highest visible light absorption (in Fig. 2-33), it presented relatively poorer visible and UV light induced deNO_x ability compared with C-$NaTaO_3$-EG40, which was probably ascribed to the existence of impurity phase of Ta_2O_5 in C-$NaTaO_3$ and lower crystallinity (see Fig. 2-32). In addition, $NaTaO_3$-EG60 prepared in a pure EG solution showed the poorest photocatalytic activity owing to the limited visible light absorption and the crystalline phase of Ta_2O_5 instead of $NaTaO_3$ phase.

Based on the above analysis, it could be concluded that the visible light induced C-$NaTaO_3$ sample were successfully prepared by a facile solvothermal method in EG aqueous solution, and when 20/40 volume ratio of water and EG mixed solution was employed as a solvent, the C-$NaTaO_3$ sample presented the best visible and UV light induced deNO_x ability. In order to improve the visible light induced photocatalytic activity of C-$NaTaO_3$ sample, a C-$NaTaO_3$/Cl-TiO_2 composite was prepared using C-$NaTaO_3$-EG40 as the C-$NaTaO_3$ source.

2.2.1.3.2 Preparation of C doped $NaTaO_3$/Cl doped TiO_2 composite

Figure 2-37 shows the XRD patterns of C-$NaTaO_3$/Cl-TiO_2 composites with various weight ratios (1:0, 2:1, 1:1, 1:2, 1:3 and 0:1). It is explicit that the pure Cl-TiO_2 powders presented the mixed phases consisted of brookite and rutile. With increasing the amounts of Cl-TiO_2 in the C-$NaTaO_3$/Cl-TiO_2 composite, the peak intensities belonged to the TiO_2 phases were gradually increased, and those of C-$NaTaO_3$ decreased, while the C-$NaTaO_3$ still exhibited the same orthorhombic phase, indicating that series of the C-$NaTaO_3$/Cl-TiO_2 composites had been successfully prepared via a facile solvothermal process. The doping status of Cl in TiO_2 will be explained in the following according to the XPS analysis result.

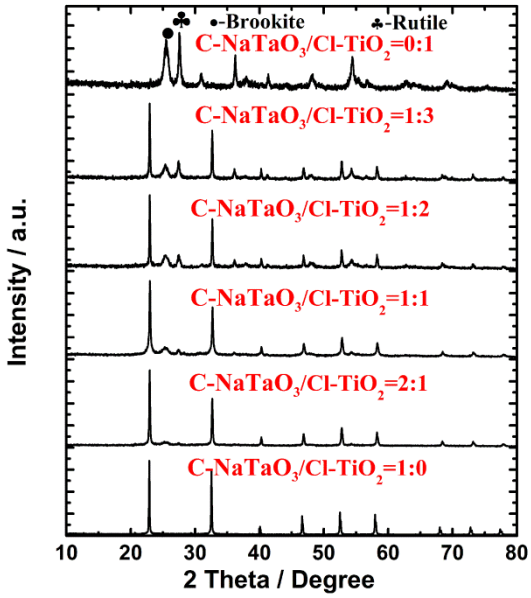

Figure 2-37. XRD patterns of C-$NaTaO_3$/Cl-TiO_2 composites with various weight ratios of C-$NaTaO_3$ and Cl-TiO_2.

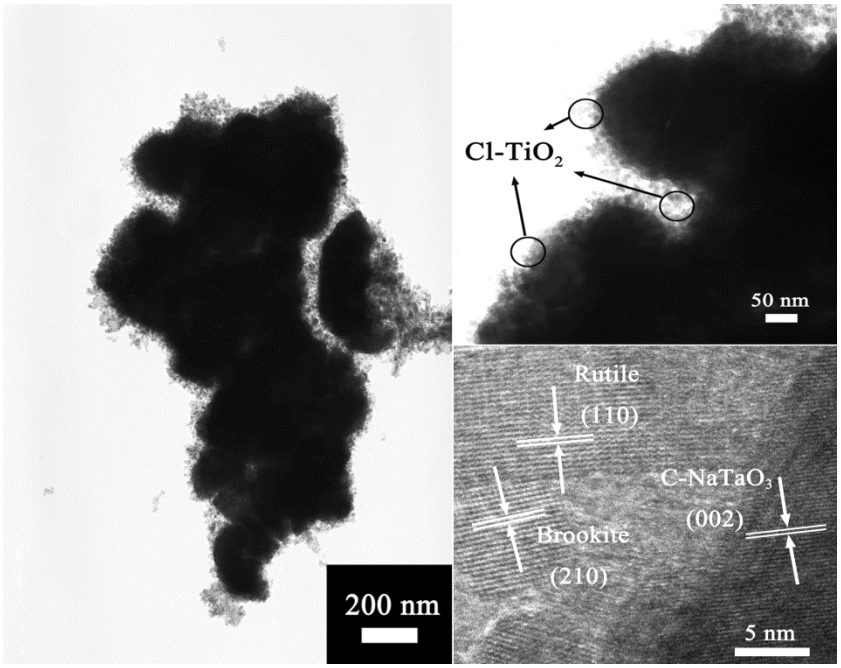

Figure 2-38. TEM and HRTEM images of the sample of C-$NaTaO_3$/Cl-TiO_2 with the weight ratio of 1:1.

The TEM and HRTEM images of C-$NaTaO_3$/Cl-TiO_2 (1:1) composite are shown in Fig. 2-38. It is clear that the small particles of Cl-TiO_2 well covered the surface of the large particles of C-$NaTaO_3$ to form a so-called core-shell structure, where Cl-TiO_2 was consisted of rutile and brookite phases and C-$NaTaO_3$ consisted of an

orthorhombic phase. The specific surface area of C-$NaTaO_3$/Cl-TiO_2 (1:1) composite was determined as 43.5 m^2g^{-1}. Fig. 2-39 presents the XPS spectrum of Cl 2p for Cl-TiO_2 and (1:1) C-$NaTaO_3$/Cl-TiO_2. It was obvious that two peaks appeared on Cl-TiO_2. The peak located at 198.3 eV was assigned to physically adsorbed Cl^- ions on the surface of TiO_2, and the peak situated at 199.8 eV might be attributed to the doped Cl in TiO_2 crystal by replacing O site.[81] After combining with C-$NaTaO_3$, no obvious peak shift could be observed (see Fig. 3-8). The contents of the doped Cl in TiO_2 were determined for Cl-TiO_2 and (1:1) C-$NaTaO_3$/Cl-TiO_2 as about 0.45 and 0.49 at.%, respectively. Therefore, it could be learned that the Cl was actually doped in TiO_2, and no serious change was happened after coupling with C-$NaTaO_3$ particles.

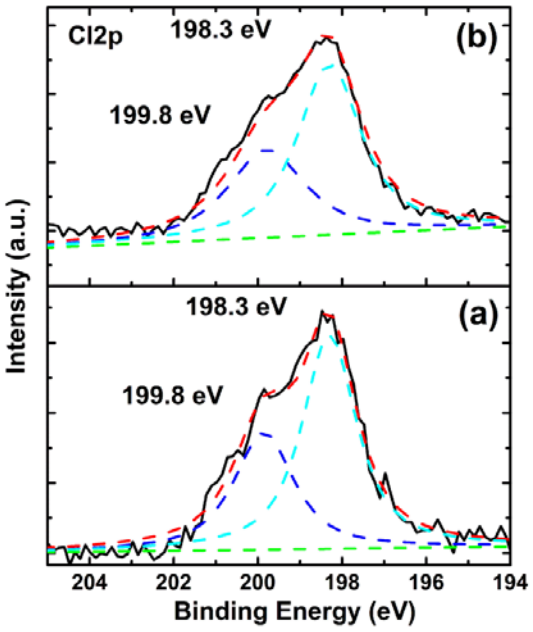

Figure 2-39. XPS profiles of Cl 2p for Cl-TiO_2 (a) and (1:1) C-$NaTaO_3$/Cl-TiO_2 (b).

The DRS of C-$NaTaO_3$, Cl-TiO_2 and C-$NaTaO_3$/Cl-TiO_2 composites are illustrated in Fig. 2-40. It is obvious that Cl-TiO_2 exhibited a little visible light absorption in the range of 400-550 nm, due to the Cl doping in TiO_2 lattice, which introduces some Cl impurity energy levels into the position below the conduction band of TiO_2.[82] When Cl-TiO_2 was coupled with C-$NaTaO_3$, the visible light absorption was increased due to the relatively higher visible light absorption of C-$NaTaO_3$.

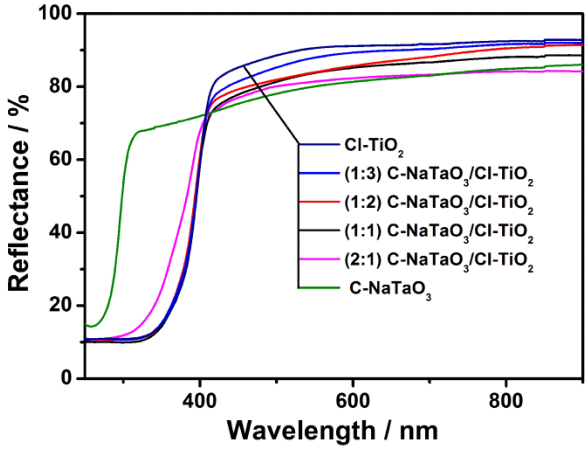

Figure 2-40. Diffuse reflectance spectra of of $C\text{-}NaTaO_3$, $Cl\text{-}TiO_2$ and $C\text{-}NaTaO_3/Cl\text{-}TiO_2$ composites with different weight ratios.

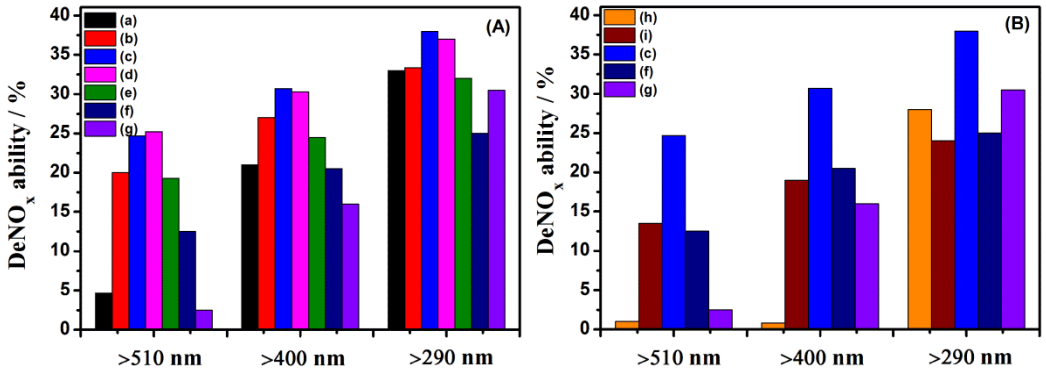

Figure 2-41. $DeNO_x$ ability of $C\text{-}NaTaO_3$ (a), (2:1) $C\text{-}NaTaO_3/Cl\text{-}TiO_2$ (b), (1:1) $C\text{-}NaTaO_3/Cl\text{-}TiO_2$ (c), (1:2) $C\text{-}NaTaO_3/Cl\text{-}TiO_2$ (d), (1:3) $C\text{-}NaTaO_3/Cl\text{-}TiO_2$ (e), $Cl\text{-}TiO_2$ (f), P25 (g), $NaTaO_3$ (h) and (1:1) $NaTaO_3/Cl\text{-}TiO_2$ (i) irradiated by different wavelengths of light.

The photocatalytic activities of prepared samples are exhibited in Fig. 2-41 by investigating the continuous NO_x gas destruction ability under the irradiation of different wavelength of light. From Fig. 2-41-(A), it could be obviously seen that about 12.5% and 20.5% of NO_x gas were degraded by $Cl\text{-}TiO_2$ when excited by the light of >510 nm and >400 nm, respectively. These are much better than the performance of P25. This increased visible light induced photocatalytic activity should be attributed to the Cl doping, which induced some visible light absorption for TiO_2. Furthermore, when the $Cl\text{-}TiO_2$ was combined with $C\text{-}NaTaO_3$, both the UV

and visible lights responsive $deNO_x$ abilities were significantly improved compared with those of Cl-TiO_2 and C-$NaTaO_3$. In addition, the C-$NaTaO_3$/Cl-TiO_2 composite exhibited the highest UV, and visible lights induced NO_x gas destruction performance as the weight ratio of C-$NaTaO_3$ and Cl-TiO_2 was tuned to 1:1. In order to investigate the advantage of C-$NaTaO_3$/Cl-TiO_2 composite for NO_x gas destruction further, the $deNO_x$ performances of some selected samples are also plotted in Fig. 2-41 (B). When $NaTaO_3$ was used, the UV and visible lights driven photocatalytic activity of (1:1) $NaTaO_3$/Cl-TiO_2 was similar to that of Cl-TiO_2 but much poorer than that of (1:1) C-$NaTaO_3$/Cl-TiO_2. Therefore, it could be learned that C-$NaTaO_3$ should be indispensable in composite for high UV and visible lights induced $deNO_x$ ability rather than $NaTaO_3$. More importantly, in this work, the visible light excited $deNO_x$ activity of C-$NaTaO_3$ and Cl-TiO_2 could be effectively improved by forming a core-shell structure.

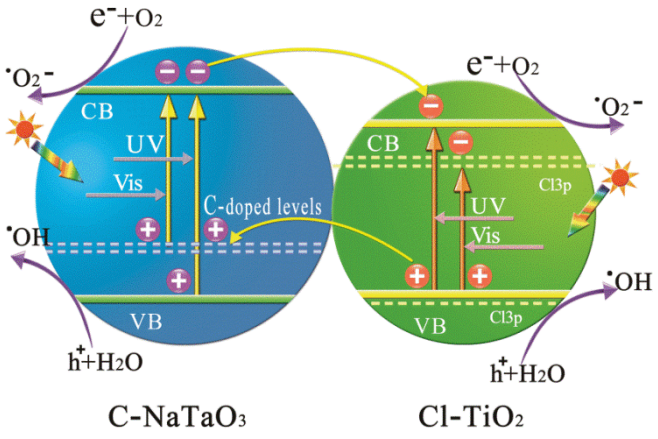

Figure 2-42. Schematic illustration of the photocatalytic process on C-$NaTaO_3$/Cl-TiO_2 composite.

It is well known that the band gaps of $NaTaO_3$, brookite and rutile phases of TiO_2 are estimated about 3.8-4.0, 3.1-3.4 and 3.0 eV, respectively.[83] In this work, the deduced band gaps of $NaTaO_3$ and mixed phases of TiO_2 were about 3.82 and 3.18 eV based on the result of DRS, which were relatively good coincident with those of the values reported in other papers.[83,84] In addition, the conduction and valence band positions of semiconductor at the point zero charge can be appropriately calculated

according to the following two equations:[85]

$$E_{CB} = \chi - E^e - 0.5E_g \qquad (2\text{-}7)$$

$$E_{VB} = E_{CB} - E_g \qquad (2\text{-}8)$$

Where E_{CB} and E_{VB} are corresponding to the conduction and valence band positions of semiconductor, respectively; χ is the absolute electronegativity of the semiconductor, obtained by the geometric mean of the absolute electronegativity of the atoms in semiconductor; E^e is owing to the energy of free electrons on the hydrogen scale (4.5 eV); and E_g is the band gap of the semiconductor. The calculated χ values for $NaTaO_3$ and TiO_2 were about 5.49 and 5.83 eV, respectively. In this case, the conduction and valence band positions of $NaTaO_3$ were approximately determined to be -1 and 2.97 eV,[86] and -0.26 and 2.92 eV for TiO_2. On the other hand, when C was doped into the $NaTaO_3$, some impurity energy levels would be formed above the valence band of $NaTaO_3$ to induce visible light absorption. As for Cl-TiO_2, the corresponding reports about the position of Cl impurity energy levels in TiO_2 were few. J. B. Lu et al.[82] calculated by DOS that the Cl 3p states would be mixed with the O 2*p* states in the valence band to the lower valence band a little and also would introduce some Cl 3p states below the conduction band of TiO_2, which was similar to the doping condition of F but different from that of N doping in TiO_2. Based on the above description, the possible concrete mechanism for improved visible light induced deNO_x ability of C-$NaTaO_3$/Cl-TiO_2 composites is considered as shown in Fig. 2-42. When visible light was irradiated to the C-$NaTaO_3$/Cl-TiO_2 composite, the electron might be excited from the C impurity energy levels into the conduction band of C-$NaTaO_3$, and from the valence band of Cl-TiO_2 to the conduction band of Cl-TiO_2. Furthermore, the photogenerated hole in the valence band of Cl-TiO_2 would be transferred to the C impurity energy levels of C-$NaTaO_3$ as well as the transfer of photogenerated electron from the conduction band of C-$NaTaO_3$ to the conduction band of Cl-TiO_2 due to the potential difference. In this regards, the photogenerated electron and hole in Cl-TiO_2 could be effectively separated by forming a composite

with C-$NaTaO_3$, leading to an outstanding visible light induced photocatalytic activity. The similar phenomena were also observed in other works.[87,88] Because $NaTaO_3$/Cl-TiO_2 just presented the same degree of visible light induced deNO_x ability as Cl-TiO_2, and much poorer performance than C-$NaTaO_3$/Cl-TiO_2, it was suspected that the effective electron or hole transfer did not happen between $NaTaO_3$ and Cl-TiO_2, and the C impurity energy levels were indispensable for high visible light driven photocatalytic performance of C-$NaTaO_3$/Cl-TiO_2 composite. With respect to excellent UV light responsive deNO_x activity, the explanation was analogous to that of visible light induced one. [78]

2.2.2 Preparation of nanosized visible light responsive C modified $NaTaO_3$ mesocrystal

2.2.2.1 Introduction

Mesocrystal, that is defined as a colloidal crystal in which all elemental units grow oriented in the same crystallographic direction to form an ordered superstructure, has drawn increasing attention from researchers and is warmly expected to be used as catalysts, electrodes, optoelectronics, sensors, biomedical materials, lightweight structural materials, etc. due to its unique properties with nanoparticulate, mesoporous and single crystal-like structure.[89,90] In particular, mesocrystal is a promising strategy to produce large specific surface area and much more active sites for photocatalysis. As for $NaTaO_3$, few relevant researches about mesocrystals were reported, let alone well-dispersed mesoporous particles with excellent visible light absorption property.

In this section, nanosized carbon modified $NaTaO_3$ mesocrystals with high efficiency of visible light driven NO gas destruction activity (deNO_x) was prepared by a facile one-pot solvothermal method using $TaCl_5$ and NaOH as starting materials, ethylene glycol (EG) and distilled water mixed solution as a solvent in the presence of glucose. The non-classic oriented aggregation mechanism via a self-assembly was

proposed for the formation of mesocrystal in this work. [91]

2.2.2.2 Experimental

2.2.2.2.1 Sample preparation

A series of carbon modified $NaTaO_3$ mesocrystals were prepared by a simple solvothermal method. In a typical procedure, 2 g glucose were ultrasonically dispersed in 60 mL distilled water/EG (30:30) mixed solution for 15 min. After that, 0.1 g $TaCl_5$ was added into the mixed solution with magnetic stirring for 30 min, followed by the addition of 2.4 g NaOH. After another 60 min magnetic stirring, the mixed solution was transferred into a 100 mL Teflon-lined stainless steel autoclave and heat-treated at 180 ^oC for 20 h. Eventually, the powders were centrifuged, washed and dried in a vacuum oven at 60 ^oC overnight. The samples prepared by using different amounts of glucose (0, 1, 2 and 2.5 g) were denoted as $NaTaO_3$-E-G0, $NaTaO_3$-E-G1, $NaTaO_3$-E-G2 and $NaTaO_3$-E-G2.5, respectively.

For comparison, the sample $NaTaO_3$-W-G2 was synthesized using 60 mL distilled water as a reaction solvent instead of distilled water/EG mixed solution, while other conditions were the same as $NaTaO_3$-E-G2. The sample $NaTaO_3$-W-G0 was prepared by the same procedure as $NaTaO_3$-W-G2 without the addition of glucose. The sample $NaTaO_3$-E-G2-500 was also synthesized by calcining sample $NaTaO_3$-E-G2 at 500 ^oC for 2 h.

2.2.2.2.2 Photocatalytic activity tests

The photocatalytic performance of the $NaTaO_3$ based sample was evaluated by investigating the destruction of continuous NO_x gas ($deNO_x$) using a flow type reactor with the irradiation of a 300 W simulated solar light (ASAHI SPECTRA HAL-302) at room temperature.

2.2.2.3 Results and discussion

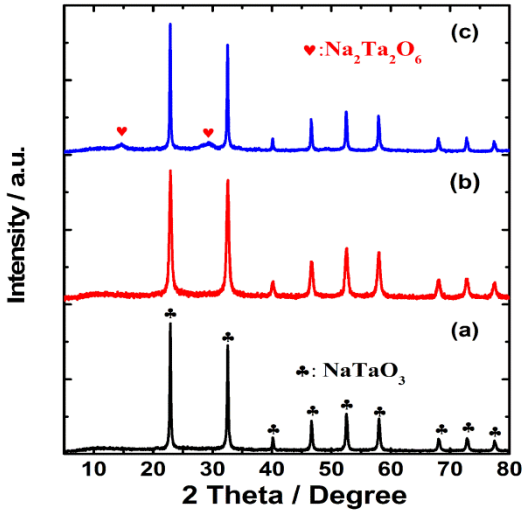

Figure 2-43. XRD patterns of samples $NaTaO_3$-E-G0 (a), $NaTaO_3$-E-G2 (b) and $NaTaO_3$-W-G2 (c) prepared under various reaction conditions.

Figure 2-43 shows the XRD patterns of the carbon modified $NaTaO_3$ specimens prepared under different conditions. It is clear that the sample $NaTaO_3$-E-G0 (Fig.2-43 (a)) synthesized by distilled water/EG mixed solution in the absence of glucose could be indexed well to the orthorhombic phase of $NaTaO_3$ (JCPDS file No. 25-0863) with high crystallinity. After the addition of glucose, the sample $NaTaO_3$-E-G2 (Fig.2-43 (b)) also presented the pure $NaTaO_3$ phase but with decreased intensity of diffraction peaks, suggesting the formation of smaller particle size of products in the presence of glucose. In addition, when the glucose was still employed but the mixed solution was replaced by distilled water, some impurity peaks belonged to $Na_2Ta_2O_6$, which is an intermediate phase in the formation of $NaTaO_3$ phase, appeared in the sample $NaTaO_3$-W-G2 (Fig.2-43 (c)), indicating the existence of EG in the reaction solution was favourable for the production of $NaTaO_3$ phase with relatively small particle size. Additionally, the amplified XRD patterns of these three samples in the range of 20-35^o were also confirmed (not presented here) that in addition to the difference between the relative intensity of peaks, there was no obvious peak shift for these three samples, indicating that the carbon was probably not doped into the as-prepared

$NaTaO_3$ crystal lattice.

The corresponding TEM images of the carbon modified $NaTaO_3$ samples fabricated under various conditions are exhibited in Fig. 2-44, and the corresponding reaction conditions, surface areas, pore sizes and volumes of samples are listed in Table 3-2. In Fig. 2-44 (a), the $NaTaO_3$-E-G0 particles synthesized by mixed solution in the absence of glucose presented agglomeration, to some extent, with non-uniform sizes. Meanwhile, some mesopores also existed in the part of particles with the pore size of 4.0 nm as well as pore volume of 0.180 $cm^3 \cdot g^{-1}$ as shown in Table 2-4. When the glucose was employed, it is apparent that the particles of sample $NaTaO_3$-E-G2 were well dispersed with relatively uniform size about 20 nm as shown in Fig. 2-44 (b). Moreover, the specific surface area of the sample $NaTaO_3$-E-G2 was significantly increased to 90.8 $m^2 g^{-1}$, which is about four times higher than that of sample $NaTaO_3$-E-G0, and also much larger than the reported values for most of $NaTaO_3$ particles.[77,86] This might be owing to the much decreased particle size with well distribution, resulting to homogeneous pore structure with pore size of 7.8 nm and much improved pore volumes (0.362 $cm^3 \cdot g^{-1}$). However, when the EG was removed from the reaction solution for the sample $NaTaO_3$-W-G2 in Fig. 2-44 (c), the particle size greatly increased to about 100 nm together with the decrement of surface area (50.2 $m^2 g^{-1}$), while some smaller pores (3.6 nm) were still remained in the inner of particles.

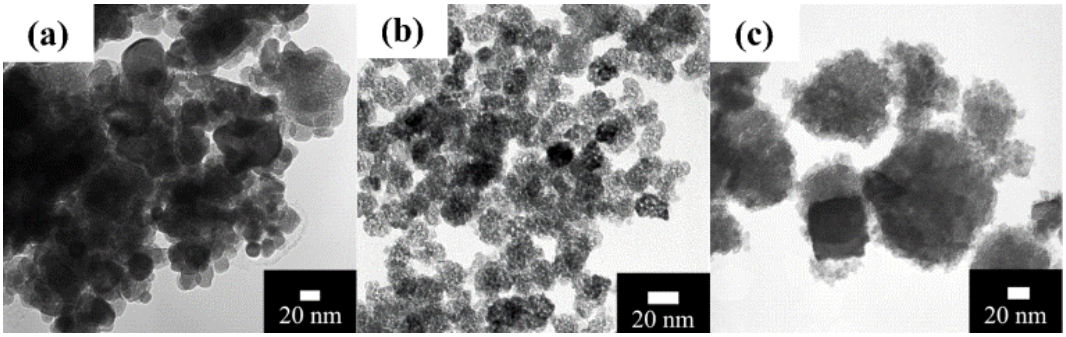

Figure 2-44. TEM images of $NaTaO_3$-E-G0 (a), $NaTaO_3$-E-G2 (b) and $NaTaO_3$-W-G2 (c).

Table 2-4. The reaction conditions and physical properties of $NaTaO_3$-E-G0, $NaTaO_3$-E-G2 and $NaTaO_3$-W-G2.

Samples	Reaction solution	Glucose (g)	Specific surface area (m^2g^{-1})	Pore size (nm)	Pore volume ($cm^3 \cdot g^{-1}$)
$NaTaO_3$-E-G0	Water/EG	0	22.7	4.0	0.180
$NaTaO_3$-E-G2	Water/EG	2	90.8	7.8	0.362
$NaTaO_3$-W-G2	Water	2	50.2	3.6	0.152

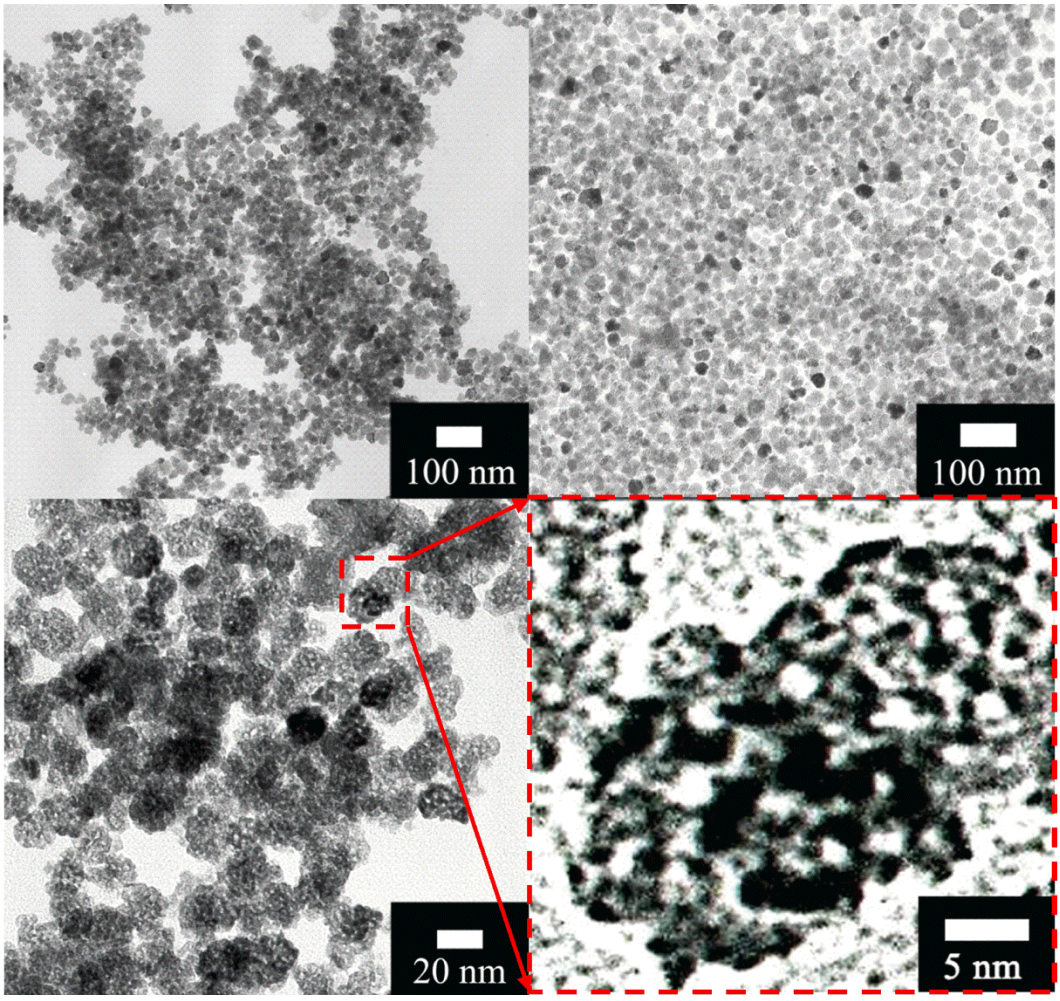

Figure 2-45. TEM images of sample $NaTaO_3$-E-G2 with different magnifications.

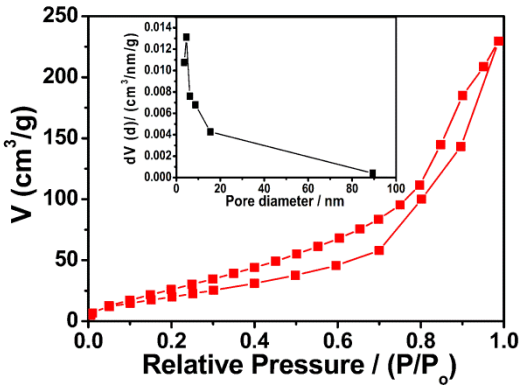

Figure 2-46. Nitrogen adsorption-desorption isotherms and the corresponding pore size distribution plots (inset) of $NaTaO_3$-E-G2.

Figure 2-45 shows the particle size and morphology of the sample $NaTaO_3$-E-G2 with different magnifications. It is explicit that the $NaTaO_3$-E-G2 particles displayed uniform distribution with soft agglomeration. More importantly, the mesopores could be clearly confirmed in all of well-dispersed particles, indicating the existence of perfect mesoporous nanostructure. Fig. 2-46 shows corresponding nitrogen adsorption-desorption isotherms and pore size distribution plots of the sample $NaTaO_3$-E-G2. The isotherm of the sample was a typical IV type with H3 hysteresis loops, implying the mesoporous structure.[92]

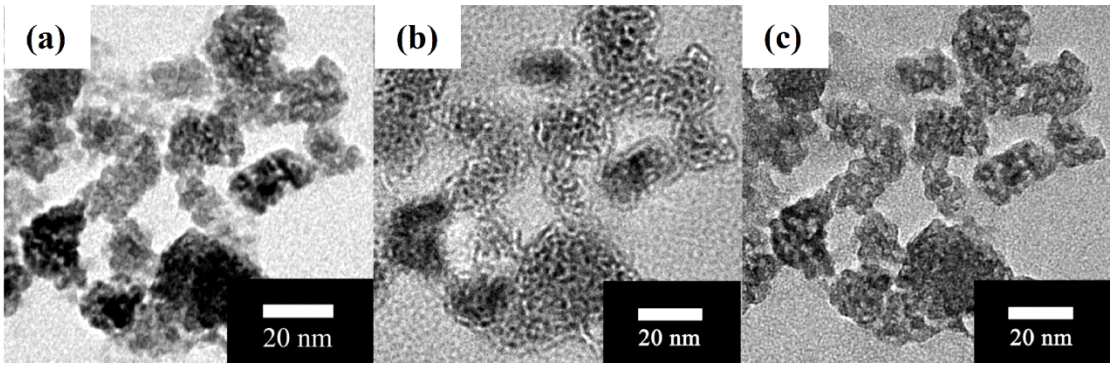

Figure 2-47. TEM images of sample $NaTaO_3$-E-G2 evaluated by different focus conditions: in-focus (a), overfocus (b) and underfocus (c).

Additionally, a focus technique in TEM measurement was employed to further investigate the mesoporous structure in the inner of sample particles. Fig. 2-47 (a), (b) and (c) show the TEM images of $NaTaO_3$-E-G2 examined under various focus

circumstances. It is well acknowledged that under the overfocus status, the black area in the inner of particles is attributed to the fringe of substance and space. While under the underfocus condition, it is contrary that the white area in the inner of particles is assigned to the fringe of substance and space, and the in-focus is the normal condition as we take a picture.[93] Therefore, it could be found that under overfocus and underfocus conditions, a lot of discrete black-and-white areas existed in the interior of the particles, respectively, confirming that huge number of continuous mesopores truly existed in the particles.

Figure 2-48 presents the HRTEM images and SAED pattern of sample $NaTaO_3$-E-G2 in different areas. It was clear that the sample particle of the diameter of ca. 20 nm exhibited well-defined crystallinity and regular lattice fringe with lattice spacing of 0.378 nm corresponded to (101) plane of orthorhombic phase $NaTaO_3$, indicating the small nanounits with oriented growth along the same direction. Furthermore, the two red square areas, covering nearly a single particle, have been analysed by the SAED. The SAED results clearly confirmed that both of these two areas exhibited the single crystal-like patterns as shown in the yellow squares of Fig. 2-48. As we all known, mesocrystal should have two features, including mesoporous structure and single crystal-like patterns. In this work, these two features have been nicely confirmed by Figs. 2-45, 2-46, 2-47 and 2-48. Therefore, it could be learned that nanosized well-dispersed mesocrystals of $NaTaO_3$ have been successfully prepared by the facile solvothermal method using distilled water/EG as the solvent in the presence of appropriate amounts of glucose.

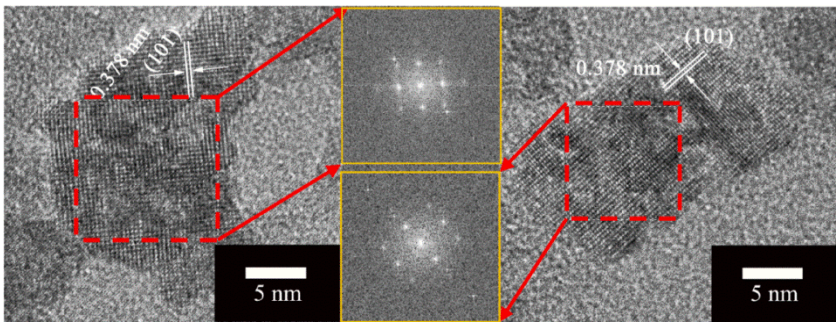

Figure 2-48. HRTEM images and SAED patterns of sample $NaTaO_3$-E-G2.

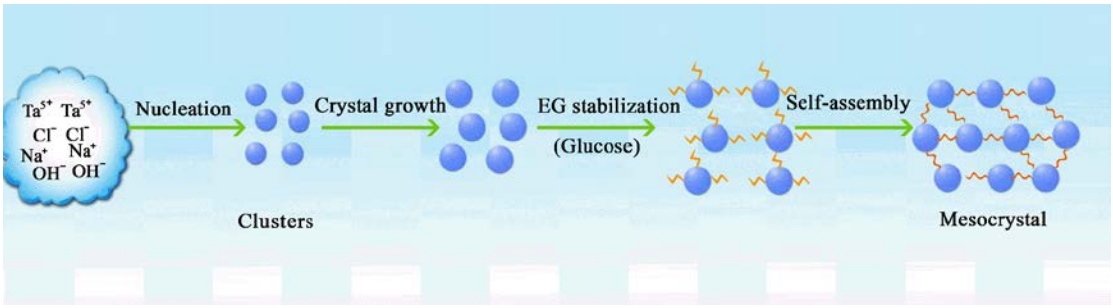

Figure 2-49. Formation mechanism of carbon modified $NaTaO_3$ mesocrystal.

Meanwhile, the corresponding possible formation mechanism of nanoscale mesocrystals for $NaTaO_3$-E-G2 was proposed as shown in Fig. 2-49. Firstly, the starting materials, $TaCl_5$ and NaOH, in distilled water/EG mixed solution started to form nucleation clusters with the increment of temperature, then gradually grew up to the critical size of crystal nucleus. In the next step, generally speaking, the further growth of primary particles is according to the rule of large particles fusing smaller particles by ion-by-ion attachment and unit cell replication, so-called Ostwald ripening process driven by the surface energy reduction.[94] While another non-classic oriented aggregation growth mechanism was also proposed by many researchers for the formation of mesocrystals in the presence of an organic stabilizer, where the larger particle is obtained by self-assembling or self-aggregating of the adjacent small nanparticles, which shared the same crystallographic orientation and were connected by organic additives or amorphous materials.[94,95] The motivation for this oriented attachment process is induced by removing numerous high energy surfaces and finally leading to the total reduction in the surface free energy. In the oriented aggregation process, the rate of particle growth via self-assembly is much higher than that of the ion-by-ion attachment, so that the self-assembly can be predominance in the further growth of nanoparticles.[94] In this work, the non-classic oriented aggregation process was employed. It is well known that the EG is commonly used as a stabilizer to synthesize some special shape of nanoparticles.[96] There are also a lot of hydroxyl radicals in the glucose, which should have the similar function as EG. Therefore, as the nucleation clusters grew to the critical size, the primary nanoparticles could be

temporarily stabilized by the EG or glucose in the reaction solution simultaneously. Finally, the stabilized nanoparticles would be self-assembled by the surface organic additives to form a mesocrystal. The formation of well-dispersed mesocrystal with a large amount of mesopores should be the co-effect of the EG and appropriate glucose content. The glucose not only played the partial role of the stabilizer but also was of great importance for small particle size and well-dispersion of mesocrystals as shown in Figs. 2-44 and 2-45. It is accepted that the mesocrystal is a metastable phase, which can be further fused to form a single crystal along with the disappearance of mesopore by the thermal energy. When the sample $NaTaO_3$-E-G2-500 was annealed at 500 ^oC, no apparent mesopores was observed in the product, $NaTaO_3$-E-G2-500 particles, indirectly confirming the formation of mesocrystal for the sample $NaTaO_3$-E-G2.

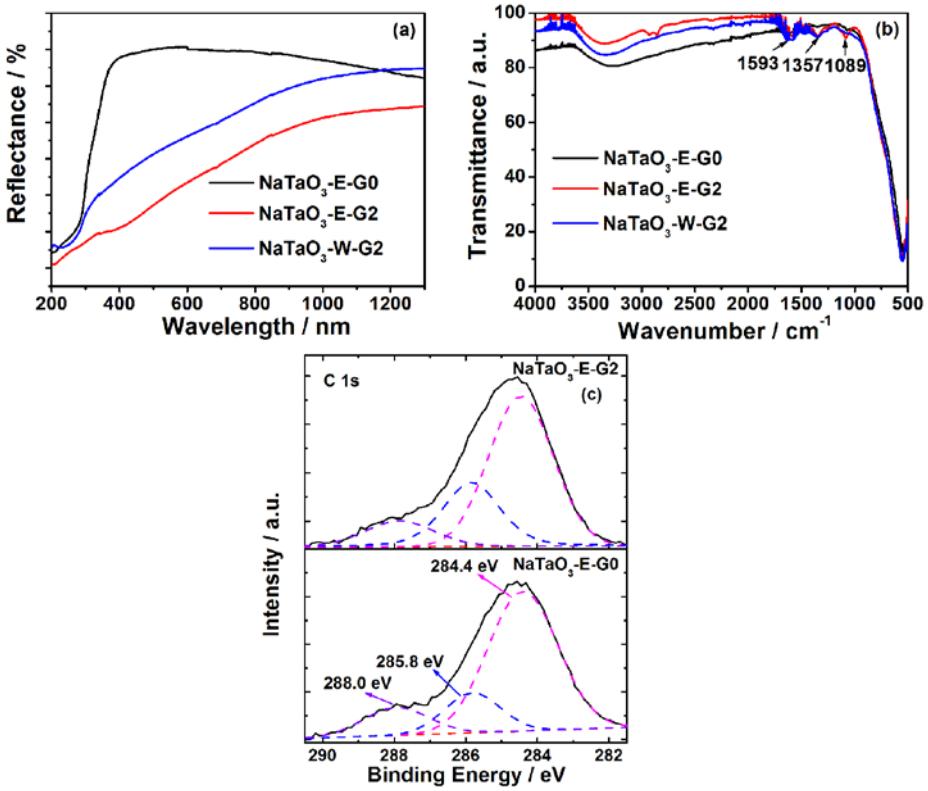

Figure 2-50. DRS (a), FTIR spectra (b) of samples $NaTaO_3$-E-G0, $NaTaO_3$-E-G2 and $NaTaO_3$-W-G2 and XPS profiles of C 1s of samples $NaTaO_3$-E-G0, $NaTaO_3$-E-G2 (c).

Figure 2-50 shows the DRS, FTIR spectra and XPS of the samples prepared under

different conditions. It was found that the sample $NaTaO_3$-E-G0 exhibited mainly UV light absorption with a little visible light absorption induced by the modification of EG on the optical property of $NaTaO_3$, while the samples, $NaTaO_3$-E-G2 and $NaTaO_3$-W-G2, synthesized by adding glucose showed the significantly improved visible absorption capability as shown in Fig. 2-50 (a), due to the carbon modification of the $NaTaO_3$ surface. It could be confirmed from FTIR spectra in Fig. 2-50 (b) that there were three new carbon-related peaks appeared on the surface of samples with the addition of glucose. The peak located at 1593 cm^{-1} was ascribed to the hydrogen-bonded carbonyl stretching.[97] The peak situated at 1357 cm^{-1} was assigned to the angular deformation of C-H,[98] while the peak formed at 1089 cm^{-1} was attributed to the C-C stretching of carbohydrates.[99] As shown in Fig. 2-50 (c), the XPS analysis revealed that both $NaTaO_3$-E-G0 and $NaTaO_3$-E-G2 displayed three same peaks at 284.4, 285.8, 288.0 eV. The 284.4 eV peak was corresponded to the adventitious carbon, and that at 288.0 eV to the C-O bond related species, which was probably induced by the modification of EG on the samples.[100] While the peak lied at 285.8 eV was as a result of carbon-related materials, which presented the similar binding energy with that of carbon in the graphite intercalation compounds, and could also get from the atmosphere or the reaction circumstance. Meanwhile, it could be seen that the relative area of 285.8 eV peak in the sample $NaTaO_3$-E-G2 was much larger than that of sample $NaTaO_3$-E-G0, indicating that the carbon-related material was also originated from glucose or EG added in the reaction solution. Furthermore, according to Qian Li et al.'s report,[101] the C 1s related peak shift should be observed to some extent when the C was doped into the sample lattice. However, in this work, no obvious C 1s peak shift was observed for both samples, and also no corresponding diffraction peak shift happened in the XRD pattern of samples, indicating that the C probably covered on the surface of sample particles as carbonaceous species instead of doping in the $NaTaO_3$ crystal lattice. In addition, the chemical bonding between Ta and C around 22.5eV could not be observed, also indicating carbon was not doped into the lattice of $NaTaO_3$. It is well known that the glucose is commonly used to

prepare spherical carbon particles by the solvothermal or hydrothermal method.[102] In our case, there was no obvious carbon formation after the solvothermal reaction with the addition of glucose. However, when the solution was heat-treated in the same condition without the addition of NaOH, a great deal of carbon appeared in the final solution, indicating that the transformation from glucose to carbon could be significantly hindered in the basic circumstance, and the detailed reasons for this phenomenon is still unclear, which would be our next work. From this, it could be induced that a trace of carbonaceous species has been produced in the sample $NaTaO_3$-E-G2 in the presence of glucose, finally leading to the high visible light absorption activity of the sample.

The TG and organic elementary analysis were conducted to check the content of C in the samples. Fig. 2-51 shows the TG curves of samples from the room temperature to 1000 ^oC. There were three steps of weight losses. The first weight loss from room temperature to ca. 250 ^oC was ascribed to the elimination of absorbed water. The second loss stage from 250 to 450 ^oC should be attributed to the decomposition of carbonaceous species on the surface of samples. For the sample $NaTaO_3$-E-G0, about 1.17% weight was lost, probably originating from the residual EG or similar organic materials on the surface of sample. Regarding sample $NaTaO_3$-E-G2 prepared in the presence of glucose, 4.15% of sample was lost in this process, indicating that corresponding carbonaceous species should be produced from EG and glucose during the solvothermal reaction. According to the C-H analysis, only 0.52 and 2.15% of C were determined in the samples $NaTaO_3$-E-G0 and $NaTaO_3$-E-G2, respectively. These contents were much lower than the results from TG, indicating that the C was existed as the carbon related compounds rather than C solely. These results can indirectly confirm that the carbon was not doped into the $NaTaO_3$ crystal lattice. The last stage from 450 to 1000 ^oC was probably assigned to the remove of surface hydroxyl.[103]

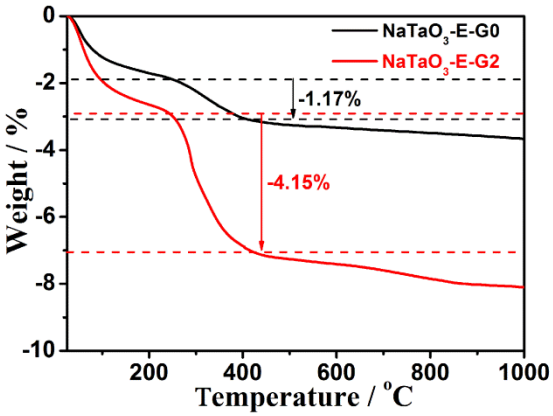

Figure 2-51. TG profiles of samples $NaTaO_3$-E-G0 and $NaTaO_3$-E-G2.

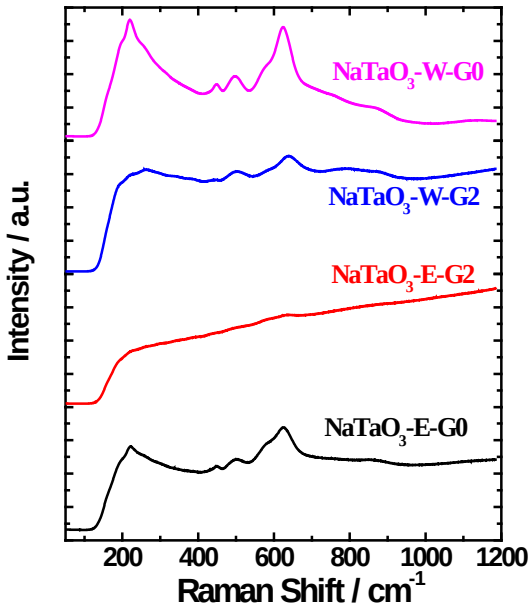

Figure 2-52. Raman spectra of samples synthesizd under different conditions.

Besides, the Raman spectra of samples $NaTaO_3$-E-G0, $NaTaO_3$-E-G2, $NaTaO_3$-W-G2 and $NaTaO_3$-W-G0 were also added in Fig. 2-52. It was worth noting that this analysis was carried out after laser irradiation for long time to eliminate some substances on the surface of samples. Because there was strong luminescence disturbance in the Raman spectra of samples $NaTaO_3$-E-G0, $NaTaO_3$-E-G2, $NaTaO_3$-W-G2, and no peaks were observed over the test range under the condition of investigation without laser irradiation. Even after the long irradiation, the peaks corresponding to $NaTaO_3$ powder were still weak. Moreover, the sample

$NaTaO_3$-E-G2 presented the weakest peaks, whereas the sample $NaTaO_3$-W-G0 exhibited the strongest peaks, which were nicely indexed to the relative C related contents in samples. Therefore, it could be deduced that the luminescence disturbance in the Raman analysis was probably owing to the existence of carbonaceous species on the surface of samples, further determining that the C was existed as a form of absorbed C related compound instead of dopant in the samples.

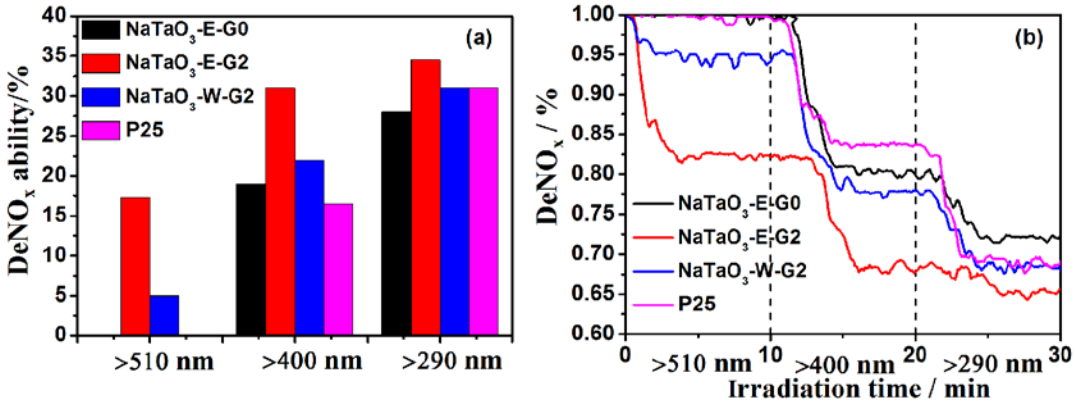

Figure 2-53. $DeNO_x$ ability (a) and time dependence of NO_x destruction activity (b) of $NaTaO_3$-E-G0, $NaTaO_3$-E-G2 and $NaTaO_3$-W-G2 as well as P25 under the irradiation of different wavelengths of lights.

Figure 2-53 (a) and (b) show the $deNO_x$ ability for the samples prepared under the different reaction conditions. $NaTaO_3$-E-G0 presented the similar $deNO_x$ activity as P25 under the irradiation of simulated solar light with different filters. The visible light responsive activity of $NaTaO_3$-E-G0 was induced by the EG modification, which has been systematically researched in the above section. The visible light driven photocatalytic performance of P25 might be owing to the impurity contaminations in the powders. While $NaTaO_3$-E-G2 prepared in the presence of glucose showed not only nice UV and short wavelength visible lights (>400 nm) induced photo-activity but also the excellent $deNO_x$ efficiency under the irradiation of long wavelength visible light above 510 nm, i.e., about 17.0% NO destruction, which was much superior to $NaTaO_3$-E-G0 and P25. The high activity of this sample should be due to the outstanding visible light absorption as shown in Fig. 2-50 (a) and extremely high

specific surface area as listed in the Table 2-4. $NaTaO_3$-W-G2 fabricated in water in the presence of glucose displayed higher performance than $NaTaO_3$-E-G0 and P25, especially under the irradiation of visible light. However, it was much less effective in comparison with that of $NaTaO_3$-E-G2, mainly owing to the much decreased specific surface area (see Table 2-4.). It is well known that the high efficiency of photocatalysis is generally determined by light absorption capability, specific surface area and the separation ability of charge carriers. In this work, $NaTaO_3$-E-G2 presented the highest deNO_x ability. Compared with $NaTaO_3$-W-G2, $NaTaO_3$-E-G2 revealed the similar UV and visible light absorption ability but with much higher specific surface area as shown in Fig. 2-50 (a) and Table 2-4.

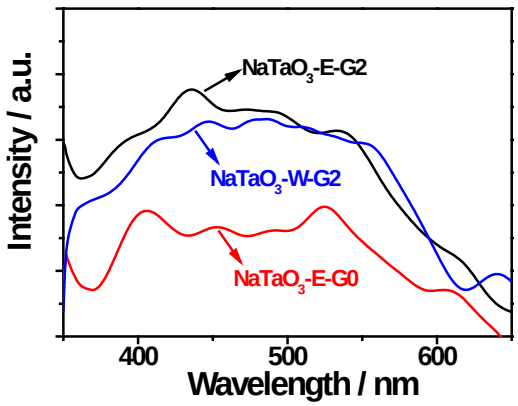

Figure 2-54. Photoluminescence spectra of samples $NaTaO_3$-E-G0, $NaTaO_3$-E-G2 and $NaTaO_3$-W-G2 with the excitation of 304 nm.

Meanwhile, the photoluminescence spectra of the samples were also represented in Fig. 2-54 to investigate the separation ability of photoinduced electron and hole. It could be learned that $NaTaO_3$-E-G2 also exhibited the similar separation ability with that of $NaTaO_3$-W-G2, but much poorer than $NaTaO_3$-E-G0, which implied that the C modification was not made a positive effect on the photoinduced electron-hole separation ability. From above discussion, it might be concluded that the high specific surface area finally led to the outstanding deNO_x ability of sample over the factors of light absorption and separation performance under the present reaction ocnditions. Even so, the much improved visible light ability of samples by C modification was

also of great importance, since the visible light induced photocatalytic performance was impossible due to the wide intrinsic band gap of $NaTaO_3$.

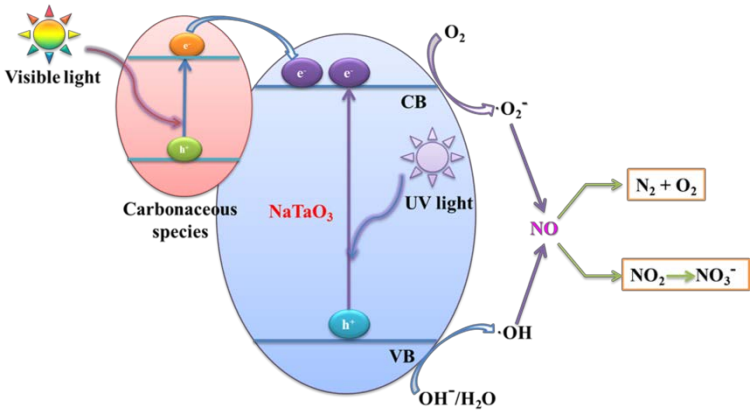

Figure 2-55. Possible photocatalytic mechanism of C modified $NaTaO_3$.

Based on above analysis and discussion, the possible photocatalytic mechanism of C modified $NaTaO_3$ was illustrated in Fig. 2-55. Under visible light irradiation, the carbonaceous species on the surface of $NaTaO_3$ could be regarded as sensitizer to absorb visible light. In this case, the photogenerated electron enabled to transfer from carbonaceous species to the conduction band (CB) of $NaTaO_3$. Then, the electron in CB would react with O_2 to produce $\cdot O_2^-$. Besides, under the excitation by UV light, in addition to the electron transferred from carbonaceous species, the electron in the valence band (VB) could also be excited to the CB. The photogenerated hole in the VB could react with OH^- or adsorbed water to produce hydroxyl radicals (·OH). Finally, the produced active radicals, $\cdot O_2^-$ and ·OH, could be used to reduce or oxidize NO gas to N_2 or NO_3^-, respectively.[49,91,104]

2.3 Preparation of visible light induced BiOX (X=Cl, Br, I) based materials

2.3.1 Introduction

Bismuth oxyhalides (BiOX; X=Cl, Br, I), as a new series of promising typical

p-type photocatalysts, have also received increasing interest for the investigation of UV and visible light induced photocatalytic activities owing to their unique layered structure, electrical and optical properties.[105] Various approaches, including the solid state melting method,[106] hydrothermal/solvothermal method,[107] sol-gel[108] and reverse microemulsion method,[109] etc., have been developed to synthesize BiOX. However, most of them required special precursors, high temperatures, long reaction times or expensive machinery, which are not popular for practical applications.

On the other hand, it is well known that the BiOCl, BiOBr and BiOI have different intrinsic band gaps due to their electrical structures, finally leading to big differences in optical properties. In general, BiOCl possessing a band gap of 3.20 eV only exhibits the ability to absorb UV light, while BiOBr and BiOI possessing band gaps of 2.76 and 1.77 eV, respectively, display visible light absorption capabilities.[110] As a result of the less positive position of the valence band of BiOI compared with that of the OH^-/•OH couple, which is one of the most active oxidative radicals, the BiOI usually reveals much poorer visible light induced photocatalytic performance than BiOBr. Besides, although BiOBr displays relatively better visible light driven photocatalytic activity, the utilization of visible light by BiOBr for photocatalysis was still limited, because it can only absorb the short wavelength visible light of below 450 nm, owing to its relatively wide band gap of about 2.76 eV. Therefore, the improvement of visible light induced photocatalytic activity of BiOX series is urgently required.

It is well acknowledged that glycerol is a main by-product of fats and oils in the process of preparing biodiesel, and is also mass-produced by the soap and fatty acid industries. Nowadays, glycerol is oversupplied and easily accessible in our daily life.[111,112] Besides, glycerol has been popularly used as a reaction solvent to control the morphology and particle size of samples, due to its high viscosity, etc.[113,114] On the other hand, J. Jiang groups not only prepared the much improved visible light-induced photocatalytic performance of BiOCl and BiOBr, but also made a reasonable explanation for the enhancement of visible light absorption capability, due

to the increment of oxygen vacancies in the BiOX lattices induced by the addition of EG in the reaction solution.[115] While the relatively high temperature of solvothermal treatment was necessary and particle size was still large. Since the glycerol has similar function groups as that of EG, it is expected to show the similar effect on the induction of oxygen vacancies in the products. Therefore, in this section, glycerol was employed as part of a reaction solvent with water to fabricate high performance visible light responsive BiOX mesoporous nanoparticles with large specific surface areas.

2.3.2 Experimental

2.3.2.1 Sample preparation

BiOX mesoporous nanoparticles have been synthesized by a facile room temperature reaction. In a typical synthesis, 0.8 mmol $Bi(NO_3)_3 \cdot 5H_2O$ was dissolved in 30 mL of distilled water/glycerol mixed solution by sonication for 10 min, and 0.8 mmol KX (X=Cl, Br, I) was dissolved in 30 mL distilled water. After that, the $Bi(NO_3)_3 \cdot 5H_2O$ glycerol aqueous solution was dropwise added into the KX aqueous solution with vigorous stirring. The as-mixed solution was magnetically stirred for 1 h before aging for 3 h at room temperature. Finally, the product was centrifuged and washed with distilled water and ethanol four times, respectively, followed by drying in a vacuum oven at 60^oC overnight. The BiOX samples prepared in glycerol aqueous solution containing 0, 10, 20 and 30 mL glycerol were designated as BiOX-G0, BiOX-G10, BiOX-G20 and BiOX-G30, respectively. By comparison, C-TiO_2 and N-TiO_2 were synthesized by solvothermal methods reported in a previous paper.[116] The BiOX-G0(C) samples (C indicates control) were also fabricated at room temperature according to the reported work[117], in which 10 mmol of KX and 10 mmol of $Bi(NO_3)_3 \cdot 5H_2O$ were dissolved in a 200 mL water containing 9 mL of acetic acid, and the other procedures were the same as those of BiOX-G0. The BiOI-G0(C) was not prepared due to its poor photocatalytic performance. Additionally, the

BiOBr-G0-G was prepared by simply dispersing BiOBr-G0 powders in a 60 mL glycerol/distilled water mixed solution (containing 20 mL glycerol) and the following steps were just as those of BiOBr-G20.

2.3.2.2 Photocatalytic activity tests

The photocatalytic activities of samples were evaluated by the decomposition of NO ($deNO_x$) using a flow type reactor under irradiation of a 450 W high pressure mercury lamp at room temperature.

2.3.2.3 Determination of •OH radical

The amount of •OH radical produced by the photocatalyst samples under the irradiation of 300 W simulated solar light (ASAHI SPECTRA HAL-302) with a cut filter of >510 nm was evaluated by a spectrofluorometer (Shimadzu RF-5300P) in the presence of terephthalic acid, which is able to react with •OH radical in a solution to produce a high efficiency fluorescent 2-hydroxyterephthalic acid with an excitation of 315 nm. The detailed process was as follows: a 0.05 g BiOX sample was dispersed in 50 mL of 5×10^{-4} M terephthalic acid solution containing 2×10^{-3} M NaOH. Then, the BiOX suspension was irradiated by the visible light of a simulated solar lamp (>510 nm) for 1 h. After that, 10 mL suspensions were withdrawn and centrifuged to monitor the relative emission intensity of the solution by recording the maximum emission peak at 425 nm with the excitation of 315 nm using a UV-vis spectrohotometer. [118]

2.3.3 Results and discussion

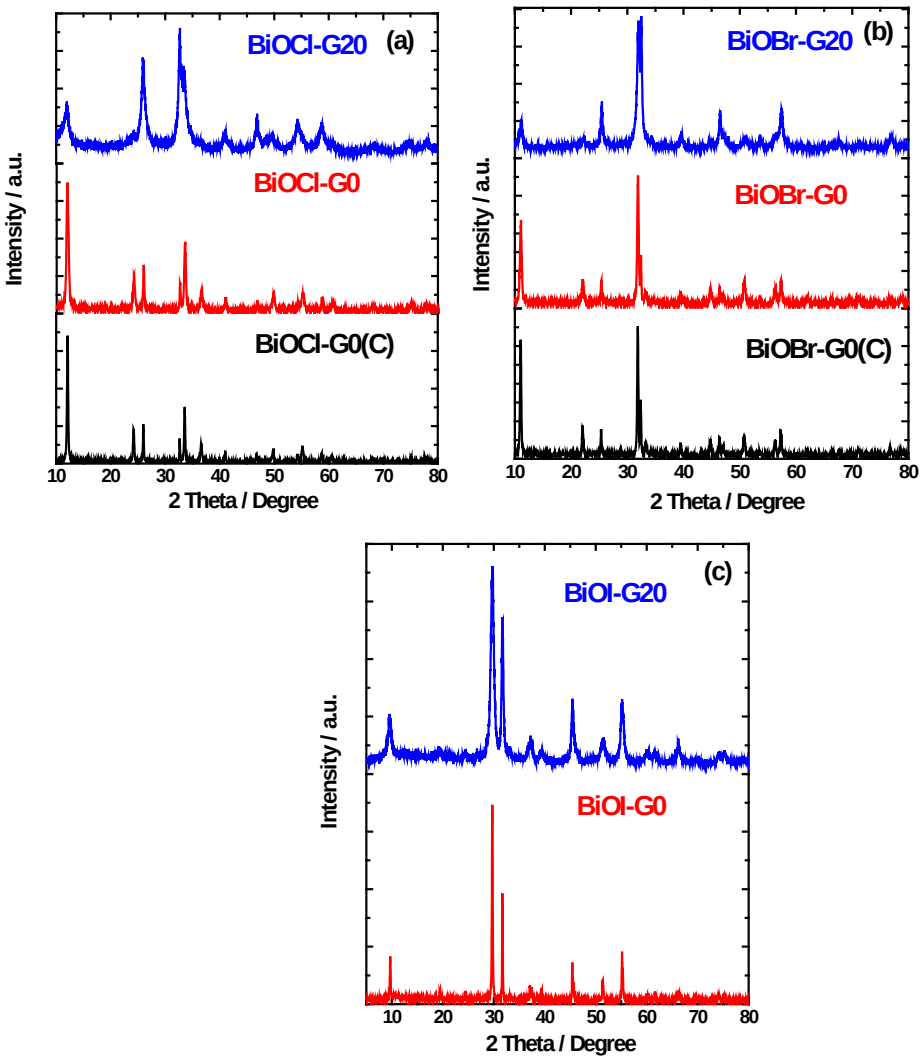

Figure 2-56. XRD patterns of BiOCl (a), BiOBr (b) and BiOI (c).

Figure 2-56 shows the XRD patterns of the BiOCl, BiOBr and BiOI. All diffraction peaks of BiOCl, BiOBr and BiOI could be well indexed to the tetragonal phase of BiOCl (JCPDS 06-0249), BiOBr (JCPDS 73-2061) and BiOI (JCPDS 73-2062), respectively. There was no other impurity peaks, indicating that pure BiOX crystals were successfully prepared at room temperature. Compared with those of BiOX-G0 and BiOX-G0(C) synthesized in water, the diffraction peaks of BiOX-G20 fabricated in the water/glycerol mixed solution were broadened, and the relative intensity was significantly decreased, implying that the particle size of BiOX-G20 was dramatically reduced in the presence of glycerol. Besides that, the relative peak intensities of (001)

of BiOX-G0(C) and BiOX-G0 were much stronger than that of BiOX-G20, indicating the oriented crystal growth of BiOX-G0(C) and BiOX-G0.

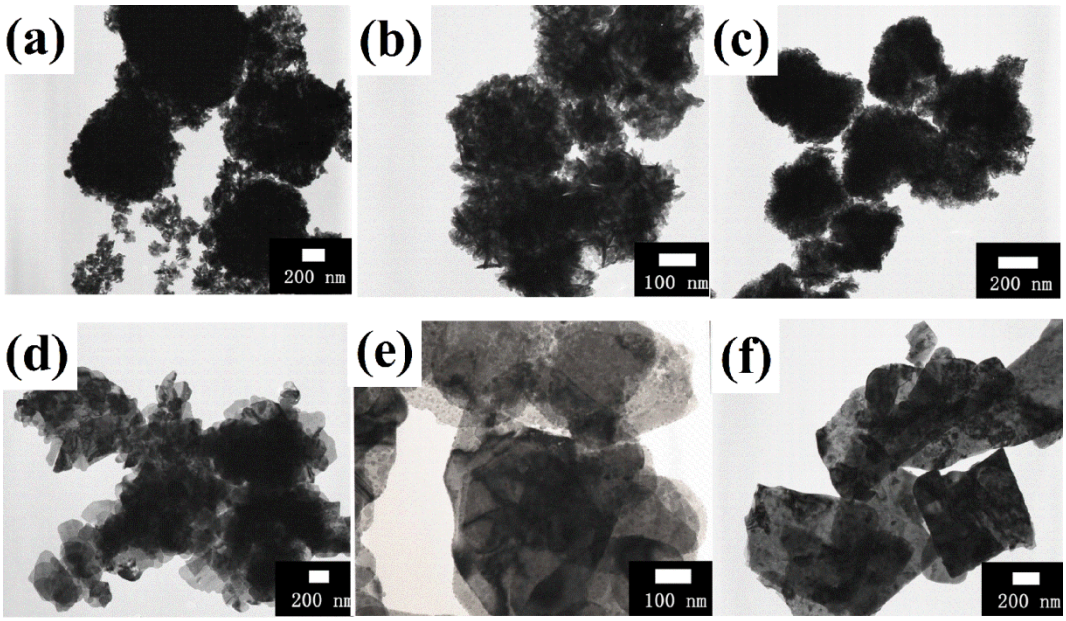

Figure 2-57. TEM images of BiOCl-G20 (a), BiOBr-G20 (b), BiOI-G20 (c), BiOCl-G0 (d), BiOBr-G0 (e) and BiOI-G0 (f).

The corresponding TEM images of BiOCl-G20, BiOBr-G20, BiOI-G20, BiOCl-G0，BiOBr-G0 and BiOI-G0 are shown in Fig. 2-57. It could be clearly seen that BiOX-G0 prepared in water revealed a nanoplate morphology, whereas the BiOX-G20 synthesized in a water/glycerol mixed solution presented a 3D nanostructure. The formation of different morphologies of BiOX-G0 and BiOX-G20 might be ascribed to the following reasons. When the water was utilized as the reaction solution, a great amount of tiny BiOX nuclei were formed as the $Bi(NO_3)_3$ aqueous solution was added into the KX aqueous solution. Due to the low viscosity of water, the reactant in the water could be quickly dispersed, and then the nuclei enabled to grow up anisotropically. The final BiOX-G0 nanoplates were produced by dissolving small BiOX crystals based on the Ostwald ripending mechanism.[119] In contrast, when the water/glycerol mixed reaction solution was used as a solvent, the $Bi(NO_3)_3$, which is insoluble in water, could be dissolved to form bismuth alkoxides at room temperature. When the $Bi(NO_3)_3$ water/glycerol mixed solution was

introduced into the KX aqueous solution, the bismuth alkoxides reacted with X^- and water to produce BiOX nuclei according to the precipitation-solubility equilibrium.[120] In addition, since the viscosity of glycerol (about 934 Pa•s) is much larger than that of water (about 0.89 Pa•s),[121] the diffusion rate of the reacting ions in the water/glycerol mixed solution could be controlled to depress the growth of BiOX crystals. Therefore, the particle size of BiOX-G20 became much smaller than that of BiOX-G0, which coincided with the XRD results. [120]

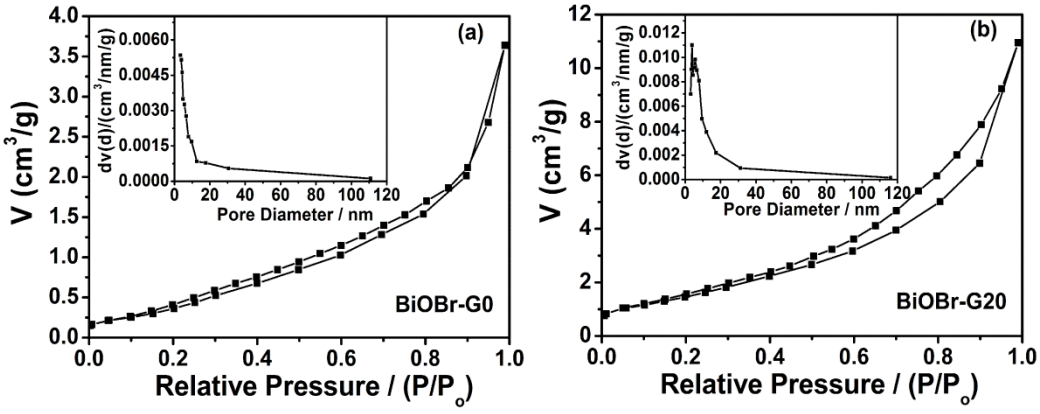

Figure 2-58. Nitrogen adsorption-desorption isotherms and the corresponding pore size distribution plots (inset) of BiOBr-G0 (a) and BiOBr-G20 (b).

The BET specific surface areas of BiOCl-G20, BiOBr-G20 and BiOI-G20 were 53.0, 39.3 and 28.5 m^2/g, respectively, which were much larger than those of BiOCl-G0 (17.3 m^2/g), BiOBr-G0 (14.2 m^2/g), BiOI-G0 (3.4 m^2/g) and lots of BiOX samples prepared previously by other ways.[117,120] The variation of BET specific surface areas in three BiOX-G20 samples is probably assigned to the difference of the diffusion rates of Cl^-, Br^- and I^- in the solution. Fig. 2-58 also exhibits the nitrogen adsorption–desorption isotherms and pore size distribution profiles of the as-synthesized BiOBr-G20 and BiOBr-G0 specimens. The isotherm of the BiOBr-G20 in Fig. 2-58 (b) was a typical IV type with H3 hysteresis loops, indicating the mesoporous structure,[122] whereas the BiOBr-G0 in Fig. 2-58 (a) presented no hysteresis loops. The average pore diameter of the BiOBr-G20 determined by the Barret–Joyner–Halenda (BJH) method was about 3.8 nm with a pore volume of 0.122

cm^3/g, indicating the formation of mesopores between small nanoparticles in the 3D nanostructure.

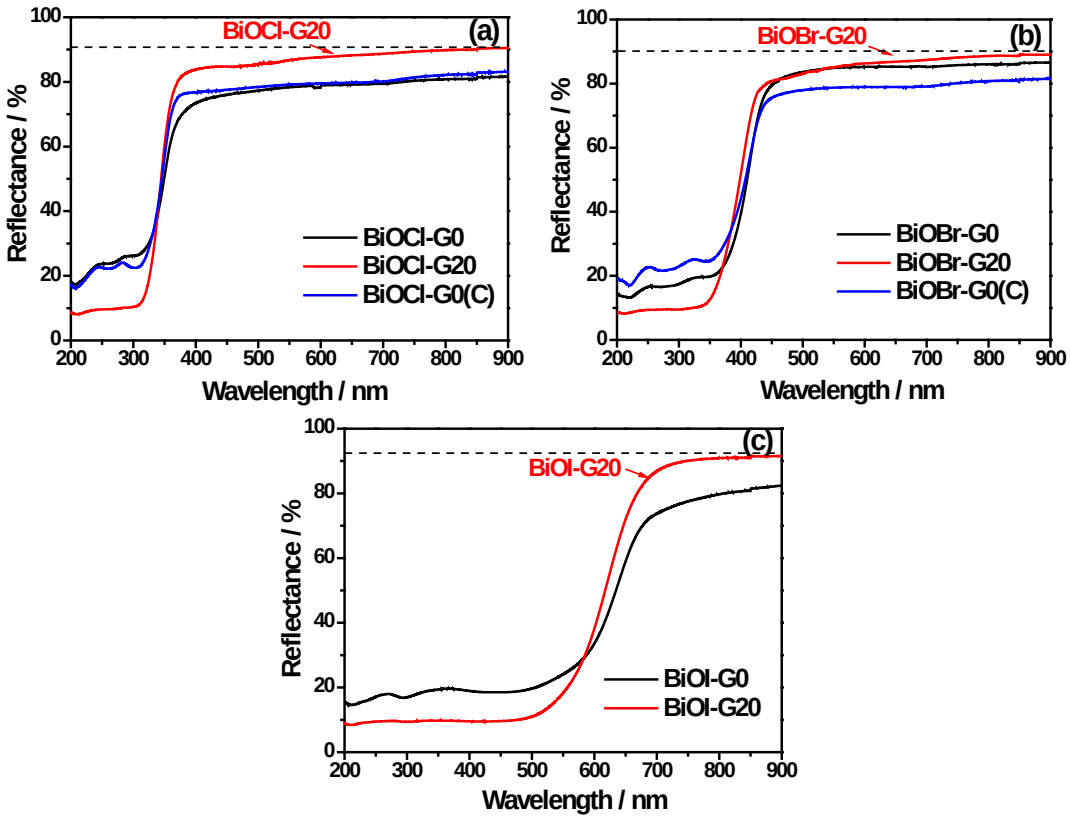

Figure 2-59. DRS of BiOCl (a), BiOBr (b) and BiOI (c) prepared under various conditions.

Figure 2-59 shows the DRS of BiOX-G0(C), BiOX-G0 and BiOX-G20. It is apparent that the total UV light absorption of BiOX-G0(C) and BiOX-G0 was much lower than that of BiOX-G20 but the total visible light absorption property was adverse. This phenomenon could be attributed to the effect of morphologies on the optical properties of the samples, which has no obviously direct influence on the photocatalytic properties of samples under UV and visible lights irradiation. Similar results had also been observed in many works.[123-125] Therefore, if we ignore the optical differences, which migh be related to the morphologyies, it could be seen that the BiOCl-G0(C) and BiOCl-G0, prepared in water, presented a main UV light absorption performance up to about 350 nm, while the BiOCl-G20, fabricated in the water/glycerol mixed solvent, displayed not only the intrinsic UV light absorption

capability, but also enhanced visible light absorption performance up to ca.700 nm, which was probably caused by the great increment of the amounts of oxygen vacancies in the BiOCl-G20 crystal. It is well acknowledged that the ethylene glycol (EG) containing reaction solvent is beneficial for the formation of oxygen vacancies in the product, where the EG can easily react with some oxygen-terminated oxide surfaces to remove some surface oxygen atoms during the preparation of specimens. In this case, large numbers of oxygen vacancies were left in the crystals, and these interesting phenomena were systematically investigated by many researchers. [111,115,126] In this work, glycerol and distilled water were used as the reaction solvent for the preparation of BiOX-G20. It is accepted that the glycerol has similar functional groups and properties as EG. Therefore, it may be deduced that the glycerol in this study was also favourable for the formation of oxygen vacancies in BiOX crystal as in EG. After great numbers of oxygen vacancies being produced in the BiOX-G20, some oxygen vacancy states could be formed under the conduction band of photocatalysts, [115,127] which finally led to the improvement of visible light absorption performance. The existence of oxygen vacancy in the crystalline BiOX-G20 would be confirmed by the XPS analysis later. In addition, due to the variation of optical properties of BiOCl-G0(C), BiOCl-G0 and BiOCl-G20 induced by oxygen vacancy, the particle colour of BiOCl-G20 was light pink, while BiOCl-G0 and BiOCl-G0(C) were white. As for BiOBr, they demonstrated similar optical variation as the BiOCl series, i.e., the BiOBr-G20 exhibited better visible light absorption capability compared to BiOBr-G0(C) and BiOBr-G0. However, the BiOI-G0 displayed much better visible light absorption capability than BiOI-G20.

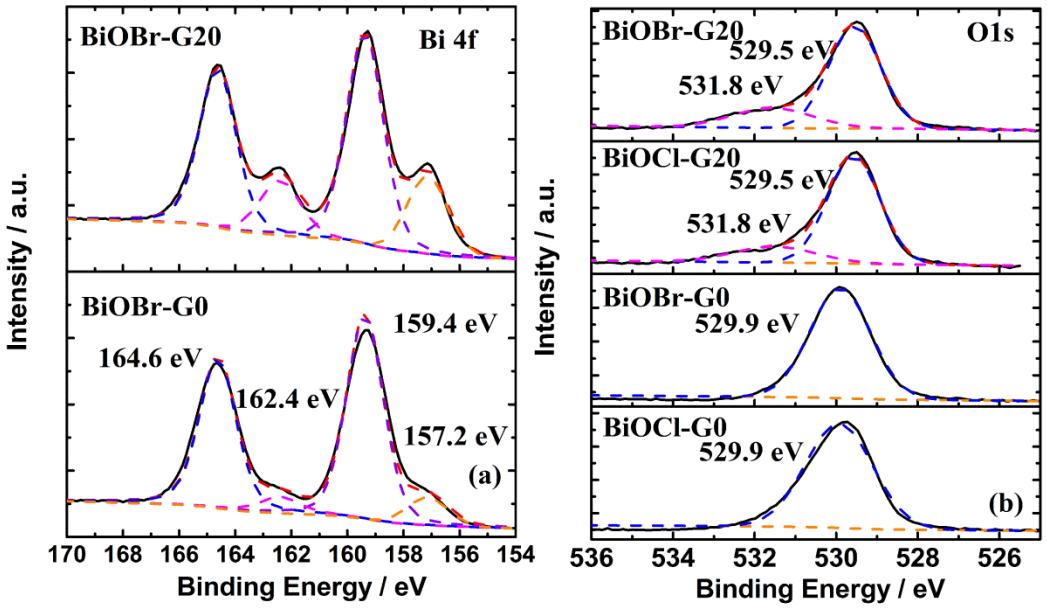

Figure 2-60. The XPS profiles of Bi 4f of BiOBr-G0 and BiOBr-G20 (a), and O1s of BiOCl-G0, BiOCl-G20, BiOBr-G0 and BiOBr-G20 (b).

Figure 2-60 (a) and (b) shows the detailed XPS profiles of Bi 4f and O 1s of the samples, respectively. In Fig. 2-60 (a), the representative high-resolution Bi 4f spectra of BiOBr-G0 and BiOBr-G20 are presented. It could be clearly seen that there were four fitted peaks in both samples. The two peaks located at 164.4 and 159.4 eV were ascribed to the common Bi^{3+} in the BiOBr,[123] while the other pair of peaks, which were situated at the relative lower binding energy (162.4 and 157.2 eV), should be corresponded to the lower valence of bismuth ions $Bi^{(3-x)+}$. The formation of $Bi^{(3-x)+}$ was attributed to the presence of oxygen vacancies in the vicinity of bismuth ions in the BiOBr,[115,128] indicating that the oxygen vacancies were truly introduced in the crystals of BiOBr. Furthermore, the relatively larger area of BiOBr-G20 implied more oxygen vacancies and deeper oxygen vacancy states between the band gaps, which led to dramatically enhanced visible light absorption as shown in Fig. 2-59. Similar phenomena were also observed in BiOCl and BiOI in other works.[111,115,127] In addition, the O 1s spectra of BiOCl and BiOBr indicated that both BiOCl-G0 and BiOBr-G0 samples showed only one strong O1s peak at about 529.9 eV, which should be ascribed the binding energy of the Bi-O bond.[129] However, BiOCl-G20 and BiOBr-G20 exhibited two main peaks located at about 531.8 eV and 529.5 eV. The

peak at 531.8 eV belonged to the OH and C-O bond, which may be induced by the surface absorbed glycerol or derivatives. The peak at 529.5 eV, which was 0.4 eV lower than those of BiOCl-G0 and BiOBr-G0, was probably caused by the increased number of oxygen vacancies.[130,131] These results indirectly confirmed that the glycerol had some essential effect on the preparation of BiOX, which eventually resulted in the enhancement of oxygen vacancy formation and visible light absorption in the BiOX-G20.

The photocatalytic activities of samples were investigated by evaluating the continuous NO gas destruction ability. In order to understand the visible light responsive photocatalytic performance better, UV light above a wavelength of 290 nm, visible lights above 400 nm and 510 nm were employed to irradiate the samples. Fig. 2-61 display the deNO_x performances of BiOCl (a), BiOBr (b) and BiOI (c) prepared under various conditions as well as the time dependence of the NO degradation ability of BiOCl-G20, BiOBr-G20, BiOBr-G0 (d) and commercial titania (Degussa P25), respectively. It could be explicitly observed in Fig. 2-61 (a) that the BiOCl-G0(C) prepared by a large molar ratio of raw materials revealed a pretty good UV light induced deNO_x ability to destruct about 44% of NO, while at the same time very poor visible light responsive performance due to the intrinsic wide band gap and small specific surface area. The BiOBr-G0(C) exhibited a little better visible light (>400 nm) induced photocatalytic performance of about 14% NO destruction, owing to its relatively narrower band gap compared with BiOCl. When the BiOX-G0 was synthesized by using a small amount of starting materials, the visible light (>400nm) driven deNO_x efficiencies of samples were improved slightly, mainly due to the enlarged specific surface areas and also induced small amount of oxygen vacancies in the crystal. The BiOI-G0 sample showed low deNO_x performance under both UV and visible lights in spite of the narrowest intrinsic band gap among the three BiOX compounds. On the other hand, the BiOCl-G20 and BiOBr-G20 samples, which were fabricated by employing the water/glycerol mixed solution as solvent, showed excellent photocatalytic performance under the irradiation of both UV and visible

lights. It is notable that the BiOBr-G20 sample displayed excellent visible light induced deNO$_x$ ability even above 510 nm. Based on these results, it could be concluded that with the addition of glycerol in the reaction solution of Bi(NO$_3$)$_3$ and KCl or KBr, the visible light driven deNO$_x$ properties of BiOCl and BiOBr could be significantly improved by the favorable increment of oxygen vacancies in crystal.

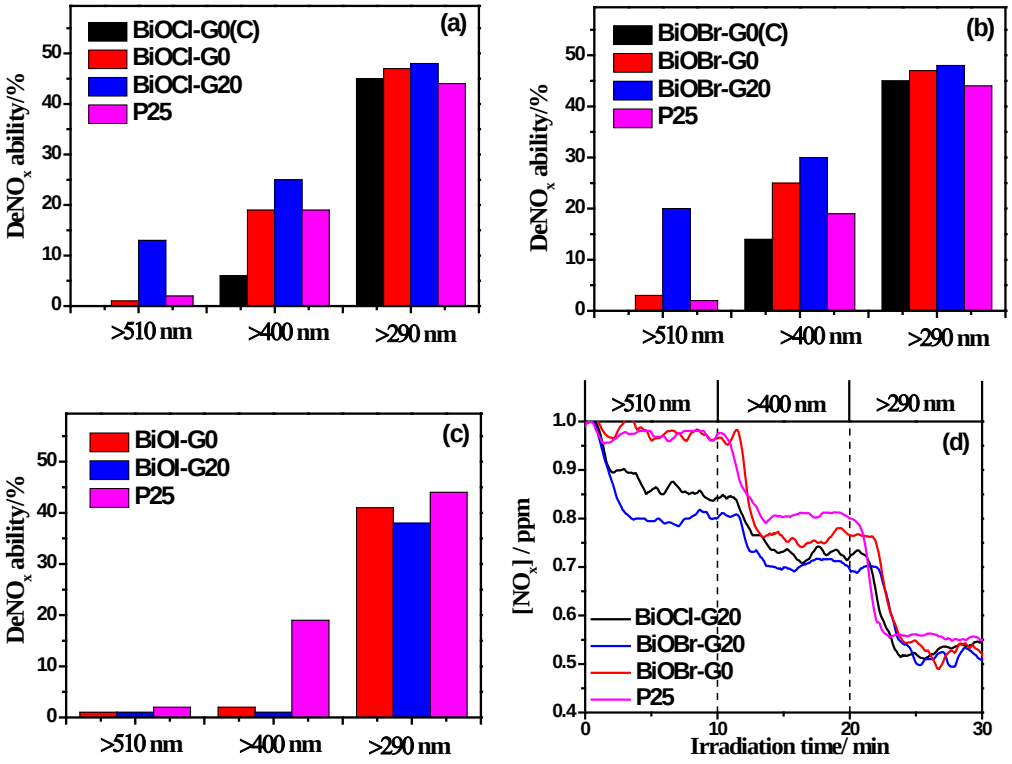

Figure 2-61. DeNO$_x$ ability of BiOCl (a), BiOBr (b) and BiOI (c), and the time dependence of NO$_x$ destruction activity of BiOCl-G20, BiOBr-G20, BiOBr-G0 and P25 (d) under the irradiation of different wavelengths of lights.

It is notable that BiOBr-G0-G prepared by dispersing BiOBr-G0 in the glycerol/distilled water mixed solution presented the modest visible light responsive deNO$_x$ ability as BiOBr-G0, implying that the glycerol truly played a vital role in the enhanced visible light induced photocatalytic performance, only when glycerol was attended during the preparation process, instead of simple adsorption on the surface of products.

The photocatalytic performance of BiOX-G20 was compared with those of the typical visible light responsive photocatalyst, C-TiO_2 and N-TiO_2. Fig. 2-62 shows the DRS and corresponding deNO_x ability of BiOBr-G20, C-TiO_2, N-TiO_2 and P25. It could be seen that the visible light absorption capabilities of C-TiO_2 and N-TiO_2 were much higher than that of BiOBr-G20, at the same time, the estimated specific surface areas of C-TiO_2 and N-TiO_2 were about 124.3 and 163.2 m^2/g, respectively, which were also much higher compared with the 39.3 m^2/g of BiOBr-G20. However, it is interesting to note that in Fig. 2-62 (b), corresponding UV and visible light induced photocatalytic activity of BiOBr-G20 was almost identical with those of C-TiO_2 and N-TiO_2, which were also much better than those of BiOX prepared by other methods for the oxidation of NO gas.[117,129] It means that the glycerol modified BiOBr-G20 presented superior visible light conversion efficiency for photocatalysis over C-TiO_2 and N-TiO_2.

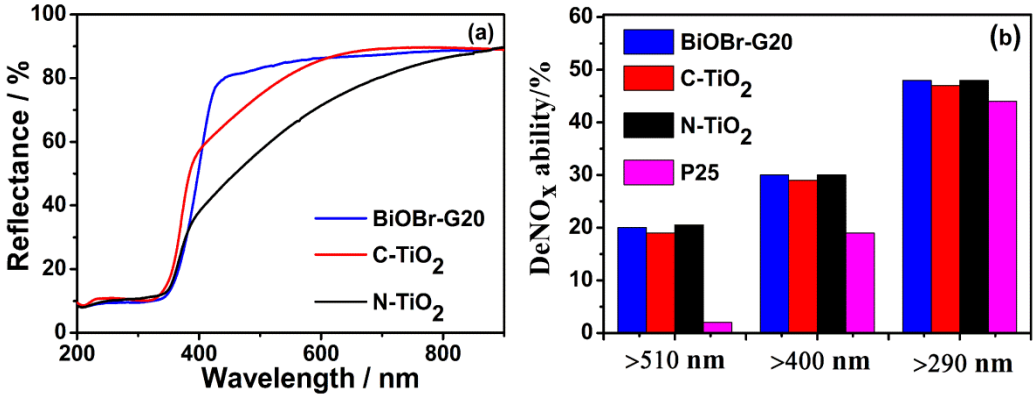

Figure 2-62. (a) DRS and (b) deNO_x ability of BiOBr-G20, C-TiO_2, N-TiO_2 and P25 under irradiation of various wavelengths of lights.

A possible mechanism for the enhanced visible light induced deNO_x ability of glycerol modified BiOX was considered as follows. Firstly, the intrinsic band gap of as-prepared BiOX in the presence of glycerol was calculated by the intercept of the Taucs plot of $(\alpha h\nu)^n$ (n = 1/2 for an indirect band gap of the BiOX semiconductor) versus photon energy ($h\nu$) according to optical properties as shown in Fig. 4-4, and the corresponding plot is presented in Fig. 2-63. Also, the conduction and valence

bands positions (E_{CB} and E_{VB}) of the BiOX semiconductor at a point zero charge can be appropriately determined by the following two equations:[132]

$$E_{CB}=X-E^{e}-0.5E_{g} \quad (2\text{-}9)$$

$$E_{VB}-E_{CB}=E_{g} \quad (2\text{-}10)$$

Where X corresponds to the absolute electronegativity of the BiOX semiconductor, obtained by the geometric mean of the absolute electronegativity of the atoms in the BiOX semiconductor; E^{e} is the energy of free electrons on the hydrogen scale (4.5 eV); and E_g is the intrinsic band gap of the BiOX semiconductor. The obtained X values for BiOCl-G20, BiOBr-G20 and BiOI-G20 along with the calculated intrinsic band gap, E_{CB} and E_{VB} of these three samples are listed in Table 2-5.[113]

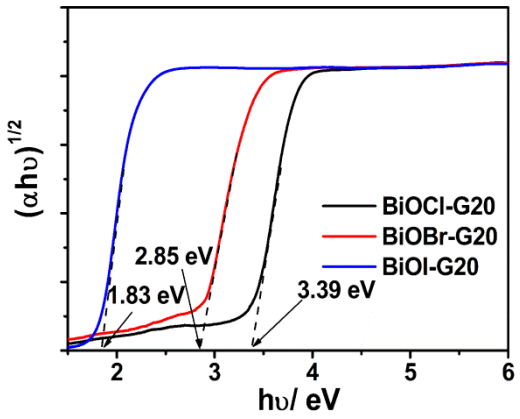

Figure 2-63. Plots of $(\alpha h\nu)^{1/2}$ versus photon energy of the BiOCl-G20, BiOBr-G20 and BiOI-G20.

Table 2-5. The calculated intrinsic band gap, X, E_{CB} and E_{VB} of BiOX-G20.

Samples	E_g (eV)	X (eV)	E_{CB} (eV)	E_{VB} (eV)
BiOCl-G20	3.39	6.34	0.15	3.54
BiOBr-G20	2.85	6.18	0.26	3.11
BiOI-G20	1.83	5.99	0.58	2.41

It could be clearly seen that the calculated intrinsic band gaps of BiOCl-G20, BiOBr-G20 and BiOI-G20 were about 3.39, 2.85 and 1.83 eV, respectively, which were a little greater than those of reported ones prepared at room temperature,[113] because of the decreased particle size of BiOX-G20 with the addition of glycerol in the reaction solution as observed in Fig. 2-57.

According to the intrinsic band gap of the samples shown in Fig. 2-64, the BiOCl should present only the UV light absorption property, BiOBr the limited visible light absorption property, and BiOI the strongest visible light absorption property. After increasing the amount of oxygen vacancies in the BiOX by the addition of glycerol in the reaction solvent at room temperature, some deep oxygen vacancy states would be formed below the conduction band of BiOX. [115, 127] Due to the induction of the deep oxygen vacancy states into the band gap, the electrons could be excited from the valence band of BiOX-G20 to the oxygen vacancy states, in addition to the electron transition from the valence band to the conduction band of BiOX-G20. In other words, the band gap of BiOX-G20 when significantly narrowed by oxygen vacancy states, finally led to the dramatic enhancement of visible light absorption as shown in Fig. 2-59. Therefore, the electrons in the valence band of BiOX-G20 could be excited by two routes under visible light irradiation for BiOBr-G20 and BiOI-G20, while only one pathway for BiOCl-G20. Namely, the photogenerated electrons could be transferred from the valence band of BiOBr-G20 and BiOI-G20 directly to the conduction band, or to the oxygen vacancy states. As for BiOCl-G20, the photoinduced electrons could only be moved from the valence band to the oxygen vacancy states due to the large intrinsic band gap. Subsequently, the photoinduced electron in the conduction band or oxygen vacancy states would form $\bullet O_2^-$ in the presence of oxygen, while the excited hole in the valence band of BiOCl-G20 and BiOBr-G20 could be trapped by water and adsorbed OH^- species in the air to produce hydroxyl radicals •OH, which are very active in the oxidative reaction. In the process of NO gas destruction, when the NO gas was flowed through the surface of sample powders with visible light irradiation, the NO gas could be oxidized to HNO_2 or

HNO_3, which might be easily eliminated by water.[49] Under this circumstance, the BiOCl-G20 and BiOBr-G20 could present excellent deNO_x ability even under the irradiation of long wavelength visible light. In addition, the higher efficiency of the visible light induced deNO_x property of BiOBr-G20 compared to BiOCl-G20 can likely be attributed to the much enhanced visible light absorption ability after the glycerol modification. Furthermore, the relatively large specific surface area of the sample with mesoporous structure prepared by glycerol mixed solvent was probably another vital point for the high activity of the samples compared to those of sample fabricated using water as the solvent. However, the absorbed water and OH^- species on the surface of glycerol modified BiOI-G20 could not react with the photogenerated hole to produce strong oxidative hydroxyl radicals •OH due to the lower positive potential of the valence band of BiOI-G20 compared with that of OH^-/•OH couple,[113] which could be further confirmed by the Fig. 2-65.

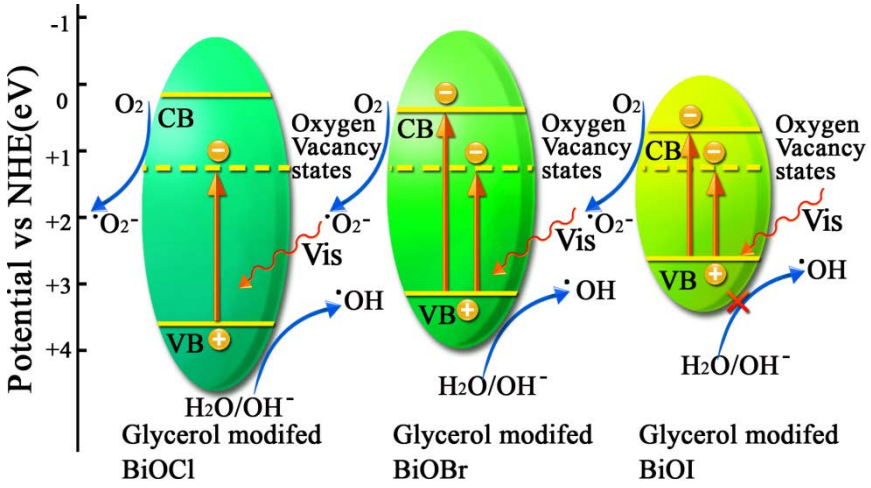

Figure 2-64. Schematic illustration of the possible visible light induced photocatalytic mechanism of glycerol modified BiOX.

In Fig. 2-65, it could be clearly seen that when the BiOCl-G20 and BiOBr-G20 were dispersed in 50 mL of 5×10^{-4} M terephthalic acid solution containing 2×10^{-3} M NaOH under irradiation of long wavelength visible light (>510 nm) for 60 min, the centrifuged terephthalic acid solution exhibited nice fluorescence emission with an excitation of 315 nm, whereas for BiOI-G20, there was no corresponding

fluorescence emission under the same condition. This phenomenon indicates that no obvious •OH radical was produced in the BiOI-G20 despersed solution under the irradiation of visible light, which finally led to the poor visible light driven deNO_x performance of glycerol modified BiOI-G20.[133]

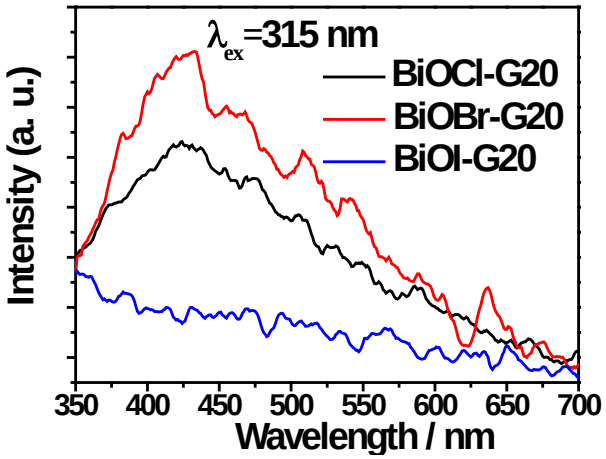

Figure 2-65. Photoluminescence spectra of terephthalic acid solution after long wavelength visible light (>510 nm) irradiation of BiOCl-20, BiOBr-G20 and BiOI-G20 samples in the terephthalic acid solution for 60 min.

2.4 Conclusions for Chapter 2

Preparation of visible light active TiO_2 based materials

Series of C doped, C and Nd codoped, W solely doped, C and W codoped TiO_2 nanoparticles as well as multi-phase of TiO_2 powders have been prepared by the calcination assisted solvothermal method. By solely and codoping, the band gap of TiO_2 has been considerably narrowed and separation ability of charge carriers was also promoted to some extent, finally leading to much improved visible liht induced photocatalytic activity of TiO_2. In particular, C and Nd codoped TiO_2 nanoparticle presented the superior visible light responsive deNO_x ability over other doped samples owing to its dramatically narrowed band gap, elevated separation ability of photogenerated hole-electron pairs and increased specific surface area. Besides, owing to the existence of reduced W^{5+} ions in TiO_2 crystal, W solely doped TiO_2

products exhibited not only relative good photocatalytic property but also excellent infrared light absorption capability, which were probably promising in the application of smart window.

Preparation of visible light induced $NaTaO_3$ based materials

A series of visible light absorbed C-$NaTaO_3$ were successfully prepared by a solvothermal method using EG aqueous solution without the addition of any other carbon precursors. The visible light absorption of $NaTaO_3$ could be enhanced considerably by C-doping induced from EG solution during solvothermal reaction, which presented excellent visible light responsive photocatalytic activity. Furthermore, the C-$NaTaO_3$/Cl-TiO_2 composites were also synthesized by the facile solvothermal method. The visible light induced deNO_x activity of the samples had been further improved significantly due to the suppression of recombination of photogenerated hole and electron.

On the other hand, carbon modified $NaTaO_3$ mesocrystals were also successfully prepared by a facile one-pot solvothermal method by using distilled water/EG as reaction solvent and glucose additive. The addition of glucose not only played a vital role for controlling the particle size and mesopore volume, but also extremely improved visible light absorption capability. The nanosized carbon modified $NaTaO_3$ mesocrystals exhibited outstanding deNO_x performance under the irradiation of UV, short wavelength visible light (>400 nm) and even long wavelength visible light above 510 nm.

Preparation of visible light induced glycerol modified BiOX at room temperature

Series of glycerol modified BiOX nanostructures have been successfully prepared by a facile low-cost method at room temperature using $Bi(NO_3)_3$•$5H_2O$ and KX (X=Cl, Br, I) as starting materials and the unique glycerol/water mixed solution as a reaction solvent. The introduction of glycerol in the reaction solution was not only

favorable for enlarging the specific surface area of samples, but also beneficial to the formation of large amounts of oxygen vacancies in the BiOX lattice, which finally led to the much improved visible light absorption capability and corresponding enhanced visible light responsive photocatalytic property.

2.5 References

1. S. C. Roy, O. K. Varghese, M. Paulose, C. A. Grimes, ACS Nano. **2010**, 4, 1259-1278.
2. S. Livraghi, M. C. Paganini, E. Giamello, A. Selloni, C. Divalentin, G. Pacchioni, J. Am. Chem. Soc. **2006**, 128, 15666-15671.
3. M. Gratzel, Nature **2001**, 414, 338-344.
4. J. Wang, S. Yin, Q. Zhang, F. Saito, T. Sato, J. Mater. Chem. **2003**, 13, 2348-2352.
5. H. H. Li, S. Yin, T. Sato, Appl. Catal. B: Environ. **2011**, 106, 586-591.
6. C. Chen, M. C. Long, H. Zeng, W. M. Cai, B. X. Zhou, J. Y. Zhang, Y. H. Wu, D. W. Ding, D. Y. Wu, J. Mol. Catal. A: Chem. **2009**, 314, 35-41.
7. T.F. Long, X.L. Dong, X.W. Liu, J.X. Liu, S. Yin, T. Sato, Res. Chem. Intermed. **2010**, 36, 61.
8. J. Wang, S. Yin, Q. Zhang, F. Saito, T. Sato, J. Mater. Chem. **2003**, 13, 2348-2352.
9. A. K. Bhattacharya, K. K. Mallick, A, Hartridge, Mater. Lett. **1997**, 30, 7-13.
10. S. Yin, B. Liu, P. L. Zhang, T. Morikawa, K. Yamanaka, T. Sato, J. Phys. Chem. C **2008**, 112, 12425-12431.
11. S. U. M. Khan, M. Al-Shahry, W. B. InglerJr., Science, **2002**, 297, 2243-2245.
12. S. Yin, Q. Zhang, F. Saito, T. Sato, Chem. Lett. **2003**, 32, 358-359.
13. V. Shanker, S. L. Samal, G. K. Pradhan, C. Narayana, A. K. Ganguli, Solid State Sci. **2009**, 11, 562-569.
14. X. Chang, J. Huang, C. Cheng, Q. Sui, W. Sha, G. Ji, S. Deng, G. Yu, Catal. Commun. **2010**, 11, 460-464.
15. Y. H. Ao, J. J. Xu, D. G. Fu, C. W. Yuan, J. Hazard. Mater. **2009**, 167, 413-417.
16. W. Ren, Z. Ai, F. Jia, L. Zhang, X. Fan, Z. Zou, Appl. Catal. B: Environ. **2007**, 69, 138-144.
17. Y. Huang, W. Ho, S. Lee, L.Z. Zhang, G. Li, J. C. Yu, Langmuir **2008**, 24, 3510-3516.
18. X. Wang, S. Meng, X. Zhang, H. Wang, W. Zhong, Q. Du, Chem. Phys. Lett. **2007**, 444,

292-296.

19. S. Yin, M. Komatsu, Q.W. Zhang, F. Saito, T. Sato, J. Mater. Sci. **2007**, 42, 2399-2404.
20. S. Sakthivel, H. Kisch, Angew. Chem. Int. Ed. **2003**, 42, 4908-4911.
21. C. D. Valentin, G. Pacchioni, A. Selloni, Chem. Mater. **2005**, 17, 6656-6665.
22. Y. Park, W. Kim, H. Park, T. Tachikawa, T. Majima, W. Choi, Appl. Catal. B: Environ. **2009**, 91, 355-361.
23. F. Dong, S. Guo, H. Q. Wang, X. F. Li, Z. B. Wu, J. Phys. Chem. C **2007**, 111, 17601-17605.
24. H. Irie, Y. Watanabe, K. Hashimoto, Chem. Lett. **2003**, 32, 772-773.
25. C. H. Ao, S. C. Lee, C. L. Mak, L. Y. Chan, Appl. Catal. B: Environ. **2003**, 42,119-129.
26. X. Y. Wu, S. Yin, Q. Dong, C. S. Guo, H. H. Li, T. Kimura, T. Sato, Appl. Catal. B: Environ. **2013**, 142-143, 450-457.
27. H. H. Li, S. Yin, Y. H. Wang, T. Sato, J. Catal. **2012**, 286, 273-278.
28. D. H. Wang, L. Jia, X. L. Wu, L. Q. Lu, A. W. Xu, Nanoscale **2012**, 4, 576-584.
29. B. Neumann, P. Bogdanoff, H. Tributsch, S. Sakthivel, H. Kisch, J. Phys. Chem. B **2005**, 109, 16579-16586.
30. X. X. Wang, S. Meng, X. L. Zhang, H. T. Wang, W. Zhong, Q. G. Du, Chem. Phys. Lett. **2007**, 444, 292-296.
31. F. Dong, S. Guo, H. Q. Wang, X. F. Li, Z. B. Wu, J. Phys. Chem. C **2011**, 115, 13285-13292.
32. V. Etacheri, M. K. Seery, S. J. Hinder, S. C. Pillai, Chem. Mater. **2010**, 22, 3843-3853.
33. J. G. Yu, G. H. Wang, B. Cheng, M. H. Zhou, Appl. Catal., B **2007**, 69, 171-180.
34. F. Z. Jia, Z. P. Yao, Z. H. Jiang, C. X. Li, Catal. Commun. **2011**, 12, 497-501.
35. X. B. Chen, C. Burda, J. Phys. Chem. B **2004**, 108, 15446-15449.
36. A. E. C. Palmqvist, M. Wirde, U. Gelius, M. Muhammed, Nanostruct. Mater. **1999**, 11, 995-1007.
37. R. K. Singhal, A. Samariya, S. Kumar, Y. T. Xing, D. C. jain, S. N. Dolia, U. P. Deshpande, T. Shripathi, E. B. Saitovitch, J. Appl. Phys. **2010**, 107, 113916.
38. E. Y. Wu, K. L. Ou, S. F. Ou, K. D. Jandt, Y. N. Pan, Mater. Trans. **2009**, 50, 891-895.
39. R. Beranek, H. Kisch, Photochem. Photobiol. Sci. **2008**, 7, 40-48.
40. F. Zhang, S. Jin, Y. Mao, Z. Zheng, Y. Chen, X. Liu, Thin Solid Films **1997**, 310, 29-33.

41. J. Y. Zhang, Z. Y. Zhao, X. Y. Wang, T. Yu, J. Guan, Z. T. Yu, Z. S. Li, Z. G. Zou, J. Phys. Chem. C **2010**, 114, 18396-18400.
42. A. K. Rumiz, J. C. Woicik, E. Cockayen, H. Y. lin, G. H. Jaffari, S. I. Shah, Appl. Phys. Lett. **2009**, 95, 262111-262113.
43. H. H. Li, S. Yin, Y. H. Wang, T. Sekino, S. W. Lee, T. Sato. J. Catal. **2013**, 297, 65-76.
44. X. Y. Pan, M. Q. Yang, X. Z. Fu, N. Zhang, Y. J. Xu. Nanoscale **2013**, 5, 3601-3614.
45. J. S. Dalton, P. A. Janes, N. G. Jones, J. A. Nicholson, K. R. Halam, G. C. Allen, Environ. Pollut. **2002**, 120, 415-422.
46. Q. P. Wu, R. V. D. Krol, J. Am. Chem. Soc. **2012**, 134, 9369-9375.
47. M. R. Hoffmann, S. T. Martin, W. Choi, D. W. Bahnemann, Chem. Rev. **1995**, 95, 69-96.
48. I. Justicia, P. OrdejÓn, G. Canto, J. L. Mozos, J. Fraxedas, G. A. Battiston, R. Gerbasi, A. Figueras, Adv. Mater. **2002**, 14, 1399-1402.
49. M. Anpo, NTS: Tokyo, **2002**, p 9. JP803371S.
50. C. C. Wang, J. Y. Ying, Chem. Mater. **1999**, 11, 3113-3120.
51. J. Livage, M. Henry, C. Sanchez, Prog. Solid State Chem. **1988**, 18, 259-341.
52. J. P. Jolivet, Metal oxide chemistry and synthesis: From solution to solid state, Wiley, New York, **2000**.
53. S. Girish Kumar, K. S. R. Koteswara Rao, Nanoscale, **2014**, 6, 11574-11632.
54. M. Wu, G. Lin, D. Chen, G. Wang, D. He, S. Feng, R. Xu, Chem. Mater. **2002**, 14, 1974-1980.
55. J. G. Li, T. Ishigaki, X. D. Sun, J. Phys. Chem. C **2007**, 111, 4969-4976.
56. K. Q. Huang, L. Chen, J. W. Xiong, M. X. Liao, Int. J. Photoenergy **2012**, 2012, 6314351-6314359.
57. J. Q. Ding, Y. L. Yuan, J. S. Xu, J. Deng, J. B. Guo, J. Biomed. Nanotechnol. **2009**, 5, 1-7.
58. X. Y. Wu, S. Yin, Q. Dong, C. S. Guo, T. Kimura, T. Sato, J. Phys. Chem. C **2013**, 117, 8345-8352.
59. G. Li, L. Li, J. Boerio-Goates, B. F. Woodfield, J. Am. Chem. Soc. **2005**, 127, 8659-8666.
60. S. K. Gupta, R. Desai, P. K. Jha, S. Sahoo, D. Kirin, J. Raman Spectrosc. **2009**, 41, 350-355.
61. C. T. Sun, D. F. Xue, J. Phys. Chem. C **2013**, 117, 5505-5511.

62. Y. Wang, D. J. Wu, Y. T. Yang, X. J. Liu, Chin. Phys. Lett. **2011**, 28, 0278041-4.

63. D. F. Xue, K. Y. Li, J. Liu, C. T. Sun, K. F. Chen, Mater. Res. Bull. **2012**, 47, 2838-2842.

64. Y. H. Xu, C. Chao, X. L. Yang, X. Li, B. F. Wang, Appl. Surf. Sci. **2009**, 255, 8624-8628.

65. V. Stengl, S. Bakardjieva, N. Murafa, Mater. Chem. Phys. **2009**, 114, 217-226.

66. A. Fissel, Z. Elassar, O. Kirfel, E. Bugiel, M. Czernohorsky, H. J. Osten, J. Appl. Phys. **2006**, 99, 0741051-0741056.

67. K. Y. Li, D. F. Xue, J. Phys. Chem. A **2006**, 110, 11332-11337.

68. Y. Li, D. S. Hwang, N. H. Lee, S. J. Kim, Chem. Phys. Lett. **2005**, 404, 25-29.

69. J. Xu, M. Chen, D. Fu, Appl. Surf. Sci. **2011**, 257, 7381-7386.

70. Y. Zhang, H. Xu, Y. Xu, H. Zhang, Y. Wang, J. Photochem. Photobiol. A **2005**, 170, 279-285.

71. X. G. Ma, Y. Wu, Y. H. Lu, J. Xu, Y. J. Wang, Y. F. Zhu, J. Phys. Chem. C **2011**, 115, 16963-16969.

72. C. S. Guo, S. Yin, Y. F. Huang, Q. Dong, T. Sato, Langmuir **2011**, 27, 12172-12178.

73. X. Y. Wu, S. Yin, Q. Dong, B. Liu, T. Sato, Materials Technology: Advanced Functional Materials, **2014**, 29, A20-A29.

74. J. M. Herrmann, J. Disdier, P. Pichat, Chem. Phys. Lett. **1984**, 108, 618-622.

75. S. Liu, E. Guo, L. W. Yin, J. Mater. Chem. **2012**, 22, 5031-5041.

76. I. S. Cho, C. H. Lee, Y. Z. Feng, M. Logar, P. M. Rao, L. L. Cai, D. R. Kim, R. Sinclair, X. L. Zheng, Nat. Commun. **2013**, 4, 1723.

77. H. W. Kang, S. B. Park, Adv. Powder Technol. **2010**, 21, 106-110.

78. X. Y. Wu, S. Yin, Q. Dong, T. Sato, Phys. Chem. Chem. Phys. **2013**, 15, 20633-20640.

79. X. Li, J. L. Zang, J. Phys. Chem. C **2009**, 113, 19411-19418.

80. P. L. Han, Y. G. Su, Y. Meng, S. W. Wang, Q. Y. Jia, X. J. Wang, J. Nanosci. Nanotechno. **2011**, 11, 9600-9606.

81. H. Xu, L. Z. Zhang, J. Phys. Chem. C **2010**, 114, 11534-11541.

82. J. B. Lu, H. Jin, Y. Dai, K. S. Yang, B. B. Huang, Int. J. Photoenergy. **2012**, 2012, 1-8.

83. W. B. Hu, L. P. Li, G. S. Li, C. L. Tang, L. Sun, Cryst. Growth. Des. **2009**, 9, 3676-3682.

84. Y. G. Su, S. W. Wang, Y. Meng, H. Han, X. J. Wang, RSC Adv. **2012**, 2, 12932-12939.

85. J. G. Yu, Y. Wang, W. J. Xiao, J. Mater. Chem. A **2013**, 1, 10727-10735.

86. Y. Y. Deng, Y. J. Chen, B. G. Chen, J. H. Ma, J. Alloys Compd. **2013**, 559, 116-122.

87. J. H. Yan, Y. R. Zhu, Y. G. Tang, S. Q. Zheng, J. Alloys Compd. **2009**, 472, 429-433.

88. K. H. Reddy, S. Martha, K.M. Parida, Inorg. Chem. **2013**, 52, 6390-6401.

89. X. F. Yang, J. L. Qin, Y. Li, R. X. Zhang, H. Tang, J. Hazard. Mater. **2013**, 261, 342-350.

90. R. Q. Song, H. Colfen, Adv. Mater. **2010**, 22, 1301-1330.

91. X. Y. Wu, S. Yin, B. Liu, M. Kobayashi, M. Kakihana, T. Sato, J. Mater. Chem. A **2014**, 2014, 2, 20832-20840.

92. S. Liu, J. Yu, J. Solid. State. Chem. **2008**, 181, 1048-1055.

93. D. Typke, R. Hegerl, J. Kleinz, Ultramicroscopy, **1992**, 46, 157-173.

94. Q. Zhang, S. J. Liu, S. H. Yu, J. Mater. Chem. **2009**, 19, 191-207.

95. T. Sugimoto, Adv. Colloid Interface Sci. **1987**, 28, 65-108.

96. D. Radziuk, A. Skirtach, G. Sukhorukow, D. Shchukin, H, MÖhwald, Macromol. Rapid Commun. **2007**, 28, 848-855.

97. S. Y. Oh, D. I. Yoo, Y. Shin, G. Seo, Carbohydr. Res. **2005**, 340, 417-428.

98. D. C. Dragunski, A. Pawlicka, Mat. Res. **2001**, 4, 77-81.

99. G. F. Mohamed, M. S. Shaheen, S. K. H. Khalil, A. M. S. Hussein, M. M. Kamil, Nature and Science **2011**, 9, 21-31.

100. Y. Z. Li, D. S. Hwang, N. H. Lee, S. J. Kim, Chem. Phys. Lett. **2005**, 404, 25-29.

101. Q. Li, J. C. Bian, L. Zhang, R. Q. Zhang, G. Z. Wang, D. H. L. Ng, ChemPlusChem **2014**, 79, 454-461.

102. X. M. Sun, Y. D. Li, Angew. Chem. Int. Ed. **2004**, 43, 597-601.

103. W. Jiang, X. L. Jiao, D. R. Chen, Int. J. Hydrogen Energy **2013**, 38, 12739-12746.

104. C. H. Huang, Y. M. Lin, I. K. Wang, C. M. Lu, Int. J. Photoenergy, **2012**, 2012, 1-13.

105. Z. Deng, D. Chen, B. Peng, F. Tang, Cryst. Growth. Des. **2008**, 8, 2995-3003.

106. X. Zhang, Z. Ai, F. Jia, L. Zhang, J. Phys. Chem. C **2008**, 112, 747-753.

107. H. Z. An, Y. Du, T. M. Wang, C. Wang, W. C. Hao, J. Y. Zhang, Rare Metals, **2008**, 27, 243-250.

108. S. J. Wu, C. Wang, Y. F. Cui, W. C. Hao, T. M. Wang, P. Brault, Mater. Lett. **2011**, 65, 1344-1347.

109. J. Henle, P. Simon, A. Frenzel, S. Scholz, S. Kaskel, Chem. Mater. **2007**, 19, 366-373.

110. H. Z. An, Y. Du, T. M. Wang, C. Wang, W. C. Hao, J. Y. Zhang, Rare Metals, **2008**, 27, 243-250.

111. L. L. Li, C. H. Zhang, J. Jiang, Nanoscale, **2014**, 6, 4627-4634.

112. V. Augugliaro, H. A. Hamed El Nazer, V. Loddo, A. Mele, G. Palmisano, L. Palmisano, S. Yurdakal, Cata. Today **2010**, 151, 21-28.

113. J. Hu, S. X. Weng, Z. Y. Zheng, Z. X. Pei, M. L. Huang, P. Liu, J. Hazard. Mater. **2014**, 264, 293-302.

114. M. Li, S. F. Zhou, Y. W. Zhang, G. Q. Chen, Z. L. Hong, Appl. Surf. Sci. **2008**, 254, 3762-3766.

115. J. Jiang, L. Z. Zhang, H. Li, W. W. He, J. J. Yin, Nanoscale, **2013**, 5, 10573-10581.

116. S. Yin, B. Liu, P. L. Zhang, T. Morikawa, K. Yamanaka, T. Sato, J. Phys. Chem. C **2008**, 112, 12425-12431.

117. W. D. Zhang, Q. Zhang, F. Dong, Ind. Eng. Chem. Res. **2013**, 52, 6740-6746.

118. S. F. Chen, X. L. Yu, H. Y. Zhang, W. Liu, J. Electrochem. Soc. **2010**, 157, K96-K102.

119. Mullin, J. W. Crystallization, 3rd ed., Butterworth-Heinemann, Oxford, **1997**.

120. G. Cheng, J. Y. Xiong, F. J. Stadler, New J. Chem. **2013**, 37, 3207-3213.

121. S. Yin, M. Shinozaki, T. Sato, J. Lumin. **2007**, 126, 427-433.

122. S. Liu, J. Yu, J. Solid. State. Chem. **2008**, 181, 1048-1055.

123. N. Talebian, S. M. Amininezhad, M. Doudi, J. Photochem. Photobiol. B **2013**, 120, 66-73.

124. J. Y. Xiong, G. Cheng, F. Qin, R. M. Wang, H. Z. Sun, R. Chen, Chem. Eng. J. **2013**, *220*, 228-236.

125. J. Z. Ma, J. L. Liu, Y. Bao, Z. F. Zhu, H. Liu, Cryst. Res. Technol. **2013**, 48, 251-260.

126. T. L. Chen, D. R. Mullins, J. Phys. Chem. C **2011**, 115, 13725-13733.

127. H. H. Li, S. Yin, Y. H. Wang, T. Sekino, S. W. Lee, T. Sato, J. Catal. **2013**, 297, 65-69.

128. S. M. Zhang, G. K. Zhang, S. J. Yu, X. G. Chen, X. Y. Zhang, J. Phys. Chem. C **2009**, 113, 20029-20035.

129. Z. H. Ai, W. K. Ho, S. C. Lee, L. Z. Zhang, Environ. Sci. Technol. **2009**, 43, 4143-4150.

130. T. Prasada Rao, M. C. Santhosh Kumar, J. Cryst. Process Tech. **2012**, 2, 72-79.

131. H. T. Cao, Z. L. Pei, J. Gong, C. Sun, R. F. Huang, L. S. Wen, J. Solid State Chem. **2004**, 177, 1480-1487.

132. Y. Y. Deng, Y. J. Chen, B. G. Chen, J. H. Ma, J. Alloys. Compd. **2013**, 559, 116-122.

133. K. Ishibashi, A. Fujishima, T. Watanabe, K. Hashimoto, Electrochem. Commun. **2000**, 2, 207-210.

Chapter 3 FABRICATIN OF VISIBLE AND NIR LIGHTS RESPONSIVE PHOTOCATALYSTS

Recently, a great amount of strategies have been developed to extend the visible light induced photocatalytic activity of semiconductor photocatalysts for the widespread application. However, the research about the NIR light induced photocatalytic property is still few. For the sake of NIR light responsive property, two main strategies are proposed. The first one is to dope some rare earth ions (e.g. Er^{3+}, Tm^{3+}, etc.) to achieve NIR light absorption by photocatalyst substrate itself. The other way is combining photocatalyst with high efficiency of up-conversion phosphor to form composite, in which the NIR light can excite the up-conversion phosphor component to emit UV or visible lights, and then this emitted UV or visible lights will be reabsorbed by the photocatalyst component in composite. Generally, the former strategy is not efficient enough for the NIR light utilization, since the materials possessing small band gap energy to absorb NIR generally show modest photocatalytic activity due to small oxidation-reduction potential. Therefore, the combination of up-conversion phosphor with photocatalyst to form a composite has drawn much more attention. For this composite, two prerequisites are required. On one hand, the emission spectrum of up-conversion phosphor under the excitation of NIR light should have a nice overlap with the absorption spectrum of photocatalyst so that the emitted light from up-conversion phosphor can be reabsorbed by the photocatalyst. On the other hand, the photocatalyst should possess a high efficiency of photocatalytic activity under the induction of emission lights from up-conversion phosphors.

As presented in Chapter 2, it can be learned that C doped TiO_2 and BiOBr-G20 samples all presented excellent UV, short and long wavelengths of visible lights

induced deNO_x ability, which would be the suitable photocatalyst substrates as the component to combine with up-conversion phosphors. Therefore, in this chapter, in order to improve solar energy utilization by enabling the effective use of not only UV, visible lights but also NIR light for photocatalysis, series of novel composites, which consisted of NIR light induced up-conversion phosphors and UV, visible lights driven C-TiO_2 photocatalyst, was synthesized by a facile calcination assisted solvothermal method without the addition of any other carbon precursors except for the Ti source and ethanol solvent. In addition, the effect of different color emitting up-conversion phosphors (blue light, green light and red light emitting ones) on the photocatalytic property of composites was also investigated. On the other hand, blue and green light-emitting up conversions coupled BiOBr composites were also developed by a facile method at room temperature, expecting to achieve visible and NIR lights responsive photocatalytic property simultaneously.[1,2]

3.1 Preparation of visible and NIR lights induced TiO_2 based composites

3.1.1 Full spectra light induced (Yb, Er)-$NaYF_4$/C-TiO_2 composite

3.1.1.1 Experimental

3.1.1.1.1 Sample preparation

A series of (Yb,Er)-$NaYF_4$/C-TiO_2 composites, with the (Yb,Er)-$NaYF_4$/C-TiO_2 weight ratios of 1:2, 1:1 and 2:1 were prepared by a simple calcination assisted solvothermal method, and were denoted as (1:2)@(Yb,Er)-$NaYF_4$/C-TiO_2, (1:1)@(Yb,Er)-$NaYF_4$/C-TiO_2, and (2:1)@(Yb,Er)-$NaYF_4$/C-TiO_2, respectively. The (Yb,Er)-$NaYF_4$ used in this experiment was purchased from Shanghai Huaming Gona

Rare Earth New Materials Co., Ltd. (China). In a typical synthesis process of (1:1)@(Yb,Er)-$NaYF_4$/C-TiO_2 particle, The appropriate amounts of (Yb,Er)-$NaYF_4$ particles were dispersed in 20 mL ethanol with continuous stirring for 30 min. After that, 0.6 mL titanium tetra-n-butoxide were introduced dropwise to the suspension solution with another 30 min magnetic stirring. Subsequently, 10.5 mL ethanol/water (10:0.5) mixed solution was added dropwise to the solution and stirred for 60 min before transferring into a 100 mL Teflon-lined stainless steel autoclave. Finally, the solution was heated at 190^{o}C for 2h, and the products were separated by centrifugation, washed and calcined at 265^{o}C for 1h in ambient condition. For comparison, C-TiO_2 was prepared by a similar process without the addition of (Yb,Er)-$NaYF_4$ particles, and (1:1)@(Yb,Er)-$NaYF_4$/TiO_2 without calcination at 265^{o}C.

For comparison, (1:1)@(Yb,Er)-$NaYF_4$/N-TiO_2 in which nitrogen doped titania (N-TiO_2) was utilized instead of the carbon doped titania (C-TiO_2) was also synthesized by a conventional hydrothermal method similar to our previous paper.[3] A desired amount of (Yb,Er)-$NaYF_4$, HMT (3 g, 99%) and 2 mL of 20 wt% $TiCl_3$ solution were mixed with 30 mL of distilled water. The mixture was placed into a stainless steel autoclave attached to a Teflon tube of internal volume of 100 mL. The autoclave was heated and kept at 90^{o}C for 1 h to realize homogeneous precipitation and then heated at 190^{o}C for 2 h. The powder product was separated by centrifugation, washed with distilled water and acetone three times, then vacuum dried at 80^{o}C overnight. In order to eliminate the effect of organics remained in the sample, the dried particles were finally calcined at 450^{o}C for 2 h.

3.1.1.1.2 Photocatalytic activity test

The photocatalytic activities of samples were investigated by evaluating the decomposition of NO_x ($DeNO_x$) using a flow type reactor under irradiation of different wavelengths of LEDs and NIR laser (see Fig. 3-1) at room temperature, where the detailed testing parameters are summarized in Table 3-1.

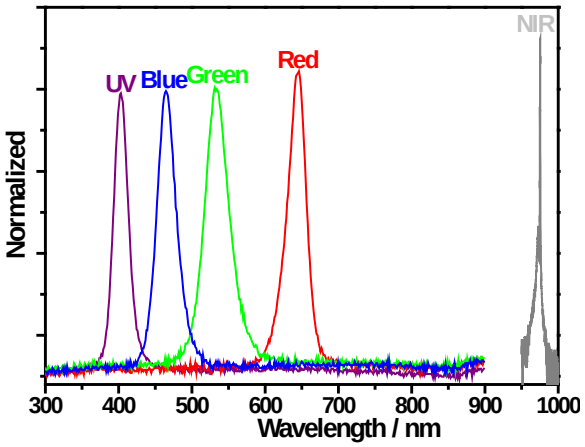

Figure 3-1. Spectra of UV, blue, green, red LEDs and NIR diode laser.

Table 3-1. Photocatalytic testing parameters of the light sources.

Light Source	Light Wavelength (nm)	Wattage (W)	Distance to the sample (cm)	Light intensity at the sample surface ($\mu mol/m^2s^{-1}$)	Irradiation area (cm^2)
NIR Diode Laser*	980	0.3	35	50.3*	0.4
Red LED	627	2.5	45	89.0	3.2
Green LED	530	2.5	5	88.3	3.2
Blue LED	445	2.5	40	88.2	3.2
UV LED	390	2.5	7	89.1	3.2

*®THORLABS, NLX-918, the maximum intensity realized by the 980nm laser.

3.1.1.2 Results and discussion

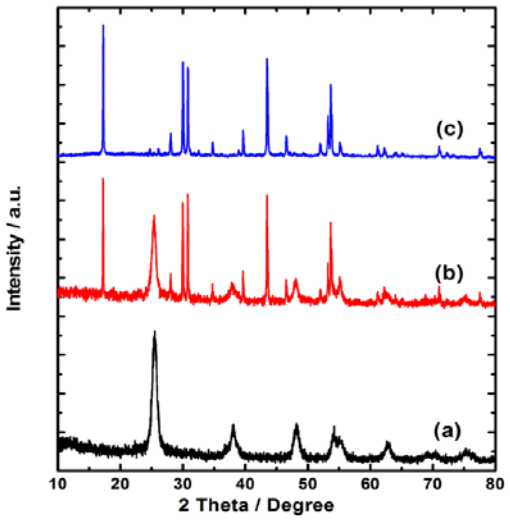

Figure 3-2. XRD patterns of (a) C-TiO_2, (b) (1:1)@(Yb,Er)-$NaYF_4$/C-TiO_2 and (c) (Yb,Er)-$NaYF_4$.

Figure 3-2 shows the XRD patterns of C-TiO_2, (1:1)@(Yb,Er)-$NaYF_4$/C-TiO_2 and (Yb,Er)-$NaYF_4$. All diffraction peaks of sample C-TiO_2 were well indexed to the anatase phase of TiO_2 (JCPDS file No. 21-1272) and no impurity peaks appeared. After combining with (Yb,Er)-$NaYF_4$ phosphor by a facile solvothermal method, no impurity peaks appeared in (1:1)@(Yb,Er)-$NaYF_4$/C-TiO_2 except for those of anatase TiO_2 and (Yb,Er)-$NaYF_4$, indicating that the introduction of (Yb,Er)-$NaYF_4$ in the solution made no visible change on the formation of anatase TiO_2 during the solvothermal process.

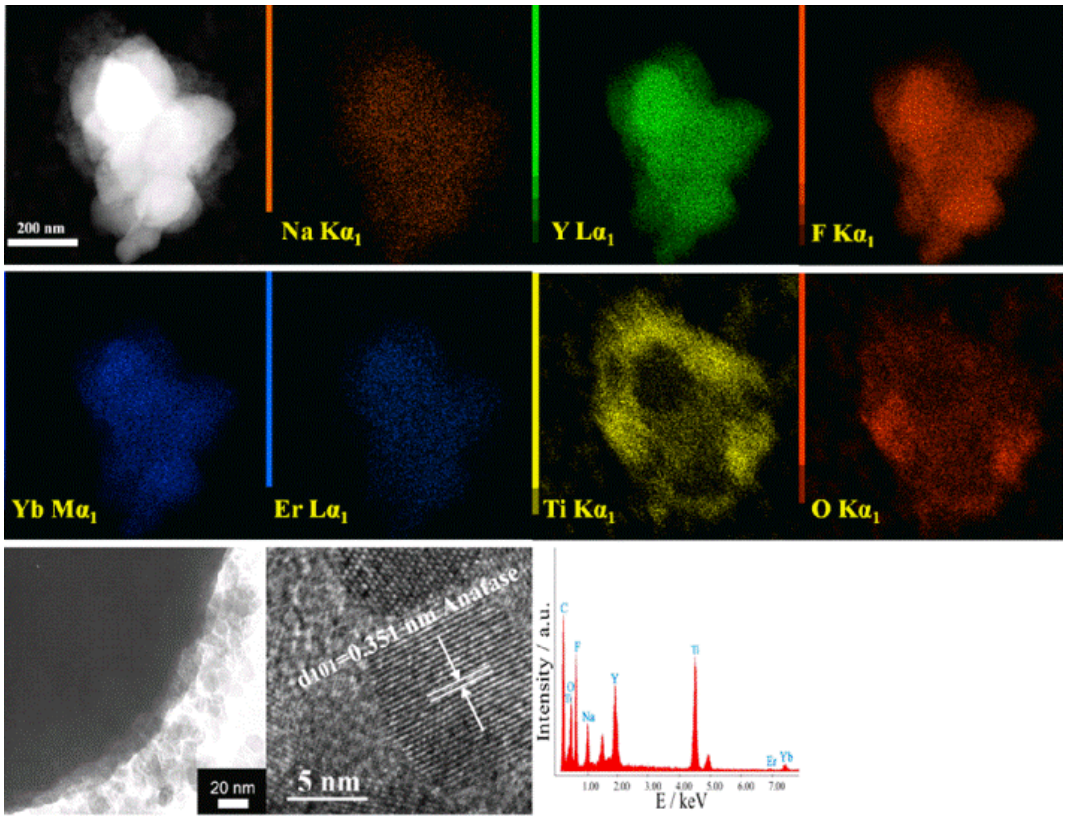

Figure 3-3. Element mapping, TEM image, HRTEM image and EDX spectrum of (1:1)@(Yb,Er)-$NaYF_4$/C-TiO_2.

Figure 3-3 shows the TEM image, HRTEM image, element mapping and EDX spectrum of (1:1)@(Yb,Er)-$NaYF_4$/C-TiO_2 composite. It could be clearly seen from element mapping that the element of Na, Y, F, Yb, Er, Ti and O truly existed in the sample. The element mapping of C was not shown because a large amount of C

existed in the support film of the TEM grid. However, actually, the existence of C in the TiO_2 could be confirmed from the EDX spectrum and the following DRS and XPS analysis. In addition, it could also be found in Fig. 3-3 that the large particle size of (Yb,Er)-$NaYF_4$ (200-400 nm) were successfully coated by small particles of C-TiO_2 (7-10 nm) to form core/shell structure. The d-spacing of covered small particle was about 0.351 nm, which agreed with the spacing of (101) of anatase TiO_2. The specific surface areas of C-TiO_2 and (Yb,Er)-$NaYF_4$ were determined as 124.3 and 11.5 m^2g^{-1}, respectively. When the C-TiO_2 nanoparticles were combined with (Yb,Er)-$NaYF_4$ powders in core/shell structure, the specific surface was changed to 70.1 m^2g^{-1}.

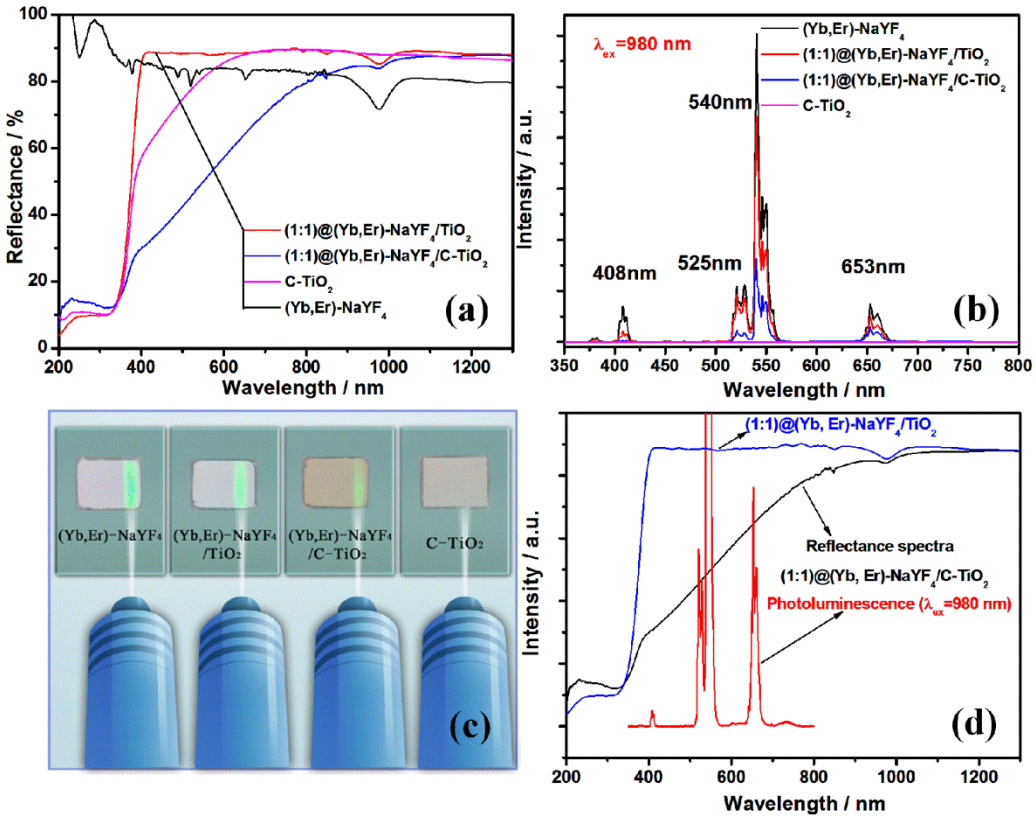

Figure 3-4. DRS (a), PL spectra (b), visual emitting map (c) of C-TiO_2, (1:1)@(Yb,Er)-$NaYF_4$/TiO_2, (1:1)@(Yb,Er)-$NaYF_4$/C-TiO_2, and (Yb,Er)-$NaYF_4$ under the excitation of 980 nm laser and (d) overlap between the DRS and PL spectrum of (1:1)@(Yb,Er)-$NaYF_4$/C-TiO_2. For comparison, the DRS of (1:1)@(Yb,Er)-$NaYF_4$/TiO_2 was also indicated in (d).

Figure 3-4 presents the DRS, PL spectra, visual emitting map of C-TiO_2, (1:1)@(Yb,Er)-$NaYF_4$/TiO_2, (1:1)@(Yb,Er)-$NaYF_4$/C-TiO_2 and (Yb,Er)-$NaYF_4$. It was apparent that C-TiO_2 exhibited a nice visible light absorption up to about 600 nm due to the C doping in TiO_2 by inducing some impurity energy levels of C above the valence band of TiO_2 (Fig. 3-4 (a)).[4] (Yb,Er)-$NaYF_4$ displayed only the absorption band from 908 to 1028 nm, corresponding to the $^2F_{7/2} \rightarrow {}^2F_{5/2}$ transition of Yb^{3+} in $NaYF_4$.[5] When TiO_2 was combined with (Yb,Er)-$NaYF_4$, (1:1)@(Yb,Er)-$NaYF_4$/TiO_2 represented a strong UV absorption of TiO_2 with the NIR light absorption band of (Yb,Er)-$NaYF_4$. Furthermore, (1:1)@(Yb,Er)-$NaYF_4$/C-TiO_2 showed the significantly enhanced visible light absorption up to 900 nm, owing to the introduction of C into TiO_2 lattice during calcination. In addition, it is interesting that the visible light absorption of (1:1)@(Yb,Er)-$NaYF_4$/C-TiO_2 was much stronger than that of uncoupled C-TiO_2, which is probably attributed to the increased C doping contents in TiO_2 in the presence of (Yb,Er)-$NaYF_4$ crystal. This phenomenon was also observed in chapter 2. The doped C contents in TiO_2 would be increased when other impurity ions (Nd^{3+}, etc.) or other phases were existed in the preparation of C-TiO_2 by solvothermal method. When the four kinds of samples in Fig. 3-4 (a) were excited by a NIR diode laser light (980 nm), different intensities of green light were emitted as shown in Fig. 3-4 (b). The (Yb,Er)-$NaYF_4$ powders showed the highest emission intensity with four emission peaks at about 408, 525, 540 and 653 nm, which are corresponding to the transitions from $^2H_{9/2}$, $^2H_{11/2}$, $^4S_{3/2}$ and $^4F_{9/2}$ to $^4I_{15/2}$ of Er^{3+}, respectively.[6] When the (Yb,Er)-$NaYF_4$ powders were mixed with undoped TiO_2 particles to form (1:1)@(Yb,Er)-$NaYF_4$/TiO_2, the relative emission intensity of peak at 540 nm decreased to about 1/4, probably due to the shielding of the excitation light by TiO_2 nanoparticles on the surface of (Yb,Er)-$NaYF_4$ core. More importantly, the relative emission intensity of sample (1:1)@(Yb,Er)-$NaYF_4$/C-TiO_2 declined more significantly. The reason for this dramatic decrement of emission intensity might be explained by Fig. 3-4 (d). It could be explicitly observed that the DRS of (1:1)@(Yb,Er)-$NaYF_4$/C-TiO_2 had a good overlap with four emission peaks in PL

spectrum, while no overlap could be observed for (1:1)@(Yb,Er)-$NaYF_4$/TiO_2, indicating that C-TiO_2 could efficiently absorb the visible fluorescence emitted from (Yb,Er)-$NaYF_4$. When the (1:1)@(Yb,Er)-$NaYF_4$/C-TiO_2 composite was excited by 980 nm laser, the up-conversion phosphor (Yb,Er)-$NaYF_4$ in the composite would emit green light with four emission peaks at 408, 525, 540 and 653 nm. Meanwhile, a large part of emitted green light would be efficiently absorbed by the C-TiO_2 particles coated on the surface of (Yb,Er)-$NaYF_4$, eventually leading to the strong reduction of emission intensity of green light compared with (Yb,Er)-$NaYF_4$ and (1:1)@(Yb,Er)-$NaYF_4$/TiO_2. As for C-TiO_2, no green light was observed when excited by 980 nm laser, since no up-conversion occurred in this sample. The corresponding visual emitting maps for these four samples monitored by 980 nm NIR light irradiation are presented in Fig. 3-4 (c), in which the laser sources and IR light paths are shown by computer graphics.

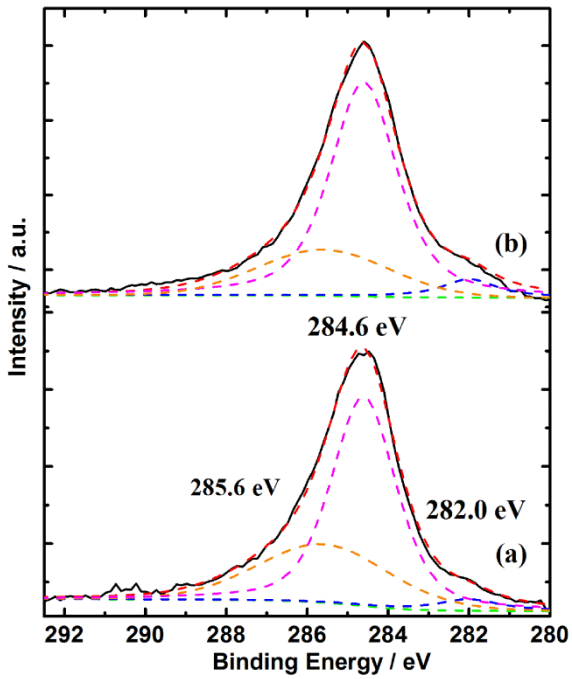

Figure 3-5. XPS spectra of C1s for (a) C-TiO_2 and (b) (1:1)@(Yb,Er)-$NaYF_4$/C-TiO_2.

In order to investigate the status of C in the TiO_2 lattice, the XPS measurement was employed. From XPS spectra of C 1s for C-TiO_2 and (1:1)@(Yb,Er)-$NaYF_4$/C-TiO_2

in Fig. 3-5, it could be obviously seen that both samples exhibited three peaks at 282.0 eV, 284.6 eV and 285.6 eV. The peak at 284.6 eV was ascribed to the adventitious carbon species from the XPS measurement, and the peak around 285.6 eV is corresponded to the elemental carbon, which has the same binding energy as that of carbon in the graphite intercalation compound.[7] More importantly, the small peak at about 282.0 eV should be ascribed to the binding energy of C-Ti bond, indicating that the C had been successfully doped into TiO_2 lattice by replacing O site.[4] The relative area of 282.0 eV peak for (1:1)@(Yb,Er)-$NaYF_4$/C-TiO_2 was larger than that of C-TiO_2, and the corresponding doped C concentrations for two samples were about 0.38 at.% and 0.19 at.%, which were well agreements with that of DRS result in Fig. 3-5 (a). It is well known that some impurity C energy levels will be introduced above the valence band of TiO_2 when C was doped in O site of TiO_2, and then the electrons can be excited from impurity C energy levels instead of the valence band of TiO_2 to the conduction band of TiO_2, which eventually leads to the strong visible light absorption of C-TiO_2.[4,7]

The photocatalytic activities of samples were investigated by testing the NO_x gas destruction ability under the irradiation of UV, visible and NIR lights. Fig. 3-6 illustrates the deNO_x activity of various samples using different wavelengths of light sources and all samples were kept in dark for 30 min before irradiation to eliminate the influence of adsorption of NO species by samples. In Fig. 3-6 (A) and (C), it can be obviously seen that there was no obvious deNO_x activity for (Yb,Er)-$NaYF_4$ (sample (c)) regardless of irradiation wavelengths. As for pure C-TiO_2 (sample (a)), 0%, 6.2%, 23.2%, 28.3% and 32.9% of NO were decomposed under the excitation of NIR diode laser, red LED, green LED, blue LED and UV LED, respectively. The nice visible light induced photocatalytic activity for this sample was mainly assigned to the excellent visible absorption of TiO_2 after C doping, but no NIR light driven deNO_x activity was performed, because C-TiO_2 could not be excited by 980 nm NIR light.

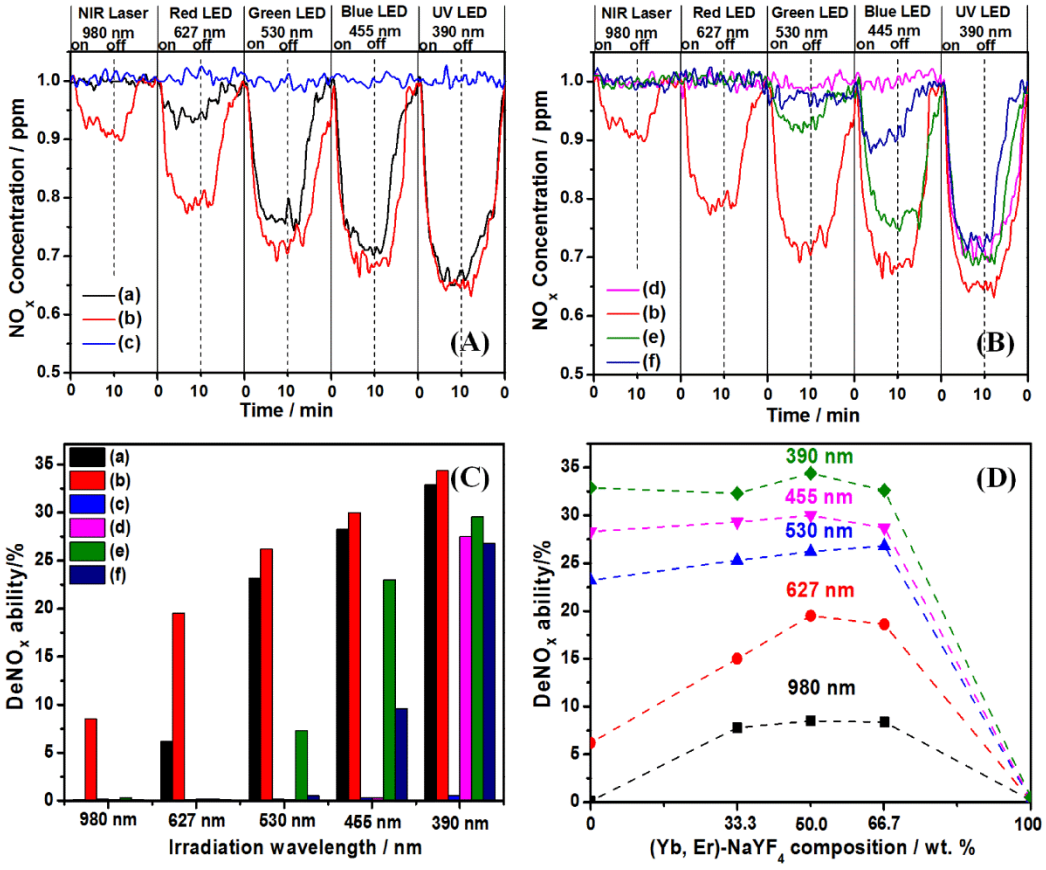

Figure 3-6. Time dependence of NO_x destruction activity (A), (B) , corresponding $deNO_x$ ability (C) of (a) C-TiO_2, (b) (1:1)@(Yb,Er)-$NaYF_4$/C-TiO_2, (c) (Yb,Er)-$NaYF_4$, (d) (1:1)@(Yb,Er)-$NaYF_4$/TiO_2, (e) (1:1)@(Yb,Er)-$NaYF_4$/N-TiO_2, (f) P25 titania under the irradiation of different wavelengths of lights, and the effect of (Yb,Er)-$NaYF_4$ content on the $deNO_x$ ability of (Yb,Er)-$NaYF_4$/C-TiO_2 composites (D).

However, when C-TiO_2 photocatalyst was combined with (Yb,Er)-$NaYF_4$ up-conversion phosphor, about 8.5% of NO_x gas was successfully destructed even when the NIR diode laser was used as the irradiation light source. This NIR light induced activity should be owing to the synergetic effect of C-TiO_2 photocatalyst and (Yb,Er)-$NaYF_4$ up-conversion phosphor, since no corresponding performance was observed by uncoupled C-TiO_2 and (Yb,Er)-$NaYF_4$ individually. In addition, the visible light induced $deNO_x$ performance was significantly enhanced to 19.5%, 26.2% and 30% with the irradiation of 627, 530 and 445 nm LED lights, respectively. This

interesting result might be dominantly due to the increased visible light absorption ability by increasing C doping content as shown in Fig. 3-4 (a). As for the effect of thermal reaction on the visible-NIR light induced photocatalytic activity, it could be ignored since no visible-NIR light responsive deNO_x activity was observed for the uncoupled (Yb,Er)-$NaYF_4$ and no NIR light driven deNO_x performance was exhibited for uncoupled C-TiO_2. Furthermore, the temperature was fixed at a constant room temperature during the photocatalytic testing.

The detailed mechanism for this synergy phenomenon will be explained in the following section. The deNO_x activity of (1:1)@(Yb,Er)-$NaYF_4$/C-TiO_2 was also compared with those of (1:1)@(Yb,Er)-$NaYF_4$/TiO_2, (1:1)@(Yb,Er)-$NaYF_4$/N-TiO_2 and P25 using different wavelengths of lights (Fig. 3-6 (B), (c)). When (Yb,Er)-$NaYF_4$ up-conversion phosphor was mixed with undoped TiO_2, only 27.5 % of UV light induced photocatalytic activity was displayed, and no distinct visible and NIR lights induced deNO_x activity was presented due to the poor visible and NIR light absorption of undoped TiO_2. As for P25, 26.8% and 9.6% of NO_x were destructed when UV and blue LEDs were used as light sources, respectively. (1:1)@(Yb,Er)-$NaYF_4$/N-TiO_2 exhibited only 7.3% and 23% of NO_x destruction ability with the visible light irradiation of 530 and 445 nm, respectively. Although the absorption spectrum of (1:1)@(Yb,Er)-$NaYF_4$/N-TiO_2 showed a little overlap with its photoluminescence spectrum, it was still not effective enough to induce the obvious deNO_x performance under the excitation of 980 nm light. Furthermore, the effect of (Yb,Er)-$NaYF_4$ content on the photocatalytic activity of (Yb,Er)-$NaYF_4$/C-TiO_2 composites was also studied using different wavelengths lights (in Fig.3-6 (D)). (1:1)@(Yb,Er)-$NaYF_4$/C-TiO_2 demonstrated a little better deNO_x ability than those of other compositions of (Yb,Er)-$NaYF_4$/C-TiO_2 composites.

In addition, the deNO_x ability of (1:1)@(Yb,Er)-$NaYF_4$/C-TiO_2 was also investigated by employing NIR laser, red LED, the combination of NIR laser and red LED as irradiation sources (Fig. 3-7). It was clearly exhibited that about 19% of NO_x

gas was destructed under the excitation of red LED. While when NIR laser was combined with red LED as the light source, further 4.5% of NO_x gas reduction was appeared and then moved back to 19% again as the NIR diode laser was eliminated. This result indicated that the NIR light induced deNO_x ability of the C-TiO_2 photocatalyst combined with (Yb,Er)-$NaYF_4$ up-conversion phosphor truly had a positive effect on the total photocatalytic activity of photocatalyst when irradiated by UV, visible, NIR lights, therefore, the solar light might be more effectively utilized for photocatalysis compared with that of uncoupled C-TiO_2 photocatalyst.

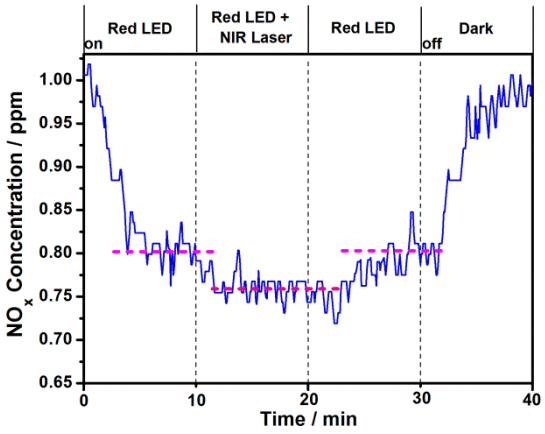

Figure 3-7. DeNO_x ability of (1:1)@(Yb,Er)-$NaYF_4$/C-TiO_2 with respect to the irradiation lights.

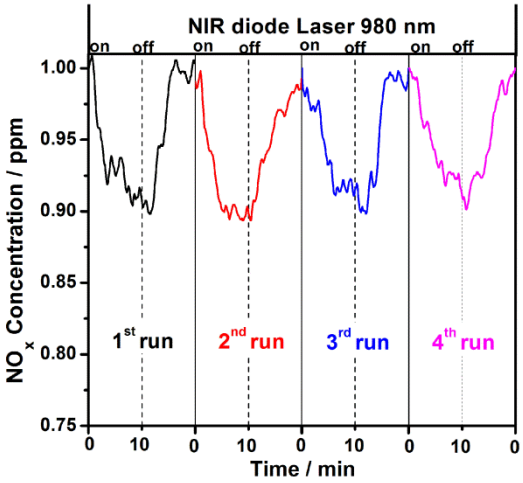

Figure 3-8. The multi-cycles of deNO_x performance of (1:1)@(Yb,Er)-$NaYF_4$/C-TiO_2 under the irradiation of 980 nm light.

It is well known that the photoluminescence of phosphor is sensitive to the operating condition, and the surround atmosphere of the photocatalyst may change after irradiation for some time.[8] Therefore, the reproducibility of NIR light induced $deNO_x$ ability of (Yb,Er)-$NaYF_4$/C-TiO_2 composite was evaluated. The $deNO_x$ reaction performance of (1:1)@(Yb,Er)-$NaYF_4$/C-TiO_2 with the repeated induction of 980 nm light is shown in Fig. 3-8. It is apparent that no noticeable change in the NIR light induced $deNO_x$ ability occurred after 4 times running, implying that the (Yb,Er)-$NaYF_4$/C-TiO_2 composite had an excellent stability for NO_x destruction when irradiated by NIR light.

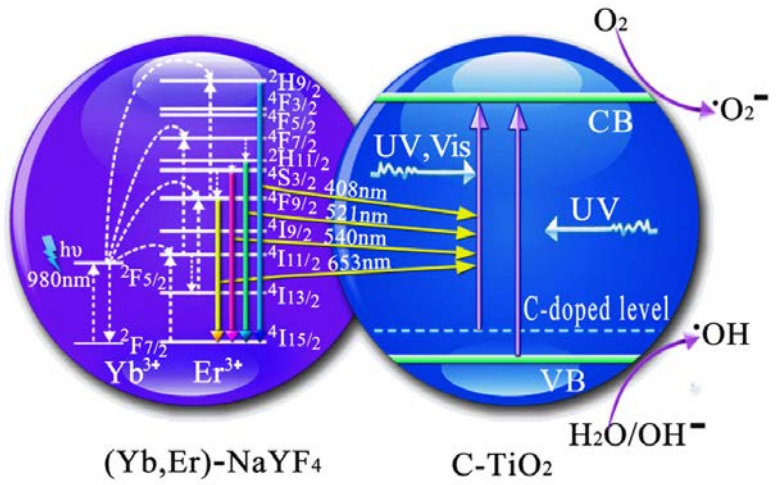

Figure 3-9. Schematic illustration of the photoluminescence and photocatalytic mechanism of (Yb,Er)-$NaYF_4$/C-TiO_2 composite.

Figure 3-9 illustrates the photoluminescence and UV, visible, NIR lights induced photocatalytic reaction mechanism of the (Yb,Er)-$NaYF_4$/C-TiO_2 composite. It is accepted that up-conversion phosphors can convert longer wavelength radiation (NIR light) to shorter wavelength fluorescence (UV or visible light) via a two-photon or multiphoton mechanism and then achieve the anti-stokes shift.[9,10] When a 980 nm NIR laser was used to excite the (Yb,Er)-$NaYF_4$/C-TiO_2, the Yb^{3+} as a sensitizer ion in (Yb,Er)-$NaYF_4$ phosphor could absorb this light, and then an electron was able to be excited from the $^2F_{7/2}$ to $^2F_{5/2}$ level. After that, the excited electron would transfer

back to the ground state of $^2F_{7/2}$ and the released energy in this process was dominantly nonradiatively transferred to active ions of Er^{3+}, leading to a population of Er^{3+} from $^4I_{15/2}$ to $^4I_{11/2}$. In addition, a second or more similar 980 nm photons from excited Yb^{3+} ion could populate to much higher $^4F_{9/2}$, $^4F_{7/2}$ and $^2H_{9/2}$ energetic levels of Er^{3+} ion. Some of the excited electrons of Er^{3+} ion then would relax nonradiatively by a fast multiphonon decay process to the $^2H_{11/2}$, $^4S_{3/2}$, $^4F_{9/2}$ etc. energy levels. Finally, these excited electrons would radiatively transfer to the Er^{3+} ground state of $^4I_{15/2}$ and present four emissions at 408 nm ($^2H_{9/2}\rightarrow{}^4I_{15/2}$), 521 nm ($^2H_{11/2}\rightarrow{}^4I_{15/2}$), 540 nm ($^4S_{3/2}\rightarrow{}^4I_{15/2}$) and 653 nm ($^4F_{9/2}\rightarrow{}^4I_{15/2}$).[11] The (Yb,Er)-$NaYF_4$ eventally emitted green light due to the main peak at 540 nm. In this case, the as-emitted green light from (Yb,Er)-$NaYF_4$ could be reabsorbed by the surface C-TiO_2 nanoparticles, which had an excellent light absorption in the range of above mentioned four peaks owing to the C doping in TiO_2 (shown in Fig. 3-4). At that time, the electron in TiO_2 was excited to the conduction band of TiO_2 from the C doped impurity energy levels, producing a pair of hole and electron in TiO_2 lattice. The photogenerated hole would then be trapped by water and adsorbed OH^- species in the air to generate hydroxyl radicals •OH. Besides, the photoinduced electron in the conduction band would form $\bullet O_2^-$ in the presence of oxygen. In addition, the detailed destruction mechanism of NO species by photocatalyst has been investigated by some researchers.[12,13] The characterization system in the present research was quite similar to that of the Japanese Industrial Standard, which was established on May 4, 2004.[14] In this JIS standard, it is recommended that the photocatalytic activity of the photocatalyst should be characterized by measuring the decrease in the concentration of NO at the outlet of a continuous reactor. In the presence of oxygen, the electrons in the conduction band are immediately trapped by the molecular oxygen to form $\cdot O^{2-}$, which can then generate active $\cdot OOH$ radicals. The nitrogen monoxide reacts with these reactive oxygen radicals, molecular oxygen, and very small amount of water in the air to produce HNO_2 and HNO_3.[15] As for UV, visible lights induced photocatalytic performance of (Yb,Er)-$NaYF_4$/C-TiO_2 composite, it was very similar to that of NIR

light induced activity. The only difference was that the irradiation light source for photocatalysis was not transferred from up-conversion phosphor but directly from the UV or visible light sources, and then the electron would be excited from the valence band of TiO_2 or C doped energy levels to the conduction band of TiO_2, eventually inducing the photocatalysis.[1]

3.1.2 Comprehensive study of B-UP/C-TiO_2, G-UP/C-TiO_2 and R-UP/C-TiO_2 composites

3.1.2.1 Experimental

3.1.2.1.1 Sample preparation

The blue, green and red colour emitting up-conversion phosphors coupled C-TiO_2 composites were prepared by a simple calcination assisted solvothermal method. The blue colour up-conversion phosphors, (Yb,Tm)-$NaYF_4$ (named B-UP), green colour one, (Yb, Er)-$NaYF_4$ (named G-UP), and red colour one, (Yb, Er)-Y_2O_3/YOF (named R-UP), used in this experiment were purchased from Shanghai Keyan Phosphor Technology Co., Ltd (China). These three commercial up-conversion phosphors were mixed with C-TiO_2 by a weight ratio of 1:1 and were denoted as (1:1) @B-UP/C-TiO_2, (1:1) G-UP/C-TiO_2 and (1:1) @R-UP/C-TiO_2, respectively. In a typical synthesis process of (1:1)@ B-UP/C-TiO_2 composite, after dispersing an appropriate amount of B-UP particles in 20 mL ethanol with continuous stirring for 60 min, 0.6 mL titanium tetra-n-butoxide was added dropwise with 30 min magnetic stirring. Subsequently, 10.5 mL ethanol/water (10:0.5) mixed solution was introduced dropwise, and the suspension solution was stirred for 60 min before transferring into a 100 mL Teflon-lined stainless steel autoclave and solvothermal treatment at 190^oC for 2 h. Finally, the products were recovered by centrifuge, followed by washing, drying and calcination at 265^oC for 1 h in an ambient condition. The uncoupled C-TiO_2 was fabricated without the addition of up-conversion phosphors. The composites of (1:1)

@G-UP/C-TiO_2, and (1:1) @R-UP/C-TiO_2 were also fabricated by similar process using corresponding up-conversion phosphors.

3.1.2.1.2 Photocatalytic activity tests

The photocatalytic activities of composites were investigated by evaluating the decomposition of NO_x ($deNO_x$) using a flow type reactor under irradiation of different wavelengths of LEDs and NIR laser at room temperature.

The photocatalytic activity of composites was also evaluated for the degradation of RhB solution under the irradiation of 980 nm NIR laser at the ambient temperature. After the addition of 0.10 g of sample powder into a 50 mL of 10^{-5} mol/L RhB solution, the solution was stirred for 2 h in the dark to reach the adsorption–desorption equilibrium of RhB prior to irradiation of the NIR laser. 5 mL suspensions were withdrawn at the desired illumination time intervals, and the particles were removed by centrifugation to monitor the concentration of RhB by recording the maximum absorbance of RhB at 553 nm with the UV-vis spectrohotometer.

3.1.2.2 Results and discussion

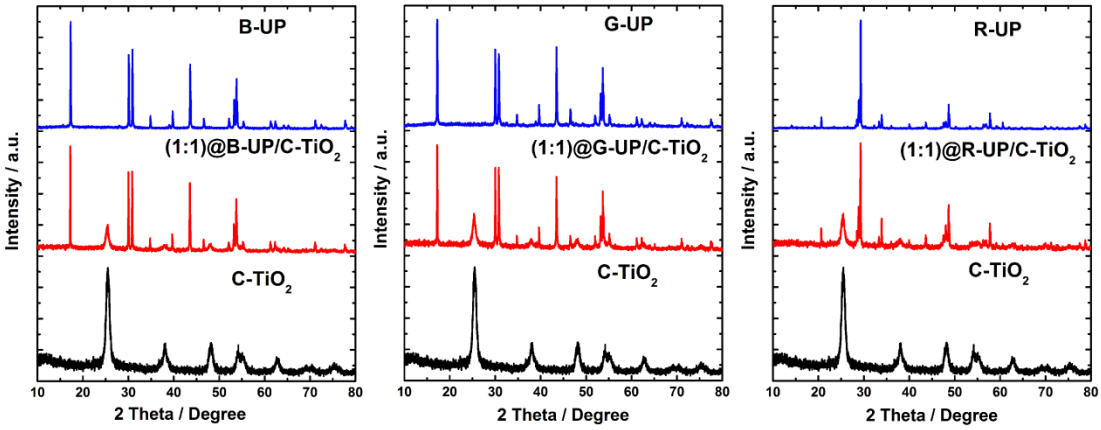

Figure 3-10. XRD patterns of C-TiO_2, B-UP, G-UP, R-UP and the composites of (1:1) @B-UP/C-TiO_2, (1:1) @ G-UP/C-TiO_2 and (1:1) @R-UP/C-TiO_2.

Figure 3-10 shows the XRD patterns of C-TiO_2, three kinds of commercial up-conversion phosphors and the corresponding composites. It could be obviously seen that C-TiO_2 presented the pure anatase phase (JCPDS file No. 21-1272) and no other impurity peaks or phases were observed. After coupling C-TiO_2 with B-UP, G-UP and R-UP by the solvothermal method, the diffraction peaks belonged to C-TiO_2 and various up-conversion phosphors were observed, implying that the composites had been successfully formed without changing the crystallinity of C-TiO_2 and commercial up-conversion phosphors. In addition, the C-TiO_2 possessed fine particle size of ca. 10 nm and large specific surface area of 124.3 m^2g^{-1}, which was much higher than that of P25 (50.2 m^2g^{-1}). After combining with B-UP, G-UP and R-UP, the specific surface areas of the composite decreased to about 66.7, 69.2 and 74.5 m^2g^{-1}, respectively, owing to the large particle size (about 2 μm in diameter) and small specific surface area of about several m^2g^{-1} of the up-conversion phosphors.

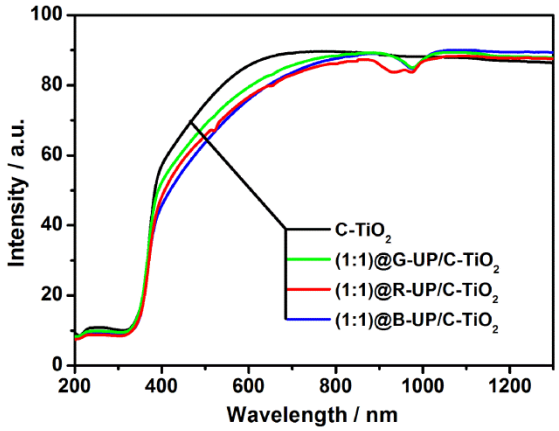

Figure 3-11. DRS of samples C-TiO_2, (1:1)@B-UP/C-TiO_2, (1:1)@G-UP/C-TiO_2 and (1:1) @R-UP/C-TiO_2.

The DRS of C-TiO_2 particle and (1:1)@B-UP/C-TiO_2, (1:1)@G-UP/C-TiO_2, (1:1) @R-UP/C-TiO_2 composites are illustrated in Fig. 3-11. It is explicit that C-TiO_2 presented nice UV and visible lights absorption but no NIR light absorption. When C-TiO_2 was combined with up-conversion phosphors, the composites not only displayed improved visible lights absorption up to 800 nm, covering the whole blue, green and red lights range, but also represented a small NIR light absorption band

around 980 nm. The increase in the visible light absorption might be owing to the increased C doping contents in TiO_2, and the absorption of NIR light might be corresponded to the absorption ability of Yb^{3+} ions in the up-conversion phosphors.[16,17] It means that the prepared composites can be excited by UV, visible and NIR lights simultaneously.

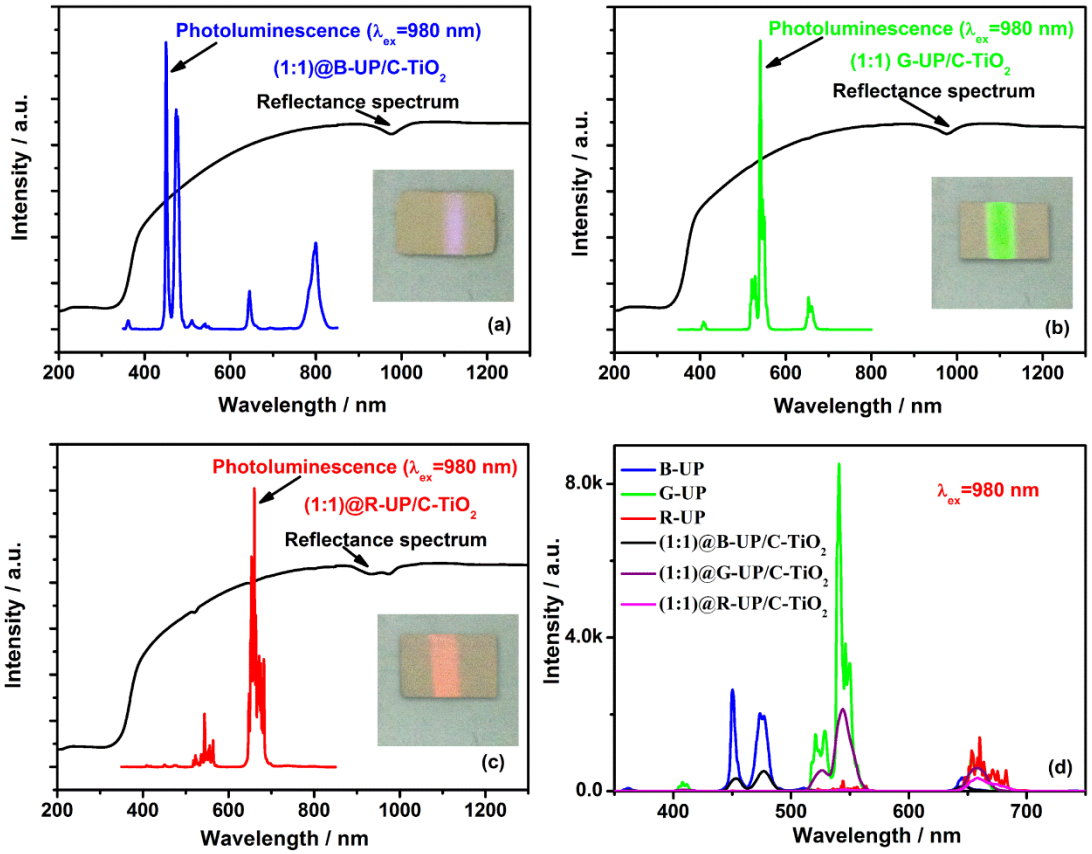

Figure 3-12. DRS, PL spectra and visual emitting map of composites (1:1) B-UP/C-TiO_2 (a), (1:1)@ G-UP/C-TiO_2 (b), (1:1)@R-UP/C-TiO_2 (c) and PL spectra of B-UP, G-UP, R-UP and three composites with the excitation of 980 nm (d).

Figure 3-12 represents the DRS, PL spectra, visual emitting map of three composites together with the PL spectra of up-conversion phosphors of B-UP, G-UP and R-UP monitored by 980 nm laser. It is obvious in Fig.3-12 (a)-(c) that (1:1)@B-UP/C-TiO_2, (1:1)@G-UP/C-TiO_2 and (1:1)@R-UP/C-TiO_2 composites displayed the good visual blue, green, red colour emissions, respectively, under the irradiation of 980 nm laser. Furthermore, the DRS and PL spectra of all composites demonstrated the nice overlap, indicating that the up-conversion emitted blue, green

and red lights could be well reabsorbed by the C-TiO_2 coexisted in the composite. Such reabsorption of up-conversion emitted lights by C-TiO_2 photocatalyst in composites could be confirmed by Fig.3-12 (d). The up-conversion phosphors, B-UP, G-UP and R-UP, revealed the high blue, green and red colour emission peaks situated at about 453, 538 and 662 nm, respectively, where the G-UP exhibited much stronger emission intensity than those of the B-UP and R-UP. After coupling with C-TiO_2, the intensity of up-conversion emission decreased dramatically, due to the absorption by C-TiO_2. The G-UP combined composite still displayed the strongest emission intensity among the three composites which well agreed with the visual emitting maps in Fig. 3-12 (a), (b) and (c). Compared with the emission intensity of uncoupled up-conversion phosphors, the intensity of blue colour emission in (1:1)@B-UP/C-TiO_2, green colour in (1:1)@G-UP/C-TiO_2 and red colour in (1:1)@R-UP/C-TiO_2 reduced about 89, 75 and 62%, respectively, mainly due to the reabsorption by C-TiO_2 in the composites.

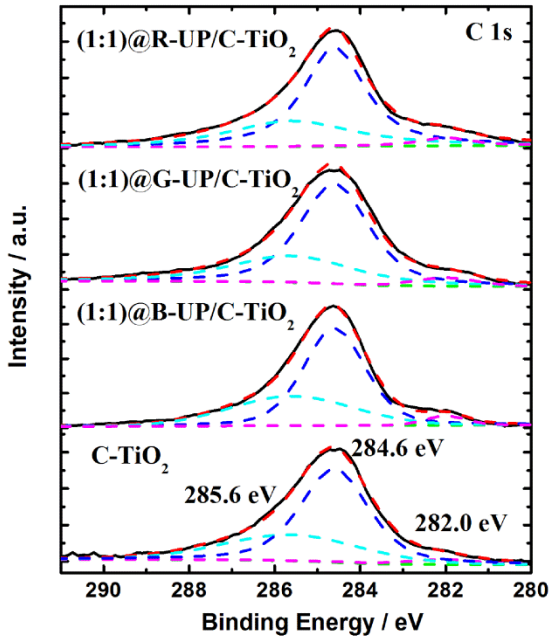

Figure 3-13. XPS profiles of C 1s for C-TiO_2, (1:1)@B-UP/C-TiO_2, (1:1)@G-UP/C-TiO_2 and (1:1) @R-UP/C-TiO_2.

The XPS analysis was also employed to check the status of C in the TiO_2 crystal. Fig. 3-13 exhibited the XPS profiles of C 1s for the C-TiO_2 particles,

(1:1)@B-UP/C-TiO_2, (1:1)@G-UP/C-TiO_2 and (1:1)@R-UP/C-TiO_2 composites after Ar^+ sputtering to clean the contamination on the surface of the samples. All samples presented three peaks located at 285.6, 284.6 and 282.0 eV, but the relative peak intensity was varied. The peak situated at 284.6 eV was belonged to the adventitious carbon species and the 285.6 eV peak was assigned to the elemental carbon which has the same binding energy as that of carbon in the graphite intercalation compound.[7] Furthermore, the peak lied at 282.0 eV was attributed to the binding energy of C-Ti bond, indicating that the C was doped into the TiO_2 crystal lattice by replacing the O site.[4] However, the relative peak intensities of 282.0 eV for these four samples were different, and the calculated contents of doped C in the samples, C-TiO_2 (1:1)@B-UP/C-TiO_2, (1:1)@G-UP/C-TiO_2 and (1:1)@R-UP/C-TiO_2 composites, were about 0.19, 0.26, 0.24 and 0.25 at.%, respectively. The doped C in the samples could introduce some impurity C energy levels into the position above the valence band of TiO_2, finally leading to the narrowed band gap and corresponding improved visible light absorption capability.

Figure 3-14 shows the deNO_x capability of C-TiO_2, (1:1)@B-UP/C-TiO_2, (1:1)@G-UP/C-TiO_2, (1:1)@R-UP/C-TiO_2 and commercial P25 under the excitation of different wavelengths of LED lights and 980 nm NIR laser. As seen in Fig 3-14 (a)-(c), it is evident that all uncoupled up-conversion phosphors displayed no obvious NO_x destruction capability regardless of the irradiation source due to the lager particle size and poor visible light absorption ability, while C-TiO_2 represented the nice deNO_x performance and about 6.2%, 23.2%, 28.3%, 32.9 % of NO gas were decomposed under the irradiation of LED lights of 627nm, 530nm, 445nm, 390 nm, respectively. As expected, there was no NIR light induced photocatalytic activity for C-TiO_2, because of non-absorption ability of C-TiO_2 in the NIR light range. When C-TiO_2 was coupled with up-conversion phosphors, the composites displayed deNO_x ability. More interesting, the composites showed much enhanced red light driven NO_x decomposition performance in compare with that of uncoupled C-TiO_2. This positive phenomenon was mainly attributed to the increased light absorption ability of C-TiO_2

in the range of visible light (shown in Fig. 3-11), due to the increased C doping content in TiO_2 after solvothermal coupling with up-conversion phosphors in comparison with that of pure C-TiO_2 as shown in Figs. 3-11 and 3-13.

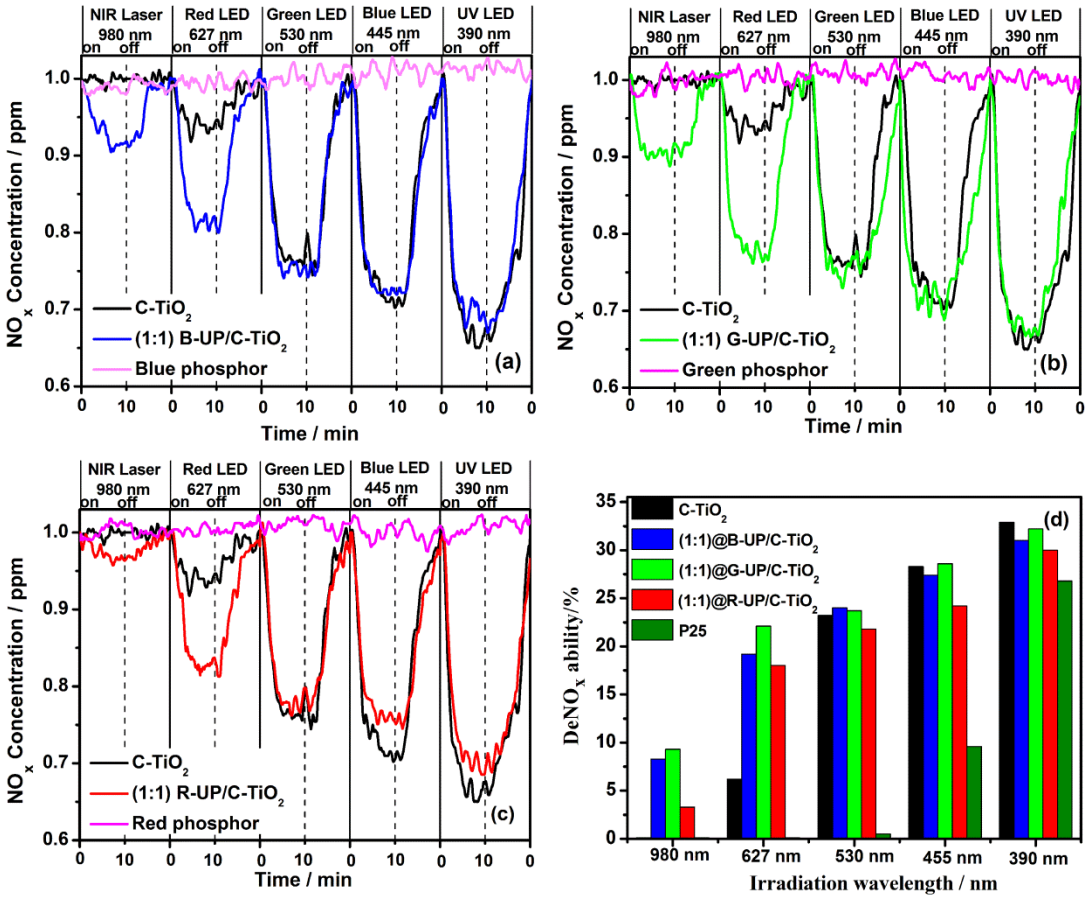

Figure 3-14. NO_x destruction activities of C-TiO_2, (1:1)@B-UP/C-TiO_2, (1:1)@G-UP/C-TiO_2, (1:1)@R-UP/C-TiO_2 and P25 under the irradiation of different wavelengths of lights.

The detailed reason for increased C doping content in TiO_2 after coupling with up-conversion phosphors was still unclear and would be our next work. With the increase of the whole range of visible light absorption capability for up-conversion phosphors coupled C-TiO_2, only red light induced photocatalytic performance was subsequently increased but no significant change for blue and green lights responsive ones. This abnormal result was probably assigned to the reason that the blue and green lights induced deNO_x ability of uncoupled C-TiO_2 was much higher than that of red light driven one. Although the blue, green and red lights absorption property of

up-conversion phosphors combined C-TiO_2 were all enhanced compared with that of uncoupled C-TiO_2, the blue and green lights induced deNO_x ability probably have almost arrived at its saturation and further increased light absorption ability to some extent would be not so effective for the deNO_x performance in contrast to that of poor red light responsive one. The corresponding NO gas degradation ability of the prepared samples and P25 are summarized in Fig. 3-14 (d). It could be explicitly seen that all samples exhibited excellent deNO_x performance superior to P25 even under the irradiation of UV light. In addition, the (1:1)@G-UP/C-TiO_2 composite emerged the best NIR light induced photocatalytic ability with about 9.3% of NO destruction, following by the (1:1)@B-UP/C-TiO_2 composite with 8.3% and (1:1)@R-UP/C-TiO_2 composite with 3.3%. The reason for the highest NIR light induced deNO_x ability of (1:1)@G-UP/C-TiO_2 composite might be discussed as follows.

Although the composites showed the higher blue light absorption ability than those of green and red lights (as seen in Fig. 3-11), the green colour emitting up-conversion phosphor, G-UP, displayed much stronger emission intensity compared with those of blue and red colours emitting up-conversion phosphors (as exhibited in Fig. 3-12 (d)) under the excitation of 980 nm NIR laser. Therefore, the amounts of green light photons generated by G-UP phosphor were much higher than those of blue and red lights photons by B-UP and R-UP phosphors, resulting in the highest photocatalytic activity of (1:1)@G-UP/C-TiO_2 composite. From these results, it may be concluded that the NIR light induced photocatalytic performance was introduced via an up-conversion of NIR light to blue, green or red lights, which are reabsorbed by C-TiO_2 for photocatalysis.

In order to further understand the UV, visible and NIR lights utilization efficiency in the composites, the apparent photonic efficiency (ξ_λ) of the samples were calculated according to the equation:[18,19]

$$\xi_\lambda = (F_{NO} * \alpha_\lambda)/(P_\lambda * S * A_\lambda) \qquad (3\text{-}1)$$

where λ indicates the wavelength of the used irradiation lights, F_{NO} (μmol s^{-1}) the flow quantity of NO molecules in the reaction gas, α_λ (%) the deNO_x ability of the

photocatalysts, P_λ (μmol m^{-2} s^{-1}) the photon number with the wavelength of light irradiated on the samples, S (m^2) the illuminated area and A_λ the absorption capability of sample at the irradiation wavelength. Taking NIR light induced deNO_x activity of (1:1)@G-UP/C-TiO_2 composite as an example, F_{NO} is 1.488*10^{-4} μmol s^{-1} (NO, 1 ppm, 200 mL/min), α_λ 9.3% (as shown in Fig. 3-14 (d)), P_λ 50.3 μmol m^{-2} s^{-1} and S 0.4*10^{-4} m^2 (as display in Table. S1), A_λ 15.3% was obtained from Fig. 3-12 (b). Under these conditions, the calculated $\xi_{980\ nm}$ was about 4.5% and all calculated ξ_λ for the samples C-TiO_2, (1:1)@B-UP/C-TiO_2, (1:1)@G-UP/C-TiO_2, (1:1)@R-UP/C-TiO_2 under the irradiation of different wavelengths of lights are summarized in Table 3-2.

Table 3-2. The calculated photonic efficiencies of the samples under the irradiation of different wavelengths of lights.

Photocatalyst	Photonic efficiency (%)				
	LED light 390 nm	LED light 445 nm	LED light 530 nm	LED light 627 nm	Infrared laser 980 nm
C-TiO_2	0.36	0.43	0.61	0.26	0
(1:1)@B-UP/C-TiO_2	0.28	0.32	0.40	0.47	3.83
(1:1)@G-UP/C-TiO_2	0.31	0.36	0.42	0.49	4.50
(1:1)@R-UP/C-TiO_2	0.28	0.30	0.37	0.42	1.61

It is apparent that the values of ξ_λ for the NIR light responsive deNO_x were excellent, being much higher than those under UV and visible lights irradiation. This high ξ_λ for NIR light irradiation should be related to the poor NIR light absorption ability of the composites and the low energy of NIR light in comparison with those of UV and visible lights. Moreover, the green colour emitting up-conversion phosphor combined C-TiO_2 composite still presented the best ξ_λ value among the three composites.

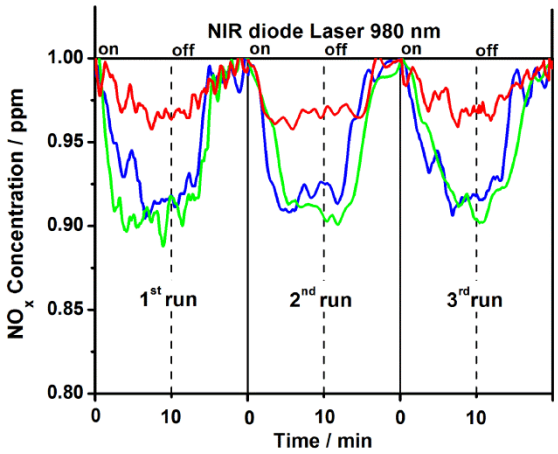

Figure 3-15. Multi-cycle tests of deNO$_x$ performance of (1:1)@B-UP/C-TiO$_2$, (1:1)@G-UP/C-TiO$_2$ and (1:1)@R-UP/C-TiO$_2$ composites under the irradiation of 980 nm light.

As well known, the photostability was also one of the key points for the practical application of photocatalysts. Fig. 3-15 shows the multi-cycles of deNO$_x$ performance of the three composites irradiated by NIR light. After three runs testing, the photocatalytic activity of three composites did not change obviously, implying the good photostability of the up-conversion phosphors combined C-TiO$_2$ composites.

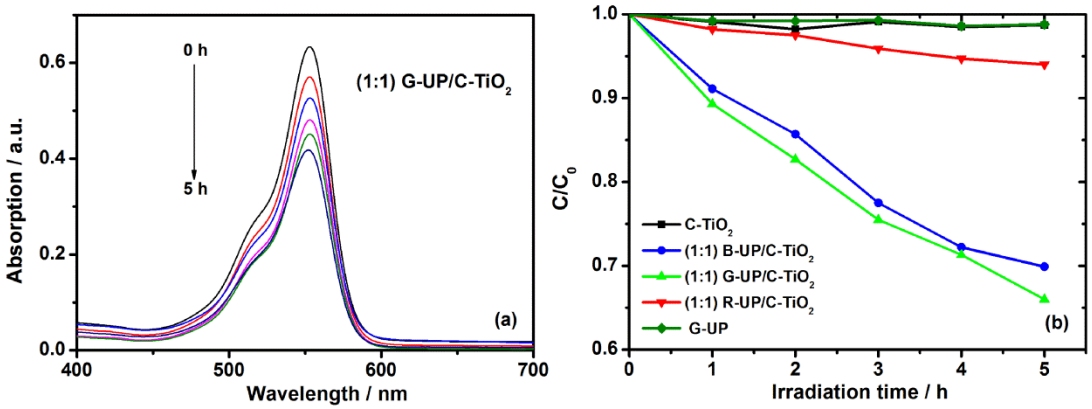

Figure 3-16. Time change in the absorbance of RhB aqueous solution in the presence of (1:1)@G-UP/C-TiO$_2$ composite (a) and RhB degradation performance of C-TiO$_2$, (1:1)@B-UP/C-TiO$_2$, (1:1)@G-UP/C-TiO$_2$, (1:1)@R-UP/C-TiO$_2$ and G-UP (b) under the irradiation of 980 nm infrared laser.

The degradation of RhB dye was also employed to evaluate the photocatalytic activity of samples in the solution system. Fig. 3-16 shows the RhB degradation

capability of the samples under the irradiation of 980 nm infrared laser. All composites exhibited excellent NIR light induced RhB degradation activity, although uncoupled G-UP and C-TiO_2 showed no destruction ability. Additionally, the (1:1)@G-UP/C-TiO_2 represented the best RhB decomposition performance similar to that of deNO_x activity, following by (1:1)@B-UP/C-TiO_2 and (1:1)@R-UP/C-TiO_2 composites. Therefore, the up-conversion phosphors coupled C-TiO_2 composites possessed photocatalytic activities for not only destruction of NO_x gas but also dye degradation in the solution under NIR lights irradiation.

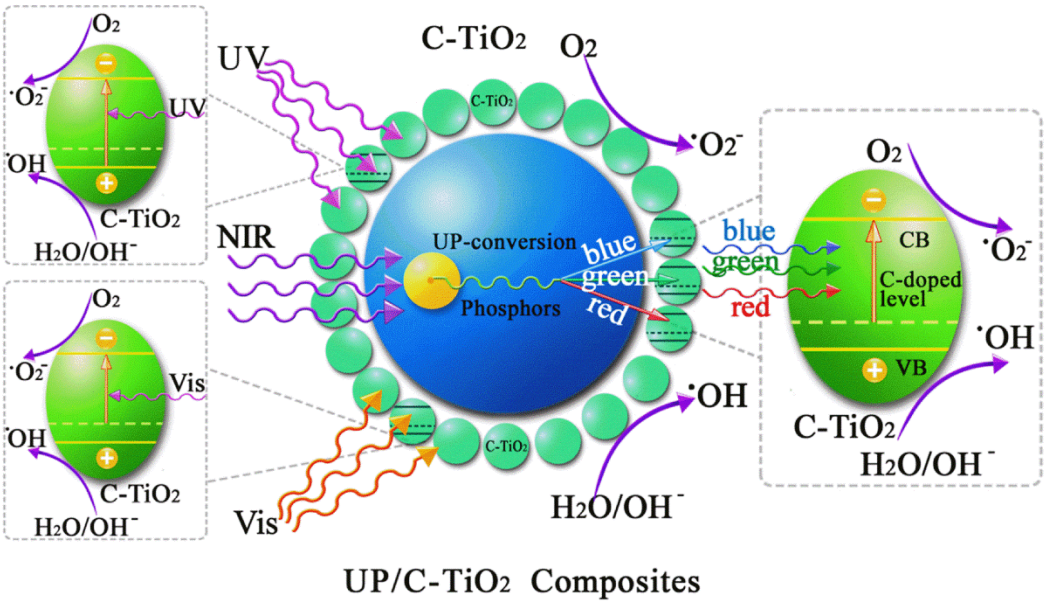

Figure 3-17. The possible mechanism of UV, visible and NIR lights induced photocatalysis of up-conversion phosphors coupled C-TiO_2 composites.

Figure 3-17 shows the possible mechanism of UV, visible and NIR lights responsive photocatalysis of the up-conversion phosphors coupled C-TiO_2 composites. It is well acknowledged that the function of up-conversion phosphors is to transfer the long wavelength of light (NIR light) to the short wavelength of light (UV, blue, green, red lights, etc.), achieving anti-stokes shift by a multi-photon mechanism.[11] When a NIR lights are irradiated to the present composites, the up-conversion phosphor would be excited, and then blue, green or red lights are emitted. The emitted visible lights

could be absorbed by the C-TiO_2 in the composites, owing to the narrowed band gap of C-TiO_2 by C doping in the O site of TiO_2 lattice (as shown in Fig. 3-12).

In this case, the electron could be excited from the C doped levels to the conduction band of C-TiO_2. The photogenerated hole in the valence band would be further trapped by water and adsorbed OH^- species in the air to produce hydroxyl radicals •OH. In addition, the photoexcited electron in the conduction band would also react with adsorbed oxygen to generate $•O_2^-$. Finally, the target nitrogen monoxide could be oxidized by these reactive oxygen radicals, hydroxyl radicals, molecular oxygen, and water in the air to produce HNO_2 and HNO_3. These reaction processes have been investigated by many researchers as presented in the following equations:[20,21]

$$NO + 2•OH \rightarrow NO_2 + H_2O \quad (3\text{-}2)$$

$$NO_2 + •OH \rightarrow NO_3^- + H^+ \quad (3\text{-}3)$$

$$NO_x + •O_2^- \rightarrow NO_3^- \quad (3\text{-}4)$$

$$NO + NO_2 + H_2O \rightarrow 2HNO_2 \quad (3\text{-}5)$$

As for UV and visible lights irradiation, these two lights could be directly absorbed by C-TiO_2 in the composites to take place the photocatalytic reaction. Therefore, the up-conversion phosphors coupled C-TiO_2 composites fabricated in the present work was feasible to be excited by UV, visible and NIR lights simultaneously, finally producing corresponding high performance of photocatalytic activities.[2]

3.2 Preparation of visible and NIR lights responsive up-conversion phosphors coupled BiOBr composites

3.2.1 Introduction

As mentioned in Chapter 2, the BiOBr as a promising photocatalyst still presents limited visible light absorption capability as a result of the relatively wide band gap (ca. 2.8 eV, 443 nm), which only accounts for small part of the visible light range. Furthermore, to the best of our knowledge, up to now, there is no research about the

NIR light induced photocatalytic activity of BiOBr.

Therefore, in this section, novel up-conversion phosphors (B-UP and G-UP) coupled BiOBr composites have been proposed to develop UV, visible and NIR lights driven photocatalytic activity simultaneously.

3.2.2 Experimental

3.2.2.1 Sample preparation

Series of up-conversion phosphors coupled BiOBr composites have been synthesized by a simple room temperature method. To begin with, 0.8 mmol $Bi(NO_3)_3 \cdot 5H_2O$ in 30 mL of distilled water/glycerol mixed solution with sonication for 10 min, meanwhile 0.8 mmol KBr and 0.24 g up-conversion phosphor (Yb, Tm-$NaYF_4$ (B-UP) or Yb, Er-$NaYF_4$ (G-UP)) were dispersed in another 30 mL of distilled water. After that, the $Bi(NO_3)_3 \cdot 5H_2O$ glycerol aqueous solution was dropwise added into the KBr and up-conversion phosphors mixed aqueous solution with vigorous stirring. The as-mixed solution was magnetically stirred for 1 h before aging for 3 h at room temperature. Finally, the product was centrifuged and washed with distilled water and ethanol four times, respectively, followed by drying in a vacuum oven at 60^oC overnight. The composite, consisted of B-UP and BiOBr, was denoted as B-UP/BiOBr-G20, and the one, be composed of G-UP and BiOBr, was designated as G-UP/BiOBr-G20. In addition, for comparison, the composites B-UP/BiOBr-G0 and G-UP/BiOBr-G0 were also prepared by using distilled water as reaction solution instead of glycerol mixed solution.

3.2.2.2 Photocatalytic activity tests

The photocatalytic activities of samples were evaluated by the decomposition of NO ($deNO_x$) using a flow type reactor under irradiation of a 450 W high pressure mercury lamp and 980 nm NIR laser at room temperature.

3.2.3 Results and discussion

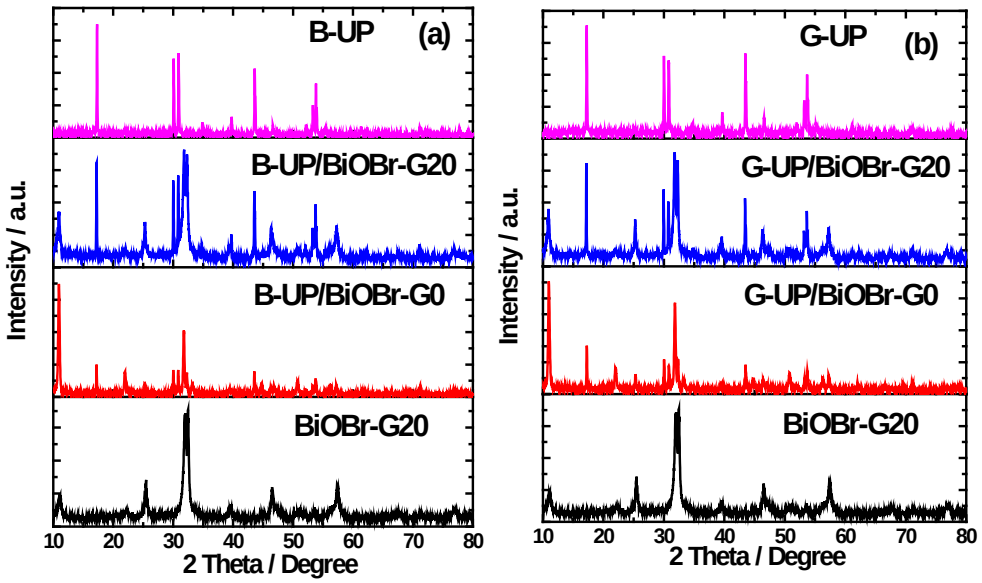

Figure 3-18. XRD patterns of B-UP, B-UP/BiOBr-G20, B-UP/BiOBr-G0 and BiOBr-G20 (a) and G-UP, G-UP/BiOBr-G20, G-UP/BiOBr-G0 and BiOBr-G20 (b).

Fig. 3-18 shows the XRD patterns of up-conversion phosphors and corresponding composites with BiOBr-G0 and BiOBr-G20 prepared by different solvents. The composites exhibited all diffraction peaks belonged to B-UP, G-UP, and BiOBr. Moreover, no other impurity peaks were observed, indicating that the up-conversion phosphors coupled BiOBr composites had been successfully prepared at room temperature.

The TEM images of BiOBr-G20, G-UP/BiOBr-G0 and G-UP/BiOBr-G20 are displayed in Fig. 3-19. It could be clearly seen that the BiOBr-G20 presented the 3D nanostructure assembled consited of nanoparticles with the specific surface area of 39.3 m^2g^{-1}, which is much larger than most of reported BiOBr particles.[22,23] While as the BiOBr-G20 was combined with G-UP to form a composite, the surface of large particle of G-UP was covered with the nanoparticles of BiOBr-G20 instead of 3D nanostructure. In contrast, when BiOBr-G0 was used to combine with G-UP, the plate-like particles of BiOBr-G0 surrounded the large particle of G-UP without change in the shape of original BiOBi-G0, implying that the apparent connection

between BiOBr-G20 and G-UP was much better than that of BiOBr-G0 and G-UP.

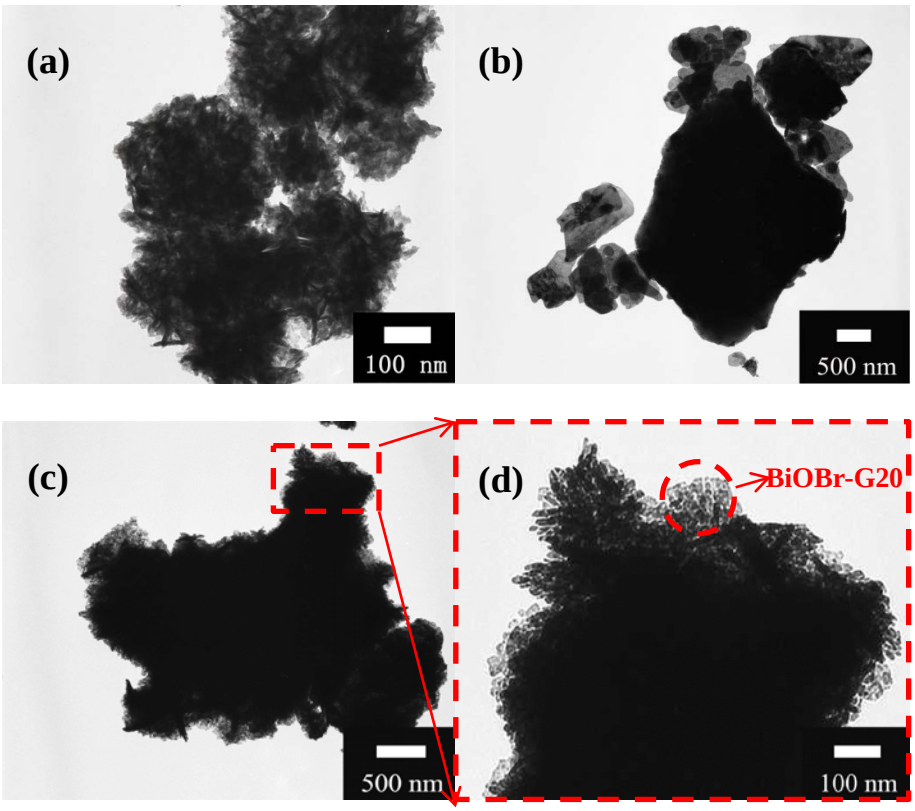

Figure 3-19. TEM images of BiOBr-G20 (a), G-UP/BiOBr-G0 (b), G-UP/BiOBr-G20 (c) and enlarged area for red square in (c) (d).

The corresponding DRS and PL spectra of samples are illustrated in Fig. 3-20. In Fig. 3-20 (a), it is explicit that all samples showed relatively nice visible light absorption capability. Nevertheless, the B-UP/BiOBr-G0 composite demonstrated better visible light-harvesting property in the whole visible light range, but weaker UV light absorption ability than those of B-UP/BiOBr-G20, which should be owing to the difference of particle morphology as explained in Chapter 2. More interesting, B-UP/BiOBr-G20 presented visible light absorption capability superior to uncoupled BiOBr-G20. This phenomenon was probably ascribed to the positive effect of up-conversion phosphor on the increment of oxygen vacancy in the BiOBr crystal in the presence of glycerol.

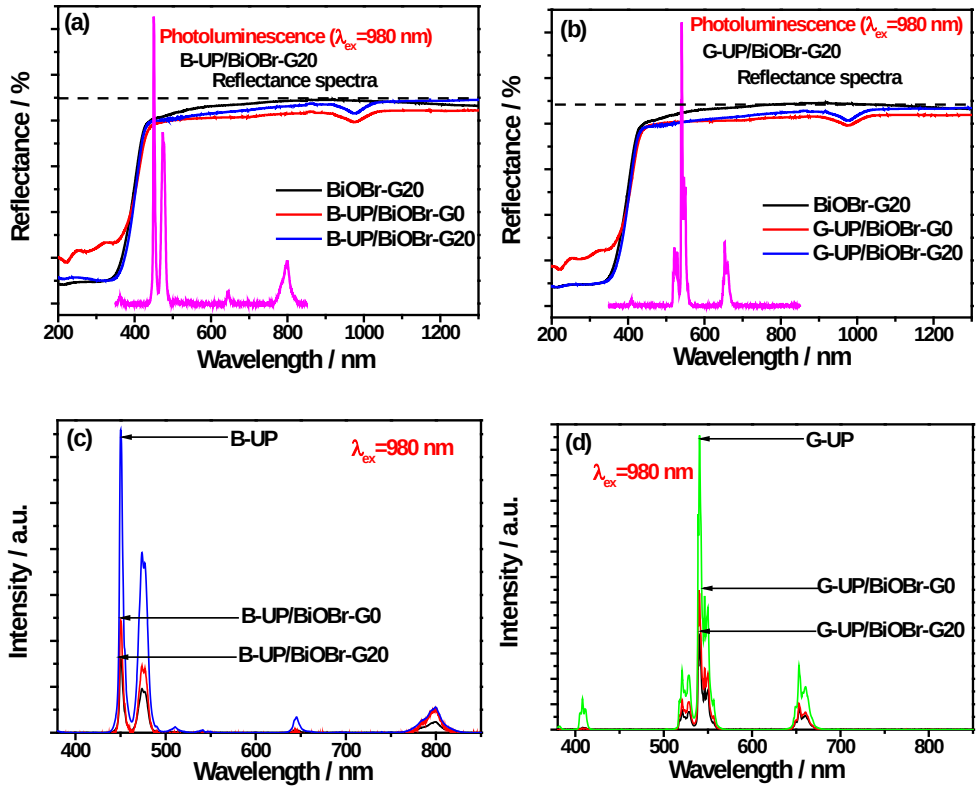

Figure 3-20. DRS of BiOBr-G20, B-UP/BiOBr-G0, B-UP/BiOBr-G20 and photoluminescence spectra (PL) of B-UP/BiOBr-G20 with the excitation of 980 nm (a), BiOBr-G20, G-UP/BiOBr-G0, G-UP/BiOBr-G20 and PL of G-UP/BiOBr-G20 with the excitation of 980 nm (b), PL of B-UP, B-UP/BiOBr-G0, B-UP/BiOBr-G20 with the excitation of 980 nm (c) and PL of G-UP, G-UP/BiOBr-G0, G-UP/BiOBr-G20 with the excitation of 980 nm (d).

In addition, the reflectance spectra of composite showed a nice overlap with the emission spectra of composite with the excitation of 980 nm, meaning that the emitted blue light from B-UP could be reabsorbed by composite again under the induction of 980 nm. This phenomenon could be directly observed in Fig. 3-20 (c). With the excitation by 980 nm laser, the B-UP/BiOBr-G20 presented much lower emission intensity than that of pure up-conversion phosphor, B-UP, and even that of B-UP/BiOBr-G0 which may be due to the better contact between B-UP and BiOBr-G20 in comparison of that of B-UP and BiOBr-G0 as well as the better visible light absorption ability of BiOBr-G20.

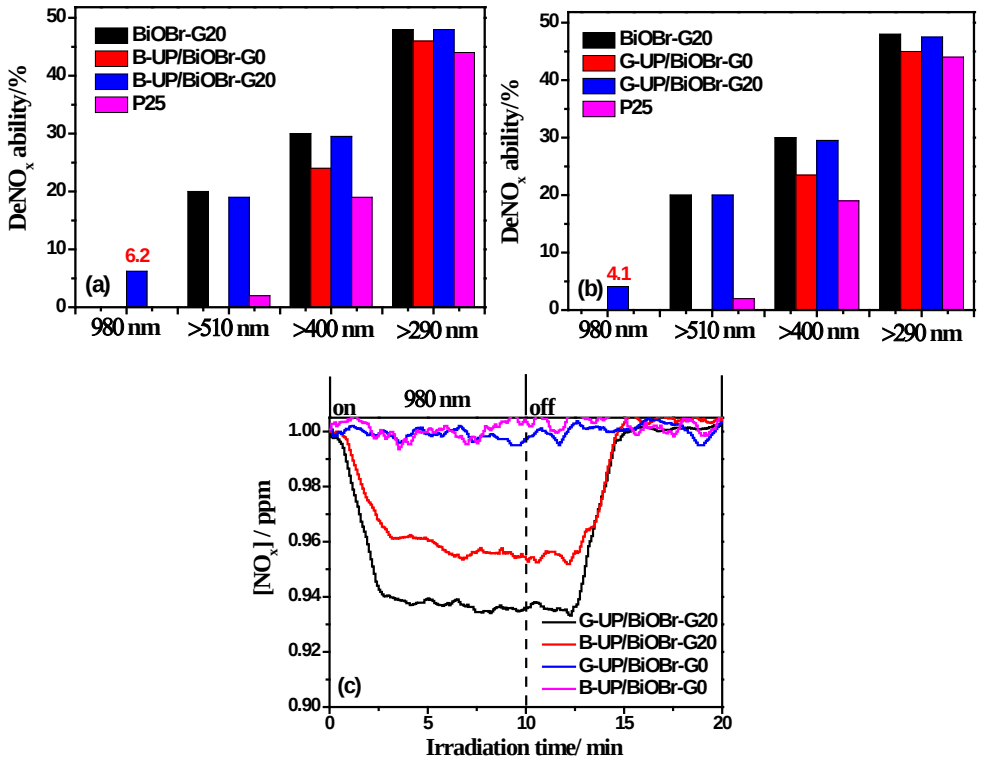

Figure 3-21. DeNO$_x$ ability of BiOBr-G20, B-UP/BiOBr-G0, B-UP/BiOBr-G20, P25 (a), BiOBr-G20, G-UP/BiOBr-G0, G-UP/BiOBr-G20, P25 (b) under the irradiation of different wavelengths of lights and the time dependence of NO$_x$ destruction activity of samples excited by 980 nm laser (c).

The destruction ability of continuous NO gas was employed to evaluate the photocatalytic activity of sample under the irradiation of UV, visible and NIR lights. Fig. 3-21 shows the deNO$_x$ ability of samples and corresponding time dependence of photocatalytic activity in the induction of NIR light. In Fig. 3-21 (a) and (c), it coud be observed that after combining B-UP with BiOBr-G20, the composite presented nice UV and visible light responsive deNO$_x$ ability as strong as the uncoupled BiOBr-G20, indicating the addition of B-UP was not detriment for the photocatalytic property of BiOBr-G20. More importantly, the composite exhibited good NIR light induced deNO$_x$ ability about 6.2%. In contrast, when the up-conversion phosphor was combined with BiOBr-G0, no NIR light driven photo-activity was appeared. It should be owing to the poor visible light induced photocatalytic activity of BiOBr-G0 as presented in Chapter 2. This phenomenon further confirmed that the photocatalyst

component in composite should have high efficiency of photocatalytic activity in the range of up-conversion phosphor emitted light under the excitation of NIR light. As for G-UP/BiOBr-G20 composite in Fig. 3-21 (b), the composite also represented similar excellent UV, visible light induced photocatalytic activity and also nice NIR light induced one about 4.1%. Therefore, based on the above discussion, it could be learned that the BiOBr based composite had been successfully developed for UV, visible and NIR light induced photocatalytic activity simultaneously at room temperature. Additionally, as the BiOBr-G20 coupled with B-UP, the composite showed the optimal NIR light responsive photocatalytic activity.

3.3 Conclusions for Chapter 3

Preparation of visible and NIR lights induced TiO_2 based composites

Firstly, a green light emitting up-conversion phosphor coupled C-TiO_2 composite was prepared by a facile solvothermal method in the help of calcination. Owing to the nice overlap between the emission spectra of up-conversion phosphor component and the absorption spectra of C-TiO_2, the composite not only could be excited by UV and visible lights, but also was active for NIR light. Eventually, the composite presented much enhanced UV, visible and NIR light responsive photocatalytic activity simultaneously. On the other hand, various color emitting up-conversion phosphors (blue, green and red light emitting ones) combined C-TiO_2 composites were also synthesized. Due to the highest up-conversion efficiency of green light emitting up-conversion phosphors compared with those of blue and red ones, the green up-conversion phosphors coupled C-TiO_2 composite presented the best UV, visible and NIR light driven photocatalytic activity. Furthermore, it was found that the NIR light induced photocatalytic property revealed apparent quantum efficiency much superior to UV and visible lights induced ones.

Preparation of visible and NIR lights responsive up-conversion

phosphors coupled BiOBr composites

Through coupling the high efficiency of up-conversion phosphors with BiOBr-G20, the composite exhibited outstanding visible and NIR lights induced photocatalytic activity, which was prepared by a facile room temperature method using distilled water and glycerol mixed solution as a solvent. More importantly, the addition of up-conversion phosphor was not disadvantage for the original UV and visible lights responsive photocatalytic activity of uncoupled BiOBr-G20.

3.4 References

1. X. Y. Wu, S. Yin, Q. Dong, B. Liu, Y. H. Wang, T. Sekino, S. W. Lee, T. Sato, Sci. Rep. **2013**, 3, 2918.
2. X. Y. Wu, S. Yin, Q. Dong, B. Liu, T. Sato, Appl. Catal. B: Environ. **2014**, 156-157:257-264.
3. S. Yin, Y. Aita, M. Komatsu, J. S. Wang, Q. Tang, T. Sato, J. Mater. Chem. **2005**, 15, 674-682.
4. C. D. Valentin, Chem. Mater. **2005**, 17, 6656-6665.
5. G. Boulon, A. Collombet, A. Brenier, M. T. Cohen-Adad, A. Yoshikawa, K. Lebbou, J. H. Lee, T. Fukuda, Adv. Funct. Mater. **2001**, 11, 263-270.
6. J. H. Zeng, J. Su, Z. H. Li, R. X. Yan, Y. D. Li, Adv. Mater. **2005**, 17, 2119-2123.
7. B. Neumann, P. Bogdanoff, H. Tributsch, S. Sakthivel, H. Kisch, J. Phys. Chem. B **2005**, 109, 16579-16586.
8. S. F. Chen, X. L. Yu, W. Liu, ECS Trans. **2009**, 21, 3-22.
9. Y. L. Dai, P. A. Ma, Z. Y. Cheng, X. J. Kang, X. Zhang, Z. Y. Hou, C. X. Li, D. M. Yang, X. F. Zhai, J. Lin, ACS Nano. **2012**, 6, 3327-3338.
10. X. J. Kang, Z. Y.Cheng, C. X. Li, D. M. Yang, M. M. Shang, P. A. Ma, G. G. Li, N. Liu, J. Lin, J. Phys. Chem. C **2011**, 115, 15801-15811.
11. J. C. Boyer, F. Van Veggel, Nanoscale **2010**, 2, 1417-1419.
12. M. R. Hoffmann, S. T. Martin, W. Choi, D. W. Bahnemann, Chem. Rev. **1995**, 95, 69-96.
13. T. Sato, P. Zhang, S. Yin, Progress Cryst. Growth Character. Mater. **2012**, 58, 92-105.

14. Japanese Industrial Standard [JIS R 1701-1:2004(J)], Test method for air purification performance of photocatalytic materials – Part 1: Removal of nitric oxide, Japanese Standards Association, established on 2004-01-20.
15. J. S. Dalton, P. A. Janes, N. G. Jones, J. A. Nicholson, K. R. Hallam,G. C. Allen, Environ. Pollut. **2002**, 120, 415-422.
16. S. Heer, K. Kompe, H. U. Gudel, M. Haase, Adv. Mater. **2004**, 16, 2102-2105.
17. Y. J. Sun, Y. Chen, L. J. Tian, Y. Yu, X. G. Kong, J. W. Zhao, H. Zhang, Nanotechnology, **2007**, 18, 275609-275617.
18. H. H. Li, S. Yin, Y. H. Wang, T. Sato, J. Catal. **2012**, 286, 273-278.
19. S. Obregón, A. Kubacka, M. Fernández-García, G. Colón, J. Catal. **2013**, 299, 298-306.
20. Y. Ohko, Y. Nakamura, A. Fukuda, S. Matsuzawa, K. Takeuchi, J. Phys. Chem. C **2008**, 112, 10502-10508.
21. R. Quesada-Cabrera, A. Mills, C. O'Rourke, Appl. Catal. B: Environ. **2014**, 150-151, 338-344.
22. W. D. Zhang, Q. Zhang, F. Dong, Ind. Eng. Chem. Res. **2013**, 52, 6740-6746.
23. G. Cheng, J. Y. Xiong, F. J. Stadler, New J. Chem. **2013**, 37, 3207-3213.

Chapter 4 SUMMARY AND CONCLUSIONS

Chapter 1 introduced the applications and mechanism of photocatalysis. In particular, three promising photocatalysts, TiO_2, $NaTaO_3$ and BiOX (X=Cl, Br, I), have been highlighted for their merits and demerits. In order to improve the photocatalytic activity of them, a brief review was presented for the potential and frequently used strategies. Finally, the thesis target was proposed.

Chapter 2 presented the preparation of C doped, C and Nd codoped, C and W codoped TiO_2 nanoparticles as well as C doped TiO_2 powder with multi-phases. They presented visible light induced photocatalytic activity owing to the narrowed band gap, enlarged specific surface area and considerably suppressed recombination rate of photogenerated electron and hole pairs. In particular, the C and Nd codoped TiO_2 samples presented the most excellent visible light induced photocatalytic activity. Meanwhile, the W solely doped TiO_2 samples not only presented relatively nice photocatalysis but also exhibited excellent infrared light absorption capability owing to the existence of reduced W^{5+} ions. In addition, we also synthesized excellent visible light active C doped $NaTaO_3$ powder. The enhanced visible light responsive photocatalytic activity was induced by C doping in the presence of ethylene glycol (EG). In order to suppress the separation ability of charge carriers, a novel C-$NaTaO_3$/Cl-TiO_2 composite was proposed, which presented significantly improved visible light responsive photocatalytic activity owing to the synergetic effect between C-$NaTaO_3$ and Cl-TiO_2. Besides, the nanosized C modified $NaTaO_3$ mesocrystals were prepared by a facile one-pot solvothermal method in the presence of glucose by an oriented attachment mechanism. The C was existed as carbonaceous materials on the surface of $NaTaO_3$ mesocrystal instead of dopant in the lattice, which induced the excellent visible light absorption capability. Due to the outstanding visible light-harvesting ability and peculiar large specific surface area, the C modified

$NaTaO_3$ mesocrystals revealed high efficiency of visible light induced photocatalytic property, much superior to those of pure $NaTaO_3$ nanoparticles and also commercial P25. Finally, we also fabricated visible light responsive glycerol modified BiOX (X=Cl, Br, I) 3D nanostructures with large specific surface area at room temperature. The increased visible light absorption capability of the sample should be owing to the increment of oxygen vacancies in the crystal in the presence of glycerol in the reaction solution. The glycerol modified BiOCl and BiOBr presented excellent visible light induced deNO_x ability superior to P25.

Chapter 3 presented the development of a novel composite, consisting of high efficiency of up-conversion phosphors and effective photocatalysts substances, to achieve UV, visible and NIR lights induced photocatalytic activity. On one hand, various color-emitting up-conversion phosphors (blue, green, red ones denoted as B-UP, G-UP and R-UP, respectively.) were employed to couple with C-TiO_2 to form composites. All samples displayed outstanding UV, visible and NIR lights driven deNO_x ability. Furthermore, the calculated quantum efficiency for photocatalytic activity confirmed that the composite, consisted of G-UP and C-TiO_2 with 1:1 weight ratio, showed the best NIR light induced photocatalytic activity, and the NIR light indused photocatalyti deNO_x presented the higher quantum efficiency compared with UV and visible lights indused ones. On the other hand, after combining up-conversion phosphors with BiOBr prepared in the glycerol and distilled water mixed solution, the composites also represented nice UV, visible and NIR light induced photocatalytic activity. More importantly, the addition of up-conversion phosphors was not negative in the UV and visible lights induced photocatalytic property of BiOBr. B-UP/BiOBr composite exhibited the best UV, visible and NIR lights responsive deNO_x photocatalysis in the present study.

PUBLICATIONS

1. Xiaoyong Wu, Shu Yin, Bin Liu, Makoto Kobayashi, Masato Kakihana, Tsugio Sato, "A Carbon Modified $NaTaO_3$ Mesocrystal Nanoparticle with Excellent Efficiency of Visible Light Induced Photocatalysis", *J. Mater. Chem. A*, **2014**, 2014, 2, 20832-20840.
2. Xiaoyong Wu, Shu Yin, Qiang Dong, Bing Liu, Tsugio Sato, "Photocatalytic performance and near infrared absorption property of tungsten and tungsten-carbon doped titania", *Materials Technology: Advanced Functional Materials*, **2014**, 29, A20-A29.
3. Xiaoyong Wu, Shu Yin, Qiang Dong, Bing Liu, Tsugio Sato, "Blue/green/red colour emitting up-conversion phosphors coupled C-TiO_2 composites with UV, visible and NIR responsive photocatalytic performance". *Appl. Catal. B: Environ.*, **2014**, 156-157:257-264.
4. Xiaoyong Wu, Shu Yin, Qiang Dong, Bin Liu, Yuhua Wang, Tohru Sekino, Soo Wohn Lee, Tsugio Sato, "UV, visible and near-infrared lights induced NO_x destruction activity of (Yb,Er)-$NaYF_4$/C-TiO_2 composite", *Sci. Rep.*, **2013**, 3, 2918.
5. Xiaoyong Wu, Shu Yin, Qiang Dong, Tsugio Sato, "Preparation and visible light induced photocatalytic activity of C-$NaTaO_3$ and C-$NaTaO_3$-Cl-TiO_2 composite", *Phys. Chem. Chem. Phys.*, **2013**, 15, 20633-20640.
6. Xiaoyong Wu, Shu Yin, Qiang Dong, Chongshen Guo, Huihui Li, Takeshi Kimura, Tsugio Sato, "Synthesis of high visible light active carbon doped TiO_2 photocatalyst by a facile calcination assisted solvothermal method", *Appl. Catal. B: Environ.*, **2013**, 142-143, 450-457.
7. Xiaoyong Wu, Shu Yin, Qiang Dong, Chongshen Guo, Takeshi Kimura, Tsugio Sato, "Photocatalytic Properties of Nd and C Codoped TiO_2 with the Whole Range of Visible Light Absorption", *J. Phys. Chem. C*, **2013**, 117, 8345-8352.
8. Xiaoyong Wu, Shu Yin, Bing Liu, Tsugio Sato, "Simple room-temperature

synthesis of long visible light responsive carbon modified BiOX (X=Cl, Br, I) mesoporous", Submitted.

9. Chongshen Guo, Xiaoyong Wu, Mei Yan, Qiang Dong, Shu Yin, Tsugio Sato and Shaoqin Liu, "The visible-light driven photocatalytic destruction of NO_x using mesoporous TiO_2 spheres synthesized via a "water-controlled release process", *Nanoscale*, **2013**,5, 8184-8191.
10. Qiang Dong, Shu Yin, Chongshen Guo, Xiaoyong Wu, Takeshi Kimura, Thihang Le, Taro Sakanakura, Tsugio Sato, "Cobalt doped ceria-zirconia supported paradium-alumina catalyst with high oxygen storage capacity for CO oxidation", *Mater. Sci. Eng.*, **2013**, 47, 012065.
11. Qiang Dong, Shu Yin, Chongshen Guo, Xiaoyong Wu, Nobuhiro Kumada, Takahiro Takei, Akira Miura, Yoshinori Yonesaki, Tsugio Sato, "Single-crystalline porous NiO nanosheets prepared from β-$Ni(OH)_2$ nanosheets: Magnetic property and photocatalytic activity", *Appl. Catal. B: Environ.*, **2014**, 147:741-747.
12. M. Sarkarat, S. Komarneni, Z. Rezvani, Xiaoyong Wu, Shu Yin TsugioSato, Zi-Feng Yan, "Multi-cationic layered double hydroxides: Calcined products as photocatalysts for decomposition of NO_x", *Appl. Catal. B: Environ.*, **2013**, 80-81:390-397.
13. Qiang Dong, Shu Yin, Chongshen Guo, Xiaoyong Wu, Takeshi Kimura, Tsugio Sato, "Aluminium doped ceria-zirconia supported palladium-alumina catalyst with high oxygen storage capacity and CO oxidation activity", *Mater. Res. Bull*, **2013**, 48:4989-4992.
14. Chongshen Guo, Shu Yin, Qiang Dong, Takeshi Kimura, Miyuki Tanaka, Le Thi Hang, Xiaoyong Wu, Tsugio Sato, "Solvothermal fabrication of rubidium tungsten bronze for the absorption of near infrared light.", *J. Nanosci. Nanotechnol.***, 2013**, 13:3236-3239.
15. Takeshi Kimura, Shu Yin, Qiang Dong, Xiaoyong Wu, Ryusuke Akita, Takatoshi Hashimoto, Atsushi Sasaki, Shuji Aisawa, Tsugio Sato, "Synthesis and electrical

properties of $(1-x)(Na_{0.5}Bi_{0.5})TiO_{3-x}Ba(Mg_{0.5}W_{0.5})O_3$ piezoelectric ceramics", *J. Asian Cerem. Soc.*, **2014**, 2: 20-26.

16. Bin Liu, Shu Yin, Yuhua Wang, Chongshen Guo, Xiaoyong Wu, Qiang Dong, Makoto Kobayashi, Masato Kakihina, Tsugio Sato, "A facile one-step solvothermal synthesis and electrical properties of reduced graphene oxide/rod-shaped potassium tungsten bronze nanocomposite", *J. Nanosci. Nanotechnol.* **2015**, 15, 1-6.

CONFERENCES

1. Xiaoyong Wu, Qiang Dong, Shu Yin, Tsugio Sato, “Synthesis and Visible Light Induced Photocatalytic Activities of $BiVO_4$ with Different Crystalline Phases. ”, Summer school of Tohoku University, Sendai, Aug. 21, **2012**.
2. Xiaoyong Wu, Shu Yin, Qiang Dong, Tsugio Sato, “Preparation and Photocatalystic Properties of $BiVO_4$/B-TiO_2 Composite.”, 平成 24 年度化学系学協会東北大会, Akita, Sep. 15, **2012**.
3. Xiaoyong Wu, Shu Yin, Qiang Dong, Tsugio Sato, “Synthesis and Visible Light Induced Photocatalytic Activities of $BiVO_4$ with Different Crystalline Phases.”, 平成 24 年度日本セラミックス協会, Nagoya, Sep. 19, **2012**.
4. Xiaoyong Wu, Shu Yin, Qiang Dong, Tsugio Sato, “High Visible Light Photocatalytic Activities of Carbon Doped TiO_2 Prepared by a Facile Calcination Assisted Solvothermal Method”, 第 51 回セラミックス基礎科学討論会, Sendai, Jan. 9, **2013**.
5. Xiaoyong Wu, Shu Yin, Qiang Dong, Tsugio Sato, “Visible Light Induced Photocatalytic Activities of C-TiO_2”, 東北大学研究所連携プロジェクト 2012, Sendai, Feb. 5, **2013**.
6. Xiaoyong Wu, Shu Yin, Qiang Dong, Tsugio Sato, “Photocatalytic Properties of Nd-C-TiO_2 in the Whole Visible Light Range.”, 平成 24 年度日本セラミックス協会 2013 年年会, Tokyo, Mar. 17, **2013**.
7. Xiaoyong Wu, Shu Yin, Qiang Dong, Tsugio Sato, “A High Visible Light Induced NO_x Gas Destruction Activity of Carbon Doped TiO_2.”, Summer school of Tohoku University, Sendai, Aug. 28, **2013**.
8. Xiaoyong Wu, Shu Yin, Qiang Dong, Tsugio Sato, “UV, Visible and Near-infrared Lights Photocatalytic Activity of (Yb,Er)-$NaYF_4$/C-TiO_2 Composite ”,化学系学協会東北大会, Sendai, Sep. 31, **2013**.
9. Xiaoyong Wu, Qiang Dong, Shu Yin, Tsugio Sato, “UV, Visible and Near-infrared Lights Induced NO_x Destruction Activity of

(Yb,Er)-$NaYF_4$/C-TiO_2 Composite",日本セラミックス協会第 26 回秋季シンポジウム, Shinshu University, Sep. 3, **2013**.

10. Xiaoyong Wu, Qiang Dong, Shu Yin, Tsugio Sato, "UV, Visible and Infrared Light Photocatalytic Activities of Carbon Doped TiO_2 Prepared by a Facile Calcination Assisted Solvothermal Method", the International Symposium on Inorganic and Environmental Materials 2013-ISIEM 2013, France, Oct. 27, **2013**.
11. Xiaoyong Wu, Qiang Dong, Shu Yin, Tsugio Sato, "UV, Visible and Near-infrared Lights Responsive Photocatalytic Activity of (Yb, Er)-$NaYF_4$/C-TiO_2 Composite", The 30th Japan-Korea International Seminar on Ceramics, Kyushu, Nov. 21, **2013**.
12. Xiaoyong Wu, Qiang Dong, Shu Yin, Tsugio Sato, "UV, Visible and Near-infrared Lights Induced Photocatalytic Activity of (Yb, Er)-$NaYF_4$/C-TiO_2 Composite ",東北大学多元物質科学研究所研究発表会，Sendai, Dec. 5, **2013**.
13. Xiaoyong Wu, Qiang Dong, Shu Yin, Tsugio Sato, "Preparation and Visible Light Induced NO_x Destruction Activity of C-$NaTaO_3$ and C-$NaTaO_3$/Cl-TiO_2", CIMTEC 2014-13th International Ceramics, Italy, June, 20, **2014**.
14. Xiaoyong Wu, Qiang Dong, Shu Yin, Tsugio Sato, "Facile Room-temperature Synthesis of Long Wavelength Visible Light Responsive Glycerol Modified BiOX",日本セラミックス協会 第 27 回秋季シンポジウム, Kagoshima, Sep. 9, **2014**.

AWARDS

1. “多元物質科学奨励賞”. “ソルボサーマル反応による紫外・可視・赤外光応答型光触媒応答性炭素ドープ参加チタンの合成と環境浄化機能.” 呉暁勇, Dec. 5, 2014.
2. "東北大学藤野先生記念奨励賞”. “紫外・可視・赤外光応ムの創製と環境浄化特性.” 呉暁勇, Sep. 18, 2014.
3. “東北大学研究所連携プロジェクト第5期平成25年度成果報告会優秀学生賞”. “Photocatalytic Performance of (Yb, Er)-$NaYF_4$/C-TiO_2 Composite Induced by UV, Visible and NIR Lights.”東北大学研究所連携プロジェクト第5期平成25年度成果報告会, 呉暁勇，殷シュウ, 佐藤次雄, Feb. 5, 2014.
4. “簸野奨学基金多元物質科学研究奨励賞”. 呉暁勇, Dec. 10, 2012.
5. “Young Research Encouragement Award”, “Visible Light Induced Photocatalytic Activities of C-TiO_2”,東北大学研究所連携プロジェクト第4期平成24年度成果報告会, 呉暁勇，殷シュウ, 佐藤次雄, Feb. 5, 2012.